University of Latvia
Faculty of Medicine and Life Sciences

Scandium radionuclide production and mass separation at CERN-MEDICIS

Edgars Mamis

Doctoral thesis

Submitted for the degree of Doctor of Sciences (Ph.D.)
in Natural Sciences (in the field of Chemistry)
Subfield of Physical Chemistry

Riga, Latvia
June 27, 2024

The doctoral thesis was carried out at the Chair of Physical Chemistry, Faculty of Medicine and Life Sciences, University of Latvia and the European Organization for Nuclear Research - Medical Isotopes Collected from ISOLDE (CERN-MEDICIS) from 2020 to 2024.

This work was supported by Latvian Council of Science, grant number: lzp-2021/1-0539 "Novel and efficient approach of medical ^{43}Sc, ^{44}Sc and ^{47}Sc radionuclide separation and purification from irradiated metallic targets towards radiopharmaceutical development for theranostics" and has received funding from the European Union's Horizon 2020 research and innovation programme under grant agreement No 101008571 (PRISMAP – The European medical radionuclides programme).

The thesis contains the introduction, 5 chapters, a reference list, 3 appendices.
Form of the thesis: dissertation in Natural Sciences (in the field of Chemistry), subfield of Physical Chemistry.

Supervisors:

1. Dr. Phys. Thierry Stora, European Organization for Nuclear Research
2. Assoc. Prof. Dr. Chem. Elīna Pajuste, University of Latvia

Co-supervisors:

1. Dr. Phys. Charlotte Duchemin, European Organization for Nuclear Research
2. Assoc. Prof. MD. Dr. Maija Radziņa, University of Latvia

Reviewers:

1. Assoc. Prof. Dr. Chem. Agris Bērziņš, University of Latvia
2. Dr. Chem. Nicholas Philip van der Meulen, Paul Scherrer Institute
3. Prof. Dr. Phys. Férid Haddad, University of Nantes

The thesis will be defended in a public session of the Promotional Committee of Chemistry, University of Latvia, at 13:00 on October 23, 2024 at the University of Latvia, Department of Chemistry, Jelgavas street 1, Riga, Latvia.

The thesis and the summary of the thesis are available at the Library of the University of Latvia, Raiņa Blvd. 19, Riga, Latvia.

This thesis is accepted for the commencement of the degree of Doctor of Philosophy in Natural Sciences on 12.07.2024 by the Doctoral Committee of Chemistry, University of Latvia.

Chairman of the Doctoral Committee _____ / Prof., Dr. Chem. Edgars Sūna/

Secretary of the Doctoral Committee _____ / Dr. Chem. Vita Rudoviča/

Abstract

Scandium radionuclide production and mass separation at CERN-MEDICIS. Mamis E., supervisors: Dr. Phys. Stora, T., Dr. Phys. Duchemin, C., Assoc. prof. Dr. Chem., Pajuste, E. and Assoc. prof. MD. Dr. Radziņa, M. Doctoral thesis in physical chemistry, 158 pages, 93 images, 40 tables, 236 references, 3 appendixes. In English.

In this thesis the metallic foil ^{nat}Ti, ^{nat}V and micrometric powder ^{nat}TiC target materials were investigated and used for medically applicable ^{43}Sc, $^{44g/m}$Sc and ^{47}Sc radionuclide production and mass separation at The European Organization for Nuclear Research (CERN)-Medical Isotopes Collected from ISOLDE (MEDICIS). Theoretical activity yields of Sc radionuclide production in Isotope Separation OnLine (ISOL) and cyclotron thick targets were estimated with Monte-Carlo codes and experimental cross sections.

Thermal Sc radionuclide release from irradiated metallic ^{nat}Ti and ^{nat}V foils was investigated to determine the impact of diffusion and adsorption processes during the mass separation and collection of radionuclides. Full Sc release from the metallic foil target materials was achieved within an hour at temperature ∼70–85 % of their corresponding material melting points.

Nevertheless, the collected Sc radionuclide activity was low (<100 kBq) even at higher target material temperatures. This led to a large program of target and ion source system (TISS) developments reported in this thesis to overcome the limiting factors associated with the gaseous particle interaction with the ISOL TISS structures. Operation parameters, various configurations and modifications of the ISOL TISS and their impact on the collection efficiency were investigated.

The aspects of Sc volatilization, molecule formation and release from ISOL target and ion source system, as well as atomic and molecular gas species ionization were analyzed. The released Sc radionuclides were mass-separated as atomic and molecular ion beams and collected for subsequent radiochemical purification. Various theoretical models were used to describe the different limiting factors of radionuclide collection efficiency, such as diffusion, molecule formation, desorption, effusion, ionization and radionuclide collection rate.

Keywords: SCANDIUM RADIONUCLIDES, MASS SEPARATION, MOLECULAR ION BEAMS, THERMAL RELEASE, TARGET MATERIALS, TARGET AND ION SOURCE SYSTEM, RADIOCHEMISTRY.

Anotācija

Skandija radionuklīdu ražošana un masas atdalīšana CERN-MEDICIS. Mamis E., zinātniskie vadītāji: Dr. Phys. Stora, T., Dr. Phys. Duchemin, C., Assoc. prof. Dr. Chem., Pajuste, E. and Assoc. prof. MD. Dr. Radziņa, M. Promocijas darbs fizikālajā ķīmijā, 158 lappuses, 93 attēli, 40 tabulas, 236 literatūras avoti, 3 pielikumi. Angļu valodā.

Šī darba ietvaros veikta metālisku ^{nat}Ti, ^{nat}V foliju un mikrometra izmēra daļiņu pulvera ^{nat}TiC mērķu materiālu izpēte ^{43}Sc, $^{44g/m}$Sc un ^{47}Sc radionuklīdu ražošanai, un izotopu masas atdalīšanai CERN-MEDICIS eksperimentā (Eiropas Kodolpētijumu organizācija - Medicīnā izmantojami izotopi, kas savākti no ISOLDE). Veikti teorētiskie aprēķini Sc radionuklīdu ražošanas iznākuma noteikšanai biezos ISOL (izotopu atdalīšana tiešsaistē) un ciklotronu mērķu materiālos, izmantojot Monte-Carlo simulāciju kodus un eksperimentāli noteiktās kodolreakciju šķērsgriezumu vērtības.

Lai novērtētu Sc difūzijas un adsorbcijas ietekmi masas atdalīšanas un radionuklīdu savākšanas gaitā, tika veikti termiskās Sc radionuklīdu izdalīšanas eksperimenti no apstarotiem metāliskiem ^{nat}Ti un ^{nat}V foliju mērķa materiāliem. Pilnīga Sc izdalīšana no metālisku foliiju mērķa materiāliem tika sasniegta stundas laikā, temperatūrā ∼70–85 % no attiecīgo metālu kušanas punktiem.

Neskatoties uz to, veicot masas atdalīšanu pat karsējot mērķa materiālus augstākās temperatūrās, masas atdalīto un savākto radionuklīdu aktivitāte bija zema (<100 kBq). Šie novērojumi noveda pie apjomīgas mērķa un jonu avota sistēmu (TISS) izpētes un attīstīšanas, lai samazinātu gāzveida daļiņu un ISOL mērķa un jonu avotu sistēmu materiālu mijiedarbību. Darbā veikta arī dažādu ISOL mērķa un jonu avotu sistēmas vadibas parametru, konfigurāciju, veikto modifikāciju izpēte un ietekme uz savākšanas efektivitāti.

Analizēta atomāra un molekulāra Sc gāzveida savienojumu jonizācija, kā arī gaistošu Sc molekulu veidošanās un izdalīšanās parametri no ISOL mērķa un jonu avotu sistēmām. Gan atomārā, gan molekulu veidā izdalītie Sc radionuklīdi tika atdalīti pēc to atommasas un savākti vēlākai attīrīšanai ar radioķīmiskām metodēm. Šajā darbā izmantoti dažādi teorētiskie modeļi, lai izpētītu un aprakstītu limitējošo faktoru, piemēram, difūzijas, molekulu veidošanās, desorpcijas, efūzijas, jonizācijas un savākšanas ātruma ietekmi uz radionuklīdu savākšanas efektivitāti.

Atslēgas vārdi: SKANDIJA RADIONUKLĪDI, MASAS ATDALĪŠANA, MOLEKULĀRO JONU KŪLIS, TERMISKĀ IZDALĪŠANA, MĒRĶA MATERIĀLI, MĒRĶA UN JONU AVOTA SISTĒMA, RADIOĶĪMIJA.

Acknowledgements

This thesis would not have been possible without the support of many people. I sincerely thank my supervisors for accepting me as a doctoral student to work in the CERN-MEDICIS and the University of Latvia, for their never-ending support, guidance, exciting and interesting discussions, patience and trust throughout and beyond this thesis.

Special thanks go to my mentor and friend Jāzeps Malnačs, who introduced me to radioactivity, radionuclides and guided me in learning and understanding practical application and radiation safety aspects. Most of all, for convincing me to take up doctoral studies.

This thesis would not be possible without Prof. Toms Torims, who made it possible and suggested the development of the thesis at the European Organization for Nuclear Research (CERN) with support throughout the whole time.

For the warm welcome at CERN, the introduction to all practical matters at MEDICIS and ISOLDE and numerous discussions, I am indebted to Charlotte Duchemin and Thierry Stora. Many thanks to Sebastian Rothe and Joachim Vollaire for their help and support from day one. For the great atmosphere and interesting discussions, I would like to thank the current and former members of the SY-STI-RBS section and office colleagues.

My deepest gratitude goes to the ISOLDE workshop team (Bernard Crepieux, Ermanno Barbero, Mike Owen, Mathieu Bovigny and Antoine Boucherie) who were always eager to share their expertise and help in practical matters. A special thanks to Bernard Crepieux for his dedication, impressive problem-solving skills and the ability to always find time to help assist and cheer up.

The success of this thesis is not imaginable without the CERN-MEDICIS operators Laura Lambert, Ralf Erik Rossel, Eric Chevallay and student Patrīcija Kalniņa, for their help at any time. Huge thanks go to the MELISSA team - Cyril Bernerd, Reinhard Heinke, Jake David Johnson and Ralitsa Mancheva who provided expertise in laser ionization, setup and operation of laser systems for various experiments.

Special appreciation goes to the Radiation Protection team (Alexandre Dorsival, Elodie Aubert, Matthieu Deschamps, Nadine Conan, Siria Maria Chiara Medici, Chris Theis and Fabio Pozzi) for their supervision, discussions, guidance, swift and efficient work, contributing significantly to the safe and smooth progression of the experiments and support throughout this thesis.

I sincerely thank my colleagues from the University of Latvia, especially Elīna Pajuste for her support and motivation, when I needed it the most as well Rūdolfs Jānis Zabolockis for being more of a mentor than a student and his help in preparation for the exams.

I would like to send my deepest gratitude to the Radionuclide Development group at Paul Scherrer Institute (PSI), Villigen, Switzerland for their help in providing samples for the research and their interest in cooperation even beyond the scope of this thesis. Special thanks also go to the CERN-CHARM facility and Robert Froeschl for providing invaluable support and the opportunity to activate the samples, enabling the successful execution of this research.

Last and most importantly, I would like to thank my family and parents (in latvian): *Paldies manai ģimenei - Kristīnei un Jēkabam par prieku, atbalstu, palīdzību un sapratni brīžos, kad nevarēju būt Jums blakus. Paldies Tomasam un Līgai par atputas mirkļiem un palīdzību brīžos, kad to vajadzēja visvairāk. Paldies maniem vecākiem Ivetai un Imantam par ieliktiem pamatiem fizikā un raksturā, kas palidzēja sasniengt šī darba rezultātus.*

Introduction

Cancer is a large 21^{st} century worldwide societal, public health, and economic problem. The global statistics for the year 2022, for example, indicate that there were almost 20 million new cases of cancer and close to 10 million cancer deaths, with indications that the annual number of new cases will reach 35 million by the year 2050 [1]. The overall scale of cancer and the diversity of cancer profiles emphasize the need for targeted cancer control and treatment measures. Investments in timely diagnostics and treatment are of utmost concern. Theranostics is a rapidly evolving personalized nuclear medicine approach, combining therapy and diagnostics. It implies cellular cancer diagnostics followed by non-invasive tumor treatment using drugs labeled with radionuclides - radiopharmaceuticals.

Most commonly such theranostic radiopharmaceutical pairs are created with radionuclides of different chemical elements, therefore the drug kinetics and sometimes their exact physico-chemical properties do match when therapeutic and diagnostic agents are compared. To resolve this issue, radionuclides of the same chemical element can be used to create so-called “matched pair” radiopharmaceuticals. They have the same chemical properties and pharmacokinetics that help in the efficient planning and monitoring of personalized targeted cancer treatment [2].

Scandium (Sc) is a promising candidate for the "matched pair" radiopharmaceutical development with ^{43}Sc, $^{44g/m}$Sc used for diagnostic and ^{47}Sc for therapeutic purposes. Another advantage of Sc radionuclides is that they decay into bio-compatible chemical elements, namely Ca and Ti. However, the availability of pure ^{43}Sc, $^{44g/m}$Sc and ^{47}Sc for clinical studies is still very limited, and their production is mostly undertaken with enriched titanium and calcium target materials. Even with rather expensive enriched target materials, the co-production of longer-lived radionuclides sometimes cannot be completely avoided, for example, ^{43}Sc with co-production of $^{44g/m}$Sc and vice versa from ^{43}Ca and ^{44}Ca.

The The European Organization for Nuclear Research (CERN)-Medical Isotopes Collected from ISOLDE (MEDICIS) specializes in a wide range of novel medical radionuclide extraction and purification by mass separation, produced in nuclear reactions from thick targets at CERN, or via externally irradiated samples from CERN-MEDICIS collaborator nuclear reactor and cyclotron facilities. The mass separation technique can be used to purify medical Sc radionuclides, which is not possible with conventional chemical methods. Because of the mass separation technique, cost-effective natural isotopic abundance target materials can be used for Sc radionuclide production.

Although mass-separated Sc radionuclides have been obtained for physics experiments before, the conditions of mass separation and achievable activity yields were not suitable for pre-clinical and clinical setting dose activity collections.

The aim of the work was to develop a routine method for high molar activity (TBq/μmol) medical Sc radionuclide production with the mass separation technique from cost-effective natural isotopic abundance and cyclotron-suitable target materials.

To achieve the aim of this work, the following **tasks** were proposed:

1. Investigate multiple, cyclotron-suitable natural isotopic abundance target materials for the production and mass separation of Sc radionuclides.
2. Study Sc radionuclide fractional thermal release from irradiated ^{nat}Ti and ^{nat}V foil target materials.
3. Investigate various Isotope Separation OnLine (ISOL) Radiactive Ion Beam (RIB) production methods and mass separation parameters with stable and radioactive Sc isotopes.
4. Identify and analyze the factors and limitations that impact Sc RIB formation and mass separation.
5. Engage in ISOL Target and Ion Source System (TISS) developments and prototype build to improve conditions of Sc radionuclide release and mass separation.
6. Perform the mass separation of a cyclotron-produced Sc radionuclide sample.
7. Develop and perform radiochemical separation method for the mass-separated Sc radionuclides to obtain a precursor, suitable for radiolabelling.

The scientific novelty of this work:

1. Thermal fractional Sc radionuclide release pattern from ^{nat}Ti and ^{nat}V multiply layered foil rolls was published. Preliminary data on Sc diffusion and adsorption constants from metallic ^{nat}V was obtained and estimated.
2. Sustainable and reproducible methods and parameters were determined for Sc radionuclide mass separation as molecular ion beams. Isotopically pure, high molar activity $^{44g/m}$Sc, ^{46}Sc, and ^{47}Sc were obtained and collected as mono-atomic and molecular ScF_2^+ ion beams.
3. ^{nat}V foil target material was used for the first time in delivering Sc radionuclide ion beams by mass separation.
4. A new two-step atomic Sc radionuclide laser resonance ionization scheme with titanium/sapphire (Ti:Sa) lasers was used and published for the first time.

The practical significance of this work:

The refined radionuclide thermal release setup and method is used to study irradiated target material radionuclide thermal release behavior and diffusion. The technique has already been applied for terbium (Tb), thulium (Tm) and barium (Ba) thermal release studies from irradiated natural tantalum ^{nat}Ta metallic foil rolls, to improve the mass separation and collection efficiency. The approach has the grounds of studying various ISOL target material radionuclide release kinetics also for the ISOLDE experiments. The

obtained experimental data from thermal release studies can also be utilized for radiation protection purposes, by benchmarking theoretical codes, used for radionuclide release simulations in case of fire accidents.

The obtained data from various target and ion source system modifications and prototypes will be used in further ISOL TISS developments, to improve their longevity and selectivity for more exotic radioactive ion beams.

The developed Sc radionuclide mass separation methods from various target materials serve as a tool to supply research centers with high molar activity and isotopically pure medical Sc radionuclides for translational research. The mass-separated high molar activity $^{44g/m}$Sc and ^{47}Sc radionuclides can be used in "matched pair" radiopharmaceutical development for cancer treatment. The obtained results can also serve as a basis for further research to upscale the mass-separated Sc and other refractory medical radionuclide activities to clinically relevant dose levels.

List of scientific publications:

1. **Mamis, E.**; Duchemin, C.; Berlin, V.; Bernerd, C.; Bovigny, M.; Chevallay, E.; Crepieux, B.; Gadelshin, V.M.; Heinke, R.; Hernandez, R.M.; Pajuste, E.; Stora, T. et al. Target Development towards First Production of High-Molar-Activity ^{44g}Sc and ^{47}Sc by Mass Separation at CERN-MEDICIS. *Pharmaceuticals* **2024**, 17, 390.
2. **Mamis, E.**; Kalnina, P.; Duchemin, C.; Lambert, L.; Conan, N.; Deschamps, M.; Dorsival, A.; Froeschl, R.; Ruiz, F.O.; Theis, C.; Vincke, H.; Crepieux, B.; Rothe, S.; Pajuste, E.; Stora, T. Scandium thermal release from activated natTi and natV target materials in mixed particle fields: Investigation of parameters relevant for isotope mass separation. *Nuclear Instruments and Methods in Physics Research Section B: Beam Interactions with Materials and Atoms* **2024**, 553, 165400.

List of scientific publications that were not included in this work:

1. Stora, T.; Duchemin. C.; Andreazza, W.; Aubert, E.; Bernerd, C.; Cocolios, T.E.; Deschamps, M.; Dorsival, A.; Duraffourg, M.; Fedosseev, V.; Somoza, J.F.; Gilardoni, S.; Grenard, J.L.; Heinke, R.; Johnson, J.D.; Koliatos, A.; Khan, Q.; Lambert, L.; **Mamis, E.**; Marsh, B.; Marzari, S.; Mitifiot, C.; Pozzi, F.; Prvakova, S.; Rinchet, J.Y.; Rodriguez, J.; Roesler, S.; Rossel, R.E.; Rothe, S.; Vollaire, J.; Widorski, M. CERN-MEDICIS: Operational indicators to support the production of new medical radionuclides by mass separation. *Journal of Physics: Conference Series* **2024**, 2687, 8, 082039, IOP Publishing.
2. Paļskis, K.; Korobeinikova, E.; Bogorada–Saukuma, D.; Camarda, A.; Taylor, R.; Benedetto, E.; **Mamis, E.**; Radziņa, M.; Ērglis, A.; Adliene, D.; Dosanjh, M. "Particle therapy-future for the Baltic states?" – synthesis of the expert workshop report. *Health and Technology* **2024**, 1-8.
3. Bernerd, C.; Johnson, J.; Aubert, E.; Au, M.; Barozier, V.; Bernardes, A.; Bertreix, P.; Bruchertseifer, F.; Catherall, R.; Chevallay, E.; Chrysalidis, K.; Duchemin. C.; Lambert, L.; **Mamis, E.**; Stora, T.; CERN-MEDICIS Collaboration et al. Production of innovative radionuclides for medical applications at the CERN-MEDICIS facility. *Nuclear Instruments and Methods in Physics Research Section B: Beam Interactions with Materials and Atoms* **2023**, 542, 137-143.

4. Radzina, M.; Saule, L.; **Mamis, E.**; Koester, U.; Cocolios, T.; Pajuste, E.; Kalnina, M.; Palskis, K.; Sawitzki, Z.; Talip, Z.; Jensen, M.; Duchemin, C.; Leufgen, K.; Stora, T. Novel radionuclides for use in Nuclear Medicine in Europe:where do we stand and where do we go? *EJNMMI radiopharmacy and chemistry* **2023**, 8(1), 27.
5. Saule, L.; Radzina, M.; Liepa, M.; Roznere, L.; Lioznovs, A.; Ratniece, M.; **Mamis, E.**; Vjaters, E. Recurrent prostate cancer diagnostics with 18F-PSMA-1007 PET/CT: a systematic review of the current state. *Diagnostics* **2022**, 12(12), 3176.
6. Saule, L.; Radzina, M.; Liepa, M.; Roznere, L.; Kalnina, M.; Lioznovs, A.; **Mamis, E.**; Mikelsone, M.; Biederer, J.; Vjaters, E. Diagnostic scope of ^{18}F-PSMA-1007 PET/CT: comparison with multiparametric MRI and bone scintigraphy for the assessment of early prostate cancer recurrence. *American journal of nuclear medicine and molecular imaging* **2021**, 11(5), 395-405.

List of conferences:

1. **Mamis, E.**; Duchemin, C.; Pajuste, E.; Stora, T. et al. Production by mass separation of non-conventional medical radionuclides at the CERN-MEDICIS facility, International Symposium on Trends in Radiopharmaceuticals (ISTR–2023) CN-310, 2023, Vienna, Austria.
2. **Mamis, E.**; Duchemin, C.; Kalniņa, P.; Pajuste, E.; Stora, T. et al. Production and mass-separation of $^{44-47}$Sc radionuclides at the CERN-MEDICIS facility", 3^{rd} International Conference on Radioanalytical and Nuclear Chemistry (RANC–2023), 2023, Budapest, Hungary.
3. **Mamis, E.**; Duchemin, C.; Kalniņa, P.; Zabolockis, R.J.; Pajuste, E.; Stora, T. et al. Target developments for Sc radionuclide mass-separation at CERN-MEDICIS facility, 3^{rd} CERN-Baltic international conference 2023 (CBC), 2023, Riga, Latvia.
4. **Mamis, E.**; Duchemin, C.; Kalniņa, P.; Pajuste, E.; Stora, T. et al. Mass separation of ^{44,47}Sc radionuclides at the CERN-MEDICIS facility, 81^{st} International Scientific Conference of University of Latvia, 2023, Riga, Latvia.
5. **Mamis, E.**; Duchemin, C.; Pajuste, E.; Stora, T. et al. Production, extraction and mass separation of medical ^{43,44g,47}Sc radionuclides at the CERN-MEDICIS facility, 2^{nd} CERN Baltic Group conference, 2022, Vilnius, Lithuania.
6. **Mamis, E.**; Duchemin, C.; Pajuste, E.; Stora, T. et al. Extraction and mass-separation of ^{43,44g,47}Sc radionuclides from irradiated natural Ti targets at the CERN-MEDICIS facility, 80^{th} International Scientific Conference of the University of Latvia, 2022, Riga, Latvia.
7. **Mamis, E.**; Duchemin, C.; Pajuste, E.; Stora, T. et al. Mass separation of ^{43,44g,47}Sc radionuclides from irradiated natural Ti targets at the CERN-MEDICIS facility, 80^{th} International Scientific Conference of the University of Latvia, 2022, Riga, Latvia.
8. **Mamis, E.**; Duchemin, C.; Pajuste, E.; Stora, T. et al. Development of molecular beams for extraction and mass separation of ^{43,44g,47}Sc radioisotopes from irradiated natural titanium targets at the CERN-MEDICIS facility, 1^{st} CERN Baltic Group conference, 2021, Tartu, Estonia.

Contents

Acronyms

AIS	Auto-Ionization State	128
amu	atomic mass unit	20, 28, 32, 33, 75, 94
BDE	Bond Dissociation Energy	106, 107
BET	Brunaeur, Emmett and Teller	45, 72
BSE	Backscattered Electrons	44
CE	Cluster Emission	3
CERN	The European Organization for Nuclear Research	4, 27, 40, 44, 80
CHARM	CERN High Energy Accelerator Mixed-field	23, 40, 49
CoA	Certificate of Analysis	74
CT	Computed Tomography	164
CZT	Cadmium Zinc Telluride	43
DGA	Diglycolamide	13, 36, 131, 132
DI	Deionized	36, 131
dim	Dimensionless unit	88
DL	Detection Limit	54
DPMJET	Dual Parton Model and JET	39
EAF	European Activation File	40
EBIS	Electron Beam Ion Source	16
EDX	Energy-Dispersive X-ray spectroscopy	44, 73
EMPIRE	Nuclear Reaction Model Code	3
ENDF	Evaluated Nuclear Data File	40
EOB	End Of Beam	23, 24, 80
EOC	End Of Collection	19, 43, 99, 101, 123
EXFOR	Experimental Nuclear Reaction Data	80
FE	Field Emission	44
FEBIAD	Forced Electron Beam Induced Arc Discharge	27, 29, 85, 122
FKK	Feshbach, Kerman and Koonin developed energy dissipation model	3
FLUKA	FLUktuierende KAskade	23, 39, 76, 77, 80, 99
FRS	Fraction Reaching Surface	41, 59

GDP	Global Desorption Probability	42, 60
GNASH	statitistical/preequilibrium nuclear reaction code	3
GPS	General Purpose Separator	16, 78
HAVAR	Heat Treatable Cobalt Base Alloy	10
HIE-ISOLDE	High Intensity and Energy ISOLDE	16
HPGe	High Purity Germanium	42, 50, 123, 124
HRS	High Resolution Separator	16, 22, 78, 80
HSC	Enthalpy (H), entropy (S) and heat capacity (Cp)	39, 104
IAEA	International Atomic Energy Agency	83
ICP-MS	Inductively Coupled Plasma - Mass Spectrometry	131, 132, 134, 137
ICP-OES	Inductively Coupled Plasma - Optical Emission Spectroscopy	134
IEC	Ion Exchange Chromatography	12, 13, 36, 38
INC	Intra-Nuclear Cascade	4
IP	Ionization Potential	26, 27
ISIS	ISolde Irradiation Station	17, 22, 78
ISOCS	In Situ Object Counting System	42
ISOL	Isotope Separation OnLine	11, 15, 19, 45, 66
ISOLDE	Isotope Separation OnLine DEvice	4, 16, 27, 48, 67, 103
IT	Isomeric Transition	3
JEFF	Joint Evaluated Fission and Fusion File	40
LOD	Limit of Detection	132
MC	Monte-Carlo	39
MCNP	Monte Carlo N-Particle Transport	42
MDA	Minimum Detectable Activity	50, 54
MEDICIS	Medical Isotopes Collected from ISOLDE	4, 17, 27, 68, 133
MELISSA	MEDICIS Laser Ion Source for Separator Assembly	27, 32, 97
MWCNT	MultiWalled Carbon NanoTubes	119
ODF	Out-Diffused Fraction	40, 42, 59–61, 66
ORNL	Oak Ridge National Laboratory	68
PEANUT	PreEquilibrium Approach to NUclear Thermalization	39
PEEK	Polyether ether ketone	162
PET	Positron Emission Tomography	6, 13
PoT	Protons on Target	22
ppb	parts per billion	73
ppm	parts per million	73
PS	Proton Synchrotron	23
PSB	Proton Synchrotron Booster	4, 16, 22, 39, 69

PSI	Paul Scherrer Institute	86, 100, 124
PTFE	PolyTetraFluoroEthylene	33
QE	Quasiequilibrium	35, 110
REX	Radioactive Beam EXperiment	16
RGA	Residual Gas Analyzer	33
RIB	Radioactive Ion Beam	15, 25, 26, 32, 48, 69
RILIS	Resonant Ionization Laser Ion Source	27, 85
RPH	Radiopharmaceutical	8, 12, 36
SC	Synchrocyclotron	16, 17, 69
SE	Secondary Electron	44
SEM	Scanning Electron Microscopy	44, 73, 117, 119
SF	Spontaneous Fission	3
SOC	Start Of Collection	76, 99, 110
SPECT	Single-Photon Emission Computed Tomography	6, 13
SRIM	The Stopping and Range of Ions in Matter	80, 83
SSA	Specific Surface Area	45, 72, 112
TALYS	Nuclear Reaction Modeling Code	3, 80
Ti:Sa	Titanium Sapphire laser	128
TISS	Target and Ion Source System	15, 18, 25, 31, 47, 98
TREC	Traceability of potential Radioactive Equipment at CERN	49
TRIUMF	TRI University Meson Facility	68
TRU	Transuranium	36
TTY	Thick Target Yield	80, 81
UTEVA	Uranium and TEtra-Valent Actinide	36
VADIS	Versatile Arc Discharge Ion Source	27, 29–31, 45, 85
VADLIS	Versatile Arc Discharge Laser Ion Source	129

Symbols

a_{A}	Value factor of adsorbate A [V^{-1}]	64
A	Radioactivity [Bq]	2, 54, 81
$A_{Collected}$	Radionuclide activity at the end of mass separation [Bq]	99
A_{Start}	Radionuclide activity at the start of mass separation [Bq]	99
amu	Atomic mass unit [a.u.]	122
A_{pn}	Atomic mass number or number of protons and neutrons in a nuclei	1, 3, 15
A_R	Richardson's constant [$\mathrm{Acm}^{-2}\mathrm{K}^{-2}$)]	29, 30
a_s	Characteristic dimension parameter [m]	62
N_A	Avogadro constant, 6.022×10^{23} [mol^{-1}]	45, 81
B	Magnetic field [T]	15
C_b	BET constant [dim]	45
D	Diffusion coefficient [$\mathrm{m}^2\,\mathrm{s}^{-1}$]	xxii, 41, 64, 103
d	Distance between the cathode and anode grid [m]	30
D_0	Pre-exponential frequency factor of the Arrhenius expression for diffusion [$\mathrm{m}^2\,\mathrm{s}^{-1}$]	41, 66
ΔH_{ads}	Enthalpy of adsorption [$\mathrm{kJ\,mol}^{-1}$]	64–66, 88, 104
d_{half}	Half of a foil thickness [cm]	62
ΔH^0_{DA}	Standard de-sublimation enthalpy of pure adsorbate A [eV]	65
DH^o	Bond dissociation energy [$\mathrm{kJ\,mol}^{-1}$]	104, 106
ΔH_{OVB}	Enthalpy of surface vacancy formation of adsorbent B [eV]	65
ΔH_{sub}	Reaction enthalpy change [$\mathrm{kJ\,mol}^{-1}$]	109
$\Delta \bar{H}_s$	Enthalpy of first partial molar solution [$\mathrm{kJ\,mol}^{-1}$]	64, 65, 102
ΔH_{sub}	Enthalpy of sublimation [$\mathrm{kJ\,mol}^{-1}$]	102
ΔH_{VVB}	Enthalpy of volume vacancy formation in adsorbent B [eV]	65
DNN	Distance between the nearest atomic neighbor in the surface material lattice [cm]	42
ΔH_{sub}	Reaction entropy change [$\mathrm{kJ\,mol}^{-1}$]	109
D_w	Weight distribution ratio for resin	xxii, 37
E	Energy [J]	15
e	Elementary charge $e \approx 1.602 \times 10^{-19}\,\mathrm{C}$	30
E_a	Activation energy [$\mathrm{J\,mol}^{-1}$]	41
e_{corr}	Dimension correction factor [eV^2]	64
E_{des}	Desorption activation energy [$\mathrm{kJ\,mol}^{-1}$]	42

E_{exc}	Nuclear reaction activation energy [MeV]	4
ϵ_0	Vacuum permittivity $\epsilon_0 \approx 8.854 \times 10^{-12}\,\mathrm{F\,m^{-1}}$	30
ϵ_{col}	CERN-MEDICIS radionuclide collection efficiency	98, 99
ϵ_{feb}	Ionization efficiency of a FEBIAD source	29
ϵ_{ion}	Ionization efficiency	30
$\epsilon_{\mathrm{molecule}}$	Efficiency of molecule formation (chemical yield)	106
$\epsilon_{\mathrm{Stable}}$	Stable sample mass separation efficiency	98
$\epsilon_{\mathrm{transm}}$	Mass separator transmission efficiency	122
f	Global fraction of extracted ions from the FEBIAD/VADIS ion source	29, 30, 121, 122
F	Faraday constant $F = 96485$ [$\mathrm{C\,mol^{-1}}$]	98
f_{elec}	Factor characterizing electron transport from cathode to ionization volume [a.u.]	121
F_{rel}	Fraction of radionuclides released from the target material	54, 56, 57
F_{rem}	Fraction of radionuclides remaining in target material	53, 62
FRS	Fraction of isotopes reaching the matrix surface in a given time and temperature [%]	40, 41
GDP	Global radionuclide desorption probability at a given time and temperature [%]	40
$\hat{t}$	Diffusion number (time divided by a characteristic diffusion time) [a.u.]	62, 63
V_{ioniz}	First ionization potential [eV]	29
$I_{\mathrm{Separated}}$	Separated ion beam current [A]	98, 122
I_{Total}	Total ion beam current [A]	122
j_{cath}	Richard-Dushman current density for electrons [$\mathrm{A\,m^{-2}}$]	30
$j_{e,cl}$	Child-Langmuir-limited current density for electrons [$\mathrm{A\,m^{-2}}$]	30
$\mathrm{k_B}$	Boltzmann constant $\mathrm{k_B} \approx 8.617 \times 10^{-5}\,\mathrm{eV\,K^{-1}}$	29, 30, 42
K_{eq}	Reaction equilibrium constant [a.u.]	39, 109
k_-	Backward reaction rate coefficient [a.u.]	39
k_+	Forward reaction rate coefficient [a.u.]	39
l	Number of electrons in the valence shell	29
λ	Decay constant of an radioisotope [$\mathrm{s^{-1}}$]	2, 54, 81
M	Atomic mass [$\mathrm{gmol^{-1}}$]	15, 29, 35, 81
m_A	Target material atomic mass [$\mathrm{gmol^{-1}}$]	4
m_a	Projectile atomic mass [$\mathrm{gmol^{-1}}$]	4
m_e	Electron mass [kg]	30
N	Neutron number or number of neutrons in a nucleus	1, 2
n_{n}	Number density of neutrals [$\mathrm{m^{-3}}$]	30
n_e	Electron density in a plasma [$\mathrm{m^{-3}}$]	30
N_{evapi}	Formed and evaporated molecule i amount [pps]	106
n_{in}	Neutrals admitted to the ion source per unit time [$\mathrm{s^{-1}}$]	30
N_{maxi}	Maximum molecule amount i, that can evaporate from surface [pps]	106
n_{sample}	Stable isotope sample amount [mol]	98
N_t	Number of radionuclides present at time t	2
ν	Effusion time constant [$\mathrm{s^{-1}}$]	88
n_{wc}	Number of wall collisions [dim]	88

n_{WSA}	Electron density at the Wigner-Seitz cell boundaries of adsorbate A [density units]	64
n_{WSB}	Electron density at the Wigner-Seitz cell boundaries of adsorbent B [density units]	64
P	Pressure [Pa]	45
p	Partial pressure [Pa]	109
P_0	Saturation pressure [Pa]	45
P_{gsc}	Chemical group specific constant [$\mathrm{V}-1\mathrm{cm}^{-2}$(density units)$^{-1/3}$]	64
ϕ	Particle flux [pps]	81
Φ_{A}	Electro-negativity parameter of the adsorbate A [V]	64
Φ_{B}	Electro-negativity parameter of the adsorbent B [V]	64
p_{i}	Partial pressure of species i [Pa]	35, 36
p_{vap}	Saturation vapour pressure [mbar]	69, 75
Q	Absorbed or released energy during a nuclear reaction [MeV]	4
q	Ion charge state	15
Q_a	Diffusion activation energy [$\mathrm{J\,mol}^{-1}$]	66
R	Universal gas constant, $R \approx 8.314\mathrm{J\,mol}^{-1}\,\mathrm{K}$	35, 41, 88, 109
r	Bending radius of the ion beam [m]	15
ρ	Material density [gcm^{-3}]	81
R_i	Evaporation rate of the formed volatile species [$\mathrm{m}^{-2}\mathrm{s}^{-1}$]	35, 36
R_{ioniz}	Ionization rate per unit volume [m^{-3}]	30
R_{m}	Chemical group specific constant [$\mathrm{V}^{-1}\mathrm{cm}^{-2}$(density units)$^{-1/3}$]	64
S_b	Surface area of the bulk matrix [cm^2]	41
σ	Radionuclide production cross section [cm^2]	81
σ_{ion}	Ionization cross section [m^2]	30
σ_{mol}	Adsorbate molecule cross section [m^2]	45
S_{out}	surface of the outlet hole [cm^2]	29
SSA	Specific Surface Area [$\mathrm{m}^2\mathrm{g}^{-1}$]	45
T	Temperature [K]	29, 30, 35, 36, 41
t	Time [s]	2, 54, 62
$t_{1/2}$	Half-life time of an radioisotope [s]	2, 99
τ_0	Period of oscillation perpendicular to the surface [s]	88
τ_a	Mean adsorption sojourn time (single encounter) [s]	88
τ_d	Characteristic diffusion time [s]	62
τ_f	Mean time of flight between two collisions [s]	88
τ_v	Effusion mean delay time [s]	88
t_Δ	Time between the start of collection and collected sample measurement [s]	99
t_{irr}	Irradiation time [s]	81
T_m	Melting temperature [K]	52, 62, 66, 73, 90
T_s	Surface temperature [K]	88
t_T	Time at a given temperature T [s]	41, 42
U	Potential difference [V]	29, 30
u	nucleon	39

Γ_i	Adsorption rate at which molecules are equilibrated [$m^{-2}s^{-1}$]	35, 36
V_A	Atomic volume of pure adsorbate A [cm^3]	64
V_a	Volume of adsorbed adsorbate [m^3]	45
V_{AL}	Effective atom volume of the adsorbate A [cm^3]	64
V_B	Atomic volume of pure adsorbent B [cm^3]	65
V_b	Volume of the bulk matrix [cm^3]	41
V_{ml}	Adsorbate monolayer volume [m^3]	45
v_e	Relative velocity between electrons and ions [cm/s]	30
V_{source}	Volume of the ionization region [m^3]	30
$V_{m,sPT}$	Molar volume of 1 mol N_2 at standard temperature and pressure [m^3mol^{-1}]	45
W	Work function [eV]	26, 29, 30, 35
w_i	Target material chemical purity mass fraction	81
Z	Atomic number or number of protons in a nuclei	1–4, 15
z	Target thickness [cm]	81
ζ_i	Equilibrium probability	36, 110–113
Z_i	Collision rate for molecules of species i with a solid surface [$m^{-2}s^{-1}$]	35

List of Figures

1 Literature review and background

Contents

1.1 Radioactivity

An isotope is a nuclide with the same atomic number or number of protons in a nucleus Z but a different mass number A_{pn}[1] . The nucleus or core of an atom consists of a number of protons Z and neutrons N. Most combinations of Z and N form unstable nuclei, called radioactive isotopes or radionuclides. In a nuclear chart, the so-called "proton-rich" (neutron deficient) and "neutron-rich" (excess of neutrons) isotopes can

[1] The atomic mass number or nucleon number is typically referred to by symbol A. In this work, the abbreviation A will be used for radionuclide activity.

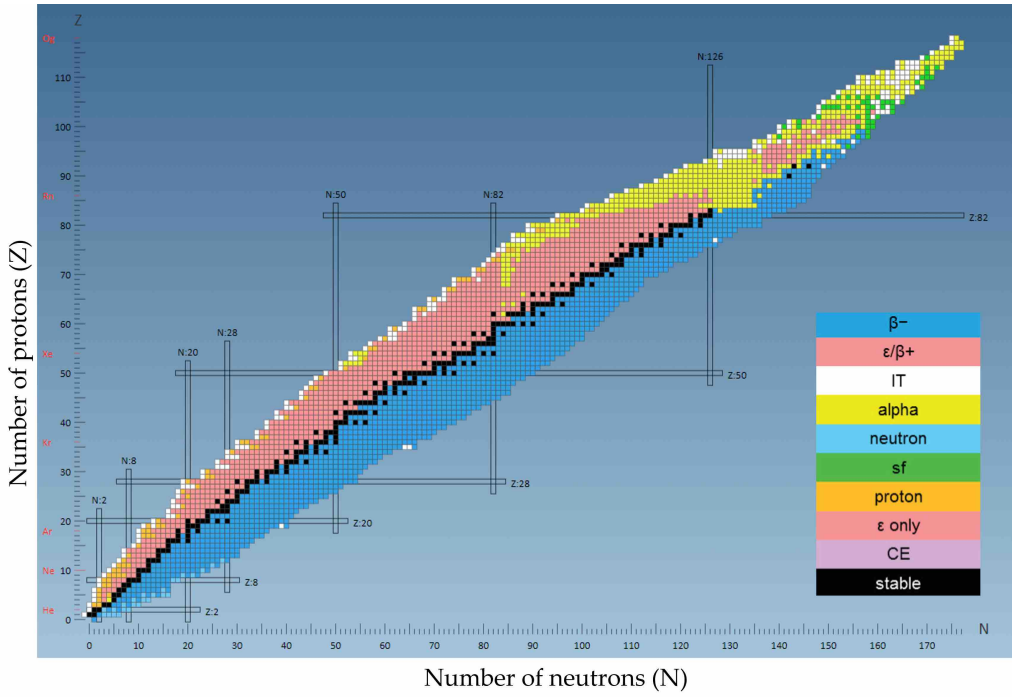

Figure 1.1: The chart of nuclides [3].

be distinguished, compared to the stable nuclei (see Figure 1.1). The stable nuclei in the nuclear chart are typically reflected in black color.

The stable nuclides deviated from a line of stability (Z=N) because the repelling Coulomb force increases with a higher proton amount in the nucleus and thus more neutrons are needed to mitigate this repulsion and form a stable nucleus.

The radionuclides transform into lower energy configuration (eventually stable) nuclides through the processes, called radioactive decay. The radioactive decay has a stochastic nature and its rate is described by the half-life of the nuclide $t_{1/2}$ (see equation 1.1). The range of half-lives is vast and ranges from $\sim 10^{-24}$ s to virtually infinite $\sim 10^{31}$ s [4].

$$-\frac{dN_t}{dt} = \frac{ln(2)}{t_{1/2}} N_t = \lambda N_t = A \tag{1.1}$$

where N_t is the number of radionuclides present at time t, t is the time [s], $t_{1/2}$ is the half-life of the radionuclide [s], λ is the decay constant [s^{-1}] and A is the radionuclide activity. The radionuclide activity A (also referred to as a just activity) is the number of decays per second and is given in Bq = s^{-1}. The activity after a given decay time can be calculated through equation 1.2.

$$A = A_0 e^{-\lambda t} \tag{1.2}$$

where A_0 is the radionuclide activity at time t = 0 [Bq].

Radioactive decay can be accompanied by four types of radiation: alpha (α), beta (β), gamma (γ) and neutrinos (ν) [5]. The α decay is the emission of a positively charged particle, identical to helium nucleus ($^4_2He^{2+}$), reducing the starting nucleus A_{pn} by 4 and Z by 2. α emission is typically observed from large radionuclide decay ($Z > 83$), however with few exceptions. After β^+ decay of a radionuclide, the Z is reduced by 1. Three types of β decay can be observed: electron emission (β^-), positron emission (β^+) and electron capture (ϵ). In electron capture, the inner shell electron is captured by the nucleus, emitting an X-ray and a neutrino [4, 5]. Typically after the α and β decay, the nucleus is left in an excited state. During deexcitation where nucleus is brought to the ground state, a highly energetic γ-ray photon is usually emitted. The γ-rays from a radionuclide decay are a characteristic of each radionuclide and are used to identify isotopes in γ-ray spectrometry [5]. There are also more exotic decay modes, such as proton decay, beta-delayed α decay, neutron and proton emission, Spontaneous Fission (SF), Isomeric Transition (IT) and Cluster Emission (CE) [6].

1.1.1 Nuclear reactions

Radioactivity can be artificially induced in non-radioactive materials and is known as activation by transforming some of the material stable nuclei into unstable ones. The activation can also occur in already radioactive materials, resulting a different unstable nuclei. This transformation is known as a nuclear reaction. It can be explained as a binary collision that changes nucleon-nucleon associations in nuclei and produces different nuclei via the exchange of nucleons or fusion.

Inelastic excitation is a type of interaction, where an incident particle excites the nucleus. The inelastic excitation may form an intermediate-composite nucleus that usually decays through a binary exit channel. If the entrance channel is lost during the composite formation, the intermediate is called a compound nucleus that decays in time longer than $\sim 10^{-21}$ s. Direct reactions bypass the compound nucleus stage and occur in the time frame of $\sim 10^{-23}$ s (see Figure 1.2) [7]. Multistep Compound Model (Feshbach, Kerman and Koonin developed energy dissipation model (FKK)), which dissipates entrance channel energy and disperse it statistically among all nucleon degrees of freedom, can be used to predict nuclear reaction products with codes such as Nuclear Reaction Model Code (EMPIRE), Nuclear Reaction Modeling Code (TALYS) and statitistical/preequilibrium nuclear reaction code (GNASH) [7, 8].

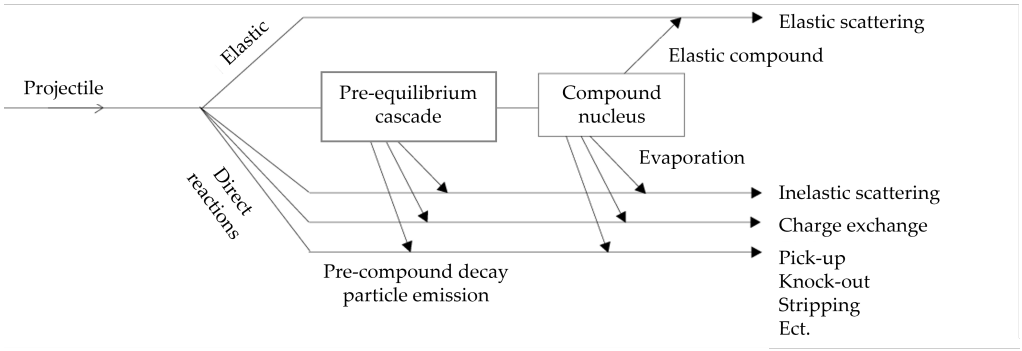

Figure 1.2: Elastic and inelastic reaction scheme [9].

In the compound-nucleus model, the capture of the projectile followed by random shar-

ing of the energy among the nucleons in the compound nucleus, reaching thermal equilibrium and evaporation of particles from the compound nucleus, can be distinguished as separate steps. It means that the compound nucleus can be formed in different entrance channels, but its subsequent decay into evaporation residues is independent of its mode of formation [4]. The excitation energy of the compound nucleus is given by equation 1.3 [10].

$$E_{exc} \approx -\frac{m_A + m_a}{m_A} \cdot Q \tag{1.3}$$

where E_{exc} is the nuclear reaction activation energy [MeV], m_A is the target material atomic mass [g/mol], m_a is the projectile atomic mass [g/mol] and Q is the absorbed or released energy during a nuclear reaction [MeV].

Radionuclide production can be induced by the collision of the target material with photons, electrons, mesons, neutrons, protons, antiprotons or light and heavy ions [5]. Depending on the projectile and its energy, different nuclear reactions can occur with their own independent probability - cross section or excitation function. Cross section is used to determine produced nuclide and its amount per incident particle and is expressed in cm^2 or barn [6,7].

At The European Organization for Nuclear Research (CERN)-Medical Isotopes Collected from ISOLDE (MEDICIS) and CERN-Isotope Separation OnLine DEvice (ISOLDE) the targets are irradiated with a pulsed beam of 1.4 GeV protons from CERN-PSB. This incident proton energy is significantly higher than the interaction energy of nucleons in a nuclei. The de Broglie wavelength of these projectiles is much smaller than the average inter-nucleon separation distance in the nucleus. Therefore the main interaction is collisions between the incident particle and single nucleons, which generates a cascade of scatterings in three dimensions until the energy is dissipated. It can be described by Intra-Nuclear Cascade (INC) model as shown in Figure 1.3 for reactions well above Fermi energy (> 100 MeV) [6,7,11]. The INC model uses experimental nucleon-nucleon scattering cross sections and angular distributions as a function of energy. The Fermi gas model with Coulomb barrier effects are used to evaluate fast cascade particles that are either thermalized and converted into excitation energy or escape the Fermi gas model within $1x10^{-22}$ s [7,11].

Latter models implement a pre-equilibrium stage after INC where incident particle and newly created nucleons reach a threshold energy of 10–30 MeV and are considered "adsorbed" by the nucleus, improving accuracy compared to experimental data [12]. The following process is deexcitation of the excited nucleus through spallation (also referred to as evaporation), fragmentation, fission or multi-fragmentation as shown in Figure 1.4. The deexcitation step is significantly slower than the INC with time frame of $1x10^{-18}$ s. Products of the spallation process are light particles or single nucleons that are emitted from the nucleus [13]. This mode of deexcitation produces isotopes 10–20 Z below the target material Z. Spallation reactions are also used for neutron production in neutron spallation source facilities by bombarding thick high-density targets with high current (intensity) proton beams [6]. Fusion-evaporation can occur when two nuclides with sufficient energy collide, overcoming the Coulomb barrier and fusing together. Such mode produces more neutrons than protons before γ-decay and therefore neutron

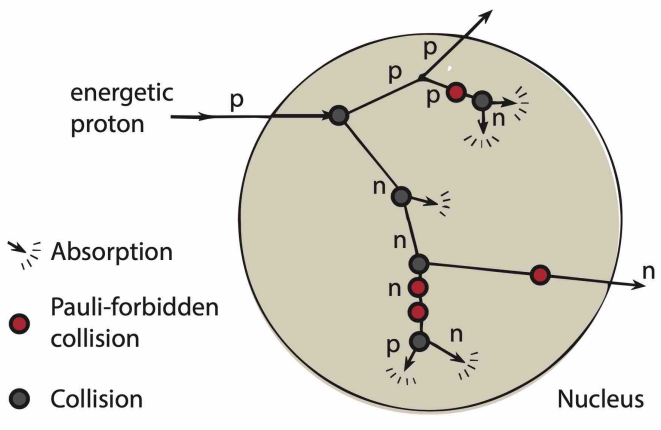

Figure 1.3: Intra-nuclear cascade model. Adapted from [11].

deficient radionuclides [6].

Fragmentation products are a vast variety of low-mass range nuclides but can extend to fission range masses. It typically occurs at high excitation energies with over 50 MeV. A hot nucleus can also break up due to thermal instabilities causing multi-fragmentation [6, 11]. Fission typically happens in heavy nuclides and the neutron-rich side of the nuclear chart. Fissility (probability of fission) is proportional to Z^2/A because of Coulomb repulsion in heavy elements that overcome short-range attractive forces of nucleons. Fission yields high energy projectiles typically around 1/3 and 2/3 of the original nuclide mass [5, 6].

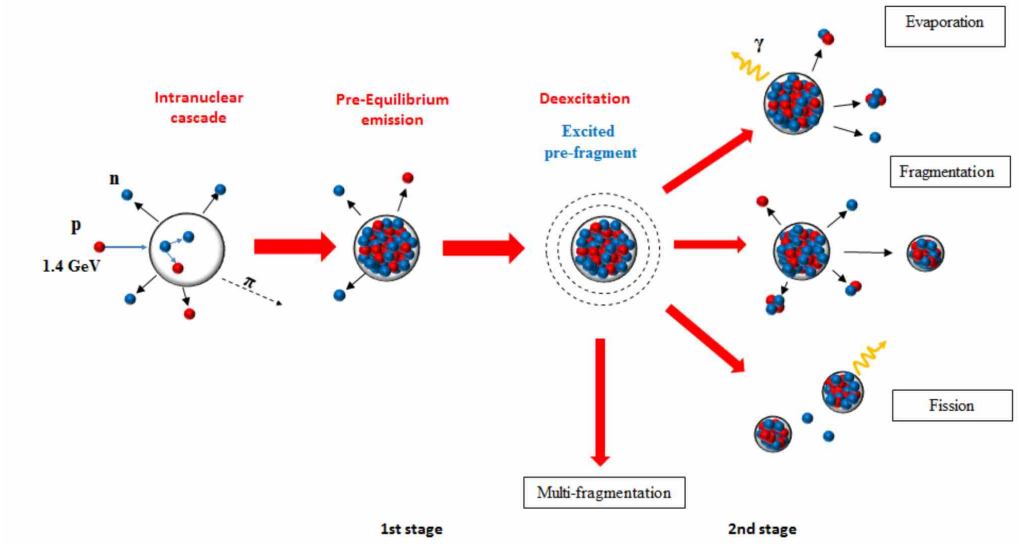

Figure 1.4: High-energy nuclear reactions [14].

1.2 Scandium radionuclides

1.2.1 Medical interest

Theranostics is a rapidly evolving personalized nuclear medicine approach, combining therapy and diagnostics. It implies cellular cancer diagnostics followed by non-invasive tumor treatment using drugs, labeled with radionuclides. Most commonly such theranostic drug pairs are created with radionuclides of different chemical elements such as the diagnostic ^{68}Ga or ^{18}F paired with therapeutic ^{177}Lu [15]. Therefore the drug kinetics and sometimes their exact physico-chemical properties do not exactly match when therapeutic and diagnostic agents are compared. To resolve this issue, radionuclides of the same chemical element can be used to create so-called “matched pair” radiopharmaceuticals. They have the same chemical properties and pharmacokinetics that help in the efficient planning and monitoring of personalized targeted cancer treatment [2]. With the use of "matched pair" radiopharmaceuticals the received dose estimation and pharmacokinetics in the body could better be understood and therefore optimized [16].

A perfect candidate for "matched pair" radiopharmaceuticals development is scandium (Sc). ^{43}Sc ($T_{1/2}$ = 3.891(12) h [17]) is a positron (β^+) emitter that holds great potential for immuno-Positron Emission Tomography (PET) and macro-molecular imaging studies, making it valuable for extended PET examinations [18]. ^{44g}Sc ($T_{1/2}$ = 4.042(25) h [17, 19]) is another promising β^+ emitter for PET and has already been translated to successful in-human proof of concept studies conducted in clinical setting [20, 21]. ^{47}Sc ($T_{1/2}$ = 3.3492(6) d [17, 19]) is a β^- emitter with a 159.4 keV (68.3 %) γ-ray emission that would be suitable as the therapeutic match and applications in Single-Photon Emission Computed Tomography (SPECT) imaging [22]. ^{47}Sc shows potential for use in radioimmunotherapy by being attachable to monoclonal antibodies and conjugates [23].

An advantage of Sc radionuclides is that they decay into bio-compatible chemical elements, namely Ca and Ti. While ^{43}Sc ($T_{1/2}$ = 3.89 h) and ^{44g}Sc ($T_{1/2}$ = 4.04 h) have similar half-life and positron emission probabilities, ^{43}Sc shows an advantage over ^{44g}Sc by the absence of high-energy γ-ray emission (1157 keV [19]) and therefore reduced radiological hazards. On the other hand, the ^{44g}Sc has the potential in a new 3-γ imaging technique, where the line of response is obtained by the two coincidence photons from positron annihilation and the third γ-ray, emitted as a prompt gamma, helps to provide better localization of the annihilation point. This approach enables higher image quality and reduced dose to the patient [24].

1.2.2 Production of Sc radionuclides

^{43,44g}Sc and ^{47}Sc availability for clinical studies is very limited and their production is mostly done with enriched titanium (Ti) and calcium (Ca) target materials. The most common and efficient production of ^{43}Sc and ^{44g}Sc proceeds via cyclotrons using low-energy protons (<30 MeV), deuterons or alpha particles on natural isotopic abundance and enriched Ca targets. Both ^{43}Ca and ^{44}Ca are present in low quantities in ^{nat}Ca. However, due to limited enrichment and abundance, the use of enriched Ca targets significantly increases production costs. Furthermore, ^{44m}Sc ($T_{1/2}$ = 58.61 h) is co-produced in most cases (see Table 1.1) [25].

The ^{47}Sc radionuclide, as the therapeutic counterpart in Sc “matched pair”, can be ef-

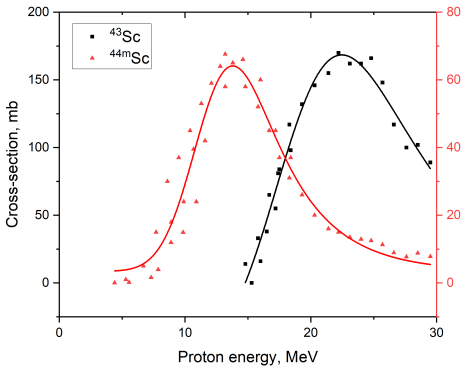

(a) ^{43}Sc and ^{44m}Sc production cross sections

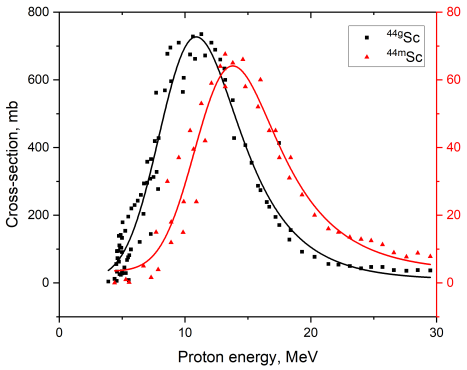

(b) ^{44g}Sc and ^{44m}Sc production cross sections

Figure 1.5: ^{43}Sc, ^{44g}Sc and ^{44m}Sc production cross sections of enriched ^{44}Ca irradiation by protons [26].

ficiently produced in nuclear reactors by activating enriched ^{47}Ti, which is naturally present in ^{nat}Ti (^{46}Ti 8.25%, ^{47}Ti 7.44%, ^{48}Ti 73.72%, ^{49}Ti 5.41%, ^{50}Ti 5.18%). ^{47}Sc is produced by activating ^{47}Ti through ^{47}Ti(n,p)^{47}Sc reaction. However, this route requires access to fast neutrons (> 1 MeV). Although highly enriched $^{47}TiO_2$ material is not as costly and rare as enriched ^{44}CaO, this production route yields with ^{46}Sc via ^{47}Ti(n,pn)^{46}Sc reaction (see Figure 1.6a) [27]. The scarce availability of nuclear reactors with necessary neutron energy fosters the use of accelerators for production. The most common accessible and commercially available cyclotrons can accelerate protons and in some cases deuterons and alpha particles up to energies of 18 MeV. Several routes by using intermediate (<30 MeV) or medium (30–70 MeV) energy cyclotrons and enriched titanium (Ti), calcium (Ca) or vanadium (V) target materials and accelerated protons or deuterons have been investigated for the production of ^{47}Sc. All of them present similar production cross sections (ranging from 30 to 60 mb), but show different production costs due to the availability of the enriched material [28].

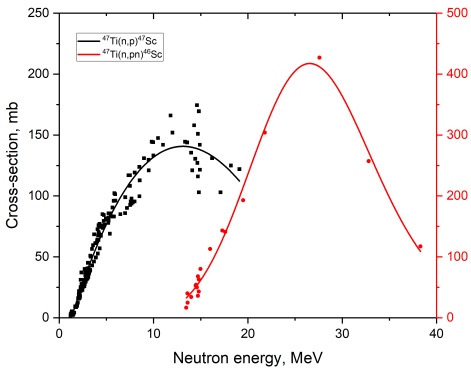

(a) ^{47}Sc and ^{46}Sc production with neutrons from ^{47}Ti

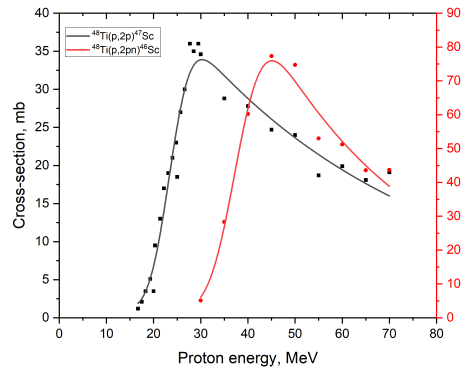

(b) ^{47}Sc and ^{46}Sc production with protons from ^{48}Ti

Figure 1.6: Enriched ^{47}Ti and ^{48}Ti excitation cross sections for ^{47}Sc and ^{46}Sc production [26]

Less common production routes involve photonuclear reactions in enriched ^{48}Ti target material [29] as well as ^{44}Ca and ^{51}V irradiation with alpha beams [30]. Same as in

^{44g}Sc production, ^{47}Sc is accompanied by long-lived, high γ-ray energy ^{46}Sc and ^{48}Sc contaminants (see Table 1.1). These types of nuclear reactions require more specific accelerator types.

Although acceptable radionuclidic purity Sc radionuclide production with cyclotrons and nuclear reactors is possible from enriched target materials (e.g. ^{43,44,46,48}Ca), this route is not sustainable in terms of production cost or availability of neutron irradiation. An alternative, more cost-efficient way in terms of target materials would be the use of natural titanium (^{nat}Ti) or vanadium targets (^{nat}V). Utilizing ^{nat}V as a target for ^{47}Sc production requires the use of medium-energy protons and leads to quite a low production yield (MBq/μA) due to a rather low cross section (< 11 mb). If one wants to avoid the production and presence of ^{46}Sc in the final product, the cross section falls to 7.4 mb [37]. Compared to ^{nat}V, ^{nat}Ti irradiation by protons with cyclotrons yields a higher Sc radionuclide production, however a mix of same long-lived, high γ-ray ^{46}Sc and ^{48}Sc contaminants are again co-produced (see Figure 1.7). Therefore the irradiated targets should undergo a physical mass separation step to remove the ^{46}Sc and ^{48}Sc contaminants before or after any radiochemical separation [38]. As indicated in Table 1.1, mass separation is required to separate ^{43}Sc from ^{44m}Sc as well. The same applies to the purification of $^{44g/m}$Sc and ^{47}Sc which is not possible with other conventional methods and even enriched target materials.

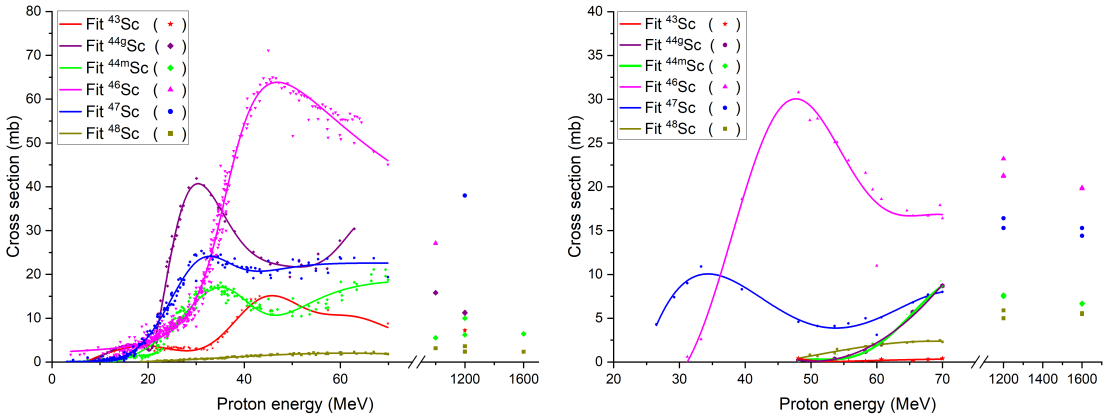

(a) ^{nat}Ti(p,x)^{xx}Sc (b) ^{nat}V(p,x)^{xx}Sc

Figure 1.7: Fit of ^{nat}Ti and ^{nat}V excitation experimental data for Sc radionuclide production with protons up to 1.6 GeV [26].

The production cross sections of Sc radionuclides from ^{nat}Ti and ^{nat}V target material irradiated with high energy protons (> 1 GeV) are in the same 10-25 mb range as the ones achievable with medium energy cyclotrons [26, 39–42].

Cyclotron targetry

Low-energy cyclotrons are the most widely available and used particle accelerators for medical radionuclide production. An emphasis is therefore placed on the investigation of various cyclotron target systems towards routine Sc radionuclide production. Cyclotron target systems that are used for radionuclide production are made to house solid, liquid or gaseous target materials. The gaseous and liquid target systems are used routinely in Radiopharmaceutical (RPH) production including radionuclides, such as

Table 1.1: Most common nuclear reactions for medical Sc radionuclide production.

Radionuclide	Reaction	Max cross section	Sc isotope impurities	Note
^{43}Sc	^{43}Ca(p,n)^{43}Sc	300 mb	^{44g}Sc	< 0.14 % ^{43}Ca in ^{nat}Ca, max enrichment 90 % [28,31,32]
	^{44}Ca(p,2n)^{43}Sc	170 mb	^{44g}Sc, ^{44m}Sc	^{44m}Sc cannot be avoided [26,28]
	^{46}Ti(p,α)^{43}Sc	45 mb	^{44g}Sc, ^{44m}Sc	[26,33]
^{44g}Sc	^{nat}Ca(p,n)^{44g}Sc	10 mb	^{43}Sc, ^{44m}Sc, ^{46}Sc*, ^{47}Sc, ^{48}Sc**	[26,28]
	^{44}Ca(p,n)^{44g}Sc	700 mb	^{44m}Sc	^{44m}Sc can be minimized with lower proton energy, but not avoided. Enrichment of ^{44}Ca >99 %, very expensive [25]
	^{47}Ti(p,α)^{44g}Sc	70 mb	^{43}Sc, ^{44m}Sc, ^{46}Sc	[26,34]
	^{44}Ca(d,2n)^{44g}Sc	540 mb	^{43}Sc, ^{44m}Sc	Requires deuterons up to 20 MeV
	^{45}Sc(p,2n)^{44}Ti/^{44g}Sc	45 mb	-	^{44}Ti ($T_{1/2}$ = 60 y), Expensive generator production
^{47}Sc	^{47}Ti(n,p)^{47}Sc	250 mb	^{46}Sc	Requires fast neutrons (>1 MeV)
	^{46}Ca(n,γ)^{47}Ca/^{47}Sc	700 mb	-	^{47}Ca ($T_{1/2}$ = 4.5 days) as ^{47}Sc generator [27]. 0.004 % ^{46}Ca in ^{nat}Ca, max enrichment 30 % [35]. Very expensive.
	^{48}Ti(p,2p)^{47}Sc	35 mb	^{46}Sc	Requires up to 30 MeV energy proton cyclotrons. Max enrichment is 96 %. ^{46}Sc cannot be avoided [36].
	^{48}Ti(γ,p)^{47}Sc	28 mb	^{46}Sc, ^{48}Sc	Natural abundance 73.72 %. Max enrichment > 96 %. Low yield [29].
	^{48}Ca(p,2n)^{47}Sc	800 mb	^{48}Sc	0.18 % ^{46}Ca in ^{nat}Ca, max enrichment 97 % [35].
	^{51}V(p,αp)^{47}Sc	11 mb	^{46}Sc	Requires 30-40 MeV protons [37].

*^{46}Sc ($T_{1/2}$ = 83.79 d, E_γ= 889; keV 1120 keV),
**^{48}Sc ($T_{1/2}$ =43.71 h, E_γ= 983 keV; 1037 keV; 1312 keV)

^{18}F, ^{11}C, ^{13}N ^{16}O and ^{68}Ga. These systems are most preferable due to their versatility and simple irradiated sample transfer to hot cells for post-processing. They also omit

a time-consuming step that is required for solid targets, which is the irradiated target dissolution for chemical separation and synthesis. Solid target systems also require specialized transfer systems and shielding for the target material loading and removal from the accelerator. Most solid target systems for cyclotrons are made out of two main components:

- the solid target system that is mounted on the accelerator beamline and can house the target material and its holder;
- the target material sample holder, which typically is a disc with a material reservoir of a few mm depth.

Typical proton accelerators are operated with a proton beam current of up to 150 μA and can go up to 300 μA. Such high beam currents result in high power deposited onto the target material. The targets therefore must be efficiently cooled during irradiation to prevent irradiated material and radionuclides from evaporation. Alternatively, lower beam currents can be used for the cooling to be sufficient to keep the material intact. However, low-current results in a lower yield of production. Certain target materials have low thermal conductivity and need additional heat sinks to avoid degradation [43]. Because of these challenges, certain radionuclide production is not yet advanced towards clinical dose production, despite their favorable production cross sections.

Two target structures are typically used for solid target systems - metallic foils or powders. Powder target materials pose a high risk of contamination if they are introduced directly into the cyclotron, because the material may evaporate during irradiation. Metallic foils can be used as covers to prevent evaporation, but the cover foil will degrade the beam energy. The degrader thickness can be altered to adjust optimal energy on the target [44]. Too thin foils may separate from the target material or burn out with higher beam currents [45]. Therefore the cover material type and thickness have to be chosen accordingly. In medical cyclotrons, the use of He-cooled Heat Treatable Cobalt Base Alloy (HAVAR) foils to separate the irradiated target material from the vacuum system of the cyclotron is preferred.

$CaCO_3$ that is commercially available as target material has low thermal conductivity. This constraint for the target material can be solved by pressing the calcium carbonate on top of graphite powder to facilitate heat transfer and to hold the calcium carbonate powder in position. The improvement of the heat conductivity, however, decreases the total yield of irradiation. Furthermore, this method is difficult to automate for routine production [44]. An alternative could be the addition of Mg or Al powders, which produce only short-lived isotopes and could be chemically separated [46]. ^{nat}Ca and ^{44}Ca oxide that is obtained through the thermal decomposition of calcium carbonate can be used in the preparation of the disk-shaped pellets and encapsulated into aluminum for irradiation. CaO has increased effective target nucleus density with respect to $CaCO_3$, but CaO is very hygroscopic and requires manipulation, storage and irradiation in dry or inert environment [47].

Due to difficulties in the installation and operation of a solid target system, a liquid target system for $^{44g/m}$Sc production has been developed and tested. Natural calcium nitrate solution has been irradiated with a 13 MeV proton beam in a small-volume liquid target. Production of 28 MBq $^{44g/m}$Sc with a 20 μA beam current for 1 h irra-

Table 1.2: Cyclotron target materials and their chemical form for Sc radionuclide production.

Target nucleus	Chemical form	Description
^{40}Ca, ^{42}Ca, ^{43}Ca, ^{44}Ca, ^{46}Ca, ^{48}Ca, ^{nat}Ca	CaO	Obtained through thermal decomposition of calcium carbonate. Low heat conductivity limits the beam current during irradiation. [43,47]
	$CaCO_3$	Heat accumulation can cause burnout and/or cracking of the irradiated target and may lead to gas production through the thermal dissociation. Low heat conductivity. [43,47]
	Ca	Difficult to handle. Metallic chunks of 400-600 mg pressed in 2.5 mm flat bottom Al holder cavity. [45]
	$Ca(NO_3)_2$	Solution for liquid target irradiation. Contains corrosive liquids. [48]
^{45}Sc	Sc	Natural isotopic abundance metallic foil. Used for ^{44}Ti/^{44g}Sc generator production [49]
^{47}Ti, ^{48}Ti, ^{49}Ti, ^{50}Ti, ^{nat}Ti	Ti	Metallic foils or reduced from TiO_2. [27,34]
	TiO_2	Powder pressed in pellets. Difficult chemical post-processing in strong, hot/fuming acids. [34]
	TiC	Good heat conductivity and very resistant material. Powder form. Not reported as a cyclotron target, however, discussed in high-energy proton irradiations (> 100 MeV) for Isotope Separation OnLine (ISOL). [6,50,51]
^{51}V, ^{nat}V	V	Natural isotopic abundance metallic foil. [37]

diation has been reported. The results show, that the GBq scale could be reached if enriched target material is used. However, the use of enriched target material with $\times$100 more quantities than for a solid target production from $^{44}CaCO_3$, makes the production very expensive [48]. Liquid targets for metallic radionuclide production offer easier daily operations and require less installation and hardware costs, but the presence of corrosive liquids in a cyclotron target is of high concern. Commercial companies offer liquid targets for metal radionuclide production, but mainly for ^{68}Ga production and their long-term use is not fully validated. Going into routine production, liquid targets should be dedicated only for single radionuclide production to avoid cross-contamination, whereas a solid target system can be used to irradiate targets for various metallic radionuclide production by using different dedicated target material holders [28].

1.3 Radionuclide separation

1.3.1 Chemical separation

The chemical separation methods originally led to the discovery of the first radioactive isotope, polonium (Po) in nature by Marie Curie and fostered the discovery of the first artificial radioactivity by Irène Joliot-Curie [5]. Nowadays, the instrumental approach

of detecting radionuclides is the preferred route, however, the radiochemical methods still hold an important role in studies, involving radionuclides. The radiochemical separation still is the most important part of RPH development, as it can determine both the effectiveness of the RPH synthesis as well as the final quality.

To perform conventional chemical separation procedures the target material with the corresponding radionuclides first must be dissolved. While this process seems to be simple, the Ti and V target materials impose difficulties due to their low solubility. Dissolution of irradiated TIO_2 or metallic Ti can be done in hot/fuming acids, such as sulfuric or hydrochloric acids in the presence of $(NH_4)_2SO_4$ [52], NH_4HF_2 [28], 35% hydrogen peroxide-ammonium carbonate solution [53] or by performing TiO_2 reduction at 900 °C with $CaCO_3$ for 1 h [27]. In general, obtaining the radionuclides from Ti and V targets in a solution requires aggressive methods and is rather time-consuming.

1.3.2 Precipitation and co-crystallization

Precipitation of a solid compound in an aqueous solution and filtration is a traditional separation method in radiochemistry. Historically precipitation as a purification procedure for radioactive isotopes was first used in year 1898 for co-precipitation of radium with barium in the treatment of pitchblende [52]. Since the concentrations of radionuclides formed in nuclear reactions are very small and the crystal products of even the most poorly soluble compounds cannot be attained, the radionuclides are often separated from the parent compound using a carrier, which carries the radionuclide along with it. The carrier amounts are much larger than that of the radionuclide itself and typically consist of the same element isotope as the radionuclide [54]. It also performs as a crystallization active center and results in co-crystallization and adsorption [52,55]. However, in such cases, the specific activity is severely decreased, which may impact the radionuclide usefulness in RPH synthesis and nuclear medicine.

1.3.3 Ion exchange chromatography

Ion Exchange Chromatography (IEC) is one of the most powerful and widely used methods for radiochemical separation. It is related to solvent extraction in that it depends upon the differential distribution of a species between two phases, except that in chromatography the phases move relative to one another. With ion exchange, the distribution of an element happens between a mobile phase (solution) and a stationary phase (resin, which is usually packed in a column). The distribution depends on the ionic form, the solute concentration, and the functional group of the resin and is described by the distribution coefficient.

All the extraction systems can be separated into two main groups:

- physical distribution - with no chemical interaction between the extractable compound and extractant. This mode is determined by the difference in the solvation and hydration energies of the extractable compound.
- reactive extraction - the transfer of a compound from the aqueous into the organic phase happens through chemical reactions yielding new compounds.

The extraction is efficient when the distribution coefficients of the desired product, target material, and radioactive impurities differ significantly. If the difference is small,

reactive ion-exchange chromatography procedures are preferred [52]. Once appropriate resin is selected, the variables for efficient extraction are ionic concentration, column volume and diameter, flow rate and the eluent. With a proper choice of conditions, IEC is very useful for separating carrier-free radionuclides from a bulk target that has a significantly lower affinity toward the resin [56]. For example, a resin with high efficiency for Sc separation and low affinity to Ti is the Diglycolamide (DGA) branched resin [57].

However, the need for chemical dissolution of radioactive matrices and targets is still required to transform the elements into physicochemical forms appropriate for chromatographic separation. The radiological safety aspects, dissolution, pretreatment of resins and strong concentration dependencies of the distribution coefficients of the radionuclide of interest and impurity compounds significantly complicate the radiochemical processing of irradiated targets [52].

1.3.4 Radionuclide generators

Radionuclide generator is a self-contained system that houses an equilibrium mixture of a mother/daughter radionuclide pair. The mother radionuclide is typically long-lived and therefore resolves the issue of radionuclide decay due to transport from the irradiation facility. The production of mother radionuclides is performed using nuclear reactors, and accelerators, such as cyclotrons, or they can be separated from fission products. Fixation of the mother nuclide and simple separation of the daughter nuclide is achieved by the use of separation columns containing a suitable ion exchanger or sorbent. The mother nuclide must be present in a stable chemical form, so that the daughter nuclide can be separated repeatedly, leaving the mother nuclide quantitatively in the generator [4].

The system is designed to provide the daughter radionuclide formed by the decay of a parent radionuclide which is free from the parent. Another advantage is that isotopically and isomerically pure radionuclides can be obtained. For example, ^{44}Ti/^{44g}Sc generator is at the moment the only way to obtain pure ^{44g}Sc without ^{44m}Sc impurities [58]. After each separation, the activity of the daughter nuclide in the generator increases, and the daughter nuclide can be separated repeatedly. For example, after three half-lives of the daughter nuclide, 87.5 % of its saturation activity is again reached. The radionuclide generators with potential medical applications can be classified as generators releasing positron-emitting radionuclides for PET, generators releasing photon emitters for SPECT, generators releasing therapeutic radionuclides and *in-vivo* generators.

1.3.5 Electromigration

The differences in ion mobilities in aqueous solutions in an electric field give grounds for electrophoretic technique - electromigration. A paper strip is moistened with an electrolyte (e.g. perchloric acid or nitrilotriacetic acid) and an irradiated sample is placed on the paper in a small spot. By applying $\sim$100–500 V/cm potential gradient, different ions migrate in different directions and distances. Se, Te, I, Tc, Rb/CS, Sr/Ba and lanthanides could be separated within 20 s–3 min with a distributed total distance of 8 cm [55, 59].

1.3.6 Thermal separation and release

The thermal release or recovery is based on the diffusion of impurity atoms to the metal-gas boundary. In the case of radionuclides, they are formed in the bulk of the material by nuclear reactions or radioactive decay [60]. The high-temperature thermal separation approach can be categorized into two modes. First - the matrix containing the radionuclides is heated and kept in an inert atmosphere (or vacuum) for a certain time, enough to recover the radionuclides. With this method, it is often difficult to obtain high-purity radionuclides because of the relatively similar vapor pressures of the elements to be separated. Furthermore, the radionuclides are accompanied by evaporated target material. Second - the sublimation recovery of radionuclides can be performed in the vapor of chemical agents, such as H_2O, HCl, HF, hexane or their mixtures [52]. The great advantage of thermal separation and sublimation is the possibility of radionuclide recovery from large and thick targets.

The diffusion of radionuclides in the bulk and near-surface layers, and their physicochemical behavior at the metal-gas boundary are abnormal, when the thermal treatment is accompanied by structural target material changes, such as melting, polymorphic transitions, thermal reconstruction of the surface and annealing of the radiation defects [52].

Selective adsorption to different surfaces may also be utilized in thermal separation. Sc radionuclides can be separated from Ti foil target in quartz ampules and can yield in preparations with > 99.7 % chemical purity. In the course of thermal treatment of the foils, the Sc radionuclides can pass to the metal surface, evaporate and concentrate (adsorb) on the ampule walls. Later the Sc can be removed from the quartz ampule with a mineral acid solution [60]. Another way is to use different temperature surfaces on which the radionuclides can condense and be later selectively removed [61].

1.3.7 Gas thermochromatography

Thermochromatography is a "dry" process that also excludes difficulties of target material dissolution [60]. Gas thermochromatography utilizes the differences in the distribution of volatile elements or molecules between mobile gaseous and stationary solid phases. In this technique, the mixture of gaseous species passes through a column with a decreasing temperature gradient towards the exit of the column. In this gradient, less volatile species are adsorbed in the high-temperature region, whereas more volatile species - in the low-temperature region. Therefore, here the adsorption enthalpy is the main parameter determining the separation and deposition [56].

Reactive sublimation can be achieved by coating the inner surface of the thermochromatographic columns (e.g. alkali and alkaline halides) and utilized to create compounds, as the species of interest enter the column. The reactive sublimation procedure, however, does not provide a very high yield of the desired radionuclides, because the bands of the volatile compounds of the desired radionuclide and target material typically overlap in the thermochromatographic column [60]. Another approach is to fill the column with materials, that slow down the species entering the column by adsorption and therefore more efficient separation according to their volatility and inner column surface area can be achieved [55].

1.3.8 Mass separation

Electromagnetic ion beam mass separation is a technique that uses a dipole magnet to induce a magnetic field and separate accelerated and ionized isotopes according to their mass-to-charge ratio, through the Lorentzian principle. The magnetic rigidity of the ion beam of interest depends both on the applied magnetic field from the dipole as well as the charged state of the isotope, mass and energy. The ionized species acceleration is achieved by placing the Target and Ion Source System (TISS) on high voltage (30–65 kV) and maintaining the mass separator at ground potential. As the ion beam transverses through the homogeneous magnetic field, its trajectory bends with a radius r that depends on the atomic mass of the ionized species (see equation 1.4) [62, 63].

$$r = \frac{Mv}{qB} = \frac{\sqrt{2mE}}{qB} \tag{1.4}$$

where r is the ion beam bending radius [m], M is the atomic mass of the ion [g/mol], q is the charge of the ion, B is the magnetic field [T], and E is the energy of the accelerated ion [eV].

Since different masses result in different bending radii, the magnetic field can be varied to select the desired mass. By blocking out unwanted trajectories, only pure beams of interest can be obtained. In contrast to chemical separation, isobars or atoms with the same atomic mass number A_{pn} but different atomic number Z are separated from the initial sample [38]. The quality of a mass separator is expressed by the mass resolving power. Certain mass separators have sufficient resolution to separate also isobars [6,11].

1.4 Radioactive ion beams

There are two ways to produce Radioactive Ion Beam (RIB) - in-flight separation and Isotope Separation OnLine (ISOL). In both methods, the nuclei of interest are transported away from their place of production, where a high radioactive background is present from the nuclear reactions. RIB are used to produce exotic isotopes with a very short half-life, far from the stability line. In the in-flight separation technique, a primary beam of energetic heavy ions (from 100–2000 MeV per nucleon) is made to collide with a thin low-Z target material (e.g. graphite or beryllium). Fragmentation and fusion-evaporation reactions happen as the heavy ions collide with the target and the charged products recoil out of the target with the same momentum and little energy difference from the primary beam. In the ISOL method, radioactive isotopes are produced by spallation, fragmentation, fission and fusion evaporation, when thick targets are irradiated with light particles, such as protons, neutrons, photons and electrons [6].

A schematic representation of the ISOL RIB production is shown in Figure 1.8. When the light energetic particles impinge on the target material, they induce nuclear reactions in the bulk of the thick target material. Once the radionuclides are produced, they are released from the bulk material, which is typically done by heating the target to (or sometimes above) 2000 °C, under vacuum (pressure of $<1 \times 10^{-5}$ mbar). The high temperatures promote the diffusion of the produced isotopes to the surface of the bulk material, which is in most cases assumed to be in the form of a neutral atom. Once

the particles reach the surface, they may desorb, based on physiochemical properties between the surface and the radionuclide as well as the vapor pressure of the element of interest. The desorbed species then undergo many collisions with the target and container materials while they effuse (migrate) out of the target material container to the ion source. Depending on the ion source type, the neutral particles have a certain probability to get ionized and accelerated for subsequent mass separation [6, 11, 64, 65].

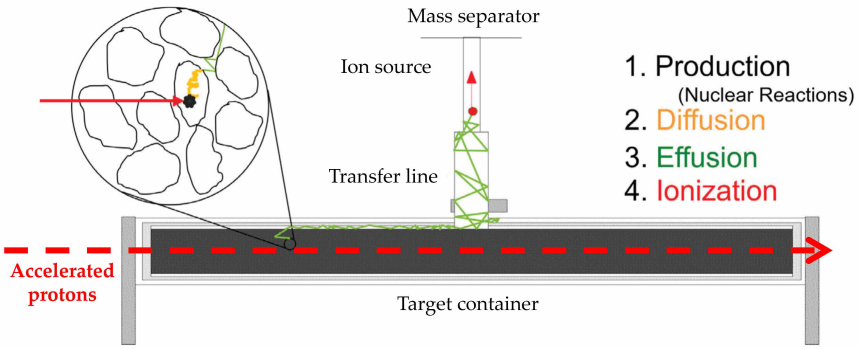

Figure 1.8: Schematic representation of the ISOL method of radioactive ion beam production. Adapted from [6].

1.4.1 CERN-ISOLDE facility

CERN-ISOLDE at Geneva, Switzerland is a facility that has used the mass separation technique for decades to deliver isotopes for atomic, nuclear and solid-state physics experiments [50, 66]. The ISOLDE experiment is one of the oldest experiments at CERN. After decommissioning of the CERN-Synchrocyclotron (SC), an upgraded version of ISOLDE was built that includes two independent target stations and mass separators, which uses protons from the CERN-Proton Synchrotron Booster (PSB) (see Figure 1.9). The pulsed proton beam supplied to ISOLDE TISS typically has an energy of 1.4 GeV and can reach the beam current of $\sim$2 µA, which equals about half of all the protons supplied by the PSB. Thus far, the ISOLDE facility has provided users with more than 1000 isotopes from 76 elements for various physics experiments. Recently also a dedicated laboratory for nano-material handling, including two pump stands for target material preparation, has been constructed [64].

ISOLDE has two online target irradiation stations which are coupled to two mass separators of different conceptual designs - General Purpose Separator (GPS) and High Resolution Separator (HRS). The GPS has the mass resolving power of R = 800 and is capable of extracting the ion beams at three different masses simultaneously [68]. The HRS has two separator magnets and possesses the mass resolving power of R = 6000. The mass-separated ions are then sent into the experimental beamlines. The linear accelerators of Radioactive Beam EXperiment (REX) and High Intensity and Energy ISOLDE (HIE-ISOLDE) offer post-acceleration possibilities. Before RIB injection in the post-acceleration stage, the low-energy beams are bunched and fed into the REX-Electron Beam Ion Source (EBIS) to boost the charge state. RIB yields[2] during ongoing ISOLDE experiments are measured at the ISOLDE tape station which is installed close to the junction point in the central beamline [11].

[2] Yield at ISOLDE is defined as atoms per μC, however throughout this thesis and at CERN-MEDICIS yield is used in the context of radionuclide activity [Bq].

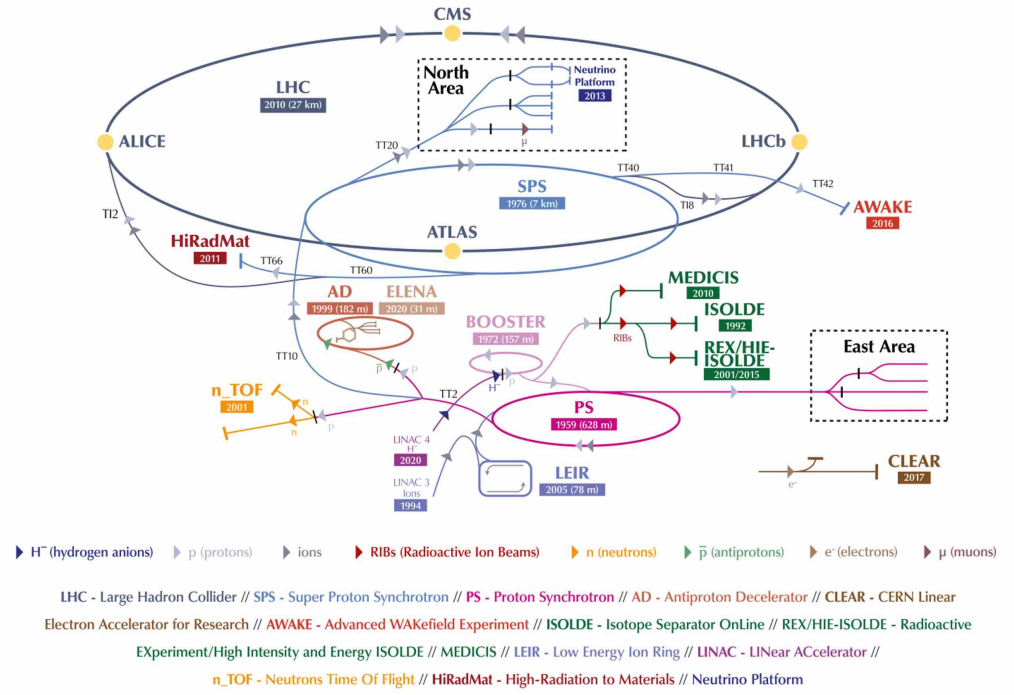

Figure 1.9: The CERN accelerator complex. Adapted from [67].

Standalone TISS or material samples can be irradiated at two additional irradiation points, located downstream of the ISOLDE target units [69]:

- ISolde Irradiation Station (ISIS), which is located by the GPS target station;
- Medical Isotopes Collected from ISOLDE (MEDICIS) which is located by the HRS target station.

Sc radionuclide RIB's have been produced at ISOLDE before, both with the SC and PSB as the primary beam source for nuclear reactions. Nevertheless, the conditions of their efficient release were extreme and not suitable for lower melting point (< 2000 °C) target materials. Spallation reactions of ^{nat}Ta foils are the primary source in obtaining Sc isotopes at ISOLDE for physics experiments due to the stability and low volatility of metallic Ta at very high operating temperatures (> 2000 °C). However, the production yield of medically relevant Sc radionuclides with mass separation from ^{nat}Ta is not yet applicable for medical research [70]. Furthermore, this production route requires high-energy protons that are not available in typical low-, intermediate- or medium-energy cyclotron centers.

1.4.2 CERN-MEDICIS facility

The RIB mass separation technique has recently been adapted at CERN-Medical Isotopes Collected from ISOLDE (MEDICIS) to obtain isotopically pure non-conventional medical radionuclides for translational research. Since commissioning in year 2017, CERN-MEDICIS has provided its partner institutes with high molar activity ^{128}Ba/^{128}Cs, ^{129}Cs, ^{149}Tb, ^{152}Tb, ^{155}Tb, ^{153}Sm, ^{165}Tm, ^{167}Tm, ^{169}Er, ^{175}Yb, ^{195m}Pt, ^{224}Ra, ^{225}Ra and ^{225}Ac radionuclides [71,72].

The MEDICIS facility is located next to the ISOLDE facility (see Figure 1.9), on the Meyrin site of CERN in Geneva, Switzerland [72]. The production and mass separation of medical radionuclides is performed via two different modes. In the first mode of operation, the TISS is placed before the beam dump of one of the two irradiation stations and irradiated with protons coming from the CERN-PSB with an energy of 1.4 GeV. Most of the protons impinging on the ISOLDE target pass it without significant energy loss, therefore CERN-MEDICIS makes use of the protons which would otherwise get lost in the beam dump. Although the current energy specifications of ISOLDE are 1.4-1.7 GeV proton beam, the CERN-MEDICIS facility has been conceived considering an energy increase to 2 GeV primary beam energy, where up to 6×10^{20} protons per year are expected [62]. The second mode of operation makes use of irradiated target materials at one of the CERN-MEDICIS collaboration external partner institutes. The irradiated samples are shipped to CERN-MEDICIS and placed inside an empty TISS target container. This approach allows CERN-MEDICIS to be one of the only facilities at CERN, which can operate during Long Shutdowns - periods when no protons are circulating in the CERN accelerator complex. In both modes of operation, the TISS is coupled to the MEDICIS frontend, where it is heated to high temperatures of up to ~2500 °C, depending on the release temperature of the species of interest and the target material [71].

The mass-separated medical radionuclides are implanted into thin metallic or salt-coated foils and dispatched to preclinical, clinical, biomedical or radiochemical research centers worldwide [72]. The handling of open radioactive sources is done in dedicated laboratories, classified according to the Swiss authorities as Type "A" (see Figure 1.10) [73].

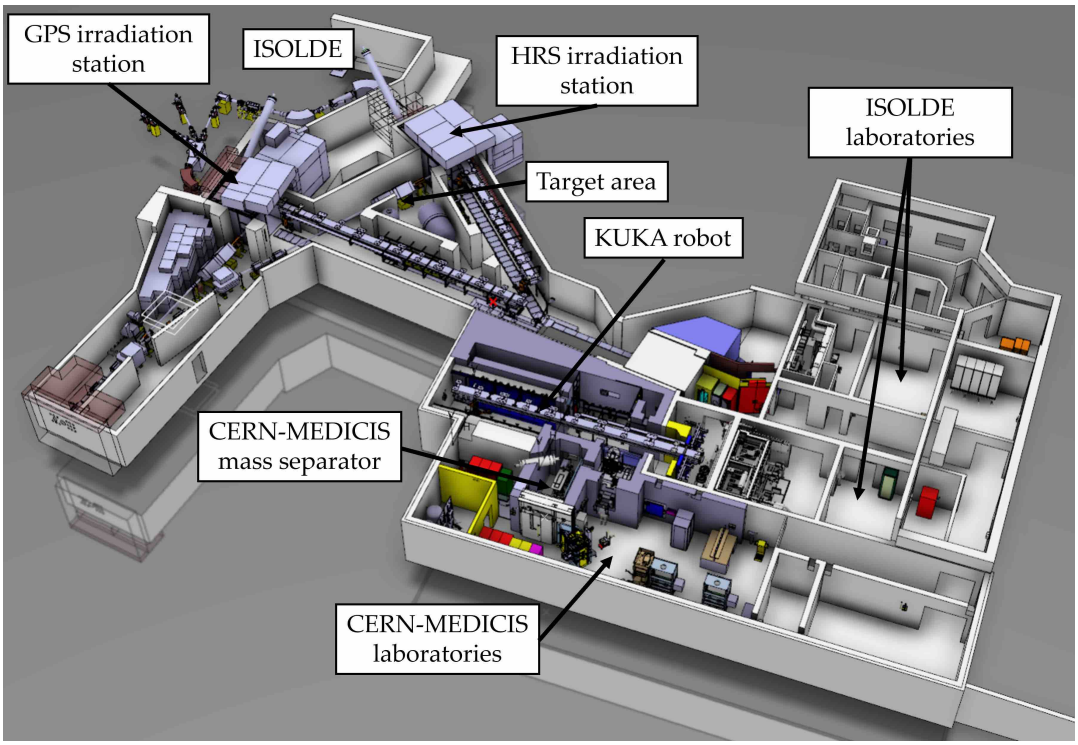

Figure 1.10: The CERN-MEDICIS facility, class "A" laboratory and target area. Adapted from [62].

One of the key performance indicators of CERN-MEDICIS is the collection efficiency. The collection efficiency is described as the activity collected at the End Of Collection (EOC) against the starting activity of a radionuclide present inside the target material [74]. While it makes more practical sense to express collection efficiency this way, throughout this work the collection efficiency will be reflected as decay-corrected collected activity against the starting activity of a radionuclide (present inside the target material) due to the various investigated physical and chemical aspects and limitations of the mass separation and radionuclide collections. The main stages of the collection are shown in Figure 1.11, indicating main factors that impact the radionuclide collection efficiency and yield.

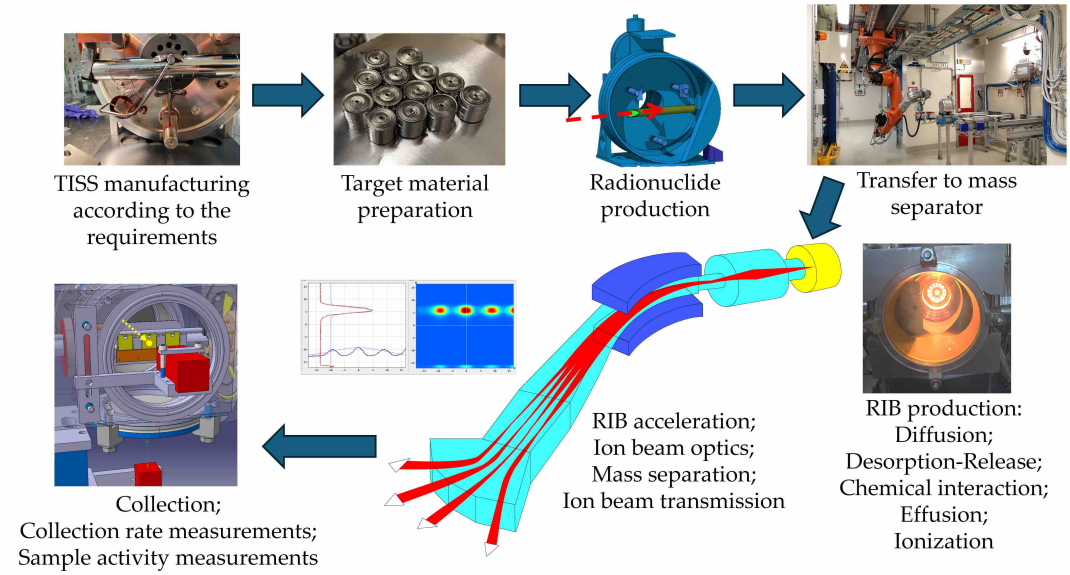

Figure 1.11: Graphical abstract of radionuclide collection at CERN-MEDICIS.

1.4.3 Molecular ion beams

Refractory elements in ISOL can be defined as those, which have very high melting points, low volatility and high adsorption enthalpies on the TISS structures. "Refractory" is typically used for metals than for any element, however some non-metallic elements with very high melting points, such as boron and carbon possess the same characteristics in the ISOL method [75]. The refractory element release from the target units (e.g. Si, B, C, Sc, Ti, V and transition metals Nb, Mo, Tc, W, Re, Os) can be promoted with chemical reactions *in-situ* the target containers and ion sources by creating more volatile molecules and extracted from the TISS as molecular ion beams [38, 64]. These molecules have lower boiling points, adsorption enthalpies and can desorb and effuse to the ion source faster and at lower temperatures (see Figure 1.12). This approach is also referred to as “chemical evaporation” [76].

Molecular ion beams have been proposed and studied at ISOLDE for decades as a way to increase the volatility and provide high-purity RIB of the refractory isotopes. Since initial studies, the target and ion source developments offer more efficient operating conditions [77–82]. The molecular beam formation can be achieved by the addition of certain chemicals into the target container and ion source. This can be achieved by

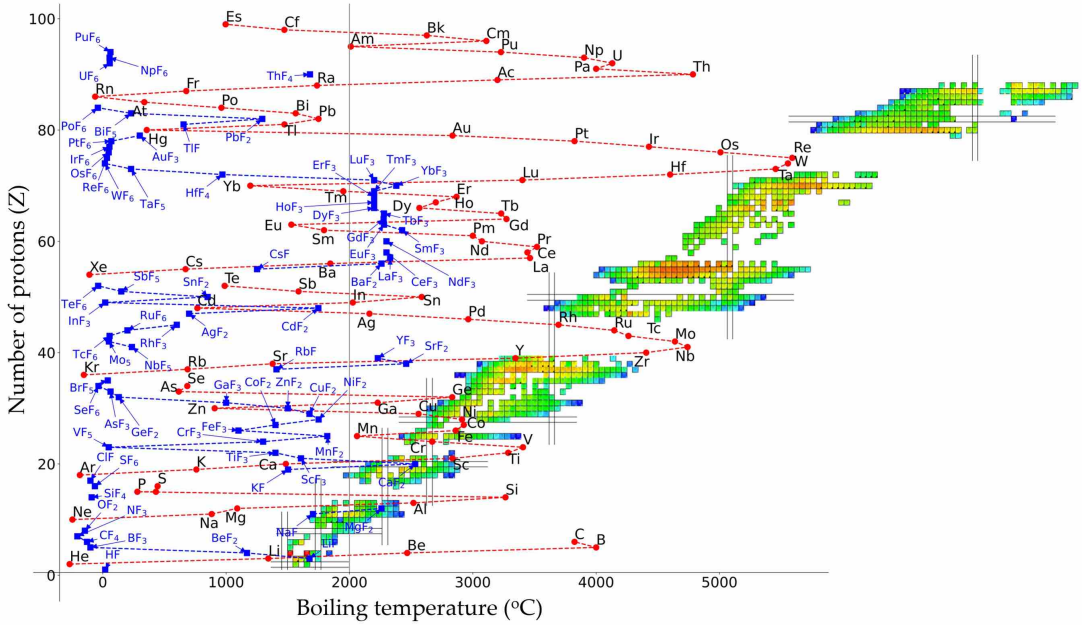

Figure 1.12: The nuclear chart of chemical elements produced and measured at ISOLDE, aligned with the chemical element atomic and fluoride boiling temperatures. Adapted from [64].

injecting reactive gas directly into the TISS target container, such as CF_4 and SF_6 [77], CO [83], or evaporating salts (e.g. CCl_4, AgCl, BF_3) from a separate container that is connected to the target container. The added chemicals can react directly or dissociate in radicals, which afterward interact with the refractory atom adsorbed on the target material or the target container, transfer line or ion source surfaces. Molecular beam formation can also be observed from impurities in raw target materials or from the target material chemical composition itself (e.g. LaF_3, Ce_3S_4, CeS) [78, 84]. In this case, the molecule formation cannot be controlled during the mass separation process.

Metals of groups 2–6 form halides, which are relatively stable even at temperatures used for RIB creation with the ISOL method. The most stable form is observed when the metal is in its highest valence state. In this state, the molecule has an electronic configuration with no free valence electrons to bind with the surface strongly. Also, the molecule must remain rather intact during wall collisions and effusion to the ion source [76].

The molecular ion beam method is often also referred to as the molecular sideband extraction [64, 81]. The extraction of radionuclides using a halide molecule sideband can be used also as a technique to decrease isobaric (same atomic mass) contamination. For example, the Sc mass separation can be shifted from 43–47 atomic mass unit (amu) region to 62–66 (mono-fluoride), 81–85 (di-fluoride) or 100–104 amu (tri-fluoride) region [38, 64].

2 Experimental setups and theoretical models and tools

Contents

2.1 Radionuclide production

2.1.1 Radionuclide Production at CERN-MEDICIS

In this study, the target materials were mainly irradiated at the CERN-MEDICIS HRS irradiation station with a 1.4 GeV proton beam delivered by the CERN Proton Synchrotron Booster (PSB). Recent developments and tests have been done to increase beam energy to 1.7 GeV and upcoming facility upgrades would allow to reach 2 GeV with a 4 μA of beam intensity [85]. The pulsed proton beam impinges on the target units with up to 2.4 μA intensity (usually 2.0 μA). The PSB cycle consists of up to 3.3 $\times 10^{13}$ protons per pulse every 1.2 s [38]. The irradiation times usually range from a few hours up to a full day resulting in $\sim 1 \times 10^{18}$ Protons on Target (PoT). At the current configuration, the TISS can withstand up to $\sim 5 \times 10^{18}$ total PoT, before radiation damages prevent the target from being used in a radionuclide collection. The target materials are irradiated in an Ar atmosphere and without active cooling, which can result in 80–120 °C temperature due to deposited power. The CERN-MEDICIS TISS is placed downstream of an ISOLDE TISS and the proton beam first intercepts through the ISOLDE target (see Picture 2.1). At the High Resolution Separator (HRS) MEDICIS irradiation station two different irradiation modes are possible:

- direct irradiation, where the proton beam intercepts through only ISOLDE TISS aluminium vessel, below the ISOLDE target container and its target material, and impinges on the CERN-MEDICIS target material;
- indirect irradiation, where the proton beam intercepts through the ISOLDE target material and then impinges on the CERN-MEDICIS target container.

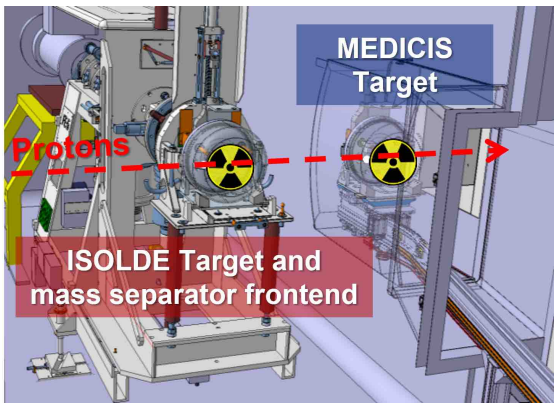

Figure 2.1: Principle of CERN-MEDICIS target irradiation together with ISOLDE target unit [86].

Therefore, the irradiation parameters at CERN-MEDICIS and the conditions strongly depend on the otherwise ongoing ISOLDE experiment (see [72] for more details). Indirect irradiation is also possible at the ISolde Irradiation Station (ISIS) irradiation station by GPS station.

CERN-MEDICIS also utilizes another mode of operation, thanks to the institutes that are part of the CERN-MEDICIS collaboration. The target materials irradiated at external cyclotron or reactor facilities can be shipped to CERN-MEDICIS and placed inside an empty target container and subsequently proceed to the mass separation [72]. A

typical example is the separation of ^{153}Sm from stable ^{152}Sm, produced at the SCK-CEN BR2 reactor in Belgium, for which an increase of the specific activity (high ratio ^{152}Sm/^{153}Sm) is necessary for the use the targeted radionuclide therapy.

The online facility - ISOLDE - typically operates with a proton beam constantly impinging on the target material during mass separation. CERN-MEDICIS operates offline in a so-called "batch mode" of production and extraction. This means that the starting activity of the radionuclide inventory for each experiment is a finite amount and decreases from both the radioactive decay and release throughout the collection. In some cases, the decay of a mother radionuclide feeds the radionuclide of interest, such as in the case of ^{47}Ca/^{47}Sa This is the main difference between an offline and an online isotope mass separation. Most of the irradiated target units used for radionuclide mass separation and collection are re-irradiated and re-used. Therefore, multiple collection batches can be done from the same target unit.

Every TISS for irradiation in the ISOLDE target area is transported via an automatic rail conveyor system. After irradiation, the dose rate at 27 cm of the retrieved target unit is measured at the CERN-MEDICIS decay station. Thus far, the highest target unit dose rate has reached 3 Sv/h, 15 min after the EOB. This high dose prevents any target measurement and desired sample fraction removal for γ-spectrometry analysis. The TISS is then transported and placed on the CERN-MEDICIS mass separator frontend by remote handling, using a KUKA® (Augsburg, Germany) robot [72]. Due to the high dose rate and amount of radionuclides produced inside each target, γ-spectrometry of the whole TISS is not yet feasible but under investigation using a low-efficiency collimated germanium detector. In-target radionuclide production is currently calculated via Monte-Carlo simulations.

The 1.4 GeV beam available at ISOLDE leads to a high level of sample activation and production of spallation products. To produce low-activity samples for the Sc thermal release study (see Chaper 3) and avoid the production of unnecessary spallation products and unjustified dose exposure, the samples have been irradiated in another facility accessible at CERN. It is the CHARM facility where passive irradiations were offered for the specific study.

2.1.2 Sample activation at CERN-CHARM

The CERN-CHARM facility studies the radiation effects on electronic components and various shielding materials [87]. It is also used for sample activation purposes to benchmark Monte-Carlo codes such as FLUktuierende KAskade (FLUKA). The CHARM facility receives a 24 GeV/c proton beam extracted from the CERN Proton Synchrotron (PS) impinging on a thick copper target. It creates a mixed radiation field including secondary neutrons. Several stations are made available for sample irradiation, depending on the required type and level of activation. Within the thermal release study, a low level of ^{nat}Ti and ^{nat}V sample activation was required (few 100 kBq) to produce Sc isotopes. For this purpose, the neutron field that can be obtained outside of the CHARM target area has been used. The particle fluence spectra generated by the characteristic 5×10^{10} p/s primary proton beam onto the CHARM target, at the specific location of the grid where the samples where placed, is shown in Figure 2.2.

The samples for activation were inserted in plastic bags and placed onto the grid (see

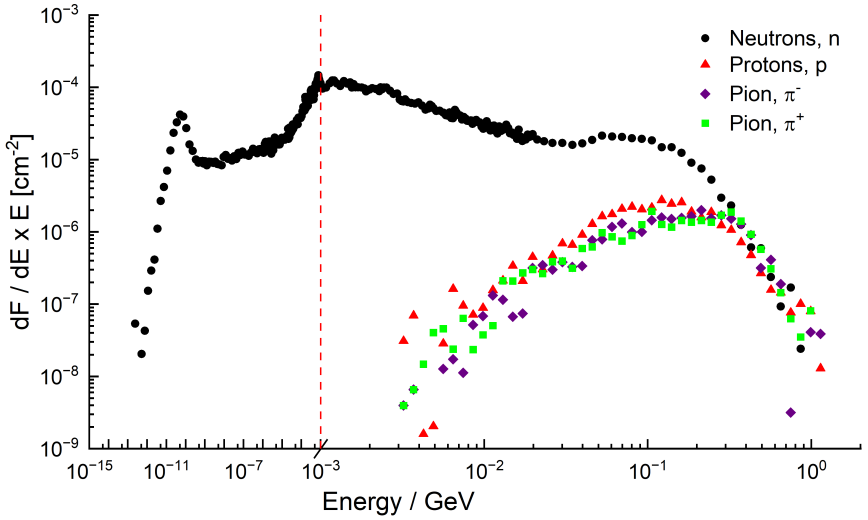

Figure 2.2: Particle fluence spectra in lethargy representation at the sample activation location (grid) of the CHARM facility.

Figure 2.3). Typical irradiation experiments at CERN-CHARM last for ∼7 days which includes 5-day irradiation followed by a 1.5-day decay (cooling) period after the EOB, leaving half a day for access. For theoretical radionuclide production estimations and experiment setup, the average values were used to get a first estimate. The values were also used for radiation protection purposes and preparation. After the activation, the values were rescaled according to the actual irradiation parameters.

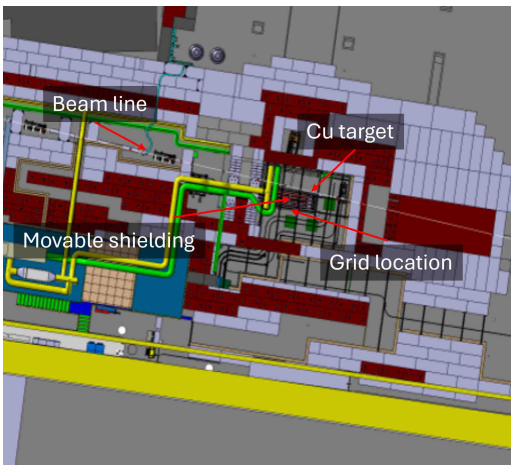

(a) Layout of the CERN-CHARM facility [87].

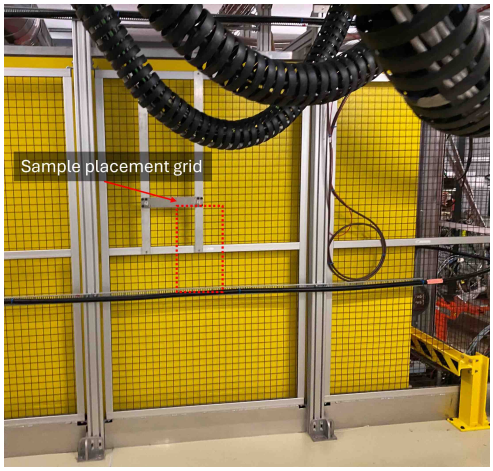

(b) The sample placement grid.

Figure 2.3: Sample activation location at the CERN-CHARM facility.

This study is shown in Chapter 3 and was performed to get a better understanding of the release of Sc inside an ISOLDE target and ion source unit.

2.2 Target and ion source system

The produced radionuclide release from the irradiated target materials and RIB produced is achieved with the Target and Ion Source System (TISS). The TISS (referred also as target unit) that are used for mass separation and collections at CERN-MEDICIS are identical to the ones being developed for and used at ISOLDE [11, 88]. The TISS typically consists of three main parts: an aluminium base and enclosure, a target container and its accessories, and an ion source. Each target unit can differ in its specification, modification, and ion source to maximize longevity, production yield, and ionization of the species of interest. The TISS are re-used multiple times until their medium-term storage for cooldown and dismantling for long-term storage [89]. The target container and ion source are covered with Ta, W, and Mo heat screens, to have more uniform heat distribution during operations. The target container housing for the target material or external samples is made out of Ta material, due to its durability and refractory nature. Possible alternatives would be W, Mo, Re, graphite or nickel-rich alloys; however, due to the complex structures needed for target-unit assembly, these materials are most difficult to manufacture [90]. As shown in Figure 2.4, the target container and ion source are fixed to a water-cooled aluminium base (temperature of $\sim$ 20 °C). The transfer line to the ion source is located in the middle of the target container perpendicular to the container. Finally, the target container and ion source assembly with their accessories are enclosed in an aluminium vessel to obtain a pressure below 1 $\times 10^{-5}$ mbar for ion beam extraction.

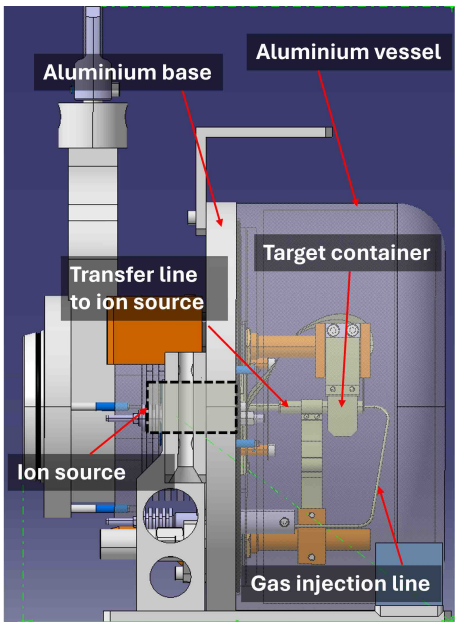

Figure 2.4: Schematic side view of a Target and Ion Source System (TISS)

The target container and transfer line/ion source are resistively heated to obtain the desired temperatures. Currents up to 370 A for the transfer line/ion source and 1200 A for the target container can be applied. Based on the ion source type, typical values are 240–360 A for the transfer line and 300–800 A for the target container. The inner diameter of a standard target container is 20 mm and it is 200 mm long, which allows it to hold a few mol of target material. In cases where exposure to Ta should be limited,

thin metal foil linings or covers such as 10–30 μm V and W foils were inserted in the target container.

A key accessory for certain ion source stability, radionuclide volatilization and molecular beam formation is a gas injection line within the target unit. It consists of two Ta tube pieces that connect the target unit base with the target container. The Ta tubes are connected via a hollow boron nitride (BN) cylinder to ensure electrical insulation. The gas injection line faces the transfer line on the target container. For controlled gas injection in the target container, calibrated gas leaks (High Technology Products Ltd., East Sussex, UK) are used. The gas leaks are small porous sintered stainless steel powder structures with a known gas conductance and housed in a stainless steel cylinder (see Figure 2.5). The calibrated gas leak is installed on the base plate at the beginning of the gas injection line.

Figure 2.5: The calibrated gas leak for a TISS

Typical leak rates for the calibrated gas leaks are within the range of 4×10^{-6} to 2×10^{-3} mbarL/s (for air) and leak pressure of up to 1.2 bar [91]. By adjusting the gas pressure applied to the gas leak from the reservoir side, the gas amount injection rate into the target container can be varied. A higher gas amount injection rate can impact the pressure within the target unit and cause high voltage arcs between the ion source and the mass separator extraction electrode.

To produce a RIB, the efficiency of an ion source is a key parameter. It describes the probability for the neutral species, generated from the target container, to get ionized in the ion source. Multiple ion sources have been developed and used for mass separation with variant selectivity. The three most widely used are surface ion source, electron impact ion source and resonant laser ion source. The appropriate ion source is chosen, based on the physical and chemical properties of the species of interest.

2.2.1 Surface ion source

A surface ion source, also called a hot cavity ion source, is a simple way to ionize species with sufficiently low Ionization Potential (IP) (typically $\leq$6 eV) [92]. The ionization takes place directly on the ionizer surface and therefore strongly depends on the ion source material work function W, the temperature of the surface and the density of gaseous particles. In solid-state physics, the work function is the minimum thermodynamic work or energy needed to remove an electron from a solid to a point in the vacuum outside the solid surface. Surface ion sources at CERN-MEDICIS are made out of hollow Ta ($W = 4.0 - 4.8$ eV), W ($W = 4.3 - 5.2$ eV) or Re ($W = 4.7 - 5.1$ eV) and operated at 2000–2400 °C [11, 62, 92–94]. The emitted electrons together with positively charged particles inside the hot cavity form an electrostatic potential and provide some confinement to the positively charged particles in the axial center of the ion source. The

cavity also has no physical constraints from the outlet orifice up to the target container. For these reasons, the surface ion source is well suited in combination with the resonant laser ionization for increased efficiency [64].

2.2.2 Laser resonant ion source

At ISOLDE, Resonant Ionization Laser Ion Source (RILIS) produces ions by resonant photon absorption delivered in the form of laser light [93]. The valence electron is excited through intermediate energy levels and stripped from the atom into a continuum by a subsequent non-resonant photo-ionization step (via an auto-ionizing state), collisional or field ionization (via Rydberg state). The lasers are tuned for the photon energies to precisely match the electron transition energies of an ionization scheme [95]. This makes RILIS a very element-selective ion source with minimal isobaric contaminants and can achieve ionization efficiencies higher than 50 % [64, 96].

At CERN-MEDICIS the surface ion sources, combined with laser ionization from MEDICIS Laser Ion Source for Separator Assembly (MELISSA), are used to deliver ion beams of ^{149,152,155}Tb, ^{153}Sm, ^{165,167}Tm, ^{169}Er, ^{175}Yb and ^{225,227}Ac for mass separation and collections [71, 96]. In this work, a combination of surface and Versatile Arc Discharge Ion Source (VADIS) and laser ionization was also used to mass separate the stable ^{45}Sc isotope and $^{44g/m}$Sc, ^{46}Sc, ^{47}Sc radionuclides.

2.2.3 VADIS ion source

Versatile Arc Discharge Ion Source (VADIS), or the so-called plasma ion source, is a Forced Electron Beam Induced Arc Discharge (FEBIAD)-type ion source, used at CERN-MEDICIS and ISOLDE [97]. VADIS is an optimized version with an increased active volume and a reduced amount of graphite compared to its FEBIAD predecessor [97]. The VADIS Ta cathode is directly connected to the transfer line, hence, they are heated together to similar temperatures. Applying 100–150 V potential (max 300 V), thermionic electrons, emitted from a hot cathode (ca. 2000 °C), are accelerated through a grid into the anode body creating plasma conditions upon electron impact with gaseous species at 1900–2100 °C. A schematic representation of a FEBIAD-type ion source is shown in Figure 2.6. The electrons are deflected by axial magnet on helical orbits.

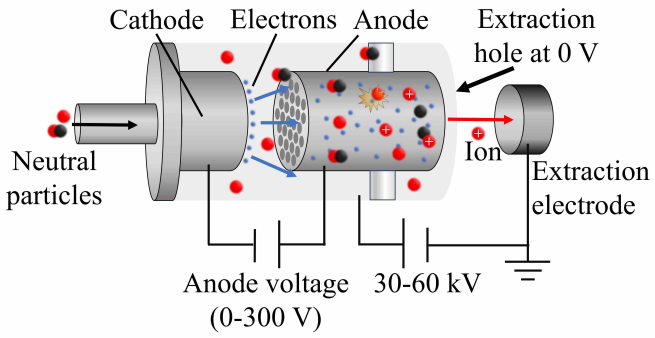

Figure 2.6: Schematics of VADIS/FEBIAD ion source.

FEBIAD-type ion sources are capable of ionizing particles with high IP (over 100 eV), including atomic and molecular species. In the anode body volume, molecules can

undergo fragmentation into neutrals and ions, dissociative or direct ionization. A representation of possible reactions happening in the plasma conditions for only CF_4 gas are shown in Table 2.1. Note that reactions in Table 2.1 directly depend only on the reactive gas applied. Other reactions occur also for the radionuclide-containing molecules. In addition, the elements of ion source structures, such as Mo, Ta, Be and O are always present in addition to vacuum impurities and can contribute to such reactions. The formation of HF^+ species (20 amu) can also be observed because fluorine has a high reactivity towards the H atom in H_2 species from the vacuum impurities [98].

Table 2.1: Heterogeneous (gas phase and surface) reactions involved in the creation and loss of fluorine atoms in plasma conditions from CF_4 gas [98].

Process	**Reaction**
Neutral dissociation	$CF_4 + e^- \rightarrow CF_3 + F + e^-$ $CF_4 + e^- \rightarrow CF_2 + 2F + e^-$ $CF_4 + e^- \rightarrow CF + 3F + e^-$ $CF_3 + e^- \rightarrow CF_2 + F + e^-$ $CF_2 + e^- \rightarrow CF + F + e^-$ $CF + e^- \rightarrow C + F + e^-$ $F_2 + e^- \rightarrow 2F + e^-$
Dissociation with ionization	$CF_4 + e^- \rightarrow {CF_3}^+ + F + 2e^-$ $CF_4 + e^- \rightarrow {CF_2}^+ + 2F + 2e^-$ $CF_4 + e^- \rightarrow CF^+ + 3F + 2e^-$ $CF_4 + e^- \rightarrow C^+ + 4F + 2e^-$ $CF_3 + e^- \rightarrow {CF_2}^+ + F + 2e^-$ $CF_2 + e^- \rightarrow CF^+ + F + 2e^-$
Ion recombination	${CF_x}^+ + F^- \rightarrow CF_x + F\,(x = 1-3)$ $C^+ + F^- \rightarrow C + F$ $F^- + {F_2}^+ \rightarrow 3F$ $F^- + F^+ \rightarrow 2F$
Charge transfer	$F^+ + CF_3 \rightarrow {CF_3}^+ + F$
Dissociation with attachment	$F_2 + e^- \rightarrow F^- + F$
Recombination with electron	$F^- + e^- \rightarrow F + 2e^-$ ${F_2}^+ + e^- \rightarrow F + F$
Ion-surface interaction	$F^+ + e^-(s) \rightarrow F$
Neutral recombination	$CF_3 + F \rightarrow CF_4 + F$ $CF_2 + F \rightarrow CF_3$ $CF + F \rightarrow CF_2$ $F + F \rightarrow F_2$
Ionization	$F + e^- \rightarrow F^+ + 2e^-$
Surface recombination	$F + s \rightarrow F(s)$ $F + F(s) \rightarrow F_2 + s$
Neutral pumping	$CF_4, CF_3, CF_2, CF, F \rightarrow$ pumped out

The whole TISS, and hence ion source, is placed at 30–60 kV potential to accelerate the ions towards the extraction electrode [11, 64]. The FEBIAD-type ion sources, however,

are not selective and one should expect a high total beam background. The VADIS ion source is most commonly used for molecular ion beam production at CERN [64]. Because of the high atomic Sc and molecule ionization or dissociation potential (>6 eV) [99], the VADIS was mainly used for the TISS in this study.

Ionization efficiency

Due to the complexity of the plasma ion sources, such as the VADIS, the ionization efficiency estimation has to take into account multiple factors, including [62]:

- electron density and space charge effects;
- ionization cross section, which depends on the atomic radius, molecule dissociation/ionization potential and electron impact ionization energy [100];
- volatility of the neutral species, density and partial pressure in the ion source;
- chemical reactivity towards ion source structures and insulators;
- particle relative velocity;
- collisions with other atoms, molecules/ions and ion recombination.

The exact modeling is not yet established for the FEBIAD ion sources and molecule ionization (including dissociative ionization). However, a model in equation 2.1 proposed for chemically inert noble gases, including the Lotz formula, can give important insights into ion source operating parameters for further understanding and estimation of Sc molecule ionization efficiency [97, 101, 102].

$$\epsilon_{feb} = 2.33 \cdot 10^4 \cdot f \cdot V_{source} \cdot A_R \cdot exp\left(\frac{-W}{k_B T}\right) \cdot l \cdot \frac{ln\left(\frac{\mathrm{U}}{V_{ioniz}}\right)}{\mathrm{U} \cdot V_{ioniz}} \cdot \frac{\sqrt{M}\sqrt{T}}{S_{out}} \tag{2.1}$$

where ϵ_{feb} is the ionization efficiency of a FEBIAD source, f-factor accounts for the global fraction of extracted ions from the FEBIAD ion source, which reflects the ion survival, extraction and electron beam from cathode to anode, A_R is the Richardson's constant [120 $\mathrm{Acm^{-2}K^{-2}}$ for Ta], W is the work function of cathode material [eV], $\mathrm{k_B}$ is the Boltzmann constant [$8.617 \times 10^{-5}\,\mathrm{eV\,K^{-1}}$], T is the ion source temperature [K], l is the number of electrons in the valence shell, U is the anode potential [V], V_{ioniz} is the first ionization potential [eV], M is the Atomic mass [$\mathrm{gmol^{-1}}$] and S_{out} is the area of the outlet hole [$\mathrm{cm^2}$].

The heavier elements have a higher ionization cross section and a longer residence time in the ion source. Therefore they have a higher probability of undergoing ionization before leaving the ion source volume [103]. Lighter elements from the anode volume are typically released faster [62].

The ionization efficiency of a FEBIAD ion source mainly depends on the rate of ionization per unit volume and the fraction of successfully extracted ions. The ionization efficiency of VADIS was studied by L. Penescu and can be expressed by equation 2.2 [83, 97, 103]:

$$\epsilon_{ion} = \frac{R_{ioniz} \cdot V_{source} \cdot f_{extr}}{n_{in}}, \qquad \text{where} \qquad R_{ioniz} = n_e \cdot n_n \cdot \sigma_{ion} \cdot v_{rel} \tag{2.2}$$

where ϵ_{ion} is the ionization efficiency, R_{ioniz} is the rate of ionization [$\text{m}^{-3}\,\text{s}$], V_{source} is the volume of the ion source [cm^3], f is the global fraction of generated ions that are extracted before recombination, n_{in} is the number of neutrals reaching the ion source [pps], n_e is the electron density [cm^{-3}], n_{n} is the neutral gas density in the ion source [cm^{-3}], σ_{ion} is the ionization cross section of the neutral gas [cm^2], and v_e is the relative velocity between electrons and ions [cm/s], which is approximated to primary electron speed [103].

While the global f-factor stays constant, the efficiency can decrease with increased cathode temperature, as the increase in electron current results in a deepening of the potential well in the ion source, thereby increasing the size of the "inactive" volume. The f-factor then stays roughly the same for noble gases with the ion source and cathode operated in the range of 1800–2010 °C temperature [62]. This assumption is therefore also used for the ScF_3 ionization efficiency estimation. For VADIS ion source ionization efficiency tests and performance comparisons, a mix of noble gases (He, Ne, Ar, Kr, Xe of 20% each, 99.999 % pure) was used.

Space charge effects

Thermionic electrons are generated from the hot VADIS cathode and accelerated towards the anode grid. Intuitively, the higher the temperature of the cathode, the higher the electron density, however, in reality, the electrons can reach the space charge limit with the Ta cathode being operated at temperatures >2000 °C [103]. A potential barrier then is formed on the cathode due to negative charge accumulation, that repels new electrons back to the cathode. The electron current in this regime is described by Child-Langmuir law in equation 2.3:

$$j_{e,cl} = \frac{4}{9}\epsilon_0 \sqrt{\frac{2e}{m_e}} \frac{U^{3/2}}{d^2} \tag{2.3}$$

where $j_{e,cl}$ is the electron current density emitted from the cathode [$\text{A}\,\text{m}^{-2}$], ϵ_0 is the vacuum permittivity $\epsilon_0 \approx 8.854 \times 10^{-12}\,\text{F}\,\text{m}^{-1}$, e is the elementary charge $e \approx 1.602 \times 10^{-19}\,\text{C}$, m_e is the electron mass [kg], U is the potential difference of the anode [V] and d is the distance between the cathode and anode grid [m] [62,103]. At lower temperatures, the electron emission follows the Richard-Dushman equation 2.4 [62].

$$j_{cath} = A_R \cdot T^2 \cdot exp\left(-\frac{W}{k_B T}\right) \tag{2.4}$$

where j_{cath} is the electron current density emitted from the cathode [$\text{A}\,\text{m}^{-2}$], A_R is the Richardson's constant [120 $\text{Acm}^{-2}\text{K}^{-2}$ for Ta], k_B is the Boltzmann constant [$8.617 \times 10^{-5}\,\text{eV}\,\text{K}^{-1}$], W is the work function of cathode material [eV], and T is the ion source temperature [K].

An increase in temperature will not result in increased electron density within the anode body and therefore higher rate of ionization, but can even harm the ion source in the long term. The space-charge limited regime is an important aspect to consider in order, to prolong the VADIS lifetime and obtain the maximum ion source efficiency during the mass separation and collection. One should aim to obtain the maximum density and ionization efficiency possible, typically around 2000–2200 °C [103]. The regime of operation then can be unfolded by comparing the measured drain current of the anode body with the theoretical thermionic electron emission current and respective anode potential.

The space charge effects are also observed for dense, charged particle ion beams, which can expand due to self-induced electrostatic forces [102]. In the case of VADIS, the maximum ion current extracted from the ion source for mass separation is limited by the plasma sheath, which also follows the Child-Langmuir law. It then computes for VADIS to being able to extract ion currents of more than 50 μA at 30 kV target unit potential and 60 mm extraction gap [103].

2.3 Mass separation

TISS testing, study of target materials, ion sources and stable (non-radioactive) isotopes and molecules is done with two offline mass separators (Offline-1 and Offline-2), available at ISOLDE and CERN-MEDICIS [104]. In this study, two mass separators were used for the development, mass separation and collection of the Sc ion beams. Offline-1 was used for TISS development, testing and stable (non-radioactive) ion beam studies. The CERN-MEDICIS mass separator was used for radioactive Sc mass separation and collection as well as stable Sc ion beam developments and atomic Sc laser ionization studies.

2.3.1 CERN-MEDICIS mass separator

The CERN-MEDICIS mass separator in its essence is an offline mass separator, as there is no primary beamline connected to the target unit. A schematic of the CERN-MEDICIS mass separator is shown in Figure 2.7. The first section is typically referred to as the frontend. Here the radionuclide release, ionization, acceleration and primary beam optics originate. The frontend consists of:

- an electrically isolated TISS coupling system where it is operated at 30–60 kV potential;
- a Target and Ion Source System that is exchanged for each batch and holds the irradiated target material and produced radionuclides;
- a Ti extraction electrode that is placed at 50-80 mm distance from the ion source orifice;
- a charged particle electrostatic Einzel lens to shape the ion beam entering the dipole magnet operated at 18-26 kV, depending on the extraction potential and ion source type);
- vertical and horizontal electrostatic deflectors that allow beam realigning ($\pm$ 200–600 V).

After the frontend a Cu Faraday cup is installed and can be inserted in the beam path to measure the total ion beam current, which enters the separator magnet. The main "separator" section part is a 55^o double focusing magnet with a bending radius of 1.5 m. It is operated up to 90 A current to induce the magnetic field [88]. Opposite the beam entrance path, a dedicated window is placed to reflect the laser beam from MELISSA directly into the ion source cavity.

The beam instrumentation box is present after the separator magnet. It houses a wire scanner to assess the beam shape and position, another Faraday cup to measure the separated ion beam current, and a recently upgraded double-slit system. The double-slit system allows isolating one specific ion beam[1] or two ion beams simultaneously with a difference of 1–3 atomic mass unit (amu) [71]. After the beam instrumentation box, one finds the sample collection chamber, where the sample holder with up to 3 collection foils (15×20 mm) are placed in the RIB path to implant the radionuclide(s) of interest. The sample holder consists of a collimator, sample plate and an electron repeller, which is used to repel secondary electrons to the sample plate and acquire more accurate reading. The impinging ion beam current can be separately measured both for the collection foil and collimator. The ions are implanted and collected in Zn or Al-coated gold foils, full-body Al or Cu foils or salt-covered Al foils in perpendicular or angular positions with respect to the RIB.

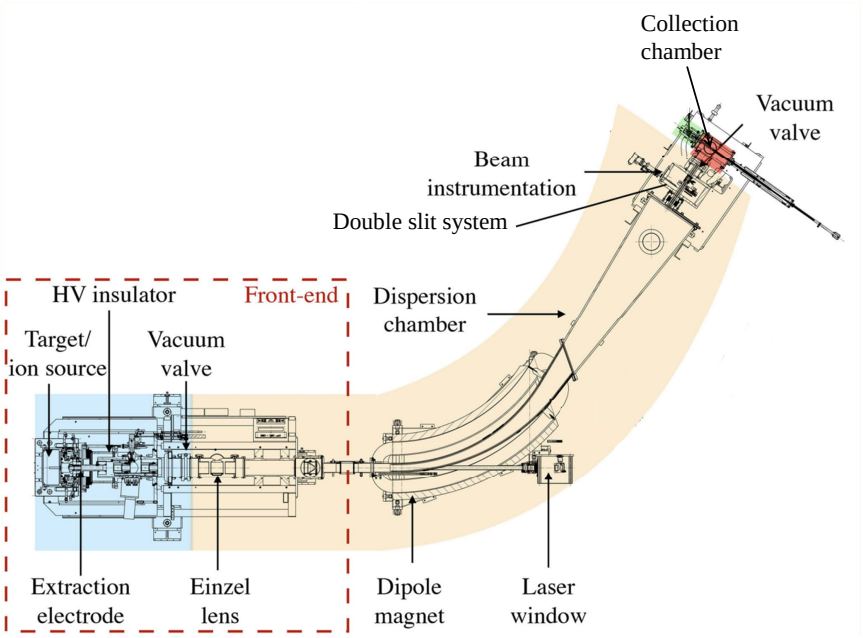

Figure 2.7: CERN-MEDICIS mass separator schematics. Adapted from [88].

The mass separator is operated at a vacuum pressure of 1×10^{-5}–1×10^{-7} mbar. Each of the described mass separator sections can be isolated by hermetic valves. Depending on the target material, radionuclides that are released, but not ionized or implanted in the collection foil during the collection are pumped from the separator volume and stored in local decay tanks. The radionuclides are stored until they decay to a sufficiently low level for release into the atmosphere [88].

To create the molecular ion beams, reactive gases are injected into the target containers.

[1] Most commonly referred to as just "mass".

Reactive and noble gas injection in the TISS is done through a gas connection system that is located inside a dedicated high-voltage and power supply room, outside the mass separator bunker. The gas injection system consists of two main subsystems of which the first is dedicated to noble gas or reactive gas injection, such as NF_3 and CF_4. The second subsystem is dedicated to pure Cl_2 gas injection and residual gas neutralization. Cl_2 must be supplied by a separate system and residuals neutralized after use as it poses additional corrosion risks for the metallic parts and safety hazards during the operations. The Cl_2 gas subsystem is then connected to the same feed line to the TISS and the calibrated stainless steel gas leak.

2.3.2 Offline-1 mass separator

The layout of the Offline-1 separator is similar to the CERN-MEDICIS mass separator. The targets on Offline-1 are placed on 30 keV potential for the ion acceleration. Figure 2.8 provides an overview of the Offline-1 mass separator main components. It is capable of separating masses of up to ∼300 amu with the ion beam energy of 30 keV. The transmission efficiency between the total beam and the separated beam Faraday cups is typically in the order of ∼75 % [11, 62]. The recent Offline-1 upgrade includes a collection chamber at the end of the instrumentation box, where a stable ion beam can be implanted in metallic foils. The implanted species then can be released by resistive heating and detected by a Residual Gas Analyzer (RGA), located on top of the collection chamber. The RGA measurement range is 1–200 amu [104].

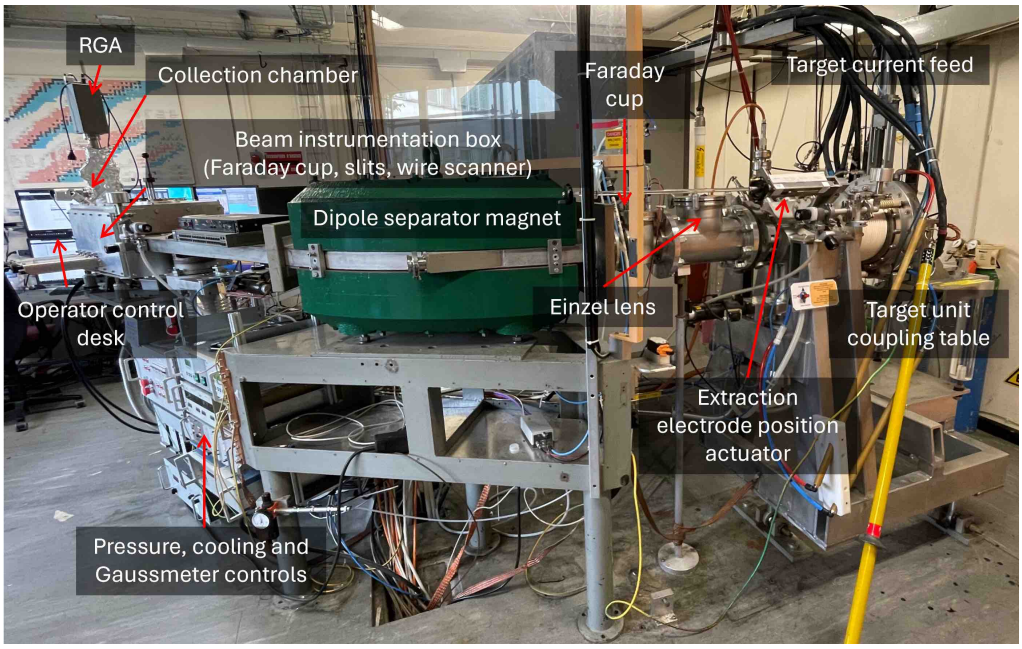

Figure 2.8: Offline-1 mass separator.

The Offline-1 mass separator frontend, from the TISS coupling table side with the manual gas injection system, is shown in Figure 2.9. The gas injection system is built of stainless steel and PolyTetraFluoroEthylene (PTFE) tubing. Here as well the maximal gas amount injection rate is limited by the pumping capabilities of the vacuum system. At Offline-1 the pressure of $<1 \times 10^{-5}$ mbar is also required to safely operate the

high-voltage system and the VADIS ion source.

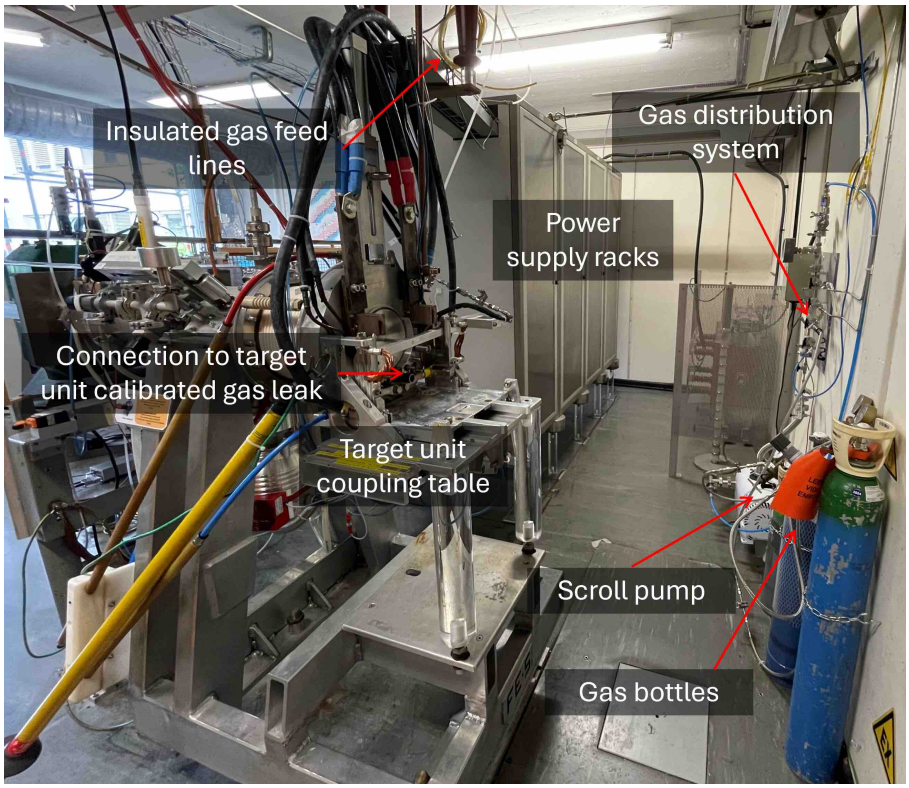

Figure 2.9: Offline-1 mass separator from within the Faraday cage.

Before proceeding to the target material irradiation, mass separation and collection of radioactive Sc isotopes at CERN-MEDICIS, the Offline-1 was used for TISS testing and quality control.

2.3.3 Pumpstand

A separate TISS coupling table - pumpstand - was used to calibrate each target container and transfer line temperature against the applied current. The pumpstand is also used for target material outgassing, such as the metallic foil rolls and ^{nat}TiC pellets. Same as for mass separators, the pumpstand can support current for heating and reach a vacuum inside the target units down to 1 $\times 10^{-7}$ mbar. Five current-regulated ($\pm$0.1 A) Delta Elektronika SM15-200D power supplies are used to heat the target container and an additional three power supplies are for the transfer line heating. A current of up to 1200 A can be applied for target heating. The pumpstand that was used for the Sc thermal release studies is equipped with a dedicated gas exhaust system for any potential radioactive gas trapping.

2.3.4 Molecular ion beams

Refractory elements are difficult or sometimes cannot be extracted from the TISS in their atomic gas form. Even if they are released from the target materials, during their migration to the ion source they will frequently collide with the walls of the TISS.

Each encounter will delay their total time for reaching the ion source. Therefore, slow desorption is more penalizing than slow diffusion [64,75].

One of such elements is proven to be Sc. Sc is known to form halides that are more volatile than the atomic counterpart. The molecule formation was therefore used for the extraction from TISS. To create scandium halide molecules in the target units, reactive gases such as carbon tetrafluoride (CF_4, 99.995 % pure), nitrogen trifluoride (NF_3, 99.99 % pure) and chlorine (Cl_2, 99.8 % pure) were applied to the target container.

Molecular and atomic Sc ion beam formation after Sc volatilization is mainly obtained through stable molecule dissociation rather than direct ionization because the dissociation potential of $ScF_x(x = 1-3)$ species is lower than their direct ionization potential [99, 105]. Both the ionization and dissociation potential of atomic Sc and ScF_x molecules is >6 eV, which exceeds the work function W of Ta, W and Re metals, suggesting surface ion source is not suitable for atomic Sc molecular ion beam mass separation. Nevertheless, radioactive Sc^+ and ScF^+ ion beams have been reported at ISOLDE with a W surface ion source [82]. This can be explained by certain released molecule fraction dissociative ionization and drift electron acceleration in the extraction field. Also, it has been reported that adsorption of oxygen from impurities or native oxide layer on W enhances its W [106, 107].

Sc mono-atomic ionization with laser resonant ion source or halide molecule ionization with a FEBIAD type ion source should be preferred [99]. Laser ionization is inefficient with a VADIS ion source due to distance and cold structures in between the transfer line and extraction electrode. Therefore W and Re surface ion sources were combined with the laser resonant ionization experiments.

Evaporation rates of volatile heterogeneous reaction products

The Quasiequilibrium (QE) treatment of heterogeneous reactions can be used to compute the evaporation (desorption) rates of volatile species formed in the reactions of gaseous molecules with solid surfaces. The QE model closely predicts the temperature and pressure influence on the evaporation rate of the volatile species and predicts that the proportions of the species will be those of an equilibrium mixture. [108].

Gaseous reaction product species are emitted in a thermodynamic equilibrium distribution fixed by the solid substrate temperature. The rate of evaporation is determined by the adsorption rate of the reactive gas. The collision rate from gas kinetic theory can be expressed as Hertz-Knudsen equation 2.5 [108–110]:

$$Z_i = \frac{p_i}{\sqrt{2\pi M_i RT}} \tag{2.5}$$

where Z_i is the rate at which molecules of species i collide with a solid surface for equilibrium conditions [$m^{-2}s^{-1}$], p_i is the partial pressure of species i [Pa], M_i is the molecular mass of the evaporating material [kg/mol], R is the gas constant [kgm^2/s^2molK] and T is the temperature of the gas and solid [K].

The rate of adsorption Γ_i must be balanced at equilibrium by an equal but opposite rate of evaporation of species i R_i from the adsorbate phase. If the reaction thermodynamics favor product formation and surfaces are smooth, then the rate will be approximately

[2] The term proposed by J.C. Batty, R.E. Stickney.
[3] The term proposed also mentioned as the gasification probability by D.L. Hildenbrand.

equal to the atomic vaporization rate of the metal at pressure p_i and temperature T, multiplied by the "equilibration probability" [2] ζ_i [108, 109]. The "equilibration probability" is defined as the experimentally observed molecule evaporation rate (or removal from the surface) against the rate at which the fluorinating gas impinges upon the surface. Therefore the kinetic aspect can be treated with simple empirical parameter - the equilibration probability or substrate atom removal probability[3] (see equation 2.6).

$$R_i = \Gamma_i = \zeta_i \cdot Z_i, \qquad \text{or} \qquad R_i = \frac{\zeta_i p_i}{\sqrt{2\pi M_i RT}} \tag{2.6}$$

where R_i is the evaporation rate of the formed volatile species [$m^{-2}s^{-1}$], Γ_i is the adsorption rate (the rate at which molecules are equilibrated) [$m^{-2}s^{-1}$], and ζ_i is the equilibrium probability or the fraction of the collisions that result in adsorption/evaporation, normalized for the stochiometric ratio of species i formation.

Values of ζ_i = 0.1–0.3 at 1000–2000 K have been obtained for refractory metals with gasification by F and F_2 [110, 111]. No ζ_i values are available for other fluorinated reactive gases (e.g. CF_4 or NF_3), however, they are assumed to be lower than those found for F and F_2.

Partial pressures of the chemically evaporated species will also depend on the pressure and thermochemical stability of the reacting gas. It is expected that ζ_i will decrease as the thermodynamic stability of the reactive gas increases. The Gibbs free energies of formation for several possible reactive gases in kJ/mol normalized per single F atom at 1500 °C are as follows: F_2 (0); Cl_2 (0); SF_6 (-97.4); CF_4 (-166.1); HF (-281.5); SiF_4 (-339.6); BF_3 (-342.1) and NF_3 (36.9) [109, 112]. Therefore the reactivity and degree of equilibration probability should follow the pattern $NF_3 > F_2 = Cl_2 > SF_6 > CF_4 > HF > SiF_4 \geq BF_3$.

2.4 Chemical separation

2.4.1 Ion exchange chromatography

Most commonly the chemical purification of medical radionuclides is done via Ion Exchange Chromatography (IEC). The principle of IEC is that the radionuclide of interest is first adsorbed on a resin inside a chromatographic column - also referred to as the loading phase. It is then followed by a washing phase, to flush out any co-adsorbed contaminants. After the washing phase, elution of the radionuclide of interest is done with an appropriate concentration solution. In RPH manufacturing, this is typically low-molarity HCl. Additionally, flushing with Deionized (DI) water can be done to remove all ions from the column. The resin then can be regenerated and reused.

Various resins for Sc ion exchange chromatography have been employed, such as Uranium and TEtra-Valent Actinide (UTEVA), Transuranium (TRU). Thus far the best separation efficiency and highest radiochemical yields were obtained with the Diglycolamide (DGA) resin, because of high Sc^{3+} retention and negligible Ti, V, Cr and Ca at HCl molarities below 6 M [28, 113, 114]. The structural formula for the DGA resin is shown in Figure 2.10. There are two DGA resin forms: branched (*N,N,N´,N´*-tetrakis-2-ethylhexyldiglycolamide) and normal (*N,N,N´,N´*-tetra-n-octyldiglycolamide). The

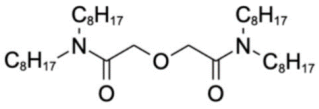

Figure 2.10: *N,N,N´,N´*-tetra-n-octyldiglycolamide (DGA Normal).

Sc^{3+} ions interact with 3 DGA molecules by forming micelle-type non-covalent complexes according to the equation 2.7. The coordination complex (micelle) can then be broken down by using an eluting agent (usually 0.1 M HCl).

$$Sc^{3+}_{(aq)} + 3\,DGA_{(s)} + 3\,NO_3^- \rightleftharpoons [Sc(DGA)_3(NO_3)_3]_{(s)} \tag{2.7}$$

In the case of collection foils at CERN-MEDICIS, the solvents typically used for radionuclide dissolution are HNO_3 and HCl, based on the chemical composition of the collection foil. The weight distribution ratio D_w on the resin describes how much corresponding metal ions get adsorbed on the resin in a given medium concentration and are shown in Figures 2.11 and 2.12 [115,116].

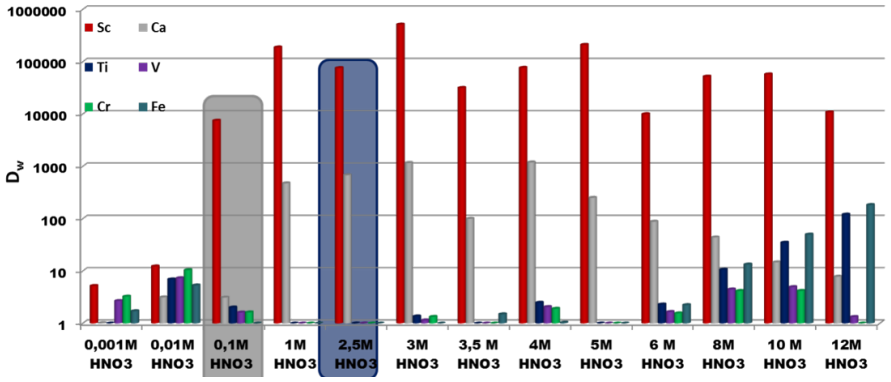

Figure 2.11: Weight distribution ratios D_w of metals on the DGA resin in HNO_3 medium [115,116].

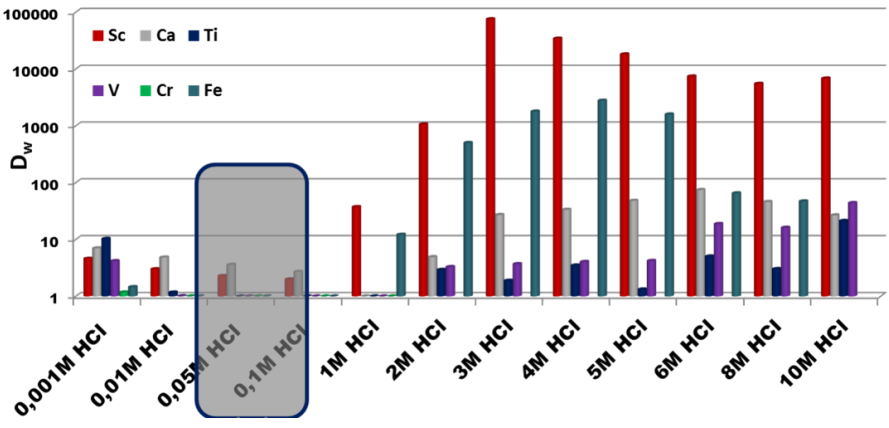

Figure 2.12: Weight distribution ratios D_w of metals on the DGA resin in HCl medium [115,116].

Based on these ratios and expected isobaric contaminants, one can develop the most appropriate chemical separation plan. For example, the Sc loading onto the column has the best retention at HNO_3 concentrations of 1–2.5 M solutions and for the elution from the column 0.05–0.1 M HCl would be most applicable.

2.4.2 Electrochemical separation

The basis of electrochemical separation is the difference in electrical potential for various metals. In comparison with a chemical reaction, where electrons are transferred directly between atoms, ions, or molecules, in electrochemistry, the electrons are transferred to an ion via an electronically-conducting circuit. The method is based on the fundamental reduction-oxidation potentials of metal atoms/ions with some summarized in Table 2.2. This way the contaminant metals or elements of interest can be directly deposited onto the electrode. The added value of electrochemical separation is that no resin and continuous mobile phases are needed. This also helps to limit contaminated liquid radioactive waste build-up.

Table 2.2: Metal standard reduction potentials [117].

Chemical element	**Reduction half reaction**	**Standard reduction potential [$E^{\ominus}$], V**
Zn	$Zn^{2+}_{(aq)} + 2e^- \rightleftharpoons Zn_{(s)}$	-0.7618
V	$V^{2+}_{(aq)} + 2e^- \rightleftharpoons V_{(s)}$	-1.13
Ti	$Ti^{3+}_{(aq)} + 3e^- \rightleftharpoons Ti_{(s)}$	-1.37
Al	$Al^{3+}_{(aq)} + 3e^- \rightleftharpoons Al_{(s)}$	-1.662
Sc	$Sc^{3+}_{(aq)} + 3e^- \rightleftharpoons Sc_{(s)}$	-2.007
Na	$Na^{2+}_{(aq)} + 1e^- \rightleftharpoons Na_{(s)}$	-2.71
Ca	$Ca^{2+}_{(aq)} + 2e^- \rightleftharpoons Ca_{(s)}$	-2.868
Rb	$Rb^{+}_{(aq)} + 1e^- \rightleftharpoons Rb_{(s)}$	-2.98

The rate of deposition on the cathode is directly proportional to the cathodic current, therefore, in cases of low electrolyte concentration (ionic strength < 1 M) the solution is heated to increase the ion mobility and current. The solution is heated up to ∼55 °C, and temperatures above 60 °C can cause rapid water evaporation [118]. The rate of deposition is of high importance due to the radiation protection and half-life factors.

By using aqueous acid solutions for the implantation layer dissolution of the collection foil, electrochemical separation must be used in conjunction with ion exchange chromatography due to the water electrolysis potential limit. The thermodynamical H_2O electrolysis potential is 1.23 V and 1.8–2.0 V due to the overpotential [119,120]. The electrochemical separation method can remove Zn, V, and Ti elements from Sc-containing aqueous samples by using potential-controlled electrodeposition. [117]. Therefore, the majority of isobaric contaminants from mass separation can be removed, leaving the IEC with less contaminant ion load for the column.

An alternative is non-aqueous electrolysis by using ethanol or acetonitrile, to avoid the electrolysis of the solvent. In that case, however, the dissolved solution must be evaporated and re-dissolved in a different medium. Similar methods have been used separately to isolate various metallic elements in both aqueous and non-aqueous media [117,121,122].

2.5 Computational tools and methods

2.5.1 HSC Chemistry software

The Enthalpy (H), entropy (S) and heat capacity (Cp) (HSC) software (version 7 and 9) is a thermodynamic chemical reaction and equilibrium calculation software. It contains data for more than 28000 chemical species. HSC offers calculation tools for studying the effects of different variables in a chemical system at equilibrium conditions based on the thermodynamic laws and formulas [112,123]. Defining the raw materials (chemical elements), amounts, temperature, pressure and other conditions of a chemical process, the software will give the amounts of the product as a result. HSC also can be used for heat and material balance calculations of different processes.

A chemical reaction is in equilibrium if the concentration of the reactants - A and B - and products - C and D - remain constant and the system has no tendency to change (see equation 2.8). Usually, both reactions still happen but without any net change in the concentration of any products or reactants. The reaction rate is then described by its reaction rate coefficients k_+, k_- and equilibrium constant K_{eq} [94].

$$\alpha\mathrm{A} + \beta\mathrm{B} \underset{\mathrm{k_-}}{\overset{\mathrm{k_+}}{\rightleftharpoons}} \gamma\mathrm{C} + \delta\mathrm{D}, \qquad \text{where} \qquad K_{eq} = \frac{k_+}{k_-} \tag{2.8}$$

2.5.2 FLUKA

The produced radionuclide inventory from target material irradiation at CERN-PSB is predicted via the use of the FLUktuierende KAskade (FLUKA) (version 4.3) multi-purpose Monte-Carlo (MC) code. FLUKA is based on stochastic three-dimensional particle tracking and allows the prediction of energy and angle differential particle fluences in complex geometries. With the FLUKA code, one can obtain the production yields of residual nuclei as well as expected dose rates [11]. It covers nucleus–nucleus, hadron–nucleus, and hadron–hadron interactions from their threshold up to 10 PeV energy. Besides heavy ions, in total sixty different particles can be transported [124].

The FLUKA code includes multiple models to describe the interactions. The nuclear interactions are sampled using the FLUKA MC code internal models or database information [73]. For particle energies < 20 TeV/u and hence the proton energy of 1.4 GeV that is obtained at the PSB, the PreEquilibrium Approach to NUclear Thermalization (PEANUT) model is used for hadronic interactions [11,125,126]. For particles with energies > 20 TeV/u the Dual Parton Model and JET (DPMJET) interface is used. The FLUKA code has been benchmarked with experimental data from radionuclide production in the corresponding energy range and is being updated regularly [127–129].

Flair (version 3.3), an advanced interface for several Monte-Carlo codes and originally

developed for FLUKA, was used for visualization and modeling of the geometry as well as processing the results generated from the FLUKA input parameters [130].

2.5.3 Actiwiz

ActiWiz (version 3.6.12/2023-2507) is a computational tool, developed at CERN, that calculates the production of each isotope from a set of particle fluence spectra as a function of the particle type and energy. That includes neutrons, protons, pions (π^+, π^-), and photons. It also provides fast and accurate assessments of radiological risks associated with various materials used in high-energy particle accelerators [131, 132].

ActiWiz uses a proprietary database of radionuclide production reactions from protons, charged pions, photons and neutrons. For neutrons below 20 MeV these data are based on evaluated Joint Evaluated Fission and Fusion File (JEFF)-3.3, Evaluated Nuclear Data File (ENDF)-VIII.0, and European Activation File (EAF)2010 libraries [80, 133]. For the neutron energies above 20 MeV as well as all other particle types, the respective production yield has been determined via an exhaustive set of FLUKA calculations. ActiWiz derives the nuclide yields for arbitrary compound materials by combining the particle fluence and the nuclide production data. These results are eventually translated into radionuclide activities by solving the Bateman equations considering a specific irradiation and decay period and pattern. [134].

In addition, ActiWiz includes many post-processing options to directly analyze the results. It was used to calculate the total radionuclide activity in irradiated TISS target materials from the FLUKA output files at a given time. ActiWiz was also used to estimate the activity and dose rate of the samples for thermal release studies from the CERN-CHARM particle fluence spectra (see Figure 2.2) and activation scenarios.

2.5.4 Out-diffused fraction model

Out-diffused radionuclides can be referred to as those radionuclides, initially placed in the matrix of a solid, which due to thermally promoted diffusion reach the surface of the object that contains them and manage to escape from it. If chemical reactions with surrounding substances and impurities in and on the material are ignored, a radionuclide reaching the surface of an object can either diffuse back into the bulk matrix or get released - desorb. The fraction of radionuclides released from a given object can also be referred to as the Out-Diffused Fraction (ODF). The ODF can be estimated according to equation 2.9 [135].

$$ODF = FRS \cdot GDP \tag{2.9}$$

where FRS is the fraction of isotopes reaching the matrix surface in a given time and temperature, and GDP is the global radionuclide desorption probability at a given time and temperature.

Diffusion

Diffusion is a process of particle transport from one part of a matrix to another and is driven by a difference in concentration. The particles continuously move along random

trajectories due to their thermal energy. The mathematical treatment of diffusion can be approximated by Fick's first and second laws. The second Fick law is also referred to as the differential diffusion equation and takes into account the time dependence [11,135].

The diffusion of a tracer is described by its diffusion coefficient D at a certain temperature. The diffusion or displacements of a tracer can be described as jumps between lattice positions which require a certain activation energy. Typically for metals, it is a function of temperature following the Arrhenius-type expression (see equation 2.10).

$$D = D_0 \exp\left(-\frac{E_a}{RT}\right) \tag{2.10}$$

where D is the diffusion coefficient for a tracer particle in a given matrix [cm^2s^{-1}], D_0 is the pre-exponential factor also referred to as the frequency factor [cm^2s^{-1}], R is the universal gas constant [J/molK], T is the absolute temperature [K] and E_a is the diffusion activation energy [kJ/mol].

The diffusion constant strongly depends on the combination of diffusing species and the host medium (matrix). The pre-exponential factor D_0 is equal to the diffusion coefficient at infinite temperature and is a constant. The exponential term reflects the fraction of species that have sufficient energy to make the jumps between lattice positions [6, 11]. Simplistically, D_0 relates to how the atoms of the lattice vibrate and E_a represents the energy required to successfully jump. The exact physical meaning of the parameters D_0 and E_a depend on the diffusion mechanisms and the lattice geometry or crystalline structure [135].

It should be noted that even small temperature, diffusion and desorption activation energy variations may have huge effects on the ODF value. Unfortunately, the available experimental data is usually very scarce and imprecise, especially for desorption.

Fraction reaching surface

In cases where the initial concentration of radionuclides and temperature is or is assumed to be uniform within the bulk matrix, the Fraction Reaching Surface (FRS) can be approximated from the equation 2.11 [135].

$$FRS \simeq \text{erf}\left(\frac{S_b}{V_b}\sqrt{D \cdot t_T}\right) \tag{2.11}$$

where erf is the error function (values of 0–1), S_b is the surface area of bulk matrix [cm^2], V_b is the volume of bulk matrix [cm^3], D is the diffusion coefficient for a tracer particle in the given matrix [cm^2s^{-1}] and t_T is the diffusion time at a given temperature [s].

The FRS can be used to set a conservative upper limit for the ODF value. For non-uniform distributions, the surface/volume ratio is replaced by a factor related to the distances from the radionuclides to different surfaces and is a function of $\sqrt{Dt_T}$ [135].

Global desorption probability

More accurate values of the ODF can be estimated by taking into account the desorption phenomena. Desorption is the opposite process of adsorption - the adhesion of atoms or molecules to a surface. The atoms or molecules can adsorb by two different mechanisms: physisorption and chemisorption. Physisorbed atoms are bound to the surface by Van der Waals forces. Chemisorbtion requires the existence of covalent or ionic chemical bonds with the surface and the potential well trapping them is typically deeper than physiosorbtion.

Assuming that at a given time t_0 all radionuclides have reached the surface, the Global Desorption Probability (GDP) can be estimated. Although it is an overestimated value, the impact of desorption can be assessed. The GDP can be estimated through equation 2.12 [136].

$$GDP = 1 - \left(1 - \frac{1}{1 + \exp\left(\frac{E_{des} - E_a}{k_B T}\right)}\right)^{0.908294\left(\frac{6Dt_T}{DNN^2}\right)^{0.500950}} \tag{2.12}$$

where E_{des} is the desorption activation energy (enthalpy) for species of interest on a given surface [kJ/mol], k_B is the Boltzman constant [kJ/molK], DNN is the distance between the nearest atomic neighbor in the surface material lattice [cm], and t_T is the time at a given temperature [s]. The desorption activation energy values in the literature are very scarce and can be approximated as sublimation enthalpy or the negative value of adsorption enthalpy [135].

2.6 Sample and material analysis

2.6.1 γ-ray spectrometry

High Purity Germanium (HPGe) detector

Systematic γ-spectroscopy measurements are performed on every retrieved sample after radionuclide collection, activated and thermally treated samples for the release study, radiochemistry procedure samples and their setup parts as well as externally irradiated samples before mass separation. The high-resolution γ-ray spectrometry is performed with a High Purity Germanium (HPGe) coaxial detector from MIRION Technologies (Canberra) S.A.S. The energy range of the detector is 3–10 000 keV with a relative efficiency of > 40 % and resolution of < 1.2 keV (at 122 keV) and < 2.0 keV (at 1332 keV) [137].

The In Situ Object Counting System (ISOCS) calibration software is used for absolute efficiency calibration [138]. With the ISOCS software, the detector modeling based on the Monte Carlo N-Particle Transport (MCNP) code can be combined with the sample dimensions, material parameters and mathematical geometry templates, resulting in quantitative γ assays of the activity present in the samples measured. The detector can be selected in the software and incorporated into the model [139]. For different geometry and material samples, ISOCS is used to create a specific energy-dependent efficiency calibration curve. APEX (version 1.4.1) software is then used to acquire and

analyze obtained spectra and calculate the measured radionuclide activities. The software takes into account and corrects for the geometry model uncertainties, the detector dead time, counting statistics, peak area fitting systematic uncertainties and γ-ray emission probabilities [140].

After collection and for sample shipping purposes, the samples are typically measured for 15 minutes (live-time). Measurement times are increased up to 24 hours or more for certain samples to reduce uncertainty when the activity in the sample is low (few kBq). For each sample, the distance from the sample to the detector is chosen to optimize the detection efficiency and low dead time (typically below 1 %). The collected radionuclide activities are decay-corrected to the time when the implantation was stopped (EOC) and used to quantify the collection efficiency.

Kromek GR detector

Short γ-ray spectrometry measurements during radioactive ion beam collection are done *online* with a 1 cm cubed Cadmium Zinc Telluride (CZT) γ-ray Kromek GR1+ semiconductor detector [141,142]. The resolution of GR1+ is < 2.0 % FWHM @ 662 keV [143]. The obtained spectra are acquired, saved, displayed and quantitatively analyzed by the Kromek Multi-Spect Analysis spectroscopy software (version 14.24.3.243).

The main Kromek GR1+ detector is placed directly behind the sample foil, outside the collection chamber (see Figure 2.13). This way the radionuclide activity and collection rate on the collection foils could be controlled starting from the first kBq and monitored during the whole experiment time. Typically the main detector is used, however, when the collected activity or background from previous collections in the collection chamber is too high and the dead time increased, a secondary Kromek GR1+ detector can be used, which is positioned further away from the sample [142]. In the near future, a system of collimators will be added to this detector to be able of measuring even higher activities and diminish the dead time.

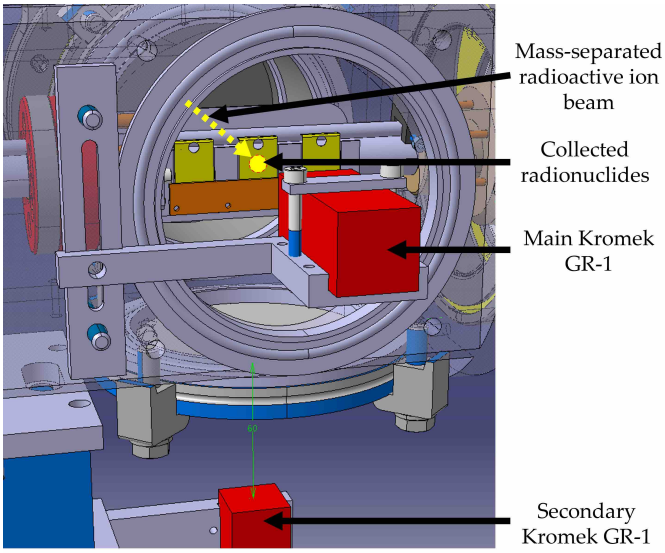

Figure 2.13: Schematic Kromek GR-1 detector placement at the CERN-MEDICIS mass separator collection chamber.

Usually, two-minute real-time acquisitions are done every 5 minutes during the collection. Any possible sputtering impact during the collection can also be assessed when the collection foils and sample holder are removed from the collection chamber, by additional measurements [144].

2.6.2 SEM–EDX

Scanning Electron Microscopy (SEM) is conducted by sweeping (scanning) the surface of a material or sample with electrons of up to tens of keV energy, reconstructing a 3D-like image from the topography of the sample [145]. The electrons interact with the matter from the sample and can be used to determine different material characteristics, such as the material surface topography, crystallography, phase composition contrast and chemical composition.

When the electrons from the beam collide inelastically with the outer shell electrons of the sample, Secondary Electron (SE) are produced and ejected. These electrons have low energies (< 50 eV) and do not travel far in the material, however, those that are close to the surface can escape and be detected by a SE detector. Due to their short travel distance, they give information mostly about the surface and are used to describe topography. SE detectors are usually located on the side, relative to the sample, and have an electrode that attracts only the low-energy SE, which are then detected on the scintillator with a photomultiplier. Due to their positioning and low solid angle, the generated images are often of low signal and suffer from a shadow effect. An *in-lens* detector counters this issue, due to its location inside the SEM accelerator column. Higher quality images are produced because they collect the SE with higher efficiency, less noise and no shadowing [6].

Electrons from the beam, whose trajectory gets close to the nucleus and therefore altered by elastic Coulomb interactions with the nucleus are called Backscattered Electrons (BSE) [145]. Their energy is close to the one of the incident electron beam and provides information about the chemical composition of the phases. Energy-Dispersive X-ray spectroscopy (EDX) can be used to qualitatively and quantitatively identify the chemical composition of a sample. When the electron beam interacts with the material, element-characteristic X-rays are generated. These X-rays are then used to assess the chemical composition of the sample. Higher electron energies can excite electron shell levels with higher energy, helping to identify the elements in the sample. However, this also results in a larger excited volume and results in lower resolution [6].

The main SEM used was *Carl Zeiss SMT Sigma*, located at CERN. It has a Field Emission (FE) Schottky ZrO/W cathode electron gun with an SE, BSE and in-lens detector. It operates up to 30 keV with a maximum resolution of 1.5 nm at 20 kV and magnification up to $\times$500 000. The SEM is coupled with an OXFORD INCA Synergy 350 X-Max 50 / Hkl ADV EDX for chemical composition analysis. A second SEM - *FE-SEM Hitachi S4800*, located at the University of Latvia - was used for metallic surface analysis. It operates up to 30 kV with a resolution of 1 nm at 15 kV and $\times$800 000 magnification. The SEM is also equipped with Quantax Esprit 1.9 EDX.

The samples were mounted on a SEM support with a conductive carbon or copper sticker. Almost all of the samples, such as TiC, Ta, W, Mo, Cu, Ti, V ScF_3 and C were electrically conductive and charge-up or electron deflection was not observed and no

need for any special sample treatment was required. Difficulties were expected for VADIS ion source BeO insulator analysis, however, the samples were un-intentionally coated with C and Ta and eventually did not affect the investigation of this sample.

2.6.3 Specific surface area determination by BET method

For an ISOL target material, the adsorption and effusion strongly depend on the material surface area. Adsorption can also be expressed as the adhesion of an atom to a surface at a pressure (P), lower than its vapor pressure or saturation pressure (P_0). The adsorption depends on the atom or molecule species (adsorbate) and the surface (adsorbent). Each species–surface combination results in a unique isotherm - the amount of adsorbate on a surface at a constant temperature, as a function of the absorbate pressure with a maximum value of $P = P_0$ [146].

Assuming that only physisorption takes place, adsorption-desorption isotherm of a material of interest can be obtained. Typically, hysteresis between adsorption and desorption can be observed and gives information about the material, such as its surface area, porosity, pore size and shape [146]. Usually, nitrogen (N_2) is used as adsorbent at its liquid temperature (77 K or -195.8 °C [147]) to determine the full adsorption-desorption isotherms.

To determine the Specific Surface Area (SSA), Quantachrome NOVA 2200 surface area and pore size analyzer was used. It is equipped with two measuring cells and two vacuum outgassing stations, capable of reaching up to 400 °C. The samples are outgassed in a vacuum at 300 °C for $\sim$1 day before the analysis to remove any unwanted sorbents from the surface, such as water. Quantachrome NovaWin (version 11) was used to calculate the SSA with the Brunaeur, Emmett and Teller (BET) model, through equation 2.13 [148].

$$SSA = \frac{N_A \cdot \sigma_{mol} \cdot V_{ml}}{V_{m,sPT}} \tag{2.13}$$

where SSA is the specific surface area [m^2g^{-1}], N_A is the Avogadro constant [mol^{-1}], σ_{mol} is the adsorbate molecule cross section [m^2], $V_{m,sPT}$ is the molar volume of 1 mol N_2 at standard temperature and pressure [m^3mol^{-1}], and V_{ml} is the adsorbate monolayer volume [m^3], which can be extracted with the software from the linear zone of the isotherm ($0.05 < P/P_0 < 0.35$) by plotting $P/V_a(P_0 - P)$ vs P/P_0

$$\frac{P}{V_a(P_0 - P)} = \frac{1}{V_{ml}C_b} + \frac{C_b - 1}{V_{ml}C_b} \cdot \frac{P}{P_0} \tag{2.14}$$

where C_b is a constant [a.u.], V_a is the volume of adsorbed adsorbate [m^3], $1/(V_{ml} \cdot C_b)$ is the intercept and $(C_b - 1)/(V_{ml} \cdot C_b)$ is the slope.

Thermal Sc release from metallic foil targets

3

Contents

To understand the diffusion and release behavior in the TISS during Sc radionuclide mass separation and collection, thermal Sc release experiments were performed for differently prepared ^{nat}Ti foil roll samples. To match the conditions during collection and mass separation, the Sc radionuclide thermal release pattern was measured from metallic ^{nat}Ti and ^{nat}V foil roll samples in the Target and Ion Source System (TISS) and Ta environment.

Obtained experimental results were compared with the results from the theoretical estimation model (see section 2.5.4), formulated and described by F. Ogallar Ruiz [135]. These calculations give the theoretical out-diffused fraction of Sc from ^{nat}Ti from a given surface area, volume, time and temperature. The first Sc thermal release experiments from ^{nat}V foils were also performed and Sc fractional thermal release values were obtained [149]. The relation of the released Sc fraction with the diffusion coefficient and adsorption enthalpy was investigated and interpreted for bulk rolled foil samples. Theoretical value estimations with the Eichler-Miedema model of Sc adsorption enthalpy on ^{nat}V and ^{nat}Ti foils are described and discussed.

3.1 Sc radionuclide release from metallic ^{nat}Ti and ^{nat}V foils

Offline radionuclide release studies from various target materials have been studied at ISOLDE in the past by irradiating target materials with protons. Online release studies during target material irradiation with pulsed beam are also performed by measuring the rise and decay times of RIB. Such release studies on top of diffusion and desorption would include more variables in the release models, such as adsorption on multiple TISS structures, ionization efficiency and unknown exact radionuclide inventory at the time of release [50,77,78,84,150,151].

*nat*TiC and *nat*Ti, *nat*V foils are not an often used target material at ISOLDE, therefore the information on the Sc release in TISS Ta environment from metallic *nat*Ti foils is rather scarce. Although there is published data for Sc release from Ti foils, it involves single-layer foils of various thicknesses [61]. Furthermore, no data on the Sc release is available for ^{nat}V foil target material. CERN-MEDICIS operates offline in the so-called "batch mode", where target material is irradiated for a certain time and the mass separation and collection is performed afterward. The foil target material is usually metallic foils rolled in a cylinder form, which can severely affect the released fraction. For these reasons, the offline Sc thermal release studies from target materials proposed for the Sc radionuclide mass separations and collections are crucial. They allow for a better understanding of the overall Sc release behavior during the offline mass separation process with the same type of target materials that are used for radionuclide collections.

Multiple mathematical expressions are available to estimate the diffusion and adsorption times for the radionuclides. Typically an assumption is made, that the radionuclide is released immediately from the target material surface, however, this is true only if the adsorption enthalpy of the corresponding material is very low [11,77,78,94,150]. The experimental results were compared with theoretical estimations obtained through the analytical expressions formulated and described by F. Ogallar Ruiz [135]. These calculations take into account both the diffusion and surface adsorption to give the out-diffused fraction of Sc in ^{nat}Ti for a given sample surface, volume, temperature and heating time.

3.1.1 Radionuclide production and theoretical estimation

Foil roll sample preparation

Three different types of samples were prepared for the Sc thermal release studies - embossed ^{nat}Ti (see Figure 3.1a), non-embossed ^{nat}Ti (see Figure 3.1b) and non-embossed ^{nat}V (similarly to Figure 3.1b) metallic foil rolls. Typically 0.25–0.30μm metallic foils are embossed to keep some distance between the layers, hinder thermal contact and help to reduce the sintering of layers. The metallic foils are then layered together with non-embossed and rolled up to a total diameter < 1.9 cm. To simulate actual Sc collection conditions, the samples for thermal release studies were also prepared in the form of compact rolls. The non-embossed foil rolls were chosen for comparison and to investigate the target material preparation impact on the Sc radionuclide release behavior.

The average diameter for a roll was 0.46 cm for non-embossed samples and 0.80 cm for embossed samples with a height of 1.5 cm. Each roll was approximately 1.0 g for ^{nat}Ti and 3.4 g for ^{nat}V samples. These dimensions were chosen, based on the

theoretically estimated activity (Bq/g of the sample) from a typical irradiation scenario at the CHARM facility and in accordance with the radiation safety hazards associated with the experiment. The radiation safety concerns, due to high production yield even with short irradiations were the main reason, why sample irradiation was not done at one of the ISLODE irradiation stations.

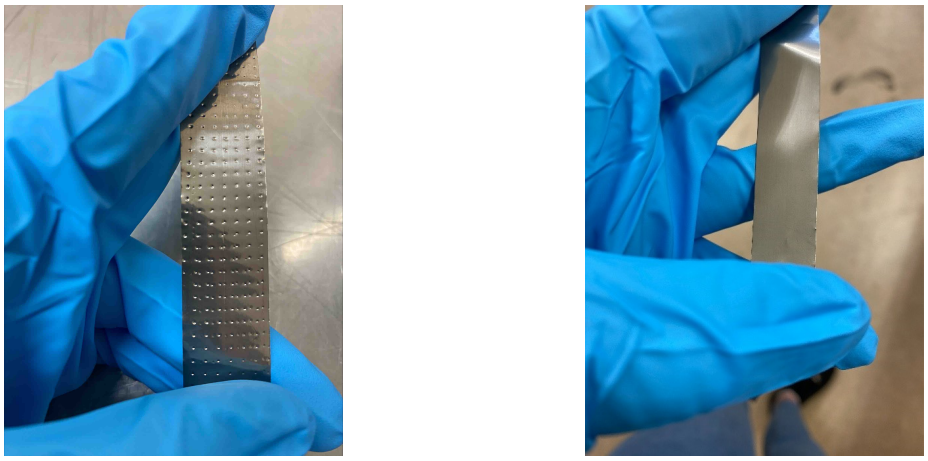

(a) Embossed ^{nat}Ti foil (b) Non-embossed ^{nat}Ti roll

Figure 3.1: ^{nat}Ti foils used in roll preparation for thermal release studies and mass separation [142].

The foil roll samples were inserted into plastic bags to provide a secure containment. Each sample was labeled with a Traceability of potential Radioactive Equipment at CERN (TREC) code and registered in the TREC database for radiation protection measurement and traceability.

Sc radionuclide production

The prepared foil roll samples were placed on the exterior surface of the CHARM grid "cage" door (see Figure 2.3b). The 24 GeV/c proton beam impinging on a thick copper target created a mixed particle field, mainly composed of neutrons, which was used to passively activate the samples. The secondary neutrons from these particles with energy > 1×10^{-3} GeV contribute to > 90 % of the total Sc radionuclide production yield (see Figure 2.2). In total 27 samples in four ^{nat}Ti and ^{nat}V target material sample batches were activated at CHARM with 6–7 samples per batch (see Table 3.1). The actual average proton beam values and irradiation times after each activation were used to estimate precise radionuclide activities with Actiwiz.

Table 3.1: Average actual proton beam intensity for each irradiation batch.

Batch	Sample type	Average intensity, protons/s	Irradiation time, h	Protons on target
I	Embossed ^{nat}Ti	6.91×10^{10}	132	3.28×10^{16}
II	Non-embossed ^{nat}Ti	6.71×10^{10}	126	3.04×10^{16}
III	Non-embossed ^{nat}V	6.91×10^{10}	139	3.45×10^{16}
IV	All	6.64×10^{10}	138	3.29×10^{16}

The produced Sc radionuclide inventory and activity per sample were measured with a HPGe γ-ray spectrometer and the average decay-corrected values, Minimum Detectable Activity (MDA) range are given in Tables 3.2 and 3.3. $^{44g/m}$Sc, ^{46}Sc, ^{47}Sc and ^{48}Sc radionuclides were produced in the samples from which ^{46}Sc and ^{47}Sc were monitored and evaluated for the release curves, because of their favorable half-life and activity. $^{44g/m}$Sc and ^{48}Sc were discarded from the analysis because of the low activity produced and high uncertainties obtained on the activity measurements due to their relatively short half-lives.

Table 3.2: Produced Sc radionuclide average activity in ^{nat}Ti samples

Radionuclide	Half-life ($t_{1/2}$)	Avg. activity/sample (Bq)	MDA range[a] (Bq)
^{43}Sc	3.89 h	$<$ MDA	141-202
^{44g}Sc	3.97 h	303 $\pm$ 56	42.6-67.6
^{44m}Sc	2.44 d	246 $\pm$ 57	44.4-68.1
^{46}Sc	83.79 d	180 $\pm$ 19	25.3-46.7
^{47}Sc	3.35 d	1730 $\pm$ 190	75.7-102
^{48}Sc	43.67 h	496 $\pm$ 75	31.9-46.7

[a] Range of obtained MDA values from all sample γ-ray spectrometry measeurements.

Table 3.3: Produced Sc and V radionuclide average activity in ^{nat}V samples.

Radionuclide	Half-life ($t_{1/2}$)	Avg. activity/sample (Bq)	MDA range[a] (Bq)
^{44g}Sc	3.97 h	53.1 $\pm$ 12.4	50.9-56.8
^{44m}Sc	2.44 d	92.6 $\pm$ 21.3	52.4-54.4
^{46}Sc	83.79 d	59.5 $\pm$ 9.5	34.8-38.8
^{47}Sc	3.35 d	304 $\pm$ 54	91.2-95.8
^{48}Sc	43.67 h	100 $\pm$ 14	42.5-47.1
^{48}V	15.97 d	107 $\pm$ 21	43.5-49.7

[a] Range of obtained MDA values from all sample γ-ray spectrometry measeurements.

The comparison of theoretical estimations with ActiWiz (see Chapter 2) and experimentally obtained Sc radionuclide activities for ^{nat}Ti samples, showcasing the alignment for ^{47}Sc is shown in Figure 3.2 and ^{46}Sc in Figure 3.3.

The average ratio between the obtained values are 1.09 $\pm$ 0.13 for the ^{47}Sc and 1.25 $\pm$ 0.15 for the ^{46}Sc radionuclides, showcasing the agreement and accuracy of the ActiWiz code for the radionuclide inventory estimations (see Section 2.5.3). The activity per each sample for ^{47}Sc and ^{46}Sc varies due to the time gap between activation and the γ-ray spectrometry and activity measurements. Such agreement was not obtained for ^{nat}V foil samples, where the average experimental values for ^{47}Sc were 4.69 $\pm$ 0.89, for ^{46}Sc were 4.12 $\pm$ 0.80 and for ^{48}Sc were 8.32 $\pm$ 1.80 times lower than theoretically estimated with ActiWiz (see Figure 3.4). Sc radionuclide production cross sections in ^{nat}Ti have been studied more thoroughly in the past and more experimental data are available [26]. These findings also reinforce the necessity of the activation results from the release studies to benchmark theoretical radionuclide production codes, such as ActiWiz.

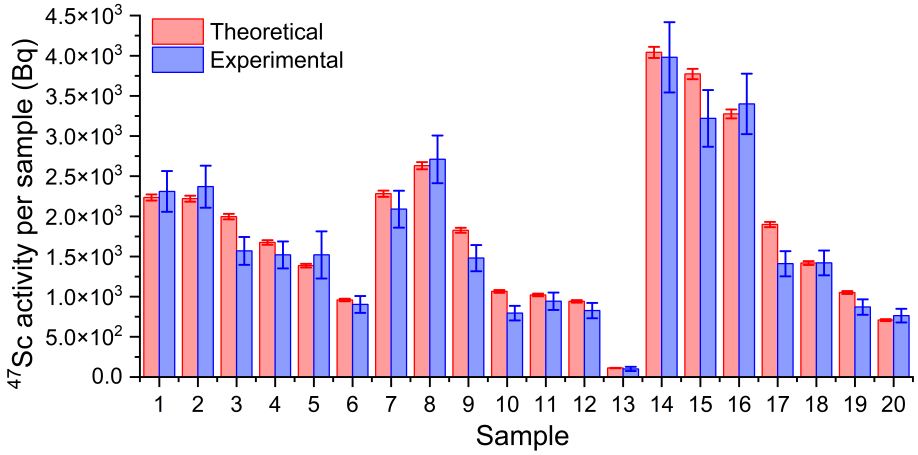

Figure 3.2: ^{47}Sc activity per sample given by ActiWiz software versus obtained experimental values for ^{nat}Ti samples

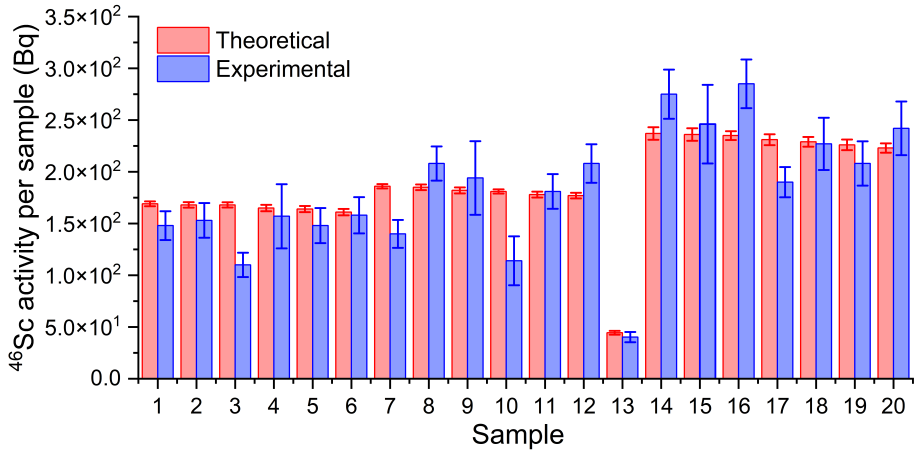

Figure 3.3: ^{46}Sc activity per sample given by ActiWiz software versus obtained experimental values for ^{nat}Ti samples

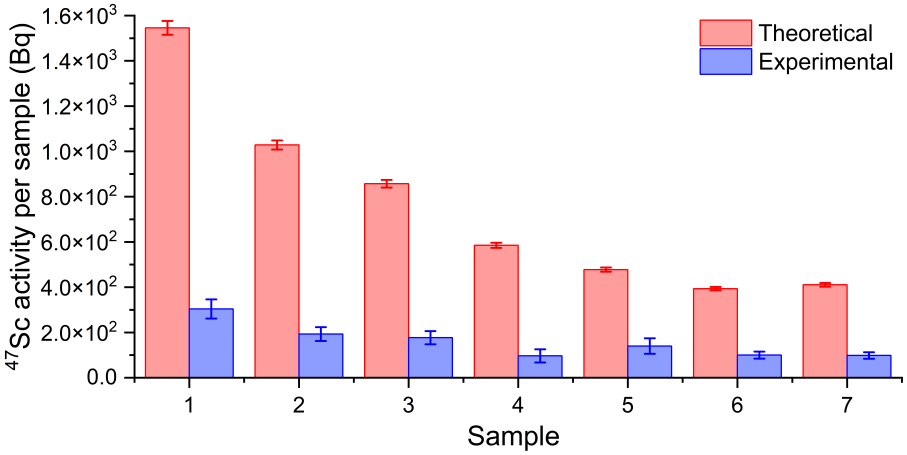

Figure 3.4: ^{47}Sc activity per sample given by ActiWiz software versus obtained experimental values for ^{nat}V samples

3.1.2 Sc thermal release from foil roll samples

Radionuclide release and mass separation is often done at very high temperatures (> 2000 °C), in less than 1×10^{-5} mbar vacuum pressure. For example, the temperature of the target container for Sc mass separation can reach up to 1600 °C for ^{nat}Ti (T_m=1668 °C) and 1850 °C for ^{nat}V (T_m=1910 °C) foils during the collection. Another important aspect, that influences the release is the Ta metal surfaces of which the target container is made. Therefore a standard empty TISS (#689M) was used for the release studies. The TISS was coupled to the pump stand as shown in Figure 3.5a and operated at pressures down to 1×10^{-7} mbar. During the release studies the pressure never reached pressure higher than 1×10^{-5} mbar.

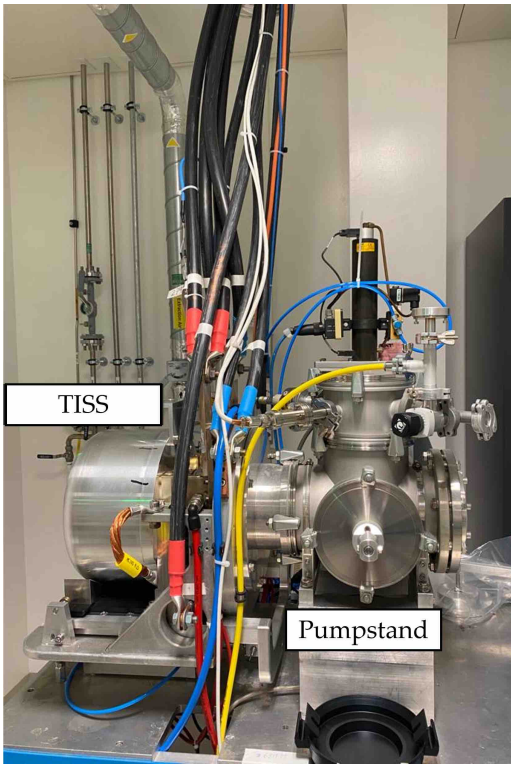

(a) Set-up for Sc thermal release experiments

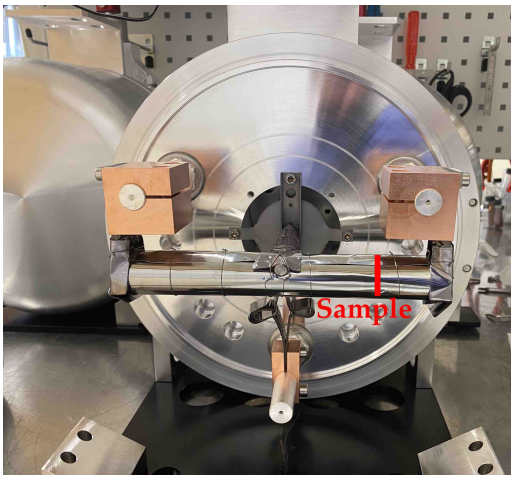

(b) Opened TISS back view

Figure 3.5: Thermal release study pumpstand setup and TISS [142]

As no radioactive ion beams were needed for this study, only the target container was heated and the ion source was kept "cold" (no current applied). This influences the temperature profile of the TISS, however, a specialized current-temperature calibration of the target container with a "cold" transfer line was performed with a micro-optical pyrometer at the exact point where samples would be placed during the release (see Figure 3.5b). The obtained calibration values with "cold" transfer line show almost no difference when compared to a calibration with a hot transfer line (see Table 3.4).

To prevent sample fusing with the Ta container at high temperatures and allow for a safe and simple exchange of the samples, small folded Ta foil "boats" were used (see Figure 3.6). Once the sample was loaded at the calibrated position, the target container was closed with a Ta cap, and the Ta and Mo foil heat screens were mounted and

Table 3.4: TISS #689 M calibration values with and without transfer line heating.

Container current, A	**Container T with "cold" line, °C**	**Container T with "hot" line[a], °C**
300	1022	1083
350	1188	1227
400	1347	1368
450	1498	1505
500	1640	1639
550	1775	1770
600	1902	1897
650	2020	2000

[a] Calibrated with transfer line at 1384 °C

secured. The pressure of the system was stabilized at a safe value of $\leq 2 \times 10^{-6}$ mbar, and each sample underwent the same temperature ramp-up process of 0.5 A every 25 seconds for the target container until the desired temperature was reached. Because of the low heating current variations from the power supplies, the uncertainty on the temperature values was determined as the standard deviation from multiple single-current-point measurements with the pyrometer during calibration, resulting in up to $\pm$ 15 °C uncertainties. The uncertainties at higher temperatures were higher due to higher light emission from the target container.

Such rather conservative pressure and heating parameters were chosen to avoid a heating halt due to severe target and sample outgassing. Once the set temperature was achieved, each sample was maintained at the chosen temperature for exactly one hour and cooled down with the same ramp speed of 0.5 A per 25 seconds. This way the mass separation conditions were simulated and the released fraction during the heating ramp can be accounted for due to the constant heating ramp.

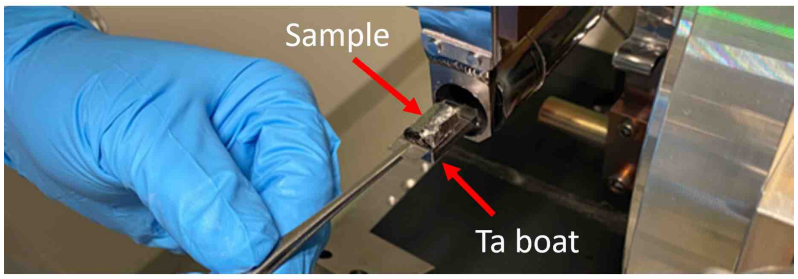

Figure 3.6: ^{nat}Ti foil roll sample in a Ta "boat" after a heating cycle [142]

The calculation of the relative release of Sc involves the decay corrected remaining fraction in the sample F_{rem} after the heating cycle as described in equation 3.1. The relative uncertainty related to this fraction is expressed as shown in equation 3.2.

$$F_{rem} = \frac{A_A}{A_B \cdot e^{-\lambda t_A}} \tag{3.1}$$

where A_A is the activity measured after the sample heating cycle [Bq], A_B is the activity measured before the sample heating cycle [Bq], λ is the radionuclide decay constant [s^{-1}] and t_A is the time between activity measurements of the sample [s].

$$\Delta F_{rem}/F_{rem} = \sqrt{\left(\frac{\Delta A_A}{A_A}\right)^2 + \left(\frac{\Delta A_B}{A_B}\right)^2} \tag{3.2}$$

Typically the uncertainty of counting experiments originates from the Detection Limit (DL) as determined by approaches like the Currie method. However, in the case of γ-ray spectrometry the MDA value is used as a threshold, which combines the detection limit, calibration efficiency, nuclear data and measurement time [152]. As such, it can be considered a fundamental characteristic of the measurement rather than an uncertainty. It does not directly stem from a single measurement but instead relies on estimations involving uncertainties. However, a result with 100 % release means that no activity above the MDA was measured and the MDA value itself becomes the uncertainty of the corresponding measurement. The released fraction F_{rel} is then expressed through equation 3.3, on which the calculated relative uncertainty is applied.

$$F_{rel} = 1 - F_{rem} \tag{3.3}$$

3.1.3 Sc release from ^{nat}Ti Samples

The thermal release of Sc from ^{nat}Ti foil rolls was conducted at various temperatures with a one-hour hold time at the chosen peak temperature. The selection of temperatures was based on typical mass separation conditions and physical properties of the material, including the target material melting point. The upper limit for ^{nat}Ti foils was set at 1550 °C to prevent material melting and sublimation. A subtle occurrence of sintering was observed for a sample studied at 1500 °C and the sample was stuck to the Ta boat. The sintering can be the source of reduced release rate over longer periods of operational time during mass separation and collection.

The experimentally obtained relative thermal release results for ^{47}Sc and ^{46}Sc from embossed and non-embossed ^{nat}Ti samples with the temperature and activity measurement uncertainties are shown in Figures 3.7 and 3.8 [142,149]. The ^{47}Sc and ^{46}Sc relative release results coincide for both types of roll samples. No apparent release of Sc was measured below 700 °C with 1 hour hold time at the peak temperature.

After 1 hour of hold time at the peak temperature of 1450 °C, close to full Sc (100 %) release was measured, signifying the complete absence of activity in the sample after the heating cycle (above the MDA). The statement of full release here would not be entirely appropriate, because the MDA values are ∼10 % from the measured activity. To obtain the same released fraction for the non-embossed foil samples, the 1-hour hold at 1200 °C is sufficient. In general, the F_{rel} for non-embossed samples are shifted to lower temperatures. These results are in good agreement with previously published studies [60, 153]. The uncertainties obtained for samples with longer decay time after the activation are notably higher because the remaining activity approached the MDA values.

The systematic differences of F_{rel} for the non-embossed and embossed target material samples, point towards a large impact of the surface treatment and morphology on the

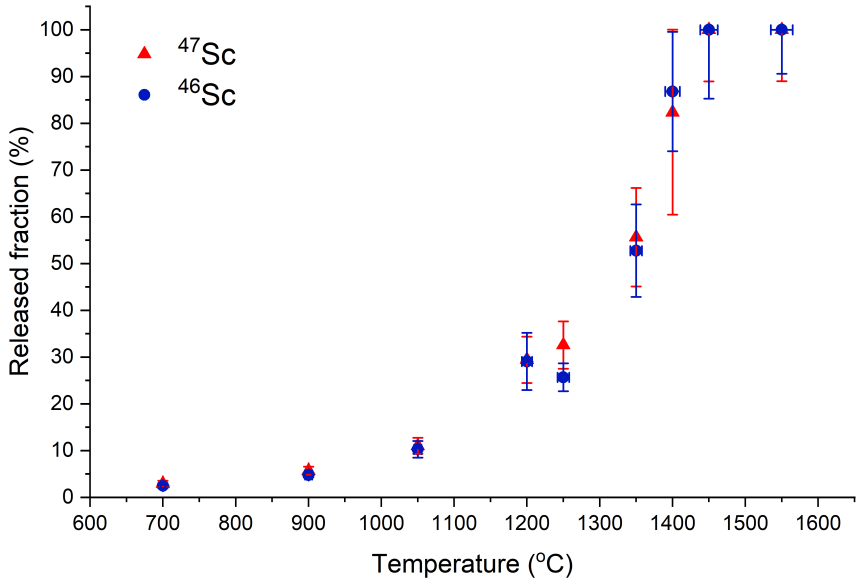

Figure 3.7: ^{47}Sc and ^{46}Sc thermal release from embossed ^{nat}Ti foil roll samples

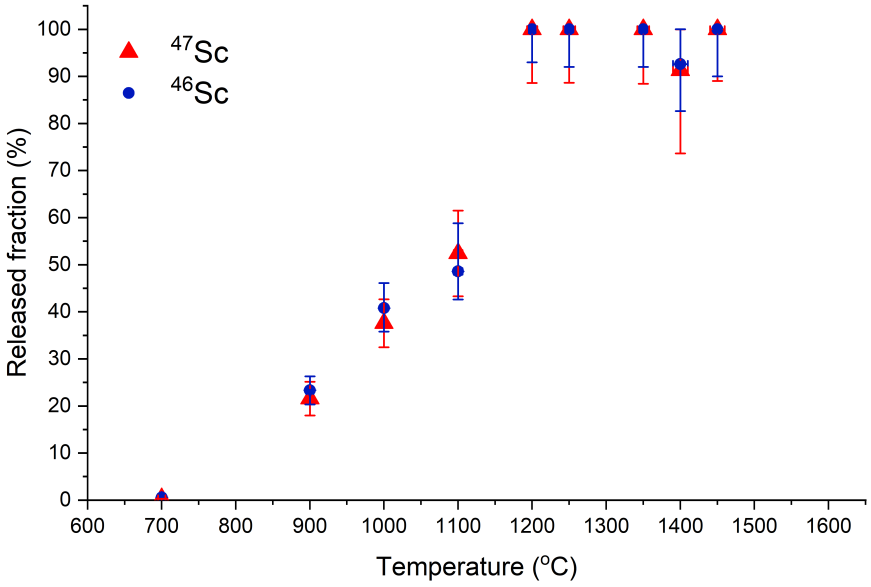

Figure 3.8: ^{47}Sc and ^{46}Sc thermal release from non-embossed ^{nat}Ti foil roll samples

thermal release characteristics. This phenomenon could be attributed to several factors. Firstly, the embossing may lead to a slightly larger specific surface area in the embossed material because of the ductile material stretching and compressing. The derived theoretical formulas emphasize the significance of the surface-to-volume ratio in the release processes. The larger surface area in the embossed material can facilitate greater release potential, theoretically promoting the faster release. However, the observed release results in Figure 3.7 contradict this expectation and indicate a delayed release for the embossed material, suggesting that the actual release kinetics are influenced by a combination of factors beyond the specific surface area. During the sample embossing,

additional defects are being produced at the embossing points on a microscale, which would result in deformation of the crystalline matrix of the native titanium oxide layer that possibly could have a notable impact on the release (see Figure 3.9).

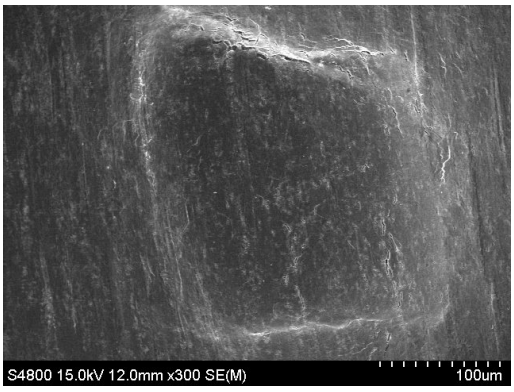

(a) SEM image of embossed ^{nat}Ti foil (x300 magn.).

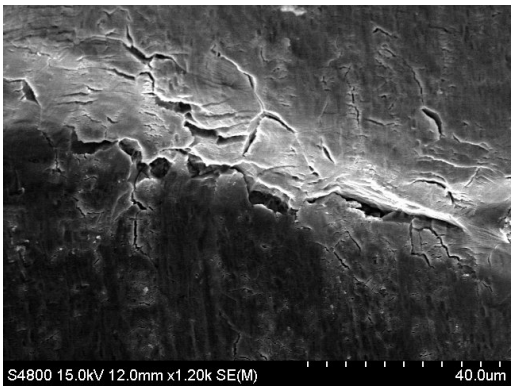

(b) SEM image of embossed ^{nat}Ti foil (x1200 magn.).

Figure 3.9: Ti foil surface and cracks after embossing and 10 min cleaning in ethanol and ultrasonic bath.

The embossing also alters the diffusion pathways within the bulk material, affecting the rate at which Sc atoms migrate to the surface and are subsequently released. Typically defects are associated with increased diffusion rate as jump rates of atoms and therefore their diffusivity along grain boundaries, dislocations and free surfaces are higher than those in the perfect crystals [154–156]. This suggests more of a chemical impact for the decreased release rate explanation of non-embossed foils.

Differences in heat conduction can also influence the release rate in this case. Better heat conduction implies a more powerful driving force for diffusion, potentially leading to an earlier release. Isotopes would arrive sooner at the surface, influencing the overall release dynamics. The embossed foils have less contact area between layers and would heat up slower than non-embossed ones. On the other hand, the already-released atoms from embossed samples have a lower chance of getting re-adsorbed on the next layer than for the non-embossed samples. Therefore, the interplay between surface topography, diffusion pathways, heat conduction and re-adsorption should be carefully considered to understand the observed release behavior comprehensively. While larger surfaces generally result in higher release, the impact of surface effects and chemical compositions on release dynamics is essential. An increased surface area might also increase the surface migration and interaction between Sc and the surrounding materials and chemical species, explaining the less efficient thermal release. The use of additional tools and equipment for target material preparation can lead to contaminant deposition into the foil surface, which can stabilize Sc in a less volatile chemical form, such as ScC and Sc_2O_3 [157].

The relative thermal release results of measured Sc radionuclides from both types of ^{nat}Ti samples are reported in Table 3.5 for embossed ^{nat}Ti and in Table 3.6 for non-embossed ^{nat}Ti. The uncertainties are presented as combined values, derived from both counting statistics before and post-heating cycles. An average F_{rel} of ^{46}Sc and ^{47}Sc at each temperature are given to showcase the overall release pattern of Sc species.

To assess the magnitude of the impact of the heating ramp on the released fraction

Table 3.5: ^{46}Sc and ^{47}Sc relative release from embossed ^{nat}Ti foil samples

Temperature, °C	Release of ^{46}Sc, %	Release of ^{47}Sc, %	Total release of Sc, %
700	2.5 ± 0.5	2.9 ± 0.7	2.7 ± 0.7
900	4.8 ± 0.6	5.7 ± 0.9	5.6 ± 1.0
1050	10.3 ± 1.8	11.0 ± 1.7	10.9 ± 2.9
1200	29.1 ± 6.1	29.4 ± 4.9	29.4 ± 7.4
1250	25.7 ± 3.0	32.6 ± 5.1	31.9 ± 5.8
1350	52.8 ± 9.9	55.6 ± 10.5	54.8 ± 11.0
1400	86.8 ± 12.8	82.3 ± 21.9	83.1 ± 28.0
1450	100.0 ± 14.7	100.0 ± 11.1	100.0 ± 20.4
1550	100.0 ± 9.4	100.0 ± 11.0	100.0 ± 14.5

Table 3.6: ^{46}Sc and ^{47}Sc relative release from non-embossed ^{nat}Ti foil samples

Temperature, °C	Release of ^{46}Sc, %	Release of ^{47}Sc, %	Total release of Sc, %
700	0.57 ± 0.09	0.33 ± 0.05	0.40 ± 0.08
900	23.3 ± 3.0	21.6 ± 3.6	22.0 ± 4.8
1000	40.8 ± 5.3	37.6 ± 5.1	38.5 ± 5.9
1100	48.6 ± 10.2	52.4 ± 9.1	51.6 ± 10.8
1200	100.0 ± 9.3	100.0 ± 11.4	100.0 ± 15.9
1250	100.0 ± 20.7	100.0 ± 11.3	100.0 ± 18.2
1350	100.0 ± 9.0	100.0 ± 11.6	100.0 ± 13.8
1400	92.6 ± 15.5	91.3 ± 17.7	91.4 ± 18.9
1450	100.0 ± 7.9	100.0 ± 11.0	100.0 ± 24.4

before peak hold time, a comparative experiment was performed. A non-embossed ^{nat}Ti foil roll sample was heated to 1400 °C and immediately cooled down without any hold time at the set temperature (0 h), resulting in F_{rel} of 51 ± 11 % for Sc released. In comparison, the value for the same type sample and temperature but with a hold time of 1 h, F_{rel} was 91 ± 19 % (see Table 3.6). Half of the radionuclides were released even before the peak hold would begin. Because diffusion and effusion are thermally activated processes, the impact of the heating ramp on the released fraction is expected to be non-linearly higher at the higher temperatures not only because of the heating time but also the faster diffusion and desorption. The diffusion rate can change at the phase transitions of the target matrix, therefore an Arrhenius-like exponential description cannot be applied for the whole heating range. However, the phase transition for Ti happens at the ∼880 °C, which is on the lower side of the release curve [158].

To put this in perspective for Sc mass separation and collection, the impact of the heating/cooling ramp time on the released fraction shows the importance of designing an appropriate collection plan, TISS and tuning the mass separator and ion source to nominal parameters (or close to them) before the release from foils had begun. Even without active target container heating, the ion source at nominal temperature (∼2000°C) indirectly heats the target container middle section. Certain TISS designs (described in Chapter 4), optimal for laser ionization, can reach 1500–2000 °C at the middle section of the container with transfer line at nominal value [38].

Keeping the samples at constant high temperatures would maximize the release [153], however, a rapid release in the offline mass separation and collection may not be suitable for maximizing the yield and collection efficiency, because of limited ion source ion capacity or ionization efficiency. It is essential to note, that these conclusions are drawn only from the target material point of view, neglecting the radionuclide effusion to the ion source and subsequent ionization.

Dose rate measurements of the target container

Supplemental information on where the released radionuclides could condense within the target container and transfer line can help in TISS developments for Sc radionuclide collections. Because of the complexity of a TISS and possible contamination, the TISS transfer for precise measurements with γ-ray spectrometry was not possible and local dose rate measurements before and after heating cycles were performed. The dense TISS structure materials attenuate β and some fraction of the γ-rays, therefore these measurements should be considered only as a relative displacement of radionuclides, indicating possible cold spots.

The dose rate measurements on the target container were performed with and without the activated samples within the container before and after each heating cycle. The measurements were taken at six pre-defined points to obtain a relative comparison. Figure 3.10 provides an example of one measurement.

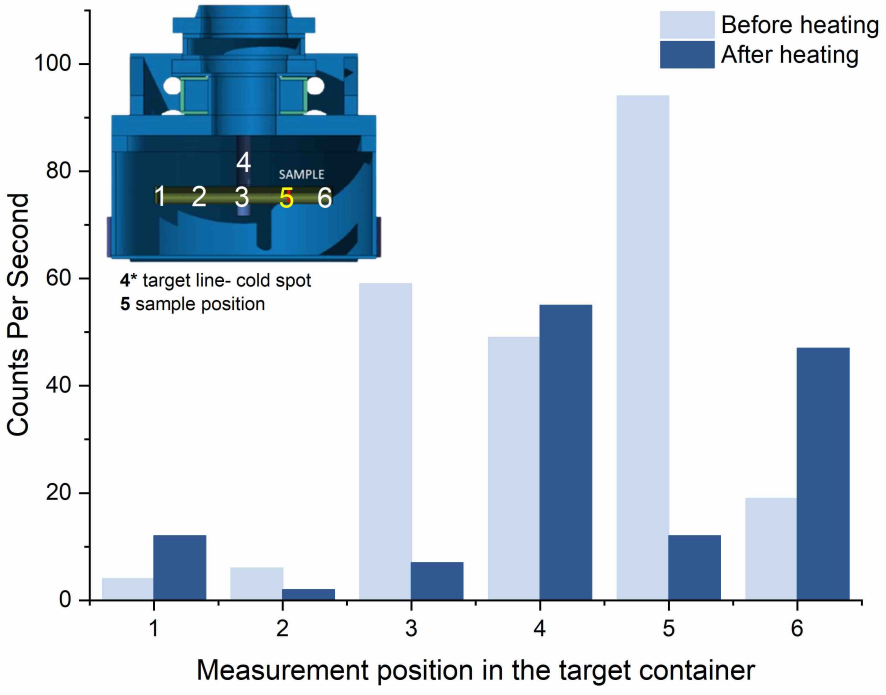

Figure 3.10: Target container dose rate measurements in 6 different locations

The position #4 is the target transfer line which was not heated during the experiments. It was considered as a cold spot and condensation here was expected. During mass separation, the ion source and transfer line would both be heated and mitigate adsorption and prevent condensation. The sample was placed at position #5 for each release

measurement, offering a consistent reference point for analysis resulting in a notable difference in dose rate measurements before and after the heating cycle. Positions #1 and #6 correspond to the extremities of the target container where the temperature is lower than the central region, leading to an increased chance of condensation [38]. It can be seen that a certain amount of released radionuclides migrate toward the ends of the target container. Even at elevated temperatures, they tend to condense not only in the cold transfer line but also on the extremities of the target container. Except for the transfer line, the highest absolute count rate is observed at the end, from which the sample exchange is done. The cold spot formation was addressed in TISS developments by attempting to homogenize the target container temperature profile across the whole target container.

Theoretical and experimental result comparison

Knowing the diffusion and adsorption constants, one can do a comparative analysis using the theoretical models described by F. Ogallar Ruiz [135], taking into account the heating ramp speed, time and radionuclide release during the heating phase. Theoretical curves of Fraction Reaching Surface (FRS) and Out-Diffused Fraction (ODF) (see Figure 3.11) were estimated to describe and discuss the obtained experimental results (see Figure 3.12). The theoretical model did not consider the Ta environment in which the experiments were conducted and only the effects in and on the target material surface were investigated.

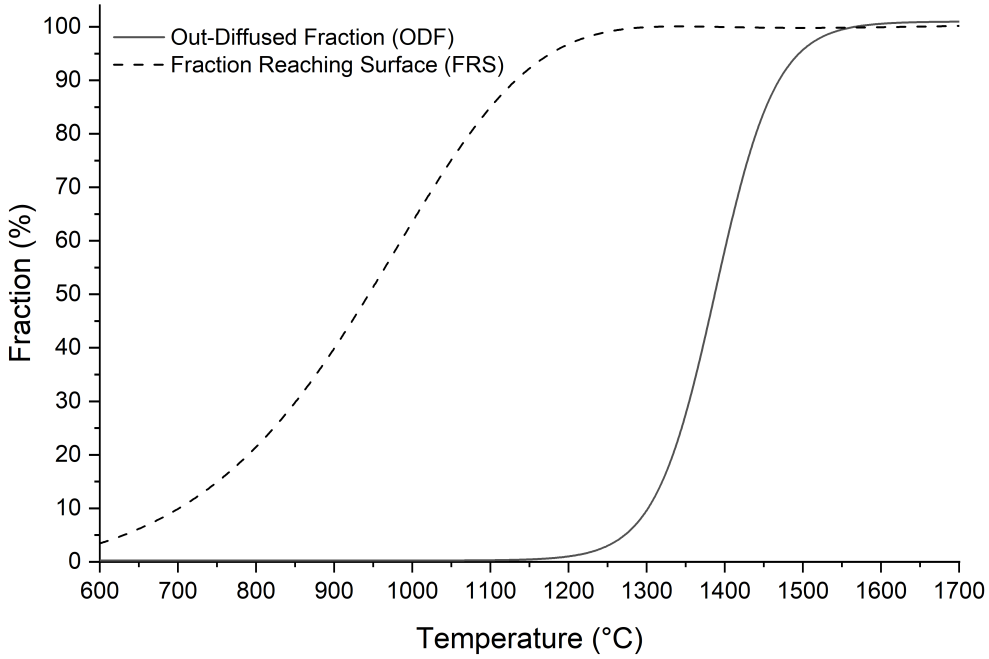

Figure 3.11: Estimated FRS and ODF curves from the theoretical model for Sc thermal release from ^{nat}Ti foil samples

In examining the thermal release curves, the focus was centered on the comparison between experimental and theoretical model data. Accurately modeling the complexities of macroscopic and microscopic surface effects poses a significant difficulty. The

theoretical models suggest that radionuclides exhibit a much faster migration to the surface than release, hinting at surface effects being the limiting factor in the thermal release process. Not all isotopes reaching the surface would eventually be released, as there are mechanisms that retain them and this implies that the release process is more constrained by surface effects rather than diffusion itself.

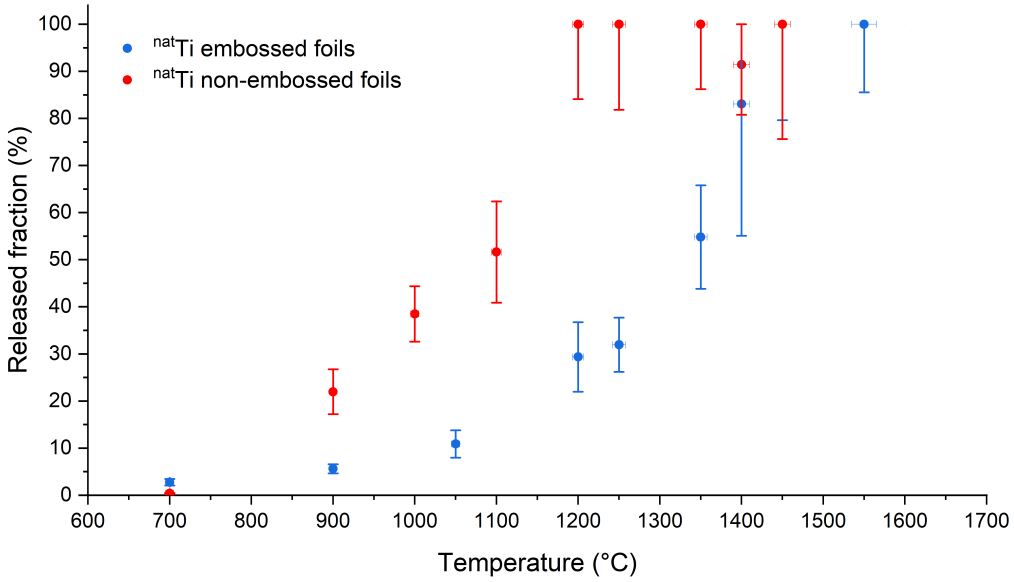

Figure 3.12: Total Sc thermal release from embossed and non-embossed ^{nat}Ti foil samples

It is important to acknowledge that the desorption enthalpy data used in the theoretical model is sparsely available in the literature, and it comes with a significant level of uncertainty, which is not explicitly documented. This uncertainty may have a substantial impact on the estimation of the Global Desorption Probability (GDP) and, consequently, on the results obtained for the ODF. Reducing the desorption enthalpy of 392.4 kJ/mol [159] by for example an arbitrary fraction of 5 % in the model would shift the onset of the ODF notably towards lower temperatures (∼100 °C) and change the steepness of the slope, as the radionuclides would desorb faster. It is important to mention that the ^{nat}Ti and ^{nat}V foils are covered with a native oxide layer that can influence the release from the surface because of chemisorption and intuitively have higher desorption enthalpy. For this reason, one cannot yet draw consistent conclusions from the theoretical model predictions with respect to the release of embossed and non-embossed samples. Nevertheless, the models are fairly accurate for first approximations. To better understand these processes further targeted experiments need to be carried out, eliminating variables, such as multiple layers, chemical impurities, oxide layer and heating time.

3.1.4 Sc Thermal Release From ^{nat}V Samples

^{nat}V has a higher melting point (1910 °C) than ^{nat}Ti (1668 °C). Moreover, the cross section values for producing $^{44g/m}$Sc and ^{47}Sc are in the same order of magnitude for both materials with the proton energy used for target irradiation at CERN-MEDICIS. This makes ^{nat}V a suitable material and is also being investigated for mass separation

and collection for the Sc radionuclides [38].

The release of Sc isotopes from non-embossed ^{nat}V foil rolls was investigated with the same methodology as per the ^{nat}Ti samples [149]. The release study temperature points were chosen according to the melting point and preliminary mass separation experiments with ^{nat}V foil target materials at CERN-MEDICIS [38]. The thermal release results for ^{46}Sc radionuclide are shown in Figure 3.13. Only two data points for ^{47}Sc release results were shown and others were discarded due to the high uncertainties from γ-spectrometry measurements and the low activity produced. Based on ^{nat}V melting point and density, the Sc release was expected to happen slower or at higher temperatures [155].

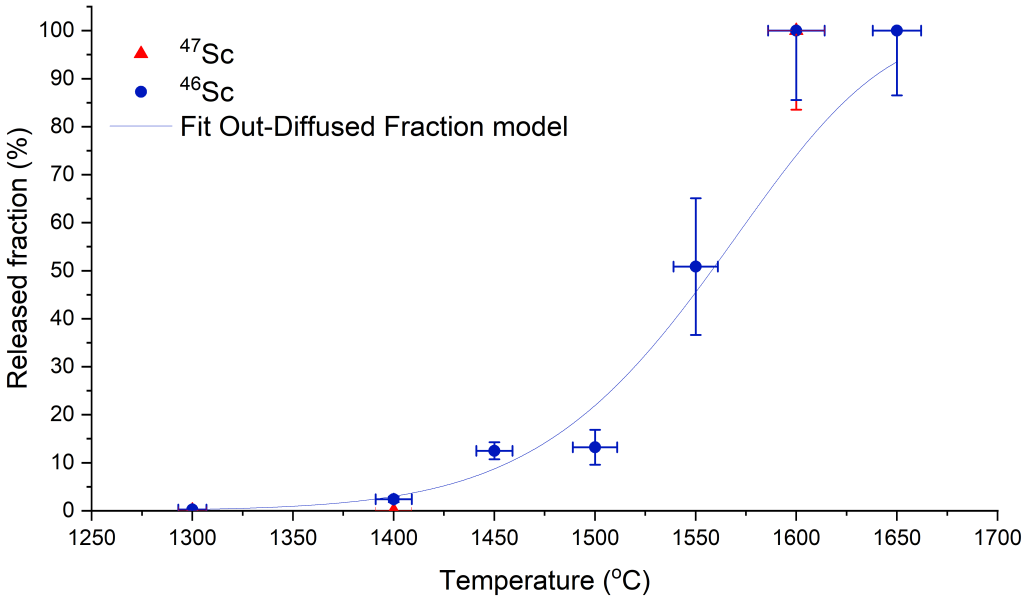

Figure 3.13: ^{46}Sc thermal release from non-embossed ^{nat}V foil samples

As shown in Figure 3.13, there is almost no Sc release below 1400 °C (2.4 ± 0.6 %), however, the allegedly full release was obtained already at 1600 °C with 1 hour peak temperature hold (see Table 3.7).

Table 3.7: ^{46}Sc and ^{47}Sc relative release from non-embossed ^{nat}V foil roll samples.

Temperature, °C	Release of ^{46}Sc, %	Release of ^{47}Sc, %	Total release of Sc, %
1300	0.27 ± 0.07	0.10 ± 0.03	0.14 ± 0.04
1400	2.4 ± 0.6	0.00 ± 0.23	0.46 ± 0.14
1450	12.5 ± 1.8		
1500	13.2 ± 3.6		
1550	50.8 ± 14.2		
1600	100.0 ± 14.5	100.0 ± 16.5	100.0 ± 23.3
1650	100.0 ± 13.5		

Currently, estimating theoretical curves with the ODF model for Sc diffusion and re-

lease from the ^{nat}V sample is not possible due to the absence of Sc adsorption enthalpy, diffusion coefficient and diffusion constant data for the ^{nat}V material within the literature. However, with a comprehensive understanding of the processes involved in the Sc thermal release, it can be possible to derive an initial approximation of the diffusion coefficient and adsorption enthalpy with theoretical models. The obtained preliminary data serves as a starting point to determine the first experimentally measured diffusion coefficient and adsorption enthalpy for Sc in the V matrix.

3.2 Radionuclide release limiting parameters

In general, the release of produced radionuclides from the target material can be divided into two parts - diffusion to the surface of the bulk matrix and its subsequent desorption. The motion of atoms in solids is a slow process. Typically diffusion distance is around one micrometer close to the melting temperature T_m of a bulk solid and one nanometer at the half of the T_m per second [154].

The probability of Sc desorption is mainly dominated by its desorption enthalpy. Depending on its value, the release of the Sc radionuclides could be significant or negligible. The scarcity of experimental data forces one to rely on empirically calculated values or rough estimates (e.g. sublimation enthalpies). Furthermore, the surface morphology, crystalline structure and chemical composition can affect these values significantly.

3.2.1 Diffusion and release from metallic foils

When radionuclide release from the target material is limited by diffusion, the release can be approximated from the solution of Fick's second-order partial differential equation 3.4, assuming that the diffusing particle desorbs rapidly when on the surface, compared to the diffusion time and does not diffuse back into the bulk material, and the initial distribution of isotopes is homogeneous [160].

$$F_{\text{rem}}(\hat{t}) = \frac{2n}{\pi^2} \sum_{m=1}^{\infty} c_m^{-1} \mathrm{e}^{-c_m \hat{t}} \tag{3.4}$$

where F_{rem} is the fraction of radionuclides remaining in the solid target material for foils ($n = 1$), fibers ($n = 2$) and particles ($n = 3$), c_m are coefficients $(m - 1/2)^2$ for foils, $(j_{0,m}/\pi)^2$ for fibers and m^2 for particles, $j_{0,m}$ is the mth positive root of the Bessel function of order zero and $\hat{t}$ is the diffusion number (time divided by a characteristic diffusion time). $\hat{t} = t/\tau_d$. $\tau_d = {a_s}^2/(\pi^2 D)$ is the characteristic diffusion time and is inversely proportional to the diffusion constant. t is the time at the respective temperature since radionuclide production [s] and a_s is the geometrical size parameter. For foils the equation 3.4 can be rewritten as equation 3.5 [150, 161].

$$F_{\text{rem}}(\%) = 100 - \frac{800}{\pi^2} \sum_{n=0}^{\infty} \frac{1}{(2n+1)^2} \cdot \exp\left[-\frac{(2n+1)^2 \pi^2 D t}{d_{half}^2} \right] \tag{3.5}$$

where d_{half} is half of the foil thickness [cm]. From here the F_{rem} becomes a function of $\hat{t}$ and the diffusion coefficient D at a certain temperature and annealing time can

be estimated. By making the above-mentioned assumptions that adsorption or strong dependence of 2^{nd} order effects do not impact the release, the D values were estimated from experimental results for Sc from non-embossed ^{nat}Ti foil rolls. The obtained results are shown in Table 3.8.

Table 3.8: D obtained from non-embossed ^{nat}Ti foil roll Sc release measurements.

Released fraction, %	**Temperature, °C**	**Diffusion number $\hat{t}$**	**Estimated D^a, cm^2/s**	**Literature D [162], cm^2/s**
22	900	0.4648	2.04×10^{-11}	2.14×10^{-9} at 919 °C
38	1000	1.015	4.46×10^{-11}	4.51×10^{-9} at 997 °C
52	1100	2.249	9.89×10^{-11}	9.49×10^{-9} at 1069 °C
100	1200	19.54	8.59×10^{-10}	3.38×10^{-8} at 1213 °C

[a] Estimated values in the case of no adsorption or strong dependence of 2^{nd} order effects, such as re-adsorption and re-diffusion.

It can be observed, that the obtained values differ from literature values by two orders of magnitude. Typically the D values are measured for a single-layer foil. In this case, multiple layers are stacked upon each other, as the foil is rolled. The impact of multiple layers can be well observed. It allows already released Sc radionuclides, to adsorb on another layer and re-diffuse inside it. Therefore, the estimated D values could only serve as a rough estimation of the overall time it would take to release the Sc radionuclides from the foil rolls. For more precise estimations, the 2^{nd} order effects, such as re-adsorption and re-diffusion should be implemented in the model. It must be noted, that in these estimations, the released fraction during the heating ramp, had not been deducted.

Following the same assumptions and model, the estimated D from experimental release data for non-embossed ^{nat}V foil rolls are summarized in Table 3.9 and in Figure 3.14. The obtained values again are 2–5 orders of magnitude lower than expected for a fractional release (typically 10^{-8}–10^{-9} cm^{2}s^{-1} [161]). This similarity with Sc diffusion and release from Ti matrix also suggests 2^{nd} order and surface-related limiting factors for Sc diffusion and release from V matrix.

Table 3.9: D obtained from non-embossed ^{nat}V foil roll Sc release measurements.

Released fraction, %	**Temperature, °C**	**Diffusion number $\hat{t}$**	**Estimated D^a, cm^2/s**
0	1300	0.0001	4.40×10^{-15}
2	1400	0.009	3.88×10^{-13}
12	1450	0.051	2.27×10^{-12}
13	1500	0.078	3.45×10^{-12}
51	1550	2.176	9.57×10^{-11}
100	1600	19.54	8.59×10^{-10}

[a] Estimated values in the case of no adsorption or strong dependence of 2^{nd} order effects, such as re-adsorption and re-diffusion.

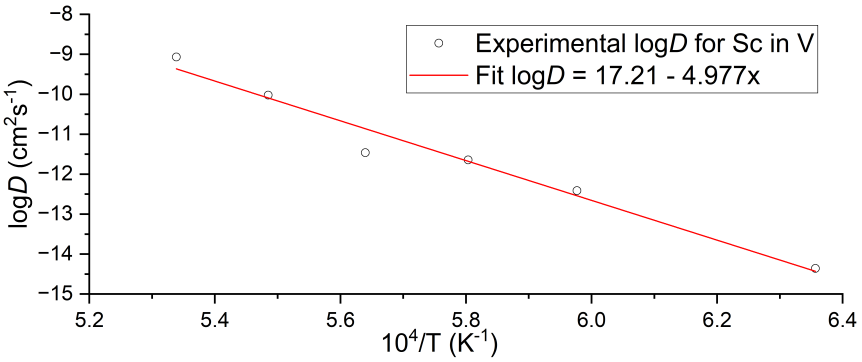

Figure 3.14: Arrhenius plot of the estimated diffusion coefficients D for Sc in ^{nat}V foil rolls.

3.2.2 Sc adsorption enthalpy on V and Ti surfaces

An important parameter for the mass separation and release studies is the adsorption/desorption or sublimation enthalpy on solid surfaces of the radionuclide of interest. Thus far no experimental adsorption enthalpy or diffusion constant values have been reported for Sc on V surfaces. An empirical model, developed by Eichler and Miedema allows calculation of the desorption enthalpy for different adsorbates (A) on metallic surfaces (B) [163–165].

$$\Delta\bar{H}_s = \frac{2 \cdot V_{AL}^{2/3} \cdot P_{gsc}}{n_{WSA}^{-1/3} + n_{WSB}^{-1/3}} \cdot \left(9.4 \cdot \left(n_{WSA}^{1/3} - n_{WSB}^{1/3}\right)^2 - (e_{corr}\Phi_A^* - e_{corr}\Phi_B^*)^2 - \frac{R_m}{P_{gsc}}\right) \quad (3.6)$$

where $\Delta\bar{H}_s$ is the first partial molar solution enthalpy [kJ/mol], V_{AL} is the effective atom volume of the adsorbate A [cm^3], P_{gsc} and $R_{\mathrm{m}}/P_{\mathrm{gsc}}$ are chemical group specific constants [V^{-1}cm^{-2}(density units)$^{-1/3}$], n_{WSA} and n_{WSB} are the electron densities at the Wigner-Seitz cell boundaries of adsorbate A or adsorbent B [density units], e_{corr} is the dimension correction factor [eV^2] and Φ_{A} and Φ_{B} are the electro-negativity parameters of the adsorbate A or the adsorbent B [V]. V_{AL} accounts for the pure original atomic volume V_{A} change due to charge transfer.

$$V_{AL} = V_A \cdot (1 + a_A \cdot (\Phi_A^* - \Phi_B^*)^{3/2} \quad (3.7)$$

where a_{A} is a factor of adsorbate A (0.7 for rare earth metals) in [V^{-1}]. If the calculated $\Delta\bar{H}_s$ is higher than 50 kJ/mol, the adsorbate is deemed insoluble in the adsorbent metal and ΔH_{ads} is estimated through equation 3.8. If $\Delta\bar{H}_s$ is lower than 50 kJ/mol, the adsorbate is deemed partially or fully soluble in the adsorbent metal and ΔH_{ads} is estimated through equation 3.9.

$$\Delta H_{ads} = \Delta H_{DA}^0 + 0.6 \cdot \left(\Delta\bar{H}_s - \frac{V_{AL}}{V_B} \cdot \Delta\bar{H}_{VVB}\right) \quad (3.8)$$

$$\Delta H_{ads} = \Delta H_{DA}^0 + 0.9 \cdot \left(\Delta\bar{H}_s - \frac{V_{AL}}{V_B} \cdot \Delta\bar{H}_{VVB}\right) + \frac{V_{AL}}{V_B} \cdot \Delta\bar{H}_{OVB} \quad (3.9)$$

where ΔH^0_{DA} is the standard de-sublimation enthalpy of pure adsorbate A [eV], V_B is the atomic volume of pure adsorbent B [cm^3], ΔH_{VVB} is the enthalpy of volume vacancy formation in adsorbent B [eV], and ΔH_{OVB} is the enthalpy of surface vacancy formation of adsorbent B [eV]. The rather good agreement of the Eichler-Miedema model with some experimentally measured adsorption enthalpy data on various metallic surfaces is shown in Table 3.10.

Table 3.10: Comparison of some measured and estimated adsorbent ΔH_{ads} values on different metal surfaces with the Eichler-Miedema model [163].

Adsorbate	**Adsorbent**	**Experimental ΔH_{ads}, kJ/mol**	**Estimated ΔH_{ads}, kJ/mol**
Sc	Ta	521	545
Y	Ta	627	615
La	Ta	531	572
	W	646 ± 20	621
Ce	Ta	521	586
	W	660 ± 30	609
	Re	589 ± 20	557
Sm	Ti	261 ± 18	314
	Mo	288 ± 18	361
	Re	415 ± 30	348
Eu	Ti	263 ± 18	271
Tb	Ta	396 ± 40	586
	W	521 ± 30	609
Yb	Mo	278 ± 18	292

The first partial molar solution enthalpy $\Delta \bar{H}_s$ for Sc on V was estimated to be 65.6 kJ/mol. As this value is > 50 kJ/mol, according to the model, the adsorption cannot happen by substituting a V atom with Sc atom in the surface, and the equation 3.8 is applied, resulting in adsorption enthalpy of ΔH_{ads} = -553.3 kJ/mol. These estimations are empirical and therefore no uncertainty could be given [163–167]. The estimation also suggests, that Sc is not soluble in V and only adsorbs on the surface and its release from V target material is surface-desorption limited.

If one would assume that Sc is partially or fully soluble in V and apply equation 3.9, based on the similarities in Sc thermal release from Ti and V foils, the ΔH_{ads} for Sc on V computes to -383.4 kJ/mol. According to the same model, the $\Delta \bar{H}_s$ for Sc on Ti is 34.4 kJ/mol and ΔH_{ads} = -384.1 kJ/mol, suggesting Sc is soluble in Ti and supports the findings of thermal release measurements from Ti foil rolls. It must be noted, that the estimation may differ from the real situation due to the passive oxide layer on the Ti and V foils, other impurities in the metal and the polycrystalline structure of the surface.

Sc diffusion coefficient in V with the ODF model

The model described in equation 3.4 does not account for the adsorption enthalpy on the matrix surface. Therefore by employing the estimated ΔH_{ads} = -553.3 kJ/mol for Sc on V to the ODF model (see section 2.5.4) and fit the model to the experimental release data, a first impression of the diffusion constants such as the frequency factor D_0 = 22.4 cm^2s^{-1} and the diffusion activation energy Q_a = 379.1 kJ/mol (see Figure 3.13) could be obtained [159,168,169]. Through the Arrhenius diffusion coefficient equation 2.10, the diffusion coefficients of Sc in V can be estimated (see Table 3.11).

Table 3.11: Sc diffusion coefficient in non-embossed ^{nat}V foil rolls with the ODF model.

Released fraction, %	Temperature, °C	Estimated D, cm^2/s
0	1300	5.77×10^{-12}
2	1400	3.26×10^{-11}
12	1450	7.20×10^{-11}
13	1500	1.52×10^{-10}
51	1550	3.07×10^{-10}
100	1600	5.99×10^{-10}
100	1650	1.13×10^{-9}

For the fit and estimation, the released fraction during the ramp-up process had not been taken into account and the results reflect the order of magnitude values. This approximation also explains the deviations in the fitted curve to the experimental data points at temperatures of 1550–1650 °C (see Figure 3.13). For more precise estimations, an additional model should be implemented, accounting for each heating ramp step. Therefore also any uncertainties for the preliminary fitted data are not applicable.

3.3 Conclusions and outlook

Full Sc radionuclide thermal release from metallic ^{nat}Ti and ^{nat}V foil roll target materials was achieved at ∼70–85 % of their corresponding melting temperatures T_m and in short timeframe (1 hour), compared to a typical mass separation and collection. The target material preparation (foil embossement) can severely impact the release behavior of the Sc radionuclides during the collection. The available theoretical models and tools are in good agreement with the obtained experimental data and useful in modeling and understanding the Sc radionuclide thermal release behavior. This study and setup will serve for radionuclide release studies of other elements from Isotope Separation OnLine (ISOL) target materials and will be used to build up an experimental database and to help benchmark theoretical diffusion and release model developments.

^{nat}Ti and ^{nat}V target materials are suitable for Sc collections from the thermal release standpoint, however their feasibility with a full-scale TISS in mass separation must be evaluated. The adsorption on refractive nature poses difficulties in extracting Sc as a radioactive ion beam even if the release from target material is efficient, thus TISS developments to increase Sc extraction efficiency and mass separation must be explored.

4 Target and ion source developments

Contents

In this Chapter, the feasibility of medical ^{43g}Sc, $^{44g/m}$Sc and ^{47}Sc radionuclide production at CERN-MEDICIS is assessed in comparison with medium to high-energy cyclotron capabilities and historical mass separation data from ISOLDE experiments. Thick target activity yields (TTY) for ^{nat}Ti, ^{nat}V metallic foil and ^{nat}TiC target materials are estimated for irradiation scenarios at CERN-MEDICIS and medium to high-energy cyclotron centers. The developments of the Target and Ion Source System (TISS) for Sc radionuclide production, mass separation and collection are described with a comprehensive list of tested and modified TISS.

4.1 Historical Target Materials at ISOLDE

4.1.1 Target Materials for Sc production

The most common thick target materials used at ISOLDE for radioactive ion beam production are uranium carbide (UC_x) and metallic natural tantalum (^{nat}Ta) foils [170, 171], which are also used at CERN-MEDICIS for radiolanthanide production and mass separation such as Tm, Cs, Ba and Tb [71]. Various forms of ^{nat}Ti and ^{nat}V target materials, capable of producing Sc isotope beams have been used at ISOLDE in the past 40 years [170] and are summarized in Table 4.1. TiO_2, Ti_2O_3, Ti_5Si_3 and TiN target materials for ISOL have been investigated by Oak Ridge National Laboratory (ORNL) (US) and TRI University Meson Facility (TRIUMF) (Canada), however, only focusing on ^{48}V release [172] and no Sc isotopes. Ti, VC, and TiC target materials have been fluorinated with CF_4 gas addition during operations at ISOLDE to promote the release of Sc. However, the release and extraction of mono-atomic Sc from the TISS was slow and did not improve with the CF_4 addition, even when reaching a temperature of 1900 °C [77, 172].

Table 4.1: Sc radionuclide release from target materials used at ISOLDE

Target material	Operated temperature, °C	Release conditions
^{nat}Ti metallic foils	>1600	W surface ion source. Fluorination with CF_4. Only Sc^+ and ScF^+ observed and target molten after mass separation [82].
^{nat}TiC (1-50 μm)	1900	Slow release, that did not increase by fluorination with CF_4 [77].
	2300	No Sc released [78].
^{nat}TiC-CNT (nanometric)	1500	No Sc released. [6].
^{nat}TiC-CB (nanometric)	1500 - 1740	Re surface source. No Sc was released. [6].
^{nat}V powder	1800	No Sc released [78].
^{nat}VC (1-50 μm)	1900	Slow release, that did not increase with reactive gas phase CF_4 addition [77].
	2300	No Sc released. Higher other radionuclide release rates than from ^{nat}TiC [78].

In previous works, the addition of CF_4 reactive gas to the ^{nat}Ti foil target material and TISS with a W surface ion source (see Table 4.1) in online operations at ISOLDE have resulted in mono-atomic $^{42}Sc^+$, $^{43}Sc^+$, $^{44g/m}Sc^+$, $^{46}Sc^+$, $^{47}Sc^+$, ^{48}Sc and $^{46}ScF^+$, $^{47}ScF^+$, $^{48}ScF^+$ ion beams. At ISOLDE and ISOL ion beams the yield is defined as atoms per μC of the incident proton beam. The ISOL yield of mono-fluoride Sc molecular beams was observed an order of magnitude higher than the respective mono-atomic. During the same experiment, it was also noted that the Ti^+ ion beam current had increased from 0.1 to 5 μA after the CF_4 gas injection, suggesting severe target material evaporation. The post-analysis of the TISS showed that the Ti foil material had been molten [82]. Such conditions are unacceptable for the sustainability of radionuclide collection for medical applications as well as the safety and longevity of the mass separator due to extraction

electrode, turbomolecular pump and insulator coatings, increased partial pressure and risk of high-voltage arcs, target material sublimation and depletion.

Ti has higher vapour pressure and lower melting temperature than V (T_m=1668 °C and p_{vap}=3.10 $\times$ 10^{-4} mbar for Ti and T_m=1910 °C and p_{vap}=4.59 $\times$ 10^{-5} mbar), however, only V in powder form has been used as a target material at ISOLDE [172]. Powders tend to sinter more easily and at lower temperatures (typically at 50–80% of their T_m), especially if irradiated with the pulsed proton beam from PSB. The sintering therefore lowers the ISOL yield over time [6]. Because of the insufficient ISOL yield, slow isotope release from the TISS, melting point of the material, powder sintering or element selectivity, these materials are not used commonly for RIB production at ISOLDE. Except in special cases for exotic radionuclide studies, there is less interest in producing TISS with Ti or V target materials, that limit isotope production to nickel (Ni) when a standard and universal UC_X or ^{nat}Ta foil target materials can be used.

Refractory Sc release from the TISS have proven to be very challenging due to the high boiling point, low vapour pressure, and high chemical reactivity of Sc. The refractory nature of Sc is one of the reasons for the low yields and inconsistent RIB delivery results obtained for mass separation up to now. Previously there was limited interest in sustained slow atomic or molecular Sc radionuclide release and production of clinically suitable activities, which explains why no further investigations of these target materials were done. However, a controlled and sustained release approach would be very suitable in radionuclide collections, where single-batch collections can last for days.

4.1.2 ISOL yields of Sc radionuclides

The mass separation and production ISOL yields of radionuclides during ongoing ISOLDE experiments are systematically measured for various target materials and ion sources [70]. The historical measurements were done with Synchrocyclotron (SC) and 600 MeV proton primary driver beam for radionuclide production and nowadays with the pulsed 1.4 GeV proton beam delivered by PSB. The data is published in an online ISOL yield database, however, only data from SC regarding medical Sc radionuclides is available including ^{nat}Ti, ^{nat}Ta metallic foils and UC_x as target materials [173].

Achievable collected activities of medical Sc radionuclides from the available historical ^{nat}Ti metallic foil targets and ISOL yields were estimated by solving the equation of Bateman, to assess the potential collection parameters. The calculated results are summarized in Table 4.2. The ISOL yields used for the estimation were obtained with the 600 MeV proton beam during an online mass separation. It is important to note this, as the target material was constantly irradiated during the radionuclide extraction and mass separation [174]. The lower primary proton beam energy at SC also suggests $\sim$20 % higher radionuclide production yield, compared to the pulsed PSB 1.4 GeV proton beam [6, 173].

Based on the historical data and available ISOL yields, the collected activity of ^{43}Sc and ^{44g}Sc would reach saturation in one day and ^{47}Sc collection upper limit would not be reached even after 5 days of collection as indicated in Figure 4.1. Therefore to maximize the collection output, one could start by collecting ^{43}Sc or ^{44g}Sc for a day and then switch to ^{47}Sc collection. In collections longer than 5 days, the overall production of the medically relevant Sc radionuclides would become unfeasible due to the operation

Table 4.2: Historical online Sc ISOL yields and collection estimate from ^{nat}Ti foils at ISOLDE.

Chemical form	Isotope	ISOL yield [1], atom/μC	Activity, Bq/μC	Activity in 24 hours, Bq	Activity in 5 days, Bq
Sc^+	^{43}Sc	3.00×10^5	1.48×10^3	2.96×10^5	3.00×10^5
	^{44g}Sc	1.00×10^8	4.85×10^3	9.85×10^7	9.99×10^7
	^{44m}Sc	1.00×10^6	3.29	2.47×10^5	7.58×10^5
	^{46}Sc	4.50×10^6	$4.31\ 10^{-1}$	3.71×10^4	1.82×10^5
	^{47}Sc	2.50×10^6	5.99	4.67×10^5	1.61×10^6
ScF^+	^{46}Sc	7.00×10^7	6.70	5.77×10^5	2.84×10^6
	^{47}Sc	3.00×10^7	7.19×10^1	5.61×10^6	1.93×10^7
Unk.[2]	^{43}Sc	2.20×10^5	1.09×10^1	2.17×10^5	2.20×10^5
	^{44g}Sc	1.20×10^9	5.81×10^4	1.18×10^9	1.20×10^9
	^{44m}Sc	1.20×10^7	3.95×10^1	2.97×10^6	9.10×10^6

[1] ISOL yield after mass separation for 1 μA and 600 MeV proton beam. The ISOL yields were obtained with a W surface source TISS.
[2] Not specified, but CF_4 gas was added during the mass separation.

costs, target material degradation and already collected radionuclide decay.

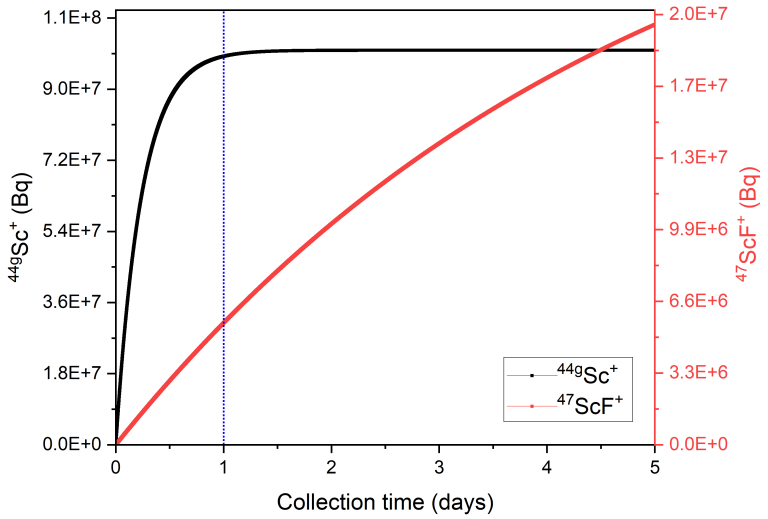

Figure 4.1: Estimated collected ^{44g}Sc and ^{47}Sc collected activity based on historic ISOL yields.

One should note, that the majority of the ISOL yields used in the estimation were obtained from the one TISS, which was fluorinated and eventually molten. Also, the target material was constantly irradiated with protons, feeding the Sc radionuclides for mass separation [82]. Therefore the obtained results are a severe overestimation of the achievable collected activities, however, still would not result in medically relevant ac-

tivities in almost all cases. On the other hand, the W surface ion source is not the most optimal ion source neither for atomic nor molecular Sc ionization because of their high ionization potential (> 6 eV) [38]. For these reasons, the various target materials and their potential to produce clinically relevant Sc radionuclide activities for medical applications in sustainable mass separation and collection conditions must be investigated more thoroughly.

4.2 Target materials for Sc production and mass separation

4.2.1 Thick target preparation for radioactive Sc ion beams

Multiple ISOLDE target materials could be used for Sc radionuclide production with high-energy protons (> 500 MeV) and mass separation. Due to the absence of high-energy protons in cyclotron centers, the focus was set on both medium-high energy cyclotron and mass separator compatible target materials with natural isotopic abundance, namely ^{nat}Ti and ^{nat}V metallic foils, and ^{nat}TiC because of their stability, high melting point and favourable Sc radionuclide production cross sections.

TISS with empty Ta containers were produced and first used in functional testing and stable isotope ion beam tests. They are then loaded with prepared target material load and outgassed at nominal operating temperatures. The outgassing is done for volatile contaminant thermal release from target material and conditioning under vacuum. This helps to reduce vapour phase chemicals that may compete with Sc molecule formation during collections. The temperature of outgassing depends on the material and foreseen collection temperatures. Once the target is conditioned, it is used for Sc radionuclide mass separation collections in multiple batches.

The metallic ^{nat}Ti and ^{nat}V foil target load were made out of thin foils (0.25 μm), that were cut into 10–15 mm wide strips, rolled in a cylindrical shape ($\varnothing < 20$ mm) and held together with a Ta wire (see Figure 4.2a). To reduce sintering effects, the foil strips were embossed creating a hill-valley pattern and more space in between the rolled layers (see Figure 4.2b). To increase the production yield (activity) from irradiation, ^{nat}Ti double-layer foil rolls were prepared, with one strip layer embossed and the second kept flat (non-embossed). The 25 μm thick metallic ^{nat}Ti and ^{nat}V foils were purchased from *Goodfellow Cambridge Ltd.* (United Kingdom). The prepared rolls were washed in 70 % ethanol and ultrasonic bath for 10 min and dried in air.

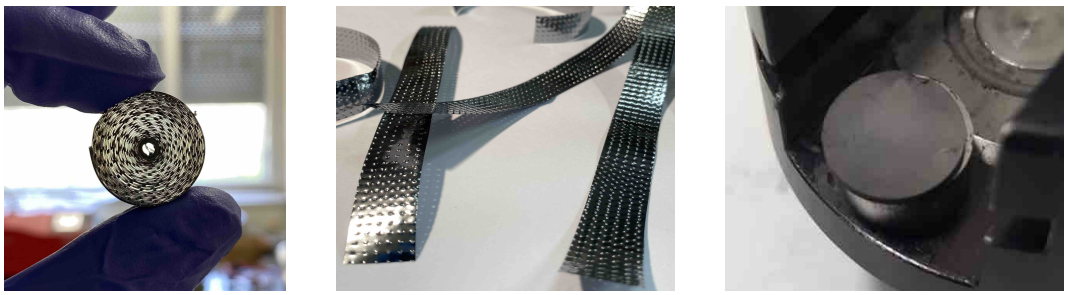

(a) ^{nat}Ti double foil roll. (b) Embossed metallic ^{nat}V foil. (c) Pressed ^{nat}TiC pellet.

Figure 4.2: Embossed ^{nat}Ti and ^{nat}V metallic foils and pressed ^{nat}TiC pellet used for target load.

Titanium carbide ^{nat}TiC has not yet been used as cyclotron target material for medical Sc radionuclide production due to its chemical resistance when it comes to target material post-processing for chemical separation and synthesis [175]. On the other hand, it is being investigated and tested as a target material for online radionuclide production in mass separation and therefore holds great potential if cyclotron production is combined with the mass separation [175]. ^{nat}TiC has high thermal conductivity and melting point, therefore making it suitable for high beam intensity irradiation [176]. ^{nat}TiC powder with a particle size of 1-2 μm (bought from Alfa Aesar, US) was pressed in 13 $\pm$ 1 mm diameter and 1.2 $\pm$ 0.2 mm thick sized compact cylindric pellets, weighing approximately 0.42 g each (see Figure 4.2c). A semi-automated 15-ton hydraulic press (Specac Ltd., United Kingdom) was used to press the ^{nat}TiC powder with 295–330 MPa pressure. The prepared pellets were loaded in a carbon sleeve (see Figure 4.3) to maintain their shape and integrity during transfer, outgassing, irradiation and mass separation. The carbon sleeve also eases the insertion of the load inside the target container. The carbon sleeve has a circular opening in the middle to allow gaseous species to effuse (see Figure 4.3b).

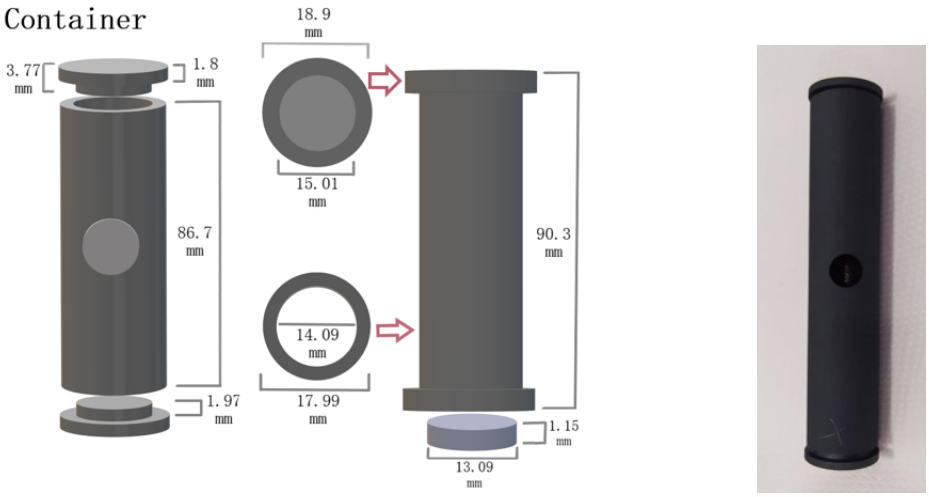

(a) Carbon sleeve schematic.

(b) Carbon sleeve for pellet load.

Figure 4.3: Carbon sleeve and ^{nat}TiC pellet dimensions used for target load production.

After the pellets were loaded in the carbon sleeve, they were placed in a dedicated outgassing TISS that consisted of only the base plate, Ta target container, and heat screens. The ^{nat}TiC pellets with the carbon sleeve were outgassed overnight at 1800 ° C temperature with the pressure of the TISS being kept below 1.5 $\times$ 10^{-5} mbar. After outgassing, a few pellets were removed for characterization and weight loss measurements. The target load was then inserted in the #702M TISS target container exactly at the middle with the sleeve opening facing the transfer line to the ion source. The list of investigated target materials and produced loads are summarized in Table 4.3.

The Specific Surface Area (SSA) of a raw pressed ^{nat}TiC pellet sample was measured by the BET method (see section 2.6.3), resulting in 2.48 m^2g^{-1}. Before the measurement, the sample was outgassed at 300 °C for 19 hours. In comparison, the SSA of foils was only 0.015 m^2g^{-1} and commercial ^{nat}TiC nano-powders can reach up to 25 m^2g^{-1}. This aspect makes the investigation of ^{nat}TiC nano-powders interesting for the Sc radionuclide

mass separation and collection, however, requires additional target load preparation steps to counter and hinder sintering [6,50].

Table 4.3: Target load details for Sc production and collection of various materials.

Material	Category	T_m, °C	TISS Nr.	Purity, %	Rolls or pellets	Load mass, g	Load surface area, m^2	Load density[1], g/cm^3
^{nat}Ti	Metallic foils	1668	723M	99.6	12	74.8	1.11	1.19
			741M	99.6	12	96.3	1.43	1.53
^{nat}V	Metallic foils	1910	766M	99.8[2]	11	44.8	0.59	0.71
			790M	99.8	10	61.7	0.81	0.98
			805M	>99.8	10	34.3	0.45	0.55
^{nat}TiC	Carbides	3160	702M	99.5	69	29.2	72.4	2.73

[1] Rolled foil target load density is considered as the total target material mass against the whole target container volume.
Because of the carbon sleeve and later FLUKA estimations, the ^{nat}TiC target load density is considered as ^{nat}TiC pellet total mass against their total volume.
The bulk material densities are 4.50 g/cm^3 (Ti), 6.10 g/cm^3 (V) and 4.93 g/cm^3.
[2] The foil surface was severely oxidized.

Since powders and ^{nat}TiC is known to sinter vety well [177], the ^{nat}TiC samples were compared after various treatments. SEM images of raw and untreated control sample are shown in Figure 4.4a and Figure 4.4b. 1-7 μm as well as sub-micrometric particles could be observed. Before preparing the full target load a ^{nat}TiC pellet sample was tested at the Offline-1 mass separator. The goal was to test the compatibility of ^{nat}TiC with mass separation and CF_4 gas at high temperatures and the main attention was brought to total beam composition. CF_4 is known to act as an etching agent at high temperatures and therefore it was important to investigate the sample for any signs of degradation after the mass separation and fluorination test [178]. The test lasted $\sim$30 hours and a temperature of 1510 °C was reached. The sample already showed signs of sintering, as most of the nanoscale particles were agglomerated with larger particles (see Figure 4.4c and Figure 4.4d). The sample, which was only outgassed in a TISS and vacuum at 1800 °C indicated even more severe sintering as almost all sub-micron particles were agglomerated (see Figure 4.4e and Figure 4.4f). The EDX analysis confirmed the 1:1 ratio of Ti to C. The main contaminants were oxygen (1.4–3.2 %), tantalum (0.2-1.1 %), and tungsten (<0.6 %). The oxygen could originate from TiO_2 impurities in the sample, tantalum from the target containers and tungsten from the pill press die.

In contrast to enriched target materials for cyclotrons, where the isotopic content is of the highest importance, target materials for mass separation should be as chemically pure from volatile or intended radionuclide isobaric impurities. Typical mass separation ion beam intensities are in the range of a few pA to μA. Assuming 100 % ionization efficiency this would translate into a few amol to pmol released per second. The target container volume is close to 60 cm^3 and can accommodate a few mol of the target material, resulting in a few hundred grams (based on the material density). Therefore, parts per million (ppm) and parts per billion (ppb) impurities may produce contaminant ion beams that hinder mass separation and isotope collections for days. Main impurities

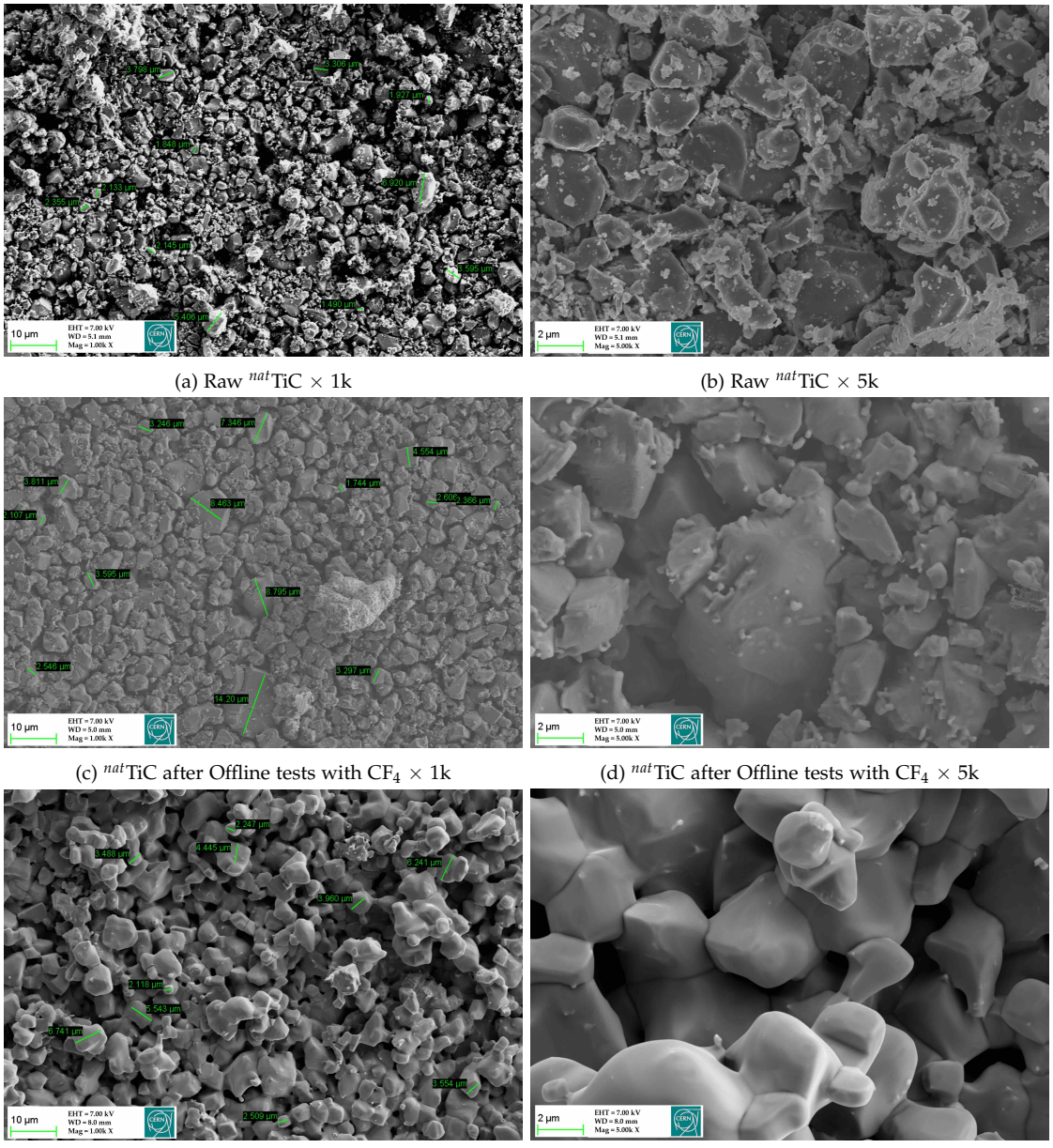

(a) Raw ^{nat}TiC × 1k

(b) Raw ^{nat}TiC × 5k

(c) ^{nat}TiC after Offline tests with CF_4 × 1k

(d) ^{nat}TiC after Offline tests with CF_4 × 5k

(e) ^{nat}TiC after outgassing × 1k

(f) ^{nat}TiC after outgassing × 5k

Figure 4.4: SEM images of differently treated ^{nat}TiC pellets

in the target materials as indicated by the supplier or Certificate of Analysis (CoA) are summarized in Table 4.4 [179]. Considering the highest obtained target load mass for each material, the impurities are expressed in total integrated current and days of the collection with 1 μA of the impurity ion beam intensity.

Not all impurities hinder the mass separation, but mainly the most volatile ones. They can affect the target container heating rate because of the ion source load limit. Another limitation is the chemical interactions of the more reactive species with the halogenating agent used for Sc volatilization or the impurity reactivity with Sc (e.g. oxygen). An example is aluminium (Al) impurities in the ^{nat}V foil. Whenever ^{nat}V foil targets were

Table 4.4: Main target material impurities and integrated currents

Element	p_{vap}[a], mbar	Target material	Amount, ppm	Mass, mg	Integrated current[b], A	Collection time[c], days
Al	1.06	^{nat}Ti foil	300	28.9	1.03×10^2	60
		^{nat}V foil (98.8%)	200	12.3	4.41×10^1	26
		^{nat}V foil (>98.8%)	100	3.4	1.22×10^1	7
		^{nat}TiC	150	4.4	1.56×10^1	9
C	7.08×10^{-10}	^{nat}Ti foil	300	28.9	2.32×10^2	134
		^{nat}V foil (98.8%)	120	7.4	5.94×10^1	34
		^{nat}V foil (>98.8%)	80	2.7	2.20×10^1	13
		^{nat}TiC	Target matrix			
Cr	0.12	^{nat}Ti foil	50	4.8	8.92	5
		^{nat}V foil (98.8%)	3	0.2	3.43×10^{-1}	0
		^{nat}V foil (>98.8%)	110	3.8	6.99	4
		^{nat}TiC	200	5.8	1.08×10^1	6
Fe	0.04	^{nat}Ti foil	1500	144.5	2.49×10^2	144
		^{nat}V foil (98.8%)	60	3.7	6.39	4
		^{nat}V foil (>98.8%)	370	12.7	2.19×10^1	13
		^{nat}TiC	600	17.5	3.02×10^1	17
O	$> 1 \times 10^4$	^{nat}Ti foil	2000	192.6	1.16×10^3	671
		^{nat}V foil (98.8%)	50	3.1	1.86×10^1	11
		^{nat}V foil (>98.8%)	200	6.9	4.13×10^1	24
		^{nat}TiC	Not indicated			
Si	4.43×10^{-3}	^{nat}Ti foil	300	28.9	9.91×10^1	57
		^{nat}V foil (98.8%)	300	18.5	6.35×10^1	37
		^{nat}V foil (>98.8%)	90	3.1	1.06×10^1	6
		^{nat}TiC	500	14.6	5.01×10^1	29

a The impurity vapour pressure at 1550 °C [180].
b The impurity amount expressed in beam current assuming singly charged atom.
c Ion beam with intensity of 1 μA and mass separation efficiency of 5 % was considered.

used for ScF_x (x=1–3) collections, relatively intense beams of Al and AlF_x (x=1–3) in few μA range were observed (see Figure 4.5) and other fluoride ion beams were suppressed. These contaminant ion beams would not diminish even after a few days of mass separation. As Al is very reactive towards the supplied fluorine, it can affect the ScF_x (x=1–3) formation rate. Silicone is another impurity that also interacts with fluorine and even creates isobars for both the atomic ^{47}Sc (amu 47) and halogen molecule $^{47}ScF_x^+$ (x=1–2) (amu 66 and 85) sideband collection. The impurities mostly originate from the production procedure of the material, therefore reinforcing the need for higher chemical purity target materials for radionuclide collection.

The impact of impurities in target materials can be assessed with the thermodynamic chemical reaction and equilibrium calculations, providing the actual composition and parameters are known (see section 2.5.1) and is discussed in Chapter 5. However, it is difficult to predict the reaction rate from the estimations.

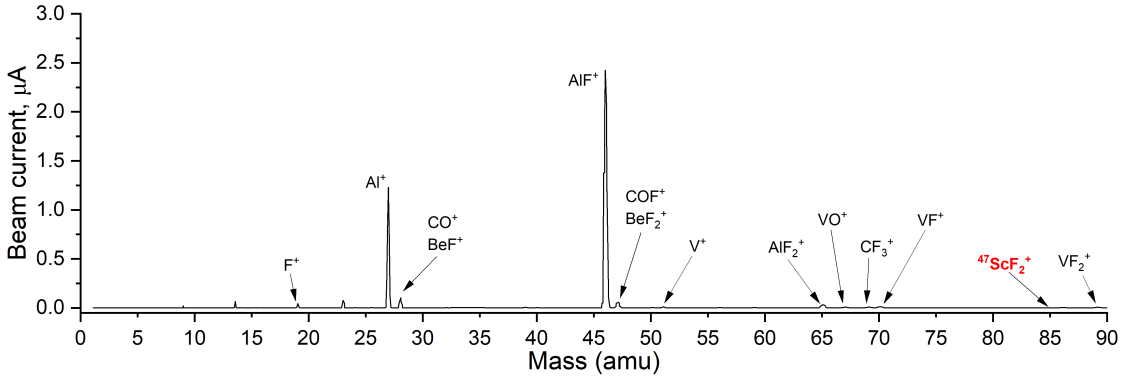

Figure 4.5: Mass scan spectra during Sc radionuclide mass separation from irradiated ^{nat}V target material, indicating AlF_X (x=1–3) impurities. Ion source at 1940 °C and target container at 1050 °C (TISS #805M)

4.2.2 In-target production estimation

One of the key performance parameters of CERN-MEDICIS facility and mass separation is the collection efficiency, which takes into account the radionuclide activity at the Start Of Collection (SOC) [74]. After the target material irradiation at the PSB, TISS and the material γ-spectrometry measurements for activity determination are impossible due to the high dose rate (0.3–1.0 Sv/h at 27 cm distance from the TISS). A project to perform such measurements once TISS is on the mass separator frontend is being discussed. Therefore the radionuclide inventory for activity yield and efficiency estimations was computed with FLUKA and ActiWiz. For the activity estimations, a few approximations and assumptions were considered:

- Each metallic roll is not precisely modeled and considered as a full cylinder. Due to the particle fluence distribution and small energy loss in the target container region, the atomic nuclei distribution inside the particle tracking (scoring) region is uniform. The same is assumed for more complex chemical compounds and molecules, as the FLUKA code takes into account the atomic nuclei density in a given volume, but not the molecule spatial arrangement of its atoms and their chemical bonds (chemical structure).

- The metallic foil rolls are inserted in the target container without additional sleeves and therefore the target load density is uniformly distributed over the target container volume and less than the corresponding pure material density. Depending on the weight and foil layers, the obtained load densities varied from 0.5–1.5 g/cm^3. Even though the actual prepared ^{nat}V foil target load densities resulted in < 1 g/cm^3, the highest prepared metallic foil load density was 1.5 g/cm^3 (for ^{nat}Ti). To compare the materials, the same density of 1.5 g/cm^3 was used for ^{nat}V in-target production FLUKA estimations and later normalized.

- The ^{nat}TiC pellet load is confined in a carbon sleeve, therefore the radionuclide production region is assumed as the inner carbon sleeve volume that is taken up by the pellets. The rest of the space inside the target container is taken up by the carbon sleeve or left empty. Therefore, the mass of all outgassed pellets per their initial volume was assumed for the estimation, resulting in the ^{nat}TiC load density of 2.7 g/cm^3.

The FLUKA production estimations give a good relative comparison of the proposed materials to maximize on direct Sc radionuclide or ^{44}Ti/^{44g}Sc and ^{47}Ca /^{47}Sc generator production feasibility. It should be noted the co-production of light radioactive N, C, B, Be, and Li species from carbon sleeve and ^{nat}TiC, however, only ^{7}Be and ^{10}Be are long-lived and the rest are very short-lived radionuclides [26, 173]. The activity yields were simulated with 1 $\times 10^6$ primary particles (protons) and results are given as produced nuclides per gram of user-defined target material, per primary particle (nuclei/g/primary). Table 4.5 compares activity production yields with statistical uncertainties for target materials used in this study at various irradiation stations and modes. For indirect irradiation, a TISS with a depleted uranium carbide target load was considered upstream of the proton beam, because it is the most widely used target for radioactive ion beam productions at ISOLDE (see Figure 4.6) [171].

Table 4.5: In-target Sc radionuclide activity production yields from FLUKA code.

Radionuclide	Target material[a]	Direct MEDICIS HRS, nuclei / g / primary	Indirect MEDICIS HRS, nuclei / g / primary	Indirect ISIS, nuclei / g / primary
^{43}Sc	^{nat}Ti	$2.97 \pm 0.05 \times 10^{-5}$	$2.45 \pm 0.15 \times 10^{-6}$	$3.6 \pm 0.2 \times 10^{-6}$
	^{nat}V	$1.81 \pm 0.03 \times 10^{-5}$	$1.5 \pm 0.2 \times 10^{-6}$	$2.19 \pm 0.15 \times 10^{-6}$
	^{nat}TiC	$2.37 \pm 0.03 \times 10^{-5}$	$1.9 \pm 0.2 \times 10^{-6}$	$2.9 \pm 0.2 \times 10^{-6}$
^{44g}Sc	^{nat}Ti	$5.91 \pm 0.09 \times 10^{-5}$	$5.2 \pm 0.3 \times 10^{-6}$	$7.8 \pm 0.2 \times 10^{-6}$
	^{nat}V	$3.67 \pm 0.02 \times 10^{-5}$	$3.0 \pm 0.2 \times 10^{-6}$	$4.67 \pm 0.19 \times 10^{-6}$
	^{nat}TiC	$4.52 \pm 0.07 \times 10^{-5}$	$3.51 \pm 0.19 \times 10^{-6}$	$5.70 \pm 0.18 \times 10^{-6}$
^{44m}Sc	^{nat}Ti	$5.91 \pm 0.09 \times 10^{-5}$	$5.2 \pm 0.3 \times 10^{-6}$	$7.8 \pm 0.2 \times 10^{-6}$
	^{nat}V	$3.67 \pm 0.02 \times 10^{-5}$	$3.0 \pm 0.2 \times 10^{-6}$	$4.67 \pm 0.19 \times 10^{-6}$
	^{nat}TiC	$4.52 \pm 0.07 \times 10^{-5}$	$3.51 \pm 0.19 \times 10^{-6}$	$5.70 \pm 0.18 \times 10^{-6}$
^{46}Sc	^{nat}Ti	$7.00 \pm 0.11 \times 10^{-5}$	$5.83 \pm 0.12 \times 10^{-6}$	$9.1 \pm 0.2 \times 10^{-6}$
	^{nat}V	$4.22 \pm 0.08 \times 10^{-5}$	$3.5 \pm 0.2 \times 10^{-6}$	$5.8 \pm 0.3 \times 10^{-6}$
	^{nat}TiC	$5.407 \pm 0.016 \times 10^{-5}$	$4.22 \pm 0.14 \times 10^{-6}$	$7.22 \pm 0.15 \times 10^{-6}$
^{47}Sc	^{nat}Ti	$1.72 \pm 0.02 \times 10^{-4}$	$1.37 \pm 0.07 \times 10^{-5}$	$2.10 \pm 0.05 \times 10^{-5}$
	^{nat}V	$5.89 \pm 0.14 \times 10^{-5}$	$4.4 \pm 0.2 \times 10^{-6}$	$6.7 \pm 0.6 \times 10^{-6}$
	^{nat}TiC	$1.296 \pm 0.013 \times 10^{-4}$	$1.03 \pm 0.04 \times 10^{-5}$	$1.69 \pm 0.06 \times 10^{-5}$
^{44}Ti	^{nat}Ti	$1.85 \pm 0.06 \times 10^{-5}$	$1.21 \pm 0.08 \times 10^{-6}$	$2.2 \pm 0.3 \times 10^{-6}$
	^{nat}V	$9.1 \pm 0.6 \times 10^{-6}$	$8.9 \pm 0.9 \times 10^{-7}$	$1.41 \pm 0.18 \times 10^{-6}$
	^{nat}TiC	$1.39 \pm 0.06 \times 10^{-5}$	$1.35 \pm 0.18 \times 10^{-6}$	$1.68 \pm 0.14 \times 10^{-6}$
^{47}Ca	^{nat}Ti	$1.4 \pm 0.3 \times 10^{-6}$	$1.1 \pm 0.9 \times 10^{-7}$	$2.0 \pm 0.2 \times 10^{-7}$
	^{nat}V	$1.5 \pm 0.2 \times 10^{-6}$	$1.5 \pm 0.6 \times 10^{-7}$	$1.5 \pm 0.4 \times 10^{-7}$
	^{nat}TiC	$8.9 \pm 1.5 \times 10^{-7}$	$6 \pm 3 \times 10^{-8}$	$7 \pm 4 \times 10^{-8}$

[a] Target load density of 1.5 g/cm^3 for ^{nat}Ti and ^{nat}V, and of 2.7 g/cm^3 for ^{nat}TiC. was considered.

The activity yields of direct production are within the same order of magnitude for proton-rich ^{43}Sc and $^{44m/g}$Sc in all materials, however, differ for ^{47}Sc. The activity yield in metallic foils of ^{nat}Ti and ^{nat}V differ by a factor of $\times 3$ and can be explained by the cross section difference of nuclear reactions, such as ^{48}Ti(p,2p)^{47}Sc, ^{49}Ti(p,3He)^{47}Sc, ^{49}Ti(p,pd)^{47}Sc, ^{50}Ti(p,α)^{47}Sc and ^{50}V(p,3pn)^{47}Sc, ^{51}V(p,3p2n)^{47}Sc, ^{51}V(p,pα)^{47}Sc, which are the main pathways due to their isotopic prevalence in the natural titanium and vana-

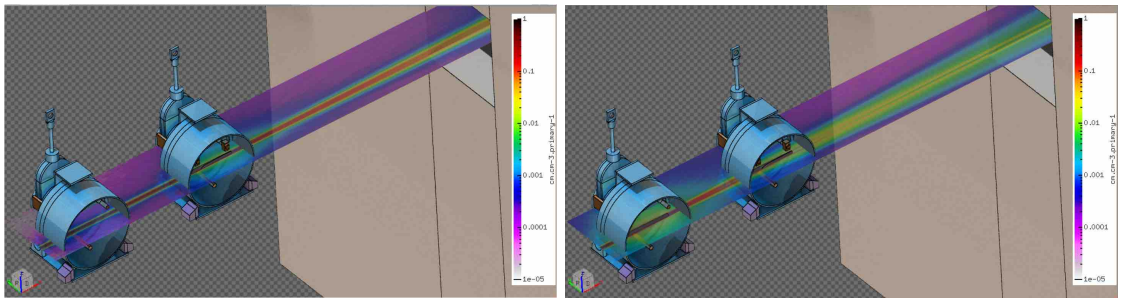

(a) Direct - through Al vessel.

(b) Indirect - through Al vessel and UC_x load.

Figure 4.6: All particle fluences from UC_x and ^{nat}Ti foil target load irradiation on MEDICIS HRS station.

dium target materials [26,37,181,182]. One should note, that at incident 1.4 GeV proton energy, multiple more exotic reaction pathways are expected as well as secondary particles, such as neutrons and α particles, coming from the interaction of protons with target material as well as the ^{nat}Ta target container and carbon. ^{44}Ti/^{44g}Sc generator production also seems feasible, however, also requires an additional mass separation step due to Ti isotope isobar collection, else resulting in lower specific activity product. On the other hand, ^{47}Ca/^{47}Sc generator production yield is 1–2 orders of magnitude lower than direct ^{47}Sc production and is less cost-efficient.

The activity yields from indirect irradiations on ISIS are higher than HRS due to less proton beam straggling because of the difference in distance between the ISOLDE and CERN-MEDICIS targets. The distance between the targets on HRS stations is 530 mm and 240 mm on GPS (see Figure 4.7). Because of proton beam straggling that travels through the ISOLDE UC_x target load, the radionuclide production yield in indirect irradiations could benefit from larger diameter and volume target containers.

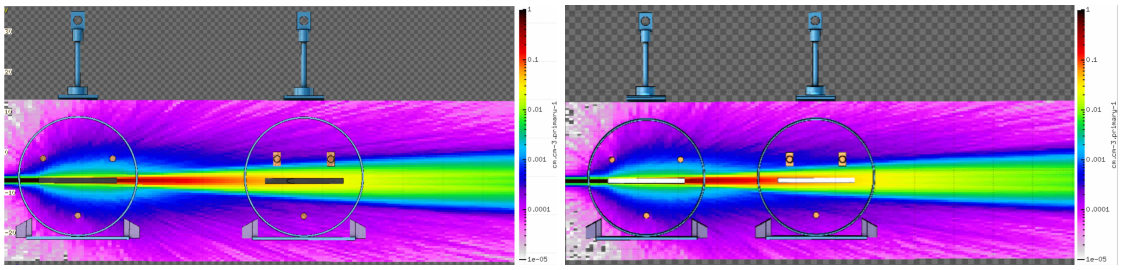

(a) HRS station.

(b) GPS station.

Figure 4.7: Proton fluence during indirect ^{nat}Ti foil target irradiation on different stations.

The obtained proton fluence spectra in all discussed target materials with different irradiation modes are shown in Figure 4.8. Because of the higher proton fluence, the activity yield and production rate of Sc radionuclides per primary particle is $\times$11 higher in the case of direct irradiation compared to indirect irradiation on the MEDICIS HRS station and $\times$7 higher than indirect irradiation at the ISIS station.

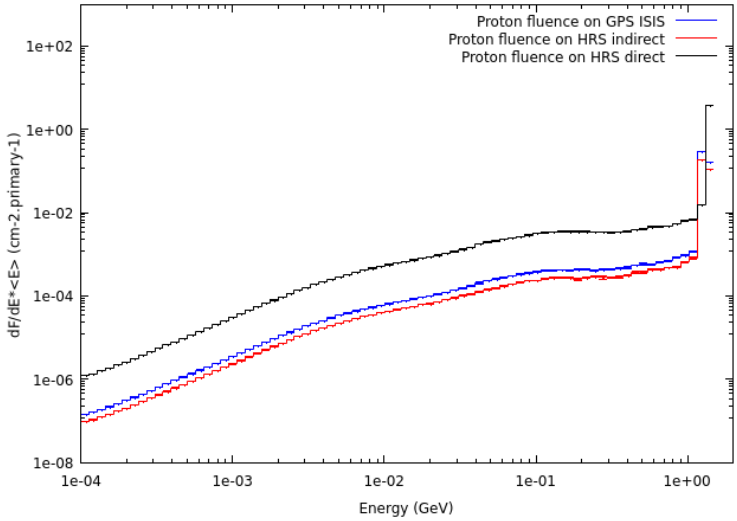

(a) Proton fluences in ^{nat}Ti.

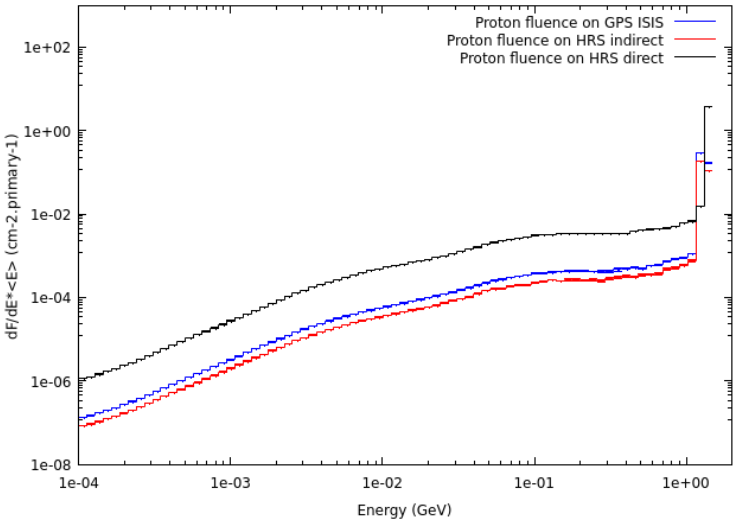

(b) Proton fluences in ^{nat}Ti.

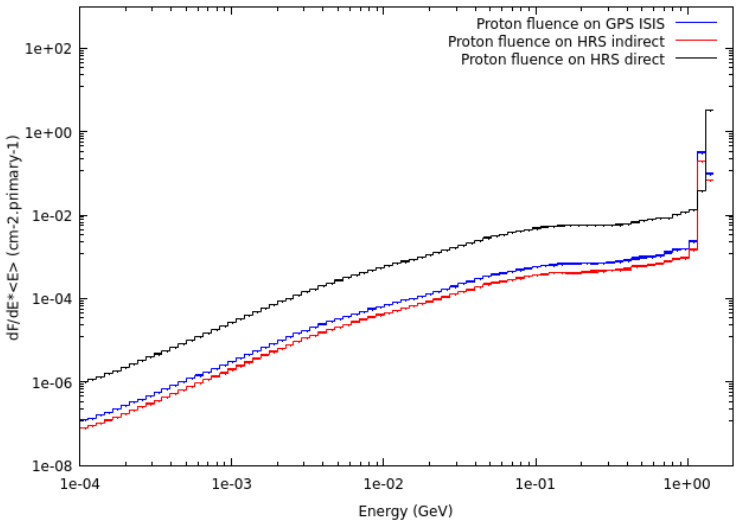

(c) Proton fluences in ^{nat}TiC.

Figure 4.8: Proton fluences in the target materials for various irradiation modes.

The production rate can be compensated by extended indirect irradiation time, however, this would be most beneficial for longer half-live radionuclides such as ^{44m}Sc, ^{46}Sc, ^{47}Sc, ^{44}Ti and ^{47}Ca. The short half-life ^{43}Sc and ^{44g}Sc would reach saturation faster due to their decay. Furthermore, during indirect irradiation, the more scattered particles impinge on TISS structures and can cause damage to seals and o-rings due to faster aging. For these reasons, direct irradiation is preferable for the longevity of TISS and diagnostic Sc radionuclide collections.

4.2.3 Thick target yield estimations

The target materials at CERN-MEDICIS are irradiated with a 2 μA proton beam whereas with a cyclotron the typical beam intensities are in the range of 10–150 μA and can reach up to 350 μA. Although the beam intensity used for radionuclide production of the CERN-PSB is much lower than a typical cyclotron, the activity production yield in ISOL TISS is compensated with the target load thickness due to the available high proton energy (1.4 GeV) when the cross sections are relevant and comparable. While the TISS target container is 200 mm thick, a typical solid target for a cyclotron houses 1–2 mm thick samples. Therefore, the feasibility of Sc radionuclide production within ISOL TISS compared to commercially available cyclotron centre solid target systems is expressed in the Thick Target activity Yields TTY.

The TTY were estimated for 1-hour irradiation with no cooling (decay) time after the End Of Beam (EOB). The CERN-MEDICIS TTY were calculated, based on the FLUKA estimations. To estimate the highest activity production yield that can be achieved with the load densities for ^{nat}Ti and ^{nat}V foils of 1.5 g/cm^3 and 2.7 g/cm^3 for ^{nat}TiC and full TISS target containers were assumed. Full target load mass of 100 g for double foil ^{nat}Ti, double foil ^{nat}V, and 65 g (154 pellets) for ^{nat}TiC were considered. Based on the particle fluence, as shown in Figure 4.8, the activity production yield was calculated for direct irradiation on the HRS station, hence the highest activity production yield.

TTY from metallic foils and pressed ^{nat}TiC targets with cyclotrons were estimated assuming a realistic scenario of targets with 1 mm thickness and 30 or 70 MeV energy proton beams. To obtain the cross section values at the desired proton energy range, a fit to the experimental data, available from the EXFOR database in Figure 4.9 was performed. The TENDL-2023 [183] theoretical cross section database was used for radionuclides that lack experimental data. TENDL is a nuclear data library that provides the output of the TALYS nuclear model code system for direct use in basic physics and other applications. The proton beam energy degradation within the targets was simulated with the The Stopping and Range of Ions in Matter (SRIM) software [184]. The mean value between the impinging beam and residual beam energy was used to estimate the activity yield, assuming that the cross sections follow linear fit within this energy range. This assumption, however, is most appropriate for relatively thin targets, such as the 1 mm thick targets. As an example, ^{44g}Sc and ^{46}Sc cross sections plots follow the linearity within the energy region the least, however, more precise values, by assuming the 1 mm sample as a stack of 10 $\times$ 100 μm foils, results in only +7 % and -4 % differences from the calculated single-piece TTY respectively. The comparison of the TTY that can be achieved at CERN-MEDICIS and cyclotrons is shown in Table 4.6. For the thin foils, the activity of each radionuclide according to the mean cross section, irradiation parameters and target thickness was calculated according to Equation 4.1:

$$A = \sigma \cdot w_i \cdot \phi \cdot \frac{N_A \cdot \rho \cdot z}{M} \cdot (1 - exp(-\lambda \cdot t_{irr})) \tag{4.1}$$

where A is the decay corrected activity of the radionuclide [Bq], σ is the production cross section of the radionuclide [cm^2], w_i is the target material chemical purity, ϕ is the incident particle flux [pps], N_A is the Avogadro constant [mol^{-1}], ρ is the target material density [g/cm^{-3}], z is the target thickness [cm], M is the target material atomic mass [g/mol], λ is the radionuclide decay constant [s^{-1}] and t_{irr} is the irradiation time [s] [10].

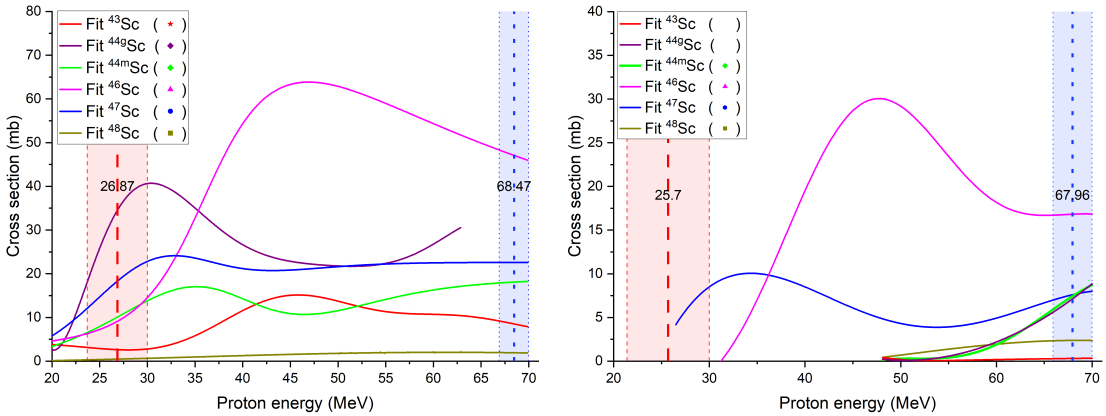

(a) ^{nat}Ti(p,x)^{xx}Sc excitation functions.

(b) ^{nat}V(p,x)^{xx}Sc excitation functions.

Figure 4.9: Experimental excitation functions for Sc radionuclide production, indicating the TTY activity calculation energy region for 30 MeV (red - dash) and 70 MeV (blue - dots) cyclotrons

Obtained TTY values for CERN-MEDICIS targets are relatively higher due to the target thickness, however, the target materials are being irradiated with lower proton beam intensity than cyclotrons. The increase in proton beam intensity to 100 μA for cyclotrons eventually places both Sc production modes in the same activity yield range, if sufficient target cooling is provided. One should note that to estimate achievable activity per production batch, the possibility of increasing the cyclotron target thickness can increase the activity yield as well, however, other Sc radionuclide contaminant buildup is inevitable. This is an important consideration for the long-lived, high γ-ray ^{46}Sc buildup, as it poses additional radiation hazards when handling the irradiated target. The obtained results for cyclotron irradiation, do not account for the production of radionuclides from secondary particle fields. To account for secondary particle fields, a Monte Carlo simulation should be done.

The mass separation efficiency (0.1–53 % depending on the chemical element [71, 72, 185]) should also be taken into account, which severely impacts the collectible Sc radionuclide activity [71, 185]. Nevertheless, with the combination of efficient release and sufficient irradiation times, thick target irradiation with low intensity and high energy protons with subsequent mass separation can yield clinical dose activities of Sc radionuclides comparable to the ones that can be achieved with medium-energy cyclotrons in medical or research centers (see Table 4.6). In comparison to cyclotron irradiated samples, mass separation facilities such as CERN-MEDICIS have the potential to produce and deliver high molar activity (TBq/μmol) and isotopic purity Sc radionuclides because of the mass separation technique and parallel collection possibility for

Table 4.6: Thick target activity yields for typical CERN-MEDICIS and cyclotron targets.

Radionuclide	Target material	CERN-MEDICIS, $Bq/\mu Ah$	30 MeV cyclotron, $Bq/\mu Ah$	70 MeV cyclotron, $Bq/\mu Ah$
^{43}Sc	^{nat}Ti	3.0×10^{9}	1.5×10^{7}	4.9×10^{7}
	^{nat}V	1.9×10^{9}	-	2.3×10^{6}
	^{nat}TiC	1.6×10^{9}	7.3×10^{6}	2.3×10^{7}
^{44g}Sc	^{nat}Ti	6.0×10^{9}	2.0×10^{8}	2.3×10^{8}
	^{nat}V	3.7×10^{9}	-	5.4×10^{7}
	^{nat}TiC	3.0×10^{9}	1.1×10^{8}	1.1×10^{8}
^{44m}Sc	^{nat}Ti	4.4×10^{8}	4.2×10^{6}	7.5×10^{6}
	^{nat}V	2.7×10^{8}	-	3.8×10^{6}
	^{nat}TiC	2.2×10^{8}	2.3×10^{6}	3.6×10^{6}
^{46}Sc	^{nat}Ti	3.0×10^{7}	1.1×10^{5}	5.7×10^{5}
	^{nat}V	1.8×10^{7}	2.4×10^{-2}	2.6×10^{5}
	^{nat}TiC	1.5×10^{7}	6.3×10^{4}	2.7×10^{5}
^{47}Sc	^{nat}Ti	9.2×10^{8}	5.6×10^{6}	6.9×10^{6}
	^{nat}V	3.2×10^{8}	1.5×10^{6}	2.9×10^{6}
	^{nat}TiC	4.5×10^{8}	3.0×10^{6}	3.3×10^{6}
^{48}Sc	^{nat}Ti	1.6×10^{8}	2.6×10^{5}	1.1×10^{6}
	^{nat}V	2.5×10^{8}	-	1.7×10^{6}
	^{nat}TiC	8.4×10^{7}	1.4×10^{5}	5.1×10^{5}
^{44}Ti	^{nat}Ti	1.5×10^{4}	1.9×10^{1}	2.5×10^{2}
	^{nat}V	7.5×10^{3}	-	2.7×10^{1}
	^{nat}TiC	7.5×10^{3}	1.3×10^{1}	1.2×10^{2}
^{47}Ca	^{nat}Ti	5.7×10^{6}	7.5×10^{-5}	1.3×10^{4}
	^{nat}V	5.8×10^{6}	-	7.7×10^{3}
	^{nat}TiC	2.3×10^{6}	2.6×10^{-2}	6.1×10^{3}

simultaneous $^{44g/m}$Sc and ^{47}Sc collection from a single batch [38]. The dissolution of metallic Ti foils, TiO_2 or TiC after irradiation is also extremely difficult, whereas mass separation would omit this step [186]. Therefore the Sc production from economically feasible, natural isotopic abundance target materials should include a mass separation step to reach a purity level high enough for medical applications.

4.2.4 Cross section measurements of ^{nat}V foil irradiation with deuterons

Another way of ^{47}Sc production with cyclotrons is via the ^{nat}Ti and ^{nat}V irradiation with deuterons. The incident particles during sample irradiation induce defects in the target materials, which can influence the radionuclide diffusion within the target material and release during the mass separation [150, 187, 188]. Compared to protons, the deuterons are larger and have higher energy deposition dE/dx than protons and for equal atom dose implants create more damage [189]. Intuitively, better release during mass separation could be expected, however, the annealing, re-crystallization, and sintering of the target material at high temperatures counteract the induced defect effect [6, 188, 190]. For better understanding, the influence of target material irradiation with deuterons on

mass separation should be investigated.

^{47}Sc can be directly produced via the ^{50}V(d,3p2n)^{47}Sc and ^{51}V(d,3p3n)^{47}Sc or indirectly via ^{47}Ca/^{47}Sc generator production from ^{50}V(d,4pn)^{47}Ca and ^{51}V(d,4p2n)^{47}Ca nuclear reactions. The indirect (generator) route results in isotopically pure ^{47}Sc, however, the activity production yield is orders of magnitude lower than via the direct production and requires an additional chemical separation step. The irradiation with deuterons is preferable also due to higher cross sections in comparison to proton irradiation as well as the possibility to produce ^{47}Sc in the absence of ^{46}Sc contamination already at 34 MeV (for deuterons) (see Figure 4.10) [191]. Although the method of production has the potential in high molar activity ^{47}Sc supply, the available experimental cross section data for ^{nat}V and ^{nat}Ti metallic foil irradiation with deuterons is still scarce due to the low availability of high-energy deuteron accelerators (> 40 MeV) [26, 191].

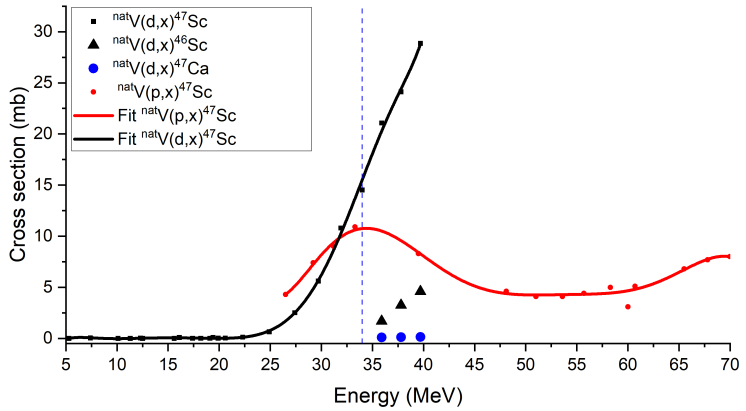

Figure 4.10: Experimental cross sections for ^{nat}V irradiation with protons and deuterons [26, 191]

A target composition with initial theoretical estimations were performed to prepare for a future cross section measurement campaign with subsequent mass separation. The radionuclide production cross sections can be efficiently measured by utilizing the stacked foil method [192]. The main advantage is that a relatively large energy range can be covered to generate the excitation curves by starting with a fixed energy particle beam. The full target consists of five sets of stacked thin 25 μm ^{nat}V target foils, 10 μm ^{nat}Ti monitor foils, 10 μm Al separator foils and 100 μm Al degrader foils (see Figure 4.11). A total target thickness of 1.01 mm with 34 MeV incident deuteron energy and 100 nA intensity was estimated. The ^{nat}Ti foil is used to measure the precise beam energy based on the produced radionuclides and International Atomic Energy Agency (IAEA) suggested beam monitor nuclear reactions [193, 194]. The Al separator foils are necessary to prevent any possible radionuclide recoil from ^{nat}V foil and contamination of the monitor foil [195].

The theoretical radionuclide inventories for each foil were estimated from the already available experimental cross section data as well as TENDL-2023, where there was no experimental data and equation 4.1 [26, 183]. The incident deuteron beam energy degradation was estimated with SRIM software and is expected to decrease from 34.0 MeV to 23.6 $\pm$ 0.2 MeV [184]. An estimated cross section plot indicating the energy of each foil for mass separation relevant ^{47}Sc and ^{48}Sc radionuclides are shown in Figure 4.12. ^{nat}V(p,x)^{48}Sc cross section measurement is also important, because both ^{48}V

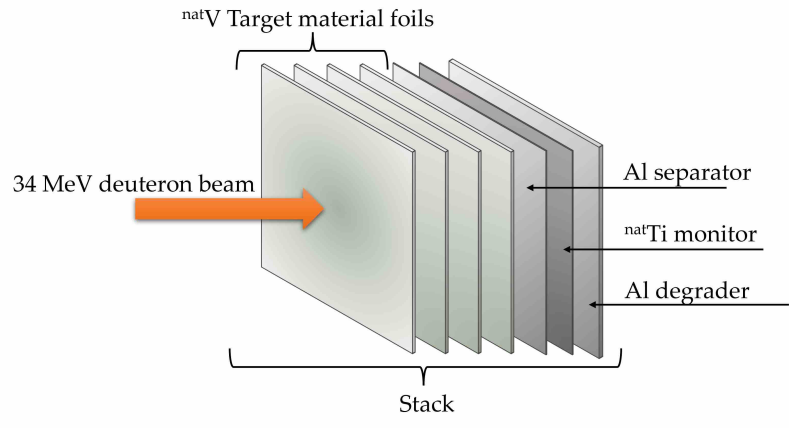

Figure 4.11: Schematic of a ^{nat}V, Al and ^{nat}Ti foil stack for cross section measurements

($t_{1/2}$ = 15.9735 d) and ^{48}Sc ($t_{1/2}$ = 43.67 h) are produced in the targets and have the same decay γ-ray lines (E_γ = 983.517 keV and E_γ = 1312.096 keV). The determination of the cross sections for these radionuclides can be done by repeated measurements after ^{48}Sc decay and also taking into account the E_γ = 1037.599 keV energy line in the activity determination (see Appendix A, Figure A.1).

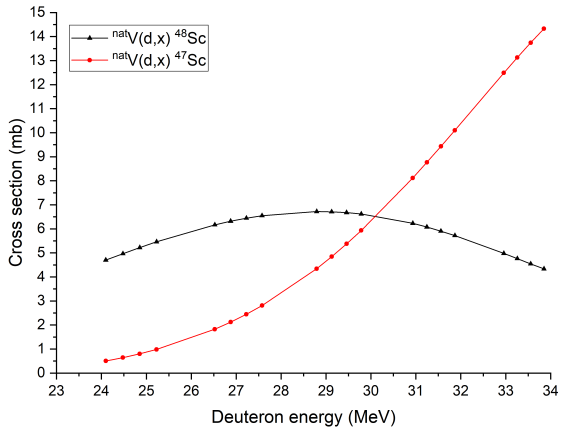

Figure 4.12: Estimated cross sections for ^{47}Sc and ^{48}Sc from ^{nat}V irradiation and deuterons.

A fraction of the irradiated foils would then be shipped to CERN-MEDICIS and placed within a dedicated TISS for mass separation and collection. The TISS differ in their specifications and can be accordingly produced and modified to account for the various samples and maximize the collection efficiency.

4.3 Target and ion source system developments

The Target and Ion Source System (TISS) are produced and assembled according to the RIB of interest for the particular collection or experiment. Although a lot of the TISS configurations have become "standard" over the years of operations, target and ion source system development is an irrevocable parallel process in improving the output of the mass separation and delivering more exotic and shorter-lived isotope RIBs [11]. For

[1] The temperature of the transfer line is typically assumed to be the same as for the VADIS cathode temperature because they are heated with the same heating connection.

Sc ion beam developments, the TISS with Versatile Arc Discharge Ion Source (VADIS) was used. The VADIS is a development of the previous MK-5 Forced Electron Beam Induced Arc Discharge (FEBIAD) type ion source. The VD-5 TISS is a model where the VADIS ion source is connected to the target container with a hot Ta transfer line. The temperature of the transfer line is similar[1] to the ion source, which is typically operated at ∼2000 °C (see Figure 4.13). The VD-5 TISS is suitable for non-volatile (refractory) species extraction. Nevertheless, the less suitable TISS with a surface ion source and transfer line at ∼2000 °C were used for Resonant Ionization Laser Ion Source (RILIS) studies. All the TISS configurations used for various Sc mass separation experiments and collections are summarized in Table 4.7. To improve the conditions for extraction, mass separation, molecular beam formation, and temperature profile of the target container and to reduce Sc adsorption on the TISS structures, multiple parts of the VADIS VD5 TISS were modified, and tested which are indicated in Figure 4.14.

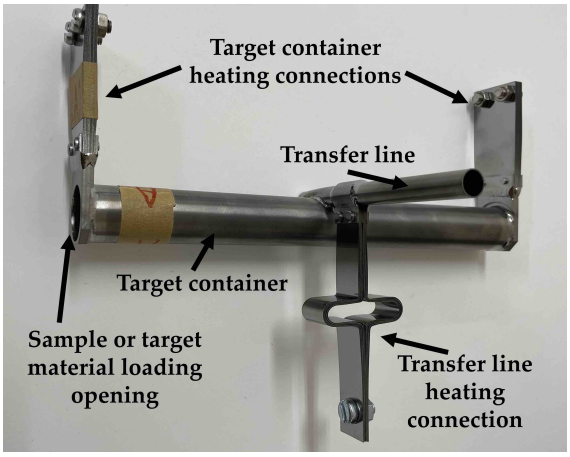

Figure 4.13: Standard Ta container and transfer line.

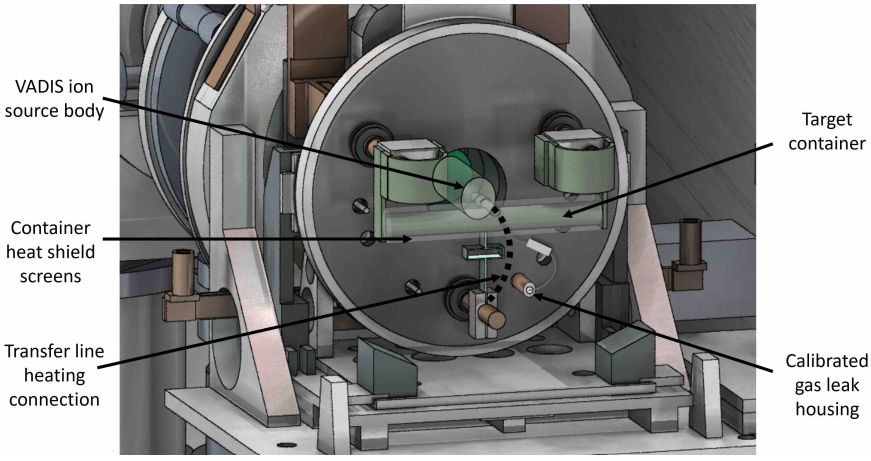

Figure 4.14: VD-5 TISS schematic on a mass separator frontend without the Al confinement vessel.

Table 4.7: Target and ion source system configurations for Sc mass separation and collection studies.

TISS Nr.	Ion source	Configuration / modification	Target load
685M	Re surface	Standard Ta target container.	$^{45}Sc_2O_3$ sample.
686M	W surface	Standard Ta target container.	$^{45}Sc_2O_3$ sample.
689M	Re surface	Standard Ta target container.	Irradiated ^{nat}Ti and ^{nat}V rolls.
702M	VADIS	Standard Ta target container.	^{nat}TiC target load.
723M	VADIS	Standard Ta target container.	^{nat}Ti foil target load.
731M	VADIS	No target container. Small Ta oven for sample heating connected to gas injection line and directly into the ion source.	$^{45}Sc_2O_3$ and $^{45}ScF_3$ samples.
741M	VADIS	VD-5 Ta target container. Gas leak cooling structure with a thermocouple.	^{nat}Ti foil target load.
766M	VADIS	VD-5 - Ta target container. Gas leak cooling structure.	^{nat}V foil target load.
790M	VADIS	VD-5 with V foil lining inside target container and W lining for VADIS cathode and transfer line.	^{nat}V foil target load.
801M	VADIS	VD-5 with an increased gap between cathode and anode grid (1.7 mm).	$^{43}ScCl_3/^{44g/m}ScCl_3$ sample externally irradiated at PSI, Switzerland [33]
805M	VADIS	VD-5 with Ta target container that has the transfer line heating connection from the backside. Prototype gradient heat screen assembly.	^{nat}V foil target load.

4.3.1 TISS calibrated gas leak cooling

Efficient VADIS operation as well as molecule formation within the TISS depend on sustaining the necessary reactive species (in this case - gas) supply to the target container. The calibrated gas leaks were identified as a weak point for the TISS when NF_3 reactive gas was used. The leak rate value of the calibrated gas leaks decreased to levels where almost no molecular ion beam production was possible anymore. Typically the leak rate decreases by up to $\times 5$ orders of magnitude. Any change in the leak rate value for the TISS is not acceptable.

It was discovered in multiple experiments, that the calibrated gas leak indirectly heats up and promotes reactions with the NF_3 gas. Due to NF_3 reactivity, the TaF_5 can form already in the gas supply line and condense on the electrical BN insulator and calibrated gas leak pores, causing leak rate decrease (see Appendix B). To reduce the temperature of the calibrated gas leak, a copper (Cu) cooling structure was developed, which had

strong direct contact with the calibrated gas leak, BN insulator and the actively cooled Al base plate (see Figure 4.15). Because of the perpendicular connection for both Ta tubes in the BN insulator, it could also perform as a cold trap to condense a fraction of the migrating particles and prevent them from condensing in the calibrated gas leak pores. During collections the BN insulator temperature still reached 110 °C, with the cooling structure in place and target container temperature at 1600 °C.

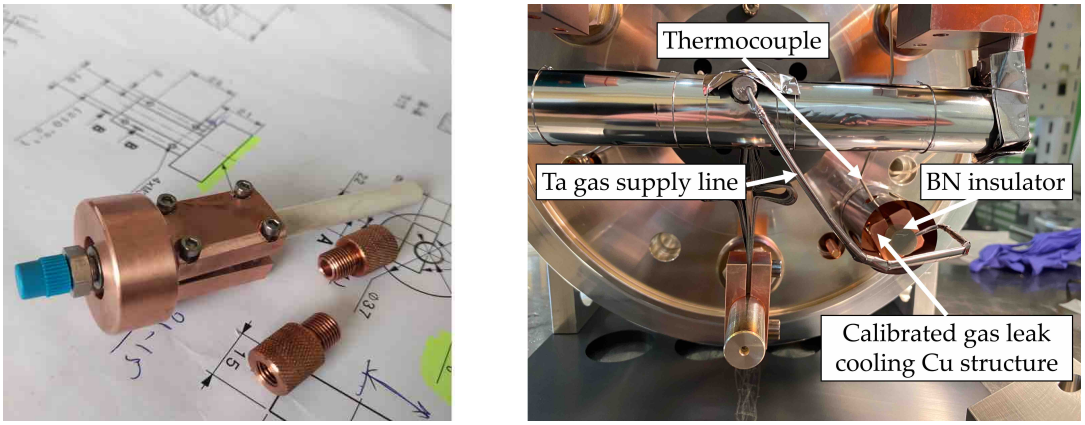

(a) Cooling structure components.

(b) TISS #741M with installed cooling structure.

Figure 4.15: Calibrated gas leak cooling structure for TISS.

Compared to a similar TISS, the additional cooling structure provided slightly reduced the Ta^{2+}, TaO^{2+}, TaF^{2+}, $TaOF^{2+}$ and TaF_2^{2+} doubly-charged beam intensities. This decrease could also be attributed to different ion source efficiency as well as slightly colder gas supply lines and is not entirely relevant as these beams do not interfere with ScF_{0-3}^{+} collections. As per its main purpose, the cooling modification eventually did not prevent the calibrate gas leaks from clogging when NF_3 gas was used and the target container was at ∼1500 °C. It caused the total beam current to drop from 2.31 to 0.34 μA.

In one instance, the "clogged" calibrated gas leak was re-opened by applying 1.4 bar and pumping out a mix of noble gasses in multiple cycles. Otherwise, the calibrated gas leaks must be mechanically exchanged, as it was successfully demonstrated during stable isotope beam test units and irradiated #723M TISS that had decay for ∼1 year. Due to these difficulties, CF_4 was used as the reactive gas in future studies.

In opposite to NF_3, during the use of the Cl_2 gas, degradation of the gas leak and an increase by ∼2 orders of magnitude in the leak rate was observed on ^{nat}V foil target material TISS (#790M). The TISS was not equipped with a gas leak cooling system. This increase can be explained by Cl_2 reaction with the Fe in stainless steel powder and possible moist air impurities from the gas injection process, leading up to the corrosion of the calibrated gas leak. Due to the possibility of controlling the pressure up to the TISS, an increase in leak rate could be countered by applying less gas pressure, however, the partial gas pressure in the target container cannot be estimated and may exceed the desired value.

4.3.2 Impact of Ta surfaces in TISS

Once the Sc radionuclides have diffused to the surface of the target material, they can get vaporized and released from the target material, followed by effusion to the ion source. Sc has a high adsorption enthalpy on poly-crystalline Ta surface (ΔH_{ads} = -521 kJ/mol [163]), of which the target container, transfer line and VADIS ion source cathode is made of. The adsorption on the target container and ion source surfaces can delay the release of radionuclides from the target to the ion source from ms to days, or in some cases to never reach the ion source. The effusion time from the target container can be approximated through delay time estimation according to equation 4.2 [196]:

$$\tau_\nu = \frac{1}{\nu} = n_{wc}(\tau_f + \tau_a) \tag{4.2}$$

where τ_ν is the effusion mean delay time [s], ν is the effusion time constant [s^{-1}], n_{wc} the number of wall collisions [dim], τ_f is the mean time of flight between two wall collisions [s] and τ_a is the mean adsorption sojourn time for a wall collision [s], which depends on the adsorption enthalpy and can be calculated with Frenkel's Equation 4.3 [197]:

$$\tau_a = \tau_0 e^{\frac{-\Delta H_{ads}}{RT}} \tag{4.3}$$

where τ_0 is the period of oscillation perpendicular to the surface [s], R is the universal gas constant 8.314 [J mol^{-1} K], T_s is the surface temperature [K], ΔH_{ads} is the partial molar adsorption enthalpy which depends on the element-surface combination [kJ/mol].

The number of wall collisions is approximated by the ratio of the inner target container surface to the size of the ion source orifice. The orifice cross section for the transfer line is 50 mm^2 and the ion source exit only 7 mm^2, compared to the surfaces of the target container (1.3 $\times 10^4$ mm^2 for the target container and 1.4 $\times 10^6$ mm^2 for a ^{nat}Ti foil target load). Therefore the number of collisions is on average around 1 $\times 10^5$–1 $\times 10^6$ for a 20 μm foil filled target container [11, 198]. As the majority of the surfaces that a Sc atom encounters are the target material foils a conservative assumption of 1 $\times 10^5$ collisions of atomic Sc with the Ta surfaces in the target container and transfer line can be made. The time for Sc release from the TISS then computes to be ∼24 hours, with the Ta surface at 1550 °C. If W was the main surface material (ΔH_{ads} (Sc on W) = -507 kJ/mol [163]) the mean effusion time would drop to ∼11 hours. It should be noted that only the TISS structure (adsorbent) material influence is compared and for this estimate comparison, re-adsorption and re-diffusion in Ti and V target materials has not been taken into account.

To reduce Sc interactions with Ta surfaces and the release delay, the lining of the transfer line and coverage of the ion source cathode with 25 μm thick W foil for TISS #790M was done as shown in Figure 4.16a. The target container was lined with 25 μm thick ^{nat}V foil (see Figure 4.16b), the same as the target material itself. Tungsten was used for the cathode and transfer line due to their operating temperatures of ∼2000 °C.

The reduced exposure to Ta surfaces, in comparison to a standard Ta target container and transfer line, however, did not noticeably influence the release of Sc from the

(a) VADIS cathode covered with W.

(b) ^{nat}V lining in the target container.

Figure 4.16: Target container and VADIS cathode lining with metallic foils.

TISS. Same as for a standard target container and transfer line, the onset of Sc release was observed when the target container reached ∼1550 °C. The low collection rates < 1 kBq/min and therefore the intensities of $^{47}ScF_2^+$ molecular ion beams were comparable to a regular VD-5 TISS with ^{nat}V target material (#766M) and any differences could be explained by the different target material mass, irradiation times and ion source efficiencies. The observed results suggest that atomic Sc migration within the TISS is not the limiting extraction and collection efficiency cause.

4.3.3 Temperature profile of the target container

Much effort and studies have been done to homogenize the temperature profile in the target container and transfer line/ion source of TISS for ISOL experiments. Temperature homogeneity is necessary to reduce cold spots and potential loss of short-lived isotopes and preserve the target material during mass separation [104].

At offline mass separation facilities the radionuclides are produced before the TISS is placed at the desired temperatures. Subsequently, by first heating the ion source to operational temperatures, the radionuclides of interest from the part, where the transfer line is connected to the target container can already diffuse and effuse to the colder parts of the target container or get pumped out through the ion source orifice before RIB is created. Typically the extremities of the target container are 100–150 °C colder than the middle section, during active target container heating. Therefore the less gaseous volatile particles can condense and get "trapped" in the colder parts of the target container. If the collection temperature is already close to the melting point of the target material in the middle section, further heating is not possible and extraction of such condensed radionuclides from these colder parts is limited. This can be the limiting factor for target materials with lower melting temperatures than the transfer line/ion source operational temperatures, such as ^{nat}Ti and ^{nat}V metallic foils. For this reason, an uneven temperature profile with slightly hotter target container ends could be of interest to force migrating species towards the central part of the target container.

The transfer line itself has a temperature gradient and is not homogeneous throughout its full length. Therefore a new target container type, as shown in Figure 4.17a, with transfer line heating from the backside of the target container was tested. The back-of-line heating offers a more homogeneous transfer line temperature profile and helps to reduce adsorption [104].

Due to the necessity of achieving high temperatures, the target container as well as

the transfer line are shielded with multiple layers of metallic foil heat screens. They help to achieve higher temperatures and a more homogeneous temperature profile by minimizing heat loss. Typically the heat screens of Ta, Mo and W are assembled in full length of the target container and separated/secured with a Ta wire ($\varnothing = 1$ mm) at four points as indicated in Figure 4.18a).

(a) Back-of-line heating target container and transfer line heating connection.

(b) Chimney-type target container

Figure 4.17: Non-standard target containers used for the heat screen investigations.

In the prototype heat screen assembly, the electric contact with the resistively heated target container and heat screens is reduced because of fewer contact points at the end parts of target container. This is assumed to force the current to flow more through the container body itself and is being investigated (see Figure 4.18). Previous investigations indicated that the temperature difference between the end and the middle sections of a chimney-type target container body 4.17b changed from -100 to +50 °C in the temperatures range of 1600–1750 °C. The new heat screen assembly was combined with the back-of-line heated target container as indicated in Figure 4.18b.

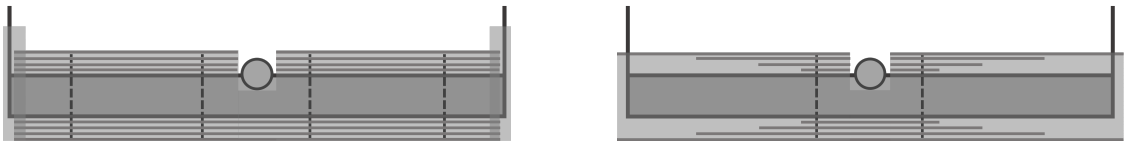

(a) Standard heat screen assembly.

(b) Prototype heat screen assembly.

Figure 4.18: Schematic representation of the heat screen assembly on target containers.

The prototype heat screen assembly combined with the back-of-line heating target container was expected to reduce the temperature difference between the end and middle parts of the target container as well as to improve the transfer line temperature homogeneity. The combination of the changes compared to a regular VD-5 TISS, however, did not meet the expected temperature gradient. By heating the transfer line to 1900–2000 °C (for efficient ionization), the middle section of the target container remained hotter than the ends. Because of such transfer line heating, the section where the transfer line attaches to the target container was close to the target material melting point (in this case T_m=1910 °C for ^{nat}V) without applying current (heating) the target container. To lower the temperature of the central part of the target container, a part of the heat screens were locally removed (see Figure 4.19). All of these modifications resulted in an uneven temperature profile with 2 gradients (see Figure 4.19). The largest temperature difference in the target container reached up to 363 °C at target heating current of 250 A.

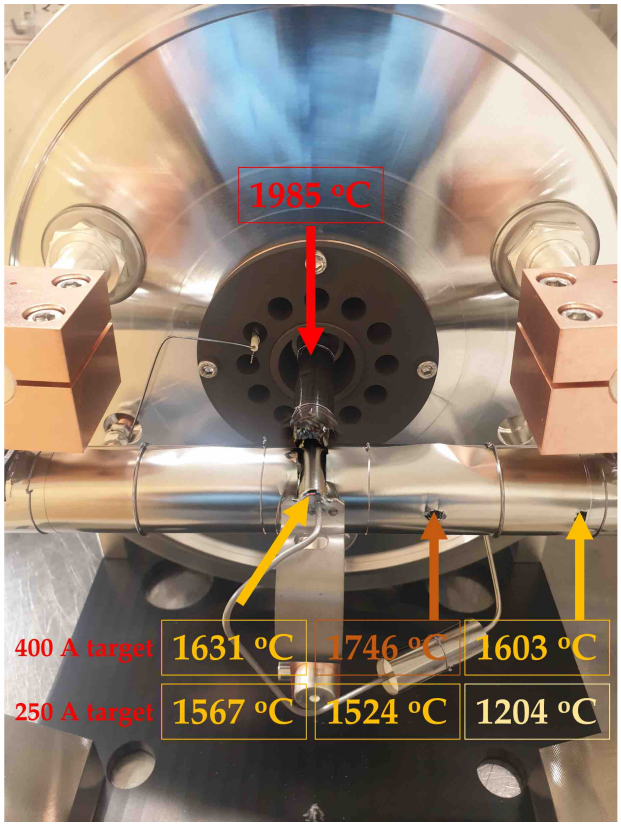

Figure 4.19: Transfer line heat screen final assembly on #805M TISS target container.

The transfer line attachment for the back-of-line heating target container requires the heat screen layers to be cut differently than for the tested chimney-type container, resulting in a lower cross section of the screen sheet underneath the transfer line and possibly and additional local heating.

Alternatively, deep container plugs could be inserted in the target container from both opening sides up to the target material, by removing the lower temperature sections. However, this approach reduces also the inner target container volume and therefore target material amount. A different approach to increase the relative target container temperature at the ends could be a heat screen assembly, where the heat screens in the middle section of the target container are completely removed, allowing for intentional local heat losses and thus a temperature gradient. These alternative methods were not yet tested.

4.3.4 TISS modes of failure and recovery

The TISS are irradiated and typically operated at ∼2000 °C temperatures in a highly radioactive environment. In addition, the reactive gases are applied. Such a combination together with complex TISS designs can become fragile and sensitive to the impact of any sudden temperature and pressure changes, chemical reactions, or the target aging due to radiation and material re-crystallization. Subsequently, multiple modes of failure were observed for the various TISS and VADIS ion sources, which are described in detail in Appendix B. Considering the hazards of radiation and contamination, very

limited possibilities of the TISS repairs were possible, however, in some cases recovery of a functional TISS was achievable. A summary of TISS modes of failure and their brief history is given in Table 4.8.

Table 4.8: Target and ion source units used for Sc mass separation and collections.

TISS Nr.	**Ion source**	**Modes of failure and history**
685M	Re surface	Interlock caused loss of power supplies for heating and damaged the ion source.
686M	W surface	Operational.
702M	VADIS	Too high concentration of particles coated ion source insulators and caused a short circuit, which was multiple times recovered. Eventually, a mass separator interlock caused a loss of power supplies for heating, rupturing the ion source cathode.
723M	VADIS	During stable beam tests, exchanged coated anode insulators. Cathode-anode contact, which resulted in an exchange of ion source and target container. During Sc radionuclide collections, the coating on ion source insulators caused a short circuit, which was multiple times recovered. Clogged calibrated gas leak - exchanged after 1 year of decay. Operational.
731M	VADIS	Used only in stable isotope beam experiments. The coating on the ion source insulators caused a short circuit. The coated insulators were multiple times exchanged. Eventually, the ion source failed due to cathode-anode contact.
741M	VADIS	The coating on ion source insulators caused a short circuit, which was multiple times recovered. Clogged calibrated gas leak, which was recovered with noble gas over-pressure cycles. Operational.
766M	VADIS	Coating on ion source insulators and short circuit, which was multiple times recovered. Eventually, a mass separator interlock caused a loss of power supplies for heating, rupturing the ion source cathode.
790M	VADIS	The coating on ion source insulators caused a short circuit, which was multiple times recovered. Corroded and increased leak rate of the calibrated gas leak from Cl_2 gas injection. Eventually, the ion source failed due to cathode-anode contact.
801M	VADIS	Cathode-anode contact, fixed by pulling back the container by 1 mm. Decrease of ionization efficiency. Operational.
805M	VADIS	The coating on ion source insulators caused a short circuit, which was multiple times recovered. Operational.

The most frequently encountered modes of TISS failure and their corresponding repair/recovery methods were:

- Changes in leak rate of the calibrated gas leaks. For irradiated TISS immediate repair is impossible due to the risk of contamination and the high dose rate. If the reduction of leak rate was accompanied by particle condensation, an over-pressure of gas could recover the functionality of the TISS as described in section 4.3.1.

- The VADIS cathode-anode distance is typically 1.5 mm and due to thermal expansion, a connection could form, preventing to creation of a potential difference for the electron acceleration. In this case, the distance between cathode and anode has to be increased, which was achieved by pulling back the target container and fixing in a reduced position. For irradiated TISS, the container cannot be pulled because of radiation and contamination hazard reasons. During collection, the recovery can be achieved by reducing the transfer line temperature. The increase of cathode-anode distance and operation of the ion source in a lower temperature regime reduces the ionization efficiency. In instances where the cathode ruptures creating the contact with anode, no recovery was possible.
- The most frequently observed VADIS failure mode was the anode body insulator (BeO) coating with conducting particles due to the formation of a high amount of volatile metallic molecules and their subsequent condensation. The reactive gas can also react with the insulators directly, forming carbides or nitrides from CF_4 and NF_3 respectively. The insulators can be replaced only for non-irradiated TISS. During radionuclide collections from irradiated TISS, recovery is possible by evaporating the contamination and is explained in Appendix B, section B.2. TISS with this mode of ion source failure could be recovered almost every time it occurred.

4.4 Target material and TISS impact on Sc mass separation

The proposed target materials for Sc radionuclide production as well as TISS and their modifications were tested on Offline-1 and CERN-MEDICIS mass separators, for TISS functionality, stable isotope ion beams, irradiated material Sc radionuclide release, and mass separation.

Radioactive Sc ion beams were only observed above the target container temperature of 1500 °C. This exposed the first main limitation of ^{nat}Ti foil used as a target material for Sc collection, which is its relatively low melting/sublimation point (1668 °C). Therefore, ^{nat}V metal or carbon stabilized ^{nat}TiC with higher melting points would be more suitable for mass separation. ^{nat}TiC powder has a high specific surface area compared to the metallic foil target materials. ^{nat}Ti or ^{nat}V powders could also be used, however, sintering effects should be addressed to reuse the TISS for multiple batches and sustain the release over long-term operations.

Another observed limitation of all the tested target materials for mass separation is the chemical impurities in the target materials and their reactivity with the reactive gas, especially for ^{nat}V and ^{nat}TiC. Even a few hundred ppm amounts of impurities in the target material can cause delays in Sc radionuclide collection for days or prevent completely due to unsatisfactory ion beam purity or competing chemical reactions. The main impurity in ^{nat}V foils was Al, which reacted with fluorine and formed volatile μA range AlF_x^+ (x=1–3) ion beams, suppressing the Sc fluoride molecule formation. The ^{nat}TiC on the other hand was releasing a few hundred nA-range Cr^+ ion beam at temperatures above 1800 °C, which was delaying further heating and increase of Sc collection rate. In contrast to Al in V, the Cr beam intensity reduced over time.

Mass scan spectra of ^{nat}Ti, ^{nat}V foils and ^{nat}TiC fluorinated with CF_4 gas at various tem-

peratures and indicated main chemical species in total beam up to amu 120 are shown in Figure 4.20, Figure 4.21 and Figure 4.22. Occasionally mass scans up to 260 amu (at Offline-1) and 230 amu (at MEDICIS) were also done to monitor tantalum, tantalum oxide, tantalum fluoride, and tantalum oxyfluoride ion beams, which also act as a probe for successful fluorination of the target container. The beam intensities between the mass scans have a noticeable difference and are not comparable due to each being taken with a different TISS, different target container temperatures, ion source parameters, ionization efficiencies, and amount of applied CF_4 gas. Nevertheless, they give an understanding of the main chemical species present in the total beam. Total beam composition for ^{nat}Ti is similar to ^{nat}TiC due to Ti, TiO_2, and stable TiC reactivity towards the halogenating gases at high temperatures. More intense titanium oxyfluoride beams are present for ^{nat}Ti foil target material due to the native oxide layer on the metallic foil. For ^{nat}V target material, the background of Sc molecular ion beam mass region is significantly lower than ^{nat}Ti or ^{nat}TiC as no vanadium fluoride or oxyfluoride side bands are overlapping the ScF_2^+ amu region. This suggests ^{nat}V as a more suitable target material for reduced isobaric background Sc molecular beam collection. This aspect also poses a potential for high melting point VC and VB investigation as target materials for Sc collections. Nevertheless, Ti or V isobars from the collected Sc can be removed with conventional chemical separation methods.

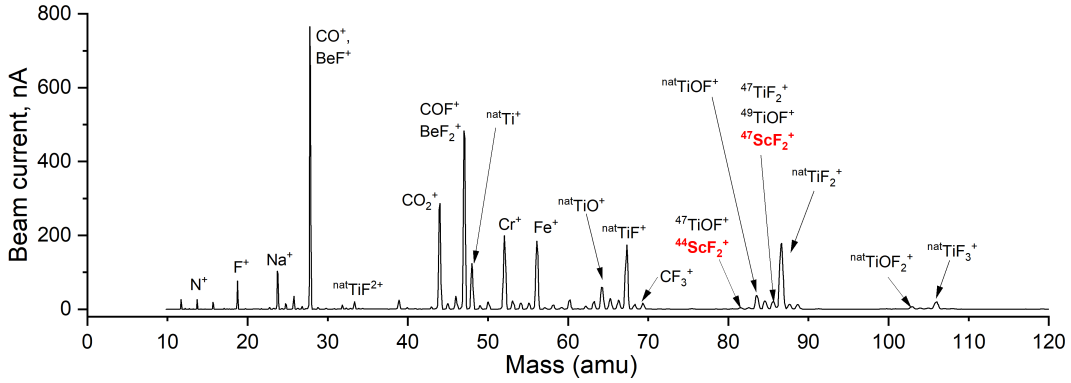

Figure 4.20: Mass scan spectra of irradiated and fluorinated ^{nat}Ti foil target material with ion source at 2060 °C and target container at 1630 °C.

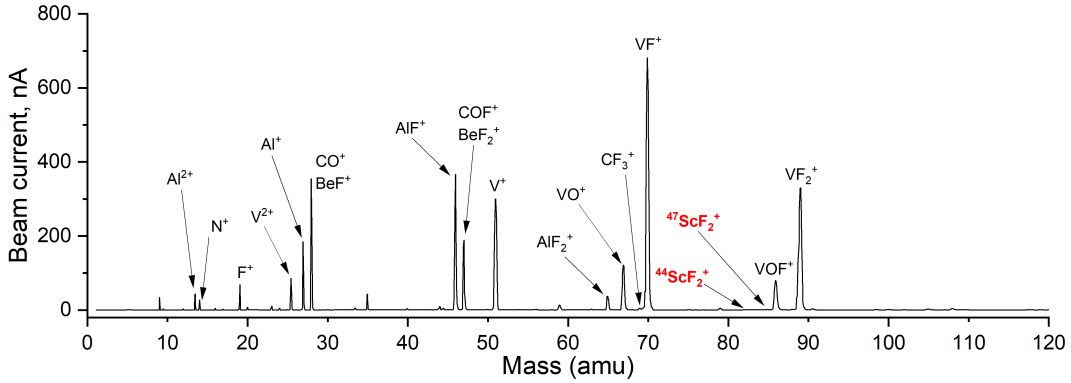

Figure 4.21: Mass scan spectra of irradiated and fluorinated ^{nat}V target material with ion source at 2000 °C and target container at 1725 °C.

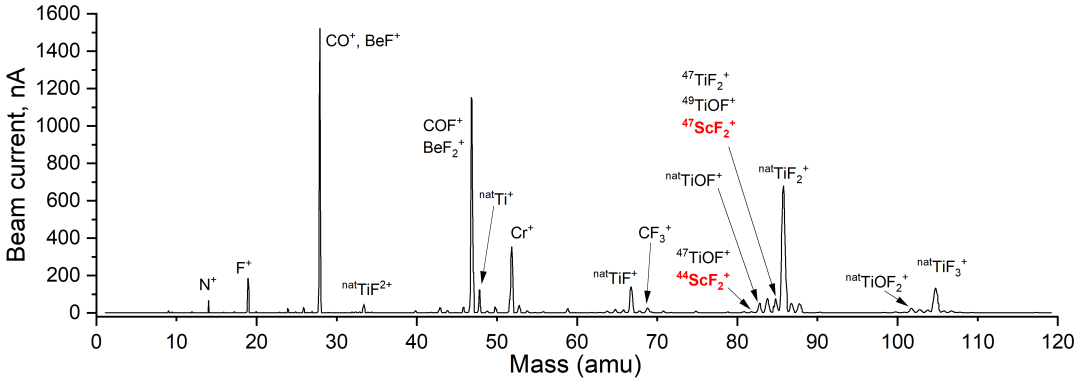

Figure 4.22: Mass scan spectra of irradiated and fluorinated ^{nat}TiC target material with ion source at 2000 °C and target container at 2000 °C.

4.5 Conclusions and outlook

Before the start-up of the CERN-MEDICIS facility, the extraction efficiency for Sc and other radionuclides from the available ISOLDE yield database were estimated to 5 % [185, 199], however, no Sc radionuclides were mass separated collected since the year 2017 [72].

Mass separation facilities, such as CERN-MEDICIS have the potential to deliver high molar activities (TBq/μmol) of medical ^{43}Sc, $^{44g/m}$Sc and ^{47}Sc radionuclides on a clinically relevant level. Suitable Sc radionuclide activities for clinical doses (few hundred MBq for ^{43}Sc, $^{44g/m}$Sc and few GBq of ^{47}Sc) by mass separation should become possible. However further TISS developments are needed to design the most appropriate conditions for maximized extraction and ionization during the collections. The VADIS ion source can safely be operated up to 15 μA beam current with a capacity of around 50 μA, however, too rapid molecule formation can cause the failure of the TISS during collections and suppression of Sc molecular ion beams.

The advantage of medical Sc radionuclide production in ISOL target with the mass separation step is the absence of long-lived, high γ-ray energy (>1 MeV) ^{46}Sc and ^{48}Sc contaminants in the final product. The developments in this study resulted in the first mass separation and collection of isotopically pure $^{44g/m}$Sc, ^{46}Sc and ^{47}Sc radionuclides with collected activity ranging from few kBq up to ~10 MBq. The Sc molecular ion beam extraction and collection efficiencies exceeded 1 % under controlled operation conditions from a micrometric particle size ^{nat}TiC target material [38].

Investigation of Sc molecular beam formation from various target materials and TISS and identification of the limiting aspects in Sc mass separation and collection experiments will help to improve the collection efficiencies and collected activities in future.

5 Sc separation and collection

Contents

In this chapter, the Sc collection efficiency and collection rate of Sc radionuclides are analyzed to determine the collection efficiency limiting parameters from the experimentally obtained data. The formation dynamics of molecular ion beams and release from TISS is explained for a "batch mode" mass separation and collection of scandium fluoride. An externally irradiated sample mass separation and collection was performed and analyzed. Experiments and first results from a two-step resonant atomic Sc laser ionization, delivered by MEDICIS Laser Ion Source for Separator Assembly (MELISSA), are described. Radiochemical and electrochemical separation of the mass-separated and collected radionuclides to obtain precursor for radiolabelling were performed and results are discussed.

5.1 Collection efficiency

5.1.1 Stable isotope molecular ion beam collection efficiency

Collection efficiency measurements for mass separation of stable isotope samples (mass markers) are done by placing a known amount of the sample in the TISS target container and compared with what is obtained after proceeding to the mass separation and collection of the isotope/mass of interest. The efficiency is obtained by measuring the mass-separated ion beam current until the sample is completely released from the Target and Ion Source System (TISS). The efficiency is calculated through equation 5.1 [200].

$$\epsilon_{Stable} = \frac{\int I_{Separated} dt}{n_{sample} \cdot F} \tag{5.1}$$

where ϵ_{Stable} is the stable mass-separated sample collection efficiency, $I_{\text{Separated}}$ is the mass-separated ion beam current [A], n_{sample} is the amount of the stable isotope sample [mol], and $F = 96485$ is the Faraday constant [C mol^{-1}].

Typically the experiment is done to estimate the ion source efficiency, assuming that no chemical interactions between the sample and the TISS structures take place. This assumption would be most appropriate for a VADIS ion source and noble gas ionization efficiency measurements. Nevertheless, adsorption of the heavier gases, such as Kr and Xe has been observed even at elevated temperatures (1000–1600 °C) [201].

For ScF_3 molecular ion beam collection efficiency measurement, a known amount of $^{45}Sc_2O_3$ sample in 5 \$ HNO_3 was dried on a Ta foil and placed inside an empty VD-5 TISS (#723M). The formation of $^{45}ScF_x$ (x = 1–3)was achieved by fluorinating the sample with NF_3 gas. The Offline-1 mass separator was set and optimized to amu 83 for the ion beam current measurements (see Figure 5.1).

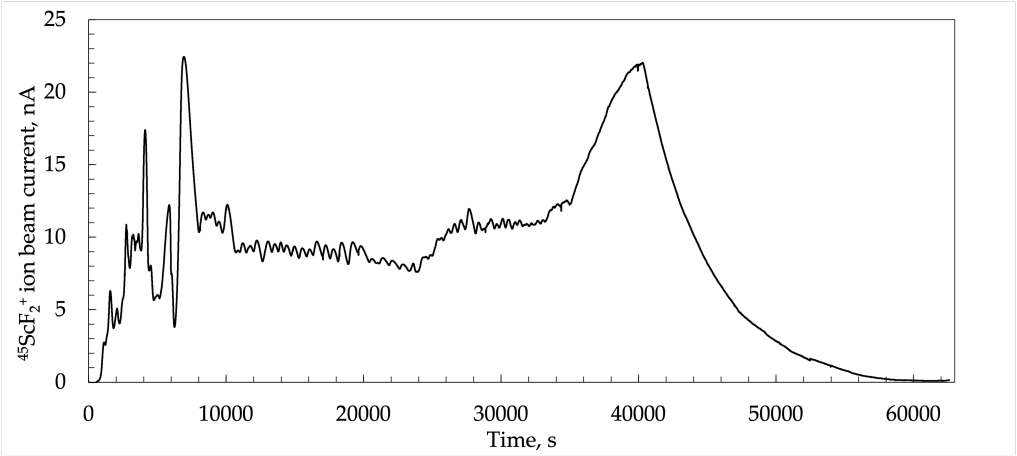

Figure 5.1: Measured $^{45}ScF_2^+$ ion beam current during the collection efficiency measurement.

The obtained efficiency of $^{45}ScF_2^+$ was 4.90 $\pm$0.07 % and is in agreement with the benchmarked value of $\sim$5 % for Sc and VADIS ion source TISS and the efficiency obtained for an analogue $^{48}TiF_3^+$ (ϵ_{col} = 4.8 % [202]) [62, 185]. In the mass marker (stable isotope)

collection efficiency measurement the uncertainty is mainly governed by the error of the pipette used for the sample preparation [62].

It must be noted, that the particular TISS was used for multiple stable beam tests with a $^{45}Sc_2O_3$ sample beforehand, possibly overestimating the efficiency if the previous sample was not fully released before the test. To counteract this issue, outgassing was performed before the sample placement inside the unit and measurements of the background at various temperatures were taken and later subtracted from the obtained integrated separated ion beam current. On the other hand, the calibrated gas leak clogged 40 000 seconds after the beginning of the experiment, preventing the fluorination of the initial sample and underestimating the efficiency. This can be seen in Figure 5.1 when a sudden exponential drop is observed. The calibrated gas leak issue was later confirmed by removing the leak for repeated leak rate calibration. Another important note is that no target material for Sc production was present during this measurement, which could compete with ScF_3 formation. Nevertheless, this measurement still gives a good "order of magnitude" estimation.

5.1.2 Mass-separated radionuclide collection efficiency

One of the key performance indicators for a medical radionuclide mass separation facility is the collection efficiency [74]. Here the main difference from a stable isotope collection efficiency is, that it shows the amount of mass-separated radionuclide activity at the End Of Collection (EOC) against the starting amount. Typically no decay correction for the collected radionuclides is done, due to the various collection times needed for the mass separation and collection and the most relevant value being the total collected radioactivity at the EOC. For the obtained Sc radionuclide collection efficiency comparison the activities are decay corrected to the Start Of Collection (SOC). The efficiency can be estimated from equation 5.2. Starting radionuclide inventory for irradiated target materials are estimated by FLUKA and ActiWiz or measured by γ-ray spectrometer for external samples.

$$\epsilon_{col} = \sum \frac{\sum A_{Collected}}{A_{Start} \cdot e^{-\frac{ln2 \cdot t_{\Delta}}{t_{1/2}}}} \tag{5.2}$$

where ϵ_{col} is the collection efficiency for the radionuclide of interest, $A_{Collected}$ is the radionuclide activity at the EOC [Bq], $t_{1/2}$ is the radionuclide half-life [s], t_{Δ} is the time between the SOC and collected sample activity measurement [s], and A_{Start} is the radionuclide activity at SOC [Bq].

The obtained collection efficiencies for the Sc radionuclides from the prepared target materials are summarized in Table 5.1 and for Sc radionuclide generators in Table 5.2. The given uncertainty is estimated from FLUKA simulation statistical error of the corresponding radionuclide starting activity combined with γ-ray spectrometry measurement uncertainty.

If Sc radionuclides were implanted in multiple collection foils, they were summed for the estimation. Importantly, the obtained efficiencies in most cases are not the maximum achievable due to prematurely stopped collections due to TISS failures (see Chapter 4, Table 4.8) or available collection time for the batch. Another key aspect is the

Table 5.1: Collection efficiencies of Sc radionuclides from various target materials and TISS.

TISS	Target material	Date	Radionuclides collected	Total Sc collection efficiency, %
#723M	^{nat}Ti foils	17–23.08.2021 02–06.12.2021	^{44m}Sc,^{47}Sc ^{46}Sc	2.49(9) $\times 10^{-4}$
#741M	^{nat}Ti foils	08–10.11.2021 25.11–01.12.2021	^{44m}Sc,^{47}Sc ^{46}Sc	4.8(5) $\times 10^{-3}$
#766M	^{nat}V foils	01–09.09.2022	^{46}Sc,^{47}Sc	9(2) $\times 10^{-3}$
#790M	^{nat}V foils	28.11–07.12.2022	^{47}Sc	4.8(3) $\times 10^{-2}$
#801M	^{43}Sc/$^{44m/g}$ScCl$_3$ [a]	19–21.07.2023	^{43}Sc,^{44m}Sc	0
#805M	^{nat}V foils	08–15.08.2023 23–28.08.2023 04–09.10.2023	^{44m}Sc,^{47}Sc ^{47}Sc ^{44m}Sc,^{47}Sc	2.5(3) $\times 10^{-2}$ 3.1(5) $\times 10^{-1}$ [b] 3.82(7) $\times 10^{-1}$
#702M	^{nat}TiC powder	25.07–01.08.2023 27.09–04.10.2023 26.10–02.11.2023 16–24.04.2024	^{44m}Sc,^{47}Sc ^{44m}Sc,^{47}Sc ^{46}Sc ^{47}Sc	9.9(3) $\times 10^{-3}$ 4.86(17) $\times 10^{-1}$ [c] 2.049(19)[d] 1.94(8)[e]

[a] External ^{44}CaO sample irradiated with a cyclotron at Paul Scherrer Institute (PSI)
[b] Assuming all ^{47}Sc was released in the previous collection on 08–15.08.2023. The lowest estimate, assuming no ^{47}Sc would compute to 0.11 % efficiency.
[c] No reactive gas was injected in the TISS since the. Fluorine was obtained from previous collection remains within the target material.
[d] Including also the collected radionuclides on the sample holder collimator and assuming no ^{46}Sc was released on the previous 27.09–04.10.2023 collection. Minimum value, as the experiment was intentionally stopped before all Sc was released.
[e] Including also the collected ^{47}Sc on sample holder collimator. Minimum value, as the experiment was stopped due to loss of power supplies and TISS failure before full Sc released was achieved.

Table 5.2: Collection efficiencies of Sc generator mother radionuclides from various target materials and TISS.

TISS	Target material	Date	Radionuclides collected	Collection efficiency, %
#723M	^{nat}Ti foils	17–23.08.2021 24.04–08.05.2023	^{44}Ti ^{47}Ca	0.062 $\pm$ 0.004 0.38 $\pm$ 0.05
#790M	^{nat}V foils	28.11–07.12.2022	^{47}Ca	0.048 $\pm$ 0.015
#805M	^{nat}V foils	08–15.08.2023	^{47}Ca	0.08 $\pm$ 0.05

operation conditions and ion source parameters during the collection which vary for each TISS, such as injected gas amount, ion source specifications and temperature, target material mass, density and impurities. Nevertheless, the obtained collection efficiencies indicate the importance of the achievable temperature for the target material during collection as well as differences between foil and powder target materials and the available mass separation temperature ranges.

Multiple attempts to test the mass separation feasibility of Sc generator mother ra-

dionuclides were made, by dedicating separate collections. The collection efficiencies are comparable to the direct Sc radionuclide collections, however, the collected activities range from 90 Bq (^{44}Ti) to 14 kBq (^{47}Ca). Since the production yields for the generator mother radionuclides are lower than the direct production of Sc radionuclides and the generator-produced isotopes can be efficiently separated by conventional radiochemical methods, mass separation does not provide a significant added value.

5.2 Collection rate

The collection rate [1] is the combined result of multiple mass separation parameters and directly influences the collected activity at the EOC. For example, the obtained collection efficiencies suggest that the obtainable ^{47}Sc activity from the #702M (^{nat}TiC) would have reached 70–80 MBq for a particular collection, however, the obtained activities due to the rate of implantation were in the range of 3–10 MBq per sample with only 2 samples. Parameters with the highest impact on the collection rate are:

- Radionuclide production - release rate is proportional to the starting activity;
- Irradiation-induced defects and heating of the target material due to proton impact and deposited energy. This target material aging impacts the radionuclide diffusion and release [203];
- Release rate from the target container which depends on the diffusion, effusion, target material type and thickness/grain size, target material sintering/aging, chemical interactions, molecule formation and evaporation from the surface, including re-adsorption (physisorption and chemisorption) [171, 172, 204, 205];
- Ionization efficiency of the species of interest [64, 79, 103];
- Mass separator mass resolving power, ion beam optical instrumentation and transmission efficiency [62];
- Interception of the ion beam in a solid substrate and collected radionuclide quantitative measurement.

Each of these parameters can be assessed and addressed separately, but require a large set of experiments for conclusive statistics. Because each TISS required for each separate experiment is hand-crafted, a variation is expected and obtaining the necessary data is complicated. Often the refractory elements such as Sc tend to adsorb within the TISS, which influences further experiment validity of the same TISS and a new TISS should be manufactured. Complex systematic studies of each separate target material are required to fully understand the chemical interactions, molecule formation mechanism and kinetics, effusion from the target container and ionization.

The first indications of limiting factors on the atomic or molecular Sc ion beam collection rates were indicated. Most notably two different limiting factors were observed involving the target material type. For the metallic foils, the limiting factors identified were the molecule formation kinetics and ionization efficiency. The release from foil target materials is rather fast (see Chapter 3), however, the molecule formation is then not efficient and a fraction of released isotopes can re-adsorb or get pumped away. The lower molecule formation efficiency could be explained by the lower cross section of

[1] The rate of radionuclides implanted in collection foil per time unit (Bq/s).

gas-gas phase collisions [123]. On the other hand, the limiting factor of the TiC powder target tends to be the Sc diffusion from the bulk material and the collection is slow and steady. In both cases, enough reactive gas must be supplied to the target material for the most effective Sc molecule formation.

5.2.1 Atomic Sc release from the TISS

The release time of radionuclides from a target material is a combination of diffusion time from the bulk material and its subsequent desorption, which is discussed in Chapter 3. To obtain the release time from the whole TISS, one needs to add also the effusion time. Effusion here is a diffusive flow of particles in a gas phase that describes their migration through the pores or open spaces in the target material, target container and transfer line into the ion source. Essentially, the evacuation of a volume of gas through an orifice.

The effusing particles undergo many collisions with the target material, target container and transfer line surfaces before reaching the ion source. Upon every collision, the particles are adsorbed for some time. For simple cases with only metal/metal interactions, the effusion time can be approximated by Frenkel's equation (equation 4.3). According to the Eichler-Miedema systematics, Sc first partial molar solution enthalpies $\Delta\bar{H}_s$ on Ti and V (see Table 5.3) suggest that Sc is partially soluble in Ti and in V and can replace the surface adsorbent atoms and eventually diffuse back into the bulk of the material. On the opposite, first solution enthalpy of Sc on a Ta surface shows that Sc is practically insoluble and would only adsorb on the surface [163]. For comparison the mean wall delay times for 1×10^5 collisions on various surfaces are estimated and shown in Table 5.3. The obtained values, however, should only be considered for an order of magnitude evaluation, because the adsorption enthalpies are either empirically calculated or sometimes measured with uncertainty of more than 10 %. The frequency factor τ_0 in the Frenkel's equation 4.3 of 10^{13} s^{-1} was used and the actual wall collisions depend on the surface area of target material, surface roughness, target material distribution and can vary in the order of 10^3 to 10^6 [11, 198, 200].

Table 5.3: Atomic Sc first partial solution and adsorption enthalpies, and mean delay time on various adsorbents and temperatures. Estimated for 10 000 particle-surface collisions.

Adsorbent	$\Delta\bar{H}_s$**, kJ/mol**	ΔH_{ads}**, kJ/mol**	$\tau_{1550\ ^oC}$**, min**	$\tau_{1850\ ^oC}$**, min**	$\tau_{2000\ ^oC}$**, min**
Ti[a]	31.0	-384.1	0	-	-
V[a]	65.6	-553.0	11626[b]	51	-
Ta	78.2	-521.0[c]	1408	11	2

[a] Values estimated from the Eichler-Miedema model [159, 163].
[b] If the ΔH_{ads} value of 383.4 kJ/mol 3 is assumed, the delay time computes to 0 min.
[c] Experimental value [163].

From looking at the approximation of mean delay time in a TISS, Sc metal seems to be refractory enough to hinder severely the collection rate. In an actual TISS, the situation is more complex and the chemisorption can take place on an oxide layers of the target material and also interact with vacuum and target material impurities. Replacing the adsorption enthalpy with sublimation enthalpy for ScF_3 (ΔH_{sub}=-367 kJ/mol [206]), a first approximation of the molecule delay time, estimates that the release of ScF_3 from

Ti, V and Ta surfaces is immediate. However, the adsorption is then also accompanied by different chemical interactions. In this case, the release is no longer the limiting factor for collection rate, but the molecule formation kinetics and ionization efficiency are.

Sc and ScF^+ release from TiC and VC target materials has been investigated previously at ISOLDE, indicating no enhanced release with CF_4 addition. It was concluded that the in-grain diffusion limits Sc release from carbide targets [77]. When Sc radionuclide release from the TISS is limited by diffusion, the release can be approximated from the solution of Fick's second-order partial differential equation 3.4, assuming that:

- the diffusing particle desorbs rapidly when on the surface, compared to the diffusion time;
- the diffusing particle does not diffuse back into the bulk material;
- the initial distribution of isotopes is homogeneous.

The rapid desorption could be achieved by volatile molecule formation. It was indeed observed, that besides the amount of reactive gas injected into the target, the collection rate was mostly affected by an increase in temperature and full release was never achieved for the ^{nat}TiC target material. It can then be concluded, that the increase in collection rate from a TiC target material can be achieved by:

- increasing the target container volume and material mass;
- decreasing the TiC particle size (nanoscale);
- increasing temperature and the diffusion coefficient D;
- preventing sintering to retain the porosity and particle size;
- applying a sufficient amount of chemical reactant (gas) to saturate and etch the surface, and form volatile Sc molecules.

Chemical form of evaporating Sc species

According to the effusion calculations in Table 5.3, the time for mono-atomic Sc to effuse to ion source is longer, than it was observed experimentally from a ^{nat}V foil target and laser resonant ionization. Experimentally, when the target container temperature reached 1500-1600 °C, the mono-atomic Sc from a stable isotope sample or Sc radionuclides from irradiated ^{nat}V foil target material were first observed within 15 minutes.

Although suggested otherwise by the mean delay time calculations, atomic Sc was released from the irradiated foils as discussed in Chapter 3. The metallic target material foils are typically covered by a few hundred nm layer of oxides, due to material exposure to air and oxidation. Traces of oxygen could also be found in ^{nat}TiC target material. High-intensity CO and less intense C, CO_2 have been observed within VADIS ion source TISS. The main source is deemed to be the ion source assembly itself, however, impurities in TISS structures and vacuum cannot be excluded. H_2, C and CO can reduce Sc_2O_3 and the release from TISS can happen as atomic Sc or diatomic ScO (T_{sub} = 1650 K [207]) molecule at a prolonged rate, controlled by the impurity amount [206].

A HSC simulation also suggests that Sc_2O_3 in Ta environment can dissociate above 1850 K according to equation 5.3 (see Figure 5.2). Sc(g) and ScO(g) are the only Sc-containing species found among the gaseous desorption products [207]. Again, the dissociation rate is expected to be low.

$$Sc_2O_3(s) \rightleftharpoons ScO(g) + ScO_2(s) \tag{5.3}$$

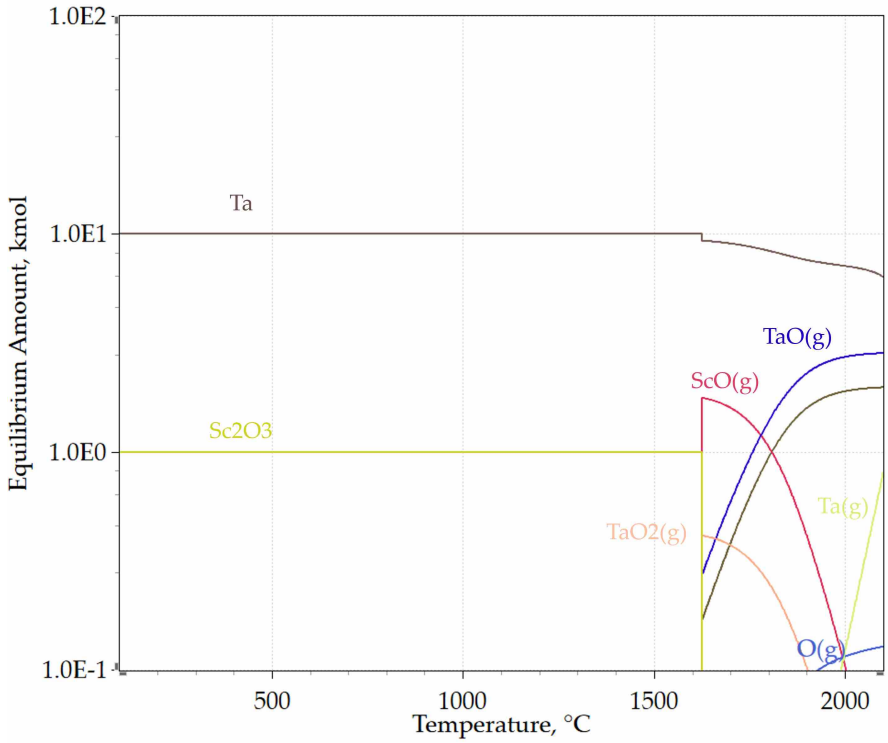

Figure 5.2: HSC simulation of reaction equilibrium for 1 kmol Sc_3O_3(s) in 10 kmol Ta(s) environment at an internal pressure of 1 $\times 10^{-6}$ mbar.

The bond dissociation energy of ScO (0 K) DH^o=673.6 kJ/mol (161 kcal/mol) and the atomization energy of Sc_2O (0 K) is 1025 kJ/mol (245 kcal/mol) [206], whereas TaO bond dissociation energy DH^o=801 $\pm$48 kJ/mol (8.3 $\pm$0.5 eV) [208, 209]. According to the chemical equilibrium in equation 5.4 and HSC simulation in Figure 5.3, once a ScO(g) molecule is chemisorbed on a Ta surface, it is more likely for the ScO bond to dissociate instead of TaO at temperature range of 1500–2000 °C. Especially when the ScO(g) molecule migrates through the transfer line (~2000 °C).

$$ScO(g) + Ta(s) \rightleftharpoons Sc(g) + TaO(g) \tag{5.4}$$

The laser resonant ionization experiments with stable $^{45}Sc_2O_3$ samples were carried out with 2 different (Ta and Re) surface source TISS. According to an HSC simulation, no reactivity of ScO(g) with Re is expected, however, atomic Sc has high adsorption enthalpy on Re (ΔH_{ads} = -565.9 kJ/mol) [163], which suggests a considerable delay time of ~15 min even at 2000 °C (estimated 1 $\times 10^3$ collisions due to a small Re ion source cavity

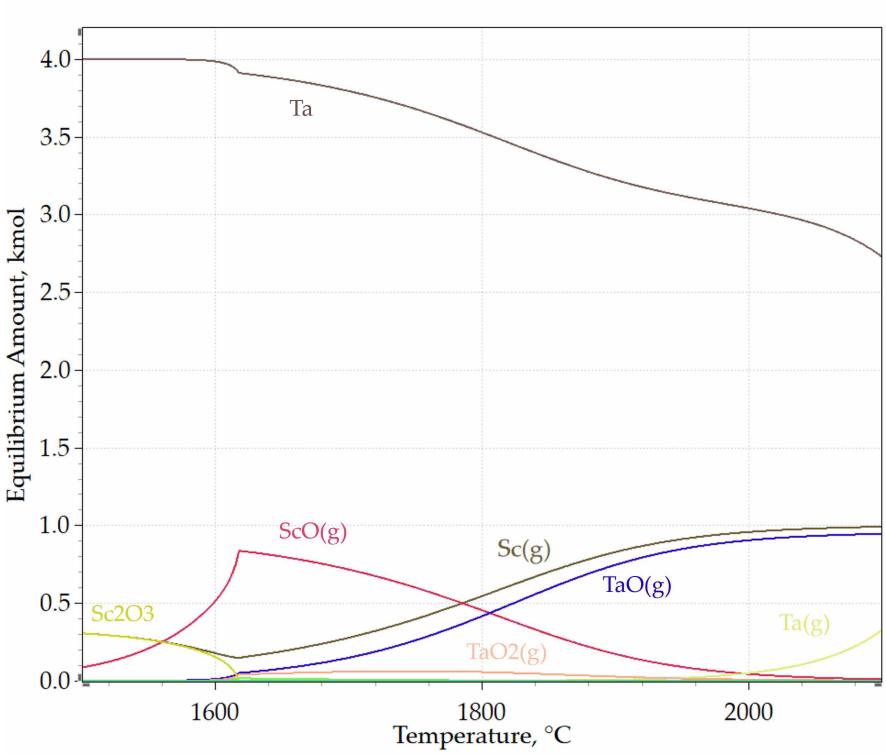

Figure 5.3: HSC simulation of reaction equilibrium for 1 kmol ScO(g) in 4 kmol Ta(s) environment (excess) at an internal pressure of 1 $\times 10^{-6}$ mbar.

volume). Atomic Sc^+ ions were observed only by laser resonant ionization, meaning that the dissociation happened without ionization.

The highest collection efficiency was obtained with a ^{nat}TiC material and VD-5 TISS. Regarding chemical interactions, Sc is known to react with carbon, stabilizing it as ScC [6, 210]. High temperatures of above 2000 °C must be achieved to vaporize and dissociate ScC_x (see equations 5.5 and 5.6), suggesting heterogeneous reactions (gas-surface) as the logical means of volatilizing the Sc radionuclides [210].

$$ScC_2(g) \rightleftharpoons Sc(g) + C_2(g) \qquad \Delta DH_o^0 = 565 \pm 21 \text{kJ/mol} \tag{5.5}$$

$$ScC_4(g) \rightleftharpoons Sc(g) + 2C_2(g) \qquad \Delta DH_o^0 = 1217 \pm 24 \text{kJ/mol} \tag{5.6}$$

5.2.2 Molecule chemical evaporation

Adding certain chemical reactants into the target container can transform elements of interest to far more volatile molecules than in their atomic state. In particular, for Sc release from the TISS and mass separation, chemical reactions with NF_3, CF_4 and Cl_2 were induced. A compound is most volatile if all its valences are saturated. Therefore the halide molecules formed are usually at the most stable oxidation state (see equation 5.7 and 5.8) [109, 206, 211].

$$Sc_{(s)} + \frac{3}{2} F_{2(g)} \rightleftharpoons ScF_{3(s)} \qquad \Delta H_f^{298} = -1251 \text{kJ/mol} \tag{5.7}$$

$$Sc_{(s)} + \frac{3}{2} Cl_{2(g)} \rightleftharpoons ScCl_{3(s)} \qquad \Delta H_f^{298} = -943 \text{kJ/mol} \tag{5.8}$$

The differences in each molecule formation and reaction kinetics in a TISS, limited knowledge of adsorption at each collection, material aging and large variables in molecule ionization efficiency make it very difficult to deduce an exact mechanism or model, involving the reaction kinetics, from the mass separation and collection. Typically an approximation from the reaction Gibbs energy calculations is sufficient to identify if the species of interest will form and interact with the TISS structures. However, multiple factors, such as possible impurities from the target material, TISS, and pressure play an important part in the desired reaction. To release the newly formed molecule, thermal dissociation and exchange reactions on the Ta surfaces must be thermodynamically unfavorable or with a low reaction rate. The reaction enthalpies of ScF_3 and $ScCl_3$ in equations 5.9 and 5.10 suggest that they would remain intact until their effusion to the ion source.

$$ScF_{3(g)} + \frac{3}{5} Ta_{(s)} \rightleftharpoons Sc_{(ads.)} + \frac{3}{5} TaF_{5(g)} \qquad \Delta H_r^{298} = 181 \text{kJ/mol} \tag{5.9}$$

$$ScCl_{3(g)} + \frac{3}{5} Ta_{(s)} \rightleftharpoons Sc_{(ads.)} + \frac{3}{5} TaCl_{5(g)} \qquad \Delta H_r^{298} = 210 \text{kJ/mol} \tag{5.10}$$

For general understanding, the molecule formation or chemical yield can be expressed as the evaporated molecule efficiency in equation 5.11.

$$\epsilon_{molecule} = \frac{N_{evapi}}{N_{maxi}} \tag{5.11}$$

where $\epsilon_{\text{molecule}}$ is the efficiency of evaporated molecule formation (chemical yield), N_{maxi} is the maximum molecule amount that can evaporate from the surface [pps] and N_{evapi} is the formed and evaporated molecule amount [pps].

Heterogeneous reactions

For a molecule to form in the mass separation conditions (low pressure of $< 1 \times 10^{-5}$ mbar and temperatures > 700 °C) solid-gas or gas-gas phase reactions can be described by the collision theory [123]. Since Sc is highly adsorbent on surfaces, the main molecule formation is expected to happen as a solid–gas phase reaction and was previously found to be the rate-limiting step for the effusion of refractory or semi-refractory metals [77]. Two simplified solid-gas reaction mechanisms are proposed for Sc molecule formation and shown in Figure 5.4, where the radionuclide is either adsorbed on the surface and interacts with an adsorbing gaseous particle or vaporized radionuclide interacts with an already adsorbed reactive species on the surface [212].

Desorption of adsorbed volatilizing reactant molecules and exchange reactions can happen faster than the newly formed molecules can leave the surface. The CF_4 reactive gas has a Bond Dissociation Energy (BDE) up to DH^o = 546 ± 13 kJ/mol [213, 214], NF_3 DH^o = 243–318 kj/mol [214,215] and Cl_2 DH^o = 238–242 kJ/mol [214,216]. This energy is less than required for Sc-F bond dissociation (see Table 5.4), suggesting that upon a collision and reaction, Sc would gain the halogen atom as the gas molecule loses one.

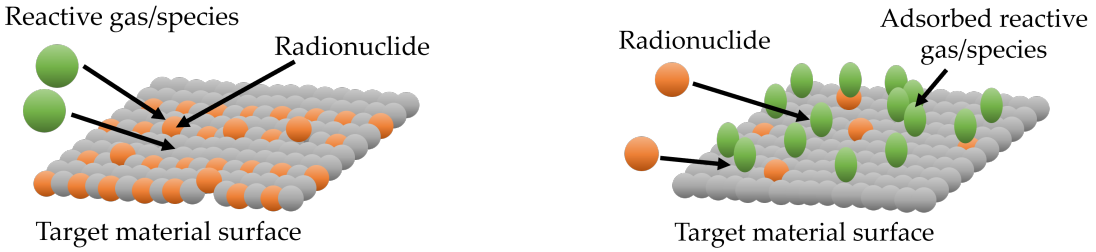

(a) Radionuclide reaction on the surface with reactant vapours.

(b) Vaporized radionuclide reaction with already adsorbed reactant molecules on the surface.

Figure 5.4: Heterogeneous reactions with radionuclides on a solid surface.

Table 5.4: Standard enthalpies of formation and BDE of scandium fluoride molecules [211,214].

	ScF_3, kJ/mol	**ScF_2, kJ/mol**	**ScF, kJ/mol**
$\Delta_f H^0$	-1251 ± 15	-683 ± 10	-141 ± 6
DH^o	645.4	619.5	593.9

An assumption that each CF_4, NF_3 or Cl_2 molecule in the target container can fully react with Sc up to its stable oxidation state of Sc^{3+}, can be made to describe the molecule formation rate regarding the supplied reactants. The summarized reactions of $Sc_{(adsorbed)}$ with the proposed reactive gases are shown in equations 5.12, 5.13 and 5.14. It can be seen that the reaction enthalpies are negative resulting in spontaneous reactions even at room temperature. Note that in reality, different multi-step reactions with various compounds and radicals can occur. The reactions are equated to a single Sc halide gas molecule, with Sc assumed to be adsorbed on a surface.

$$Sc_{(ads.)} + \frac{3}{4}CF_{4(g)} \rightleftharpoons ScF_{3(g)} + \frac{3}{4}C_{(ads.)} \qquad \Delta H_r^{298} = -548\text{kJ/mol} \tag{5.12}$$

$$Sc_{(ads.)} + NF_{3(g)} \rightleftharpoons ScF_{3(g)} + \frac{1}{2}N_{2(g)} \qquad \Delta H_r^{298} = -1117\text{kJ/mol} \tag{5.13}$$

$$Sc_{(ads.)} + \frac{3}{2}Cl_{2(g)} \rightleftharpoons ScCl_{3(g)} \qquad \Delta H_r^{298} = -669\text{kJ/mol} \tag{5.14}$$

Because the gas remains the only source of halogen atoms, the same reactant ratio would remain if the gas was already adsorbed on a surface and the vaporized Sc atoms would then interact with the adsorbed molecule. However, the possibility of reaction may be lower, if the surface material atoms themselves create volatile compounds, as is the case for titanium and vanadium fluorides. In the case of $^{44g/m}$Sc and ^{47}Sc collection (see Table 5.1 27.09.2023) from #702M TISS with previously fluorinated ^{nat}TiC target material, $^{47}ScF_x^+$ ($x = 0-2$) were still extracted after a while with no reactive gas addition. This can be explained by the presence of volatile $^{nat}TiF_4$ from previous fluorination which served as the fluorinating agent for Sc radionuclides for days. The reaction enthalpy (see equation 5.15) and HSC simulation at various temperatures (see Figure 5.5) suggest the ScF_3 formation with TiF_4 as the only source of fluorine in a Ta environment (excess amount).

$$Sc_{(ads.)} + \frac{3}{4}\,TiF_{4(g)} \rightleftharpoons ScF_{3(g)} + \frac{3}{4}\,Ti_{(ads.)} \qquad \Delta H_r^{298} = -84\text{kJ/mol} \tag{5.15}$$

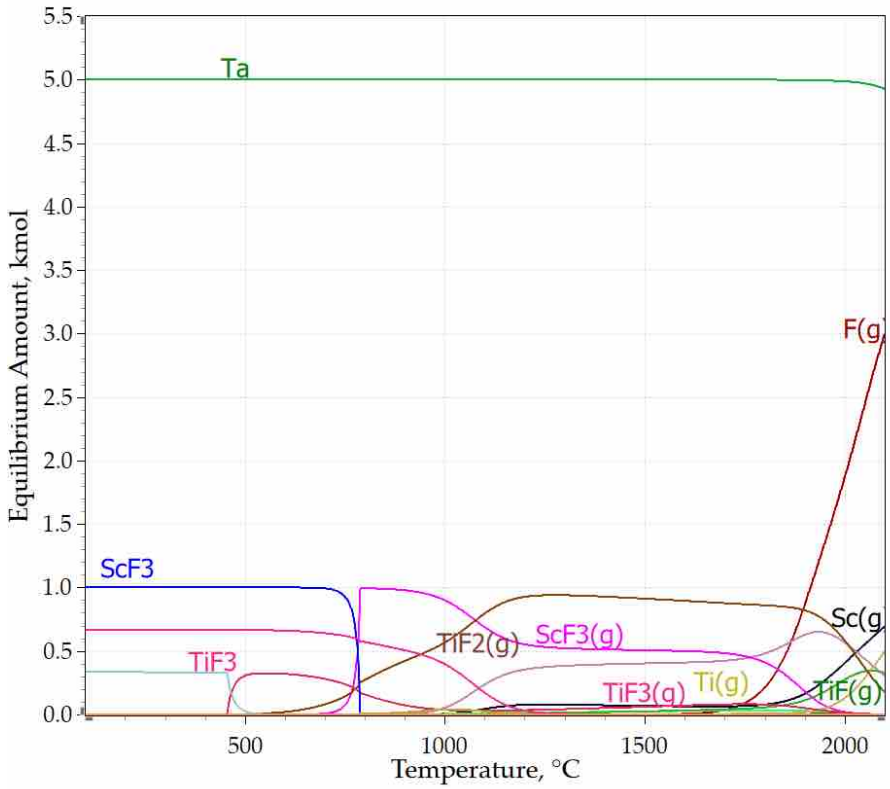

Figure 5.5: HSC simulation of reaction equilibrium for 1 kmol Sc with 1 kmol TiF_4 in 5 kmol Ta environment (excess) at internal pressure of 1 $\times 10^{-5}$ mbar.

Chemical selectivity

A universal way to characterize the thermochemistry of the volatile gaseous halide formation involves the estimations of chemical reaction equilibrium at elevated temperatures through the Gibbs free energy calculations of a given reaction or evaporation process (see equation 5.16). From known reaction enthalpies, entropies, partial pressure of the reactive gas applied and a given chemical equation of the volatile molecule formation, the equilibrium constant and partial pressure for species of interest can be expressed through equation 5.17 [109, 123].

$$Me_{(s)} + \frac{x}{y}\,AHal_{x(g)} \rightleftharpoons MeHal_{x(g)} + \frac{x}{y}A_{(s)}, \qquad \text{or} \qquad \frac{x}{y}A_{(g)}\ \text{for}\ NF_3 \tag{5.16}$$

In the case of NF_3 gas fluorination, reduction to gaseous monoatomic $N_{(g)}$, which further reacts to form nitrides is assumed, as it was observed in the target container above 1000 °C temperature during stable isotope ion beam experiments.

$$K_{eq} = e^{-\left(\frac{\Delta H^0 - T\Delta S^0}{RT}\right)} = \frac{p_{(MeHal_x)}}{p^{x/y}_{(AHal_y)}} \tag{5.17}$$

where K_{eq} is the equilibrium constant, p is the partial pressure (corrected according to stochiometry) [Pa], ΔH_{sub} is the reaction enthalpy change [J/mol], ΔH_{sub} is the reaction enthalpy change [J/mol], R is the gas constant [J/molK] and T is the temperature of the gas and solid [K].

The selectivity of halogenating gas towards most observed elements in the TISS and target materials is determined largely by the reaction thermodynamics as the most thermodynamically stable product species will predominate. The estimated ratios of partial pressures for the formed halides are summarized in Table 5.5 [112, 206, 211, 214, 217]. The estimations are normalized to the Sc halogen at 1550 °C, when radioactive ScF_3 release was experimentally observed. If a reaction product partial pressure is higher than that of ScF_3, its reaction is favored over the ScF_3 formation. This is very distinct when NF_3 is used as the reactive gas.

Table 5.5: Ratios of partial pressures of reaction products for an element of interest and halogenating gas at 1550 °C. Normalized to ScF_3 or $ScCl_3$.

Molecule	**F_2**	**CF_4**	**NF_3**	**Cl_2**
ScF_3 or $ScCl_3$	1.0	1.0	1.0	1.0
AlF_3 or $AlCl_3$	8.6×10^{-3}	1.6×10^{-2}	1.6×10^{-2}	3.3×10^{-3}
TiF_4 or $TiCl_4$	8.6×10^{1}	5.6×10^{-2}	3.4×10^{2}	1.4×10^{-4}
VF_2 or VCl_2	6.3×10^{-11}	4.9×10^{-7}	4.9×10^{5}	3.4×10^{-9}
BeF_2[a] or $BeCl_2$	1.5×10^{-8}	1.2×10^{-4}	7.4×10^{-5}	5.7×10^{-4}
TaF_5 or $TaCl_5$	6.9×10^{1}	1.3×10^{-5}	7.3	3.0×10^{-10}

[a] Berylium fluorides form from the interactions with anode body insulators.

For a chemical reaction with Sc to occur, the radionuclide first must diffuse to the surface. According to estimations and not taking into consideration all the possible side reactions within the TISS, the best choices for volatile molecule formation would be CF_4 and Cl_2, with a slight advantage to chlorine. Nevertheless, experimentally $ScCl_x^+$ (x=1–3) ion beams were never observed, whilst chlorinating the target material. Even when $ScCl_3$ samples were used as a starting chemical form, no molecular $ScCl_x^+$ (x=1–3) sidebands were observed, but only mono-atomic Cl^+.

It is expected for Al not to interfere with ScF_3 formation, however it was experimentally observed otherwise for #805M TISS (V foil target material). With AlF_x^+ (x=1–3)in the μA intensity range, $^{44m/47}ScF_x^+$ (x=1–2) ion beam onset was only observed when the injected gas flux of CF_4 was increased from 0.07 nmol/s to 0.18 nmol/s at a constant temperature of 1550 °C. This can be attributed to secondary reactions or high Al amount presence on the material surface and diffusion from the bulk of the target material. It should be noted, that intense AlF_x^+ (x=1–3) ion beam impurities were observed only for V foil target materials.

By comparing the CF_4 and NF_3 in an empty target container, the main difference is that CF_4 gas yields in partially dissociated ions, whereas NF_3 partial dissociation sideband

ions were not observed, which can be explained by the lower dissociation energies. Chemically, both gases can accompany additional nitride or carbide solid formation within the target container [206].

Reaction and evaporation rate

If the vapor pressure of a desired element is too small at an achievable temperature, extraction as a more volatile molecule is necessary. It can be seen in Figure 5.6, that the vapour pressure of ScF_3 is more than 2 orders of magnitude higher than that of atomic Sc.

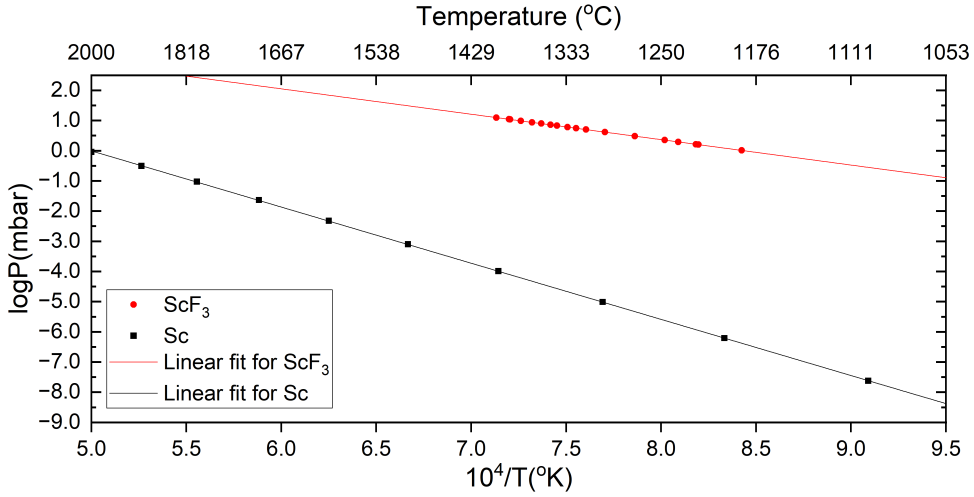

Figure 5.6: Vapour pressures of Sc and ScF_3 (reproduced from [99,180]).

According to the QE model described in section 2.3.4, the rate of adsorption must be balanced at equilibrium by an equal but opposite rate of evaporation from the adsorbent phase. In that case, the evaporation rate is equal to the reactive gas collision rate with the surface. The maximum unhindered evaporation rate at a given temperature could be estimated by applying the vapour pressure to the Hertz-Knudsen equation (see equation 2.5). The maximum estimated gas (CF_4) collision rate with the ^{nat}TiC target material for TISS #702M at various gas pressures are estimated and given in Figure 5.7.

To estimate the rate of radioactive ScF_3 evaporation, the radionuclides must first diffuse to the surface and react with the incoming reactive gas particles. As the reaction thermodynamics favor ScF_3 formation, the evaporation rate of ScF_3 will be approximately equal to the reactive gas collision rate at a given temperature and reactive gas partial pressure, multiplied by the "equilibration probability" ζ_i. The ζ_i for a each radionuclide can be estimated from the experimentally measured collection rate, knowing the ionization and transmission efficiency, applied reactive gas flux and molecular sideband ratio. For more precise estimation, the ζ_i should be corrected by the remaining radionuclide amount at a given time after the SOC, if a diffusion constant or release rate from from the corresponding target material is known. Since these constants are not available for ^{nat}TiC and ^{nat}V, the estimations are done for an "order of magnitude" assessment at a specific collection rate conditions, neglecting the already released fraction as well as the decayed amount.

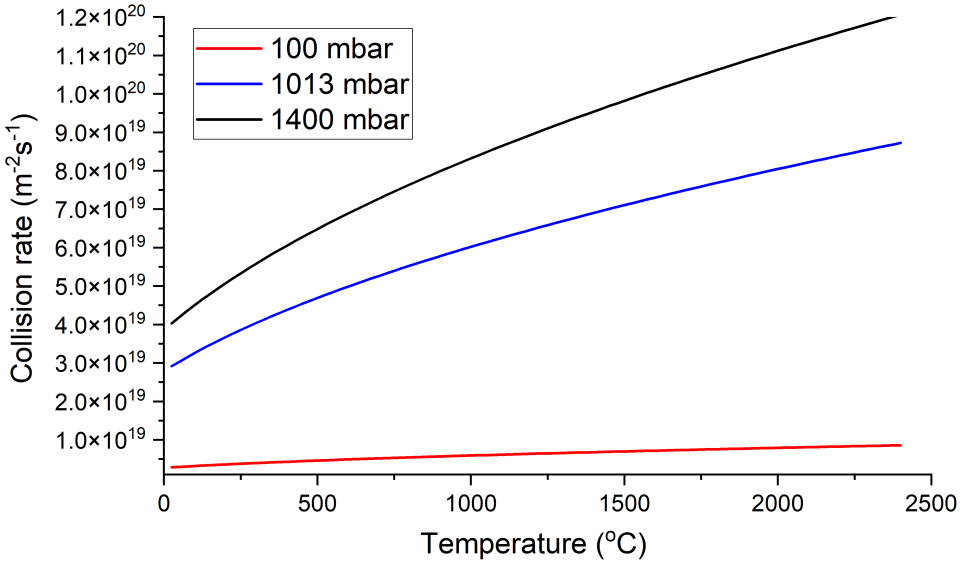

Figure 5.7: Theoretical collision rate of CF_4 gas with the ^{nat}TiC target material for TISS #702M at various temperatures and pressures applied on the calibrated gas leak (4.1 $\times 10^{-}5$ mbarl/s).

Sc radionuclide collection rates were obtained from two TISS - #805M (^{nat}V foils) and #702M (^{nat}TiC powder). Assuming the summarized reaction equation 5.18, the corresponding equilibrium probabilities are estimated and summarized in Table 5.6 and Table 5.7. For the estimation, the ionization efficiency of 7 % (see section 5.2.4) and transmission efficiency of 92 % were used.

$$\mathrm{Sc}_{(\mathrm{ads.})} + \frac{3}{4}\mathrm{CF}_{4(g)} \rightleftharpoons \mathrm{ScF}_{3(g)} + \frac{3}{4}\mathrm{C(ads.)} \tag{5.18}$$

The equilibration probability also gives an idea if the Sc radionuclide diffusion rate is faster than ScF_3 formation and evaporation, meaning that if the ScF_3 collection rate remains the same by increasing the reactive gas flux (and therefore collision rate), diffusion to the surface is the rate-limiting factor. An increase in CF_4 gas flux by a factor of $\sim$5, did not increase the equilibration probability proportionally, which can be explained by the radioactive decay of the radionuclides as well as a considerable fraction of initial radionuclides already released or evaporated as molecules. The calculated equilibration probabilities fluctuate over time at a constant temperature and depend on the reactive gas flux and available radionuclides on the material surface. This suggests, that the collection rate was not well optimized to match the diffusion rate. An exception is the last measurement on 23.04.2024, where the target was considerably depleted, ^{47}Sc radionuclides decayed by $\sim$2 half-lives and target material sintered to an unknown extent due to the high temperature of 2050 °C.

The most precise ζ_i were obtained at the onset of collection, due to less uncertainty of the remaining initial radionuclide amount in the target material and relatively small sintering effects. As the evaporation rate strongly depends on the estimated ionization efficiency (see section 5.2.4) and measured collection rate, one cannot deduce viable uncertainties. An important note is that the radioactive decay has not been accounted

Table 5.6: Equilibration probability ζ_i for $^{47}ScF_2^+$ from the measured collection rates at various temperatures from TISS #702M.

Date and time	Target container T, °C	CF_4 pressure on gas leak, mbar	Collection rate, kBq/min	Equilibration probability ζ_i
17.04.2024 03:16	1680	35	0.95	7.36×10^{-16}
17.04.2024 12:46	1800	35	2.48	1.86×10^{-15}
17.04.2024 17:16	1950	35	8.72	6.31×10^{-15}
18.04.2024 11:26	2000	35	9.97	7.13×10^{-15}
18.04.2024 16:21	2000	80	10.49	3.28×10^{-15}
18.04.2024 17:41	2000	100	16.92	4.24×10^{-15}
19.04.2024 09:35	2000	100	3.44	8.62×10^{-16}
19.04.2024 16:21	2000	150	7.51	1.25×10^{-15}
23.04.2024 16:21	2050	145	1.35	2.31×10^{-16}

[a] Calibrated gas leak rate of 4.1 $\times$ 10^{-}5 mbarl/s (air) and 72.4 m^2 ^{nat}TiC target material surface area.

Table 5.7: Equilibration probability ζ_i for $^{44m}ScF_2^+$ and $^{47}ScF_2^+$ from the measured collection rates at various temperatures from TISS #805M.

Date and time	Molecular beam	Target container T, °C	CF_4 pressure on gas leak, mbar	Collection rate, kBq/min	Equilibration probability ζ_i
07.10.2023 13:00	$^{44m}ScF_2^+$	1550	400	0.40	6.60×10^{-15}
08.10.2023 14:22	$^{47}ScF_2^+$	1550	400	6.18	1.39×10^{-13}

[a] Calibrated gas leak rate of 5.5 $\times$ 10^{-5} mbarl/s (air) and 0.45 m^2 ^{nat}V foil target material surface area.

for, nevertheless, these rates better characterize real situations, where mass separator limitations for the start of collection, such as pressure have to be respected.

Achieving a higher collection rate is an important goal because of the decay and necessity to transport the radionuclides to end users as soon as possible. In important conclusion here is also the severe impact of SSA, which suggests a higher rate potential for thinner foils or nanoparticle target materials. The highest equilibration probability was achieved for a ^{nat}V foil target material, which suggests the potential of metallic foil targets if the surface area of the target material can be significantly increased (orders of magnitude) and higher collection temperatures achieved. Compared to the ^{nat}TiC powder target TISS # 702M, with whom the highest collection efficiencies were obtained, the # 805M TISS ion source also was $\sim$4 times less efficient, based on noble gas efficiency measurement result comparison. Therefore, the obtained equilibration probabilities and collection rates for # 805M TISS (^{nat}V foil target material) are an underestimation of the realistically achievable.

Hypothetical collection rates from the given TISS and target materials with the highest

calculated equilibration probabilities were estimated and shown in Table 5.8. It should be noted, that diffusion was not considered as a limiting parameter and that these are rather unrealistic collection rates due to the high total beam produced, which could eventually damage the ion source. Therefore a higher throughput VADIS ion source would be of interest for further developments.

Table 5.8: Hypothetical $^{47}ScF_2^+$ collection rates from the given TISS and target materials and corresponding collection batches.

Target	**Target container T, °C**	**CF_4 pressure on gas leak, mbar**	**Collection rate, kBq/min**	**Equilibration probability ζ_i**
#702M (^{nat}TiC)	2000	1200	456	7.13×10^{-15}
#805M (^{nat}V)	1800	1200	26	1.39×10^{-13}

It can be concluded, that with a higher throughput FEBIAD-type ion source, it would be possible to collect ^{47}Sc with the rate of ∼30 MBq/h. This would translate to a clinical dose activity of 3.6 GBq after 5 days of collection if no degradation of the target and other collection and mass separation parameters stay constant.

5.2.3 Scandium fluoride release from TISS

To understand the release mechanics of molecules from TISS a deeper analysis was done on multiple influencing factors. Due to chemisorption, the assumption of unhindered molecule release is not entirely correct at high temperatures. To favor the equilibrium on ScF_3 in the TISS as the dominant species until it reaches the ion source and to saturate Ta surfaces with fluorine, a continuous flow of a fluorinating reactive gas is applied. A chemical equilibrium simulation with HSC software [112] in Figure 5.8 indicates, that the stable ScF_3 sample should reach the ion source intact. Although the simulation suggests ScF_3 dissociation and ScF_2 species as dominant after 1800 °C, such branching was not observed experimentally. The simulation does not take into account reaction kinetics, therefore the majority of ScF_3 molecules may or may not reach the ion source before it gains the kinetic energy for dissociation in the transfer line. Since little or no chemical interaction with Ta is expected, we can assume that ScF_3 would also not be delayed in the TISS based on estimations of delay time, sublimation enthalpy on Ta and high vapour pressure.

For the stable isotope beam tests and efficiency measurements with $^{45}ScF_3$ starting sample, two different type TISS with a VADIS ion source were used. The first TISS type was equipped with a regular target container. Here the $^{45}ScF_3$ sample was placed in a Ta boat or on a Ta foil and directly into the empty container. The ScF_3 release from the TISS was observed at 700 °C and became more pronounced at 800–1000 °C on the target container, cathode at 1925 °C and only pure Ar as a buffer gas for the ion source. The experimental observations of molecule appearance coincide with the HSC simulation in Figure 5.8a. The $^{45}ScF_3$ beam intensity was in the 10–125 pA range during this experiment and would slightly increase on each step for temperature rise and then decrease after a few minutes of stabilization.

The $^{45}ScF_2^+$ beam could be later recovered to 160 pA from the same sample with CF_4

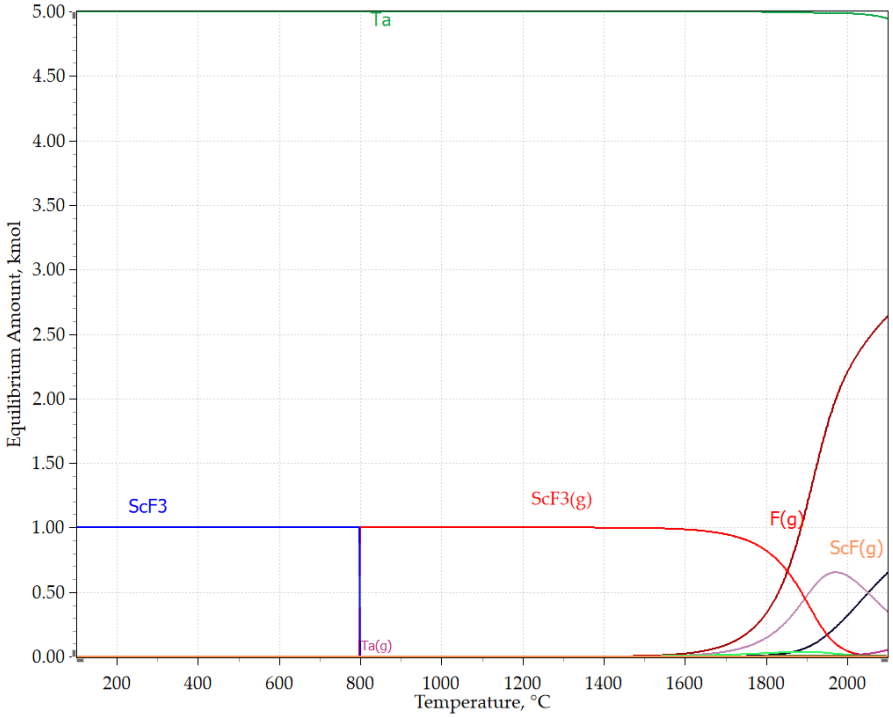

(a) 1 kmol ScF_3 with 5 kmol Ta

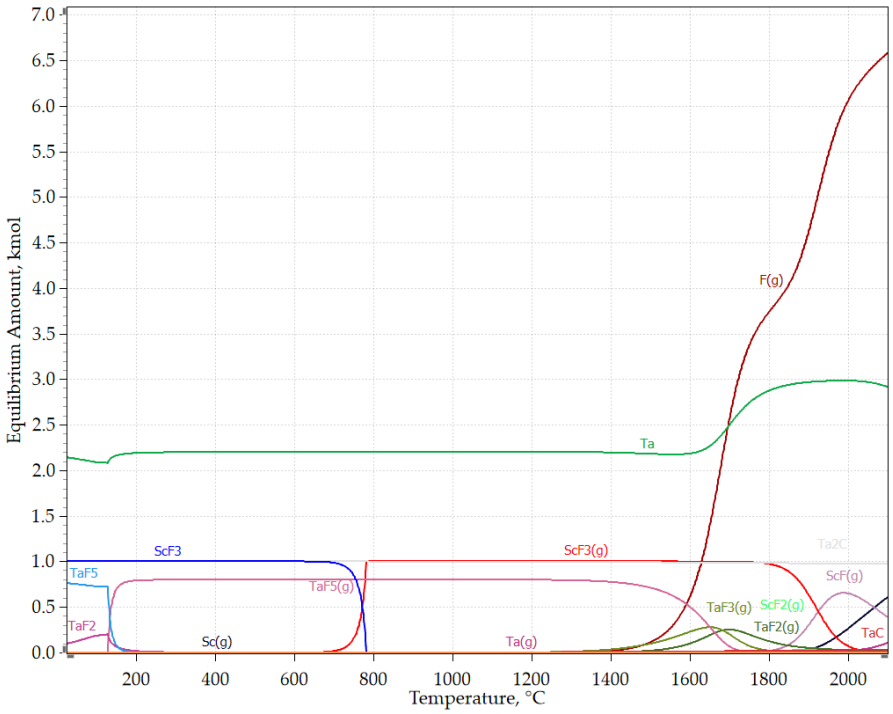

(b) 1 kmol ScF_3 with 5 kmol Ta + 1 kmol CF_4

Figure 5.8: HSC simulation of reaction equilibrium for ScF_3 in Ta environment (Ta excess) with and without CF_4 gas at internal pressure of 1×10^{-5} mbar.

addition, already in the 300–500 °C target container temperature range (see Figure 5.9. The ion source parameters were the same as per the test with Ar. This points towards some $^{45}ScF_3$ ($x = 0 - 3$) adsorption within the transfer line or ion source body from the previous $^{45}ScF_3$ + Ar experiment. The ion beam intensity would later increase significantly to 0.8–1 nA in 870–1000 °C target container temperature range, as indicated from the HSC estimations in Figure 5.8b. Here the intensities of $^{45}ScF_x$ beams reached 55 nA at 1200 °C (maximum temperature used for this experiment) and would not drop below 10 nA even with subsequent target container cooling to 300–500 °C again. Here, adsorption within the transfer line and ion source body or reaction kinetics to form $^{45}ScF_3$ from a dissociated sample could explain the observations. These observations show the importance of a fluorine source for the already-formed migrating particles within the TISS. The order-of-magnitude increase in beam intensities by CF_4 addition also may suggest that the migration of $^{45}ScF_3$ towards ion source was happening by continuous chemisorption/dissociation and subsequent desorption upon reaction with a new reactant.

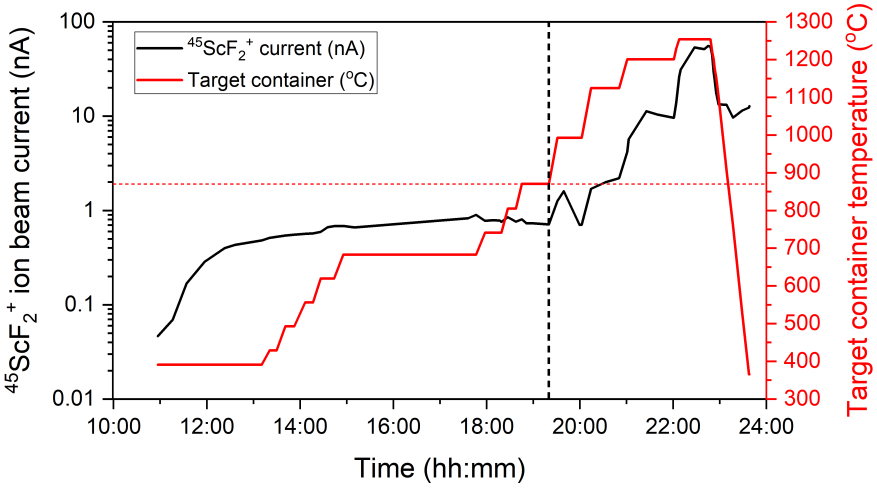

Figure 5.9: $^{45}ScF_2^+$ ion beam current and target container temperature during release and efficiency studies with target #801M.

Later investigation showed, that a large amount of the initial sample had condensed at the plug end of the target container, which would account for the decrease of intensity due to sample displacement on a "cold spot" (see Figure 5.10) during the experiments. These findings then led to additional target and heat screen developments described in Chapter 4, to reduce the temperature gradient difference and "cold spot" formation in the target container.

SEM-EDX analysis of the condensed sample indicated increased Ta and O amount, which could have come from the volatile TaF_5 and $TaOF_3$ co-condensation and crystallization (see Figure 5.11 and Table 5.9).

The second TISS was equipped with a cylindrical capillary oven (⌀=∼2mm) instead of a target container (see Figure 5.12). The oven was placed in the gas supply line, leading directly into the VADIS ion source. As per TISS #801M, the test comprised of first utilizing Ar as ion source buffer gas and later fluorination with CF_4.

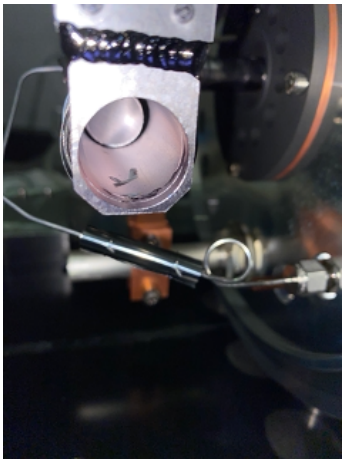

(a) Condensed and peeled $^{45}ScF_3$

(b) Condensation "cold spot"

Figure 5.10: Condensed and displaced $^{45}ScF_3$ sample in target container after stable beam test with TISS #801M.

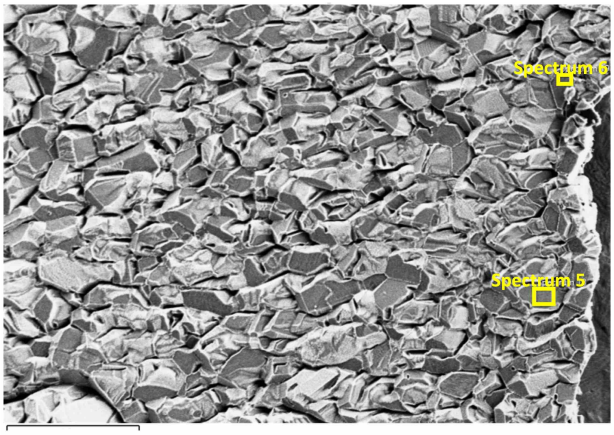

Figure 5.11: SEM-EDX image of the condensed $^{45}ScF_3$ sample from TISS #801M.

Table 5.9: EDX element mass fraction analysis of the condensed $^{45}ScF_3$ sample from TISS #801M..

Element	**Spectrum 5, W_t%**	**Spectrum 6, W_t%**
C	5.00 ± 0.10	5.40 ± 0.10
O	5.40 ± 0.10	5.40 ± 0.10
F	42.2 ± 0.2	44.6 ± 0.2
Sc	25.7 ± 0.2	25.3 ± 0.2
Cu[1]	1.00 ± 0.10	1.00 ± 0.10
Ta	20.70 ± 0.15	18.30 ± 0.10

[1] From the Cu substrate on which the sample was placed.

The ionization efficiency of the $^{45}ScF_3$ could not be estimated, due to the unknown amount of previously released sample with Ar. However, the same $^{45}ScF_x^+$ (x=0–2) beam

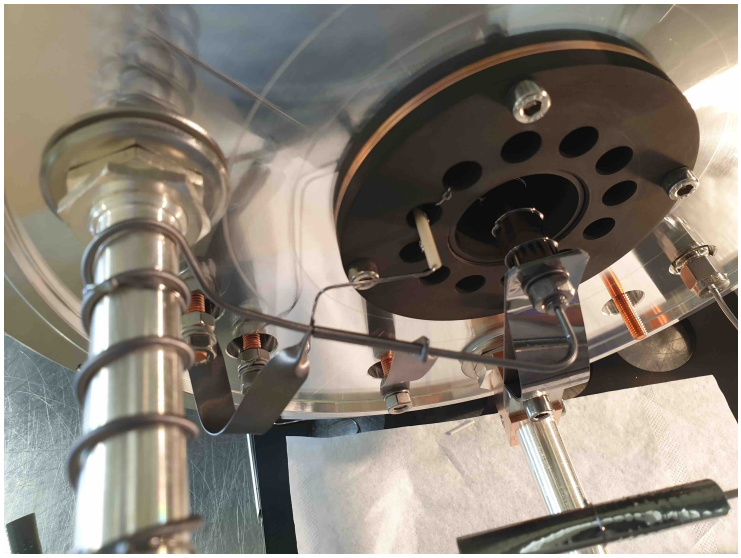

Figure 5.12: Assembly of the TISS #731 oven and gas line.

release onset at 600–800 °C was observed. Furthermore, again the effect of fluorinating gas was observed as the $^{45}ScF_2^+$ beams would increase by an order of magnitude (from 1–4 nA to 60 nA) with the same ion source settings. Another notable finding was that once the gas was exchanged from Ar to CF_4, the $^{45}ScF_2^+$ ion beam intensity rose to 10 nA within 15 min and exponentially peaked at 60 nA after 1.5 hours, within the same oven temperature of 355 °C throughout (see Figure 5.13). This observation points towards favored $^{45}ScF_3$ release in $CF4_4$ environment and reaction and release kinetics.

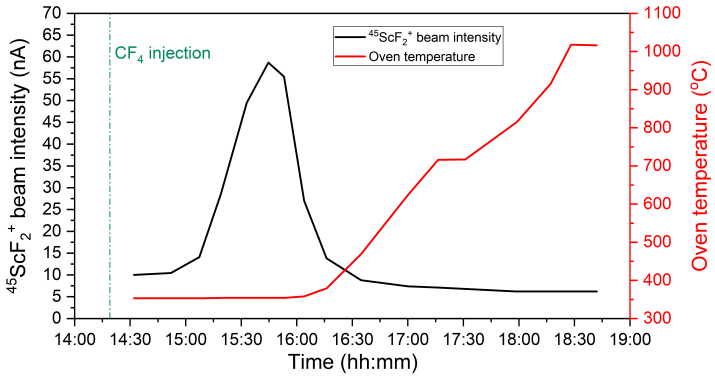

Figure 5.13: $^{45}ScF_2^+$ ion beam current and oven container temperature during release studies with TISS #731. Cathode at 1900 °C with 0.12 nmol/s CF_4 fluorination.

After reaching this peak value, no more increase in beam current could be observed even with increasing the oven temperature. Nevertheless, the ion beam current remained relatively stable at 6 nA. The tailing of 6–10 nA suggests a chemical reaction and available reactant limited release, independent of the temperature.

Later investigation of the sample remains with optical and SEM (see Figure 5.14) revealed noticeable visual and chemical composition changes in sample residues. The Ta and O ratio was increased, whereas, Sc was decreased. Almost no Fluorine could be

detected, supporting that the release at the end of the experiment was chemical reaction limited.

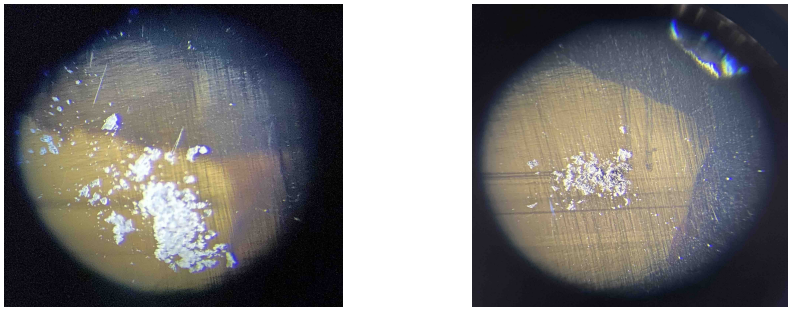

(a) $^{45}ScF_3$ sample before the test (b) $^{45}ScF_3$ sample after the test

Figure 5.14: $^{45}ScF_3$ sample before and after efficiency measurement tests with TISS #731

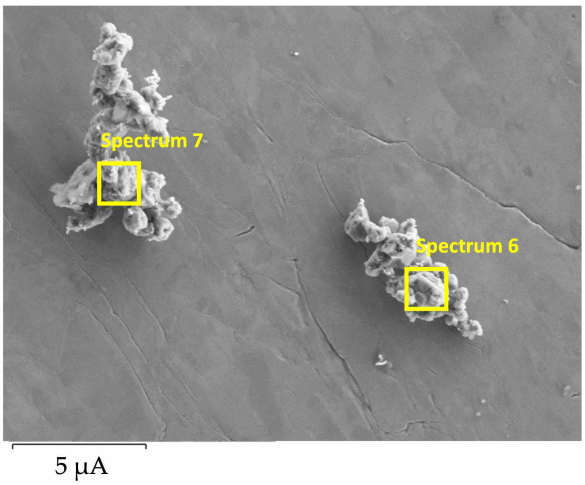

Figure 5.15: SEM-EDX image of the residue $^{45}ScF_3$ sample from TISS #731.

Table 5.10: EDX element mass fraction analysis of the $^{45}ScF_3$ sample residues from TISS #731.

Element	**Spectrum 6, W_t%**	**Spectrum 7, W_t%**
C	5.00 ± 0.10	6,30 ± 0.10
O	18.80 ± 0.10	19.50 ± 0.10
F	0.70 ± 0.03	1.30 ± 0.03
Na	-	0.10 ± 0.02
Sc	13.60 ± 0.10	11.80 ± 0.10
Ta	58.1 ± 0.2	54.70 ± 0.10
W[1]	3.80 ± 0.15	6.30 ± 0.10

[1] Sample was placed on W substrate.

Target material sintering

The target materials are sometimes operated close to their melting point to reach sufficiently short diffusion times for the radionuclide release. It has been observed that powders begin to sinter when they are heated to more than half of their melting point. Sintering results in grain growth and disappearance of pores, therefore causing the delay of radionuclide release due to increased diffusion times. The sintering rate depends on the initial particle dimension, self-diffusion coefficient, temperature and vapour pressure. It is perceived that the grain growth continues until the theoretical density of a material is reached, however, the growth typically slows down or stops at larger grain sizes. The initial rate of sintering is inversely proportional to the cube of the dimension of a particle, therefore sub-micron sized particles (<1-5 μm) are not entirely suited for isotope release at temperatures higher than 1800 °C [78, 177].

The sintering influence was observed by analyzing a ^{nat}TiC pill with SEM after outgassing and described in Chapter 4, as well as during the Sc collections from a 1–2 μm powder ^{nat}TiC target. The pre-fluorinated TISS (#702M) was capable of releasing $^{47}ScF_2^+$ with the collection rate of 1.33 kBq/min without additional CF_4 injection. After another 12 days of operations at the temperature range of 1700–2000 °C, to obtain a similar collection rate additional continuous feeding of CF_4 at the same temperature and mass separator parameters was required (see Table 5.11).

Table 5.11: Comparison of collection rates for ^{nat}TiC micrometric particle size powder TISS indicating the sintering effect.

Date	Temperature, ^{o}C	Fluorination, pmol/s	Total beam, μA	^{47}Sc activity in target[a], Bq	Collection rate, kBq/min
29.09.2023	1700	Pre-fluorinated (unsaturated)	1.56	2.738×10^9	1.33
16.04.2024	1700	32	2.50	3.313×10^9	1.19

[a] Decay-corrected amount of the starting radioactivity, assuming no ^{47}Sc is prior released due to the close onset of release at collections.

It is visible, that with a less-aged target material, the collection rate is higher, even with less starting radionuclide activity and no additional reactive gas supply. Furthermore, the target was not saturated, due to additional outgassing for an ion source insulator recovery before the collection. To produce more long-lasting efficient powder targets for Sc collections, composites with materials of sintering hindering capabilities should be introduced, such as different carbon allotropes: graphite, MultiWalled Carbon NanoTubes (MWCNT) and carbon black or [50]. Another option is to develop ^{nat}TiC fiber target materials with fewer contact points of the fibers than spherical particles [218].

Scandium fluoride branching

The Sc halides can form stable molecules in a less oxidative state, such as ScF_2 and ScF. Furthermore, the produced ions in VADIS can recombine with electrons from the anode body walls and subsequently ionized, resulting in ScF_x^+ ($x = 0 - 3$) branching or otherwise called - molecular sidebands. No directly ionized ScF_3^+ was observed, however the sidebands of ScF_x^+ ($x = 0 - 2$) have been measured and results in the ratio

of 1 Sc^+ : 1 ScF^+ : 10 ScF_2^+ : 0 ScF_3^+ as seen in Figure 5.16. The ratio was also confirmed in radioactive $^{46}ScF_x^+$ ($x = 0 - 3$) collection from TISS #702M.

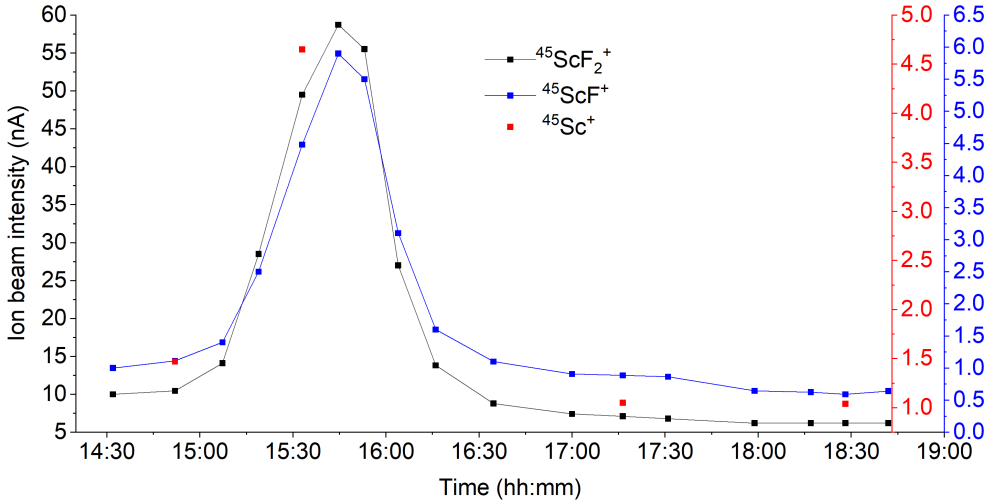

Figure 5.16: Measured ion beam intensities and ratio of molecular $^{45}ScF_2^+$, $^{45}ScF^+$ and atomic $^{45}Sc^+$

Doubly charged ions such as $^{nat}Ti^{2+}$, Ar^{2+} and Xe^{2+} have been observed in the mass spectra taken during stable beam tests and radionuclide collections, due to forced electron impact. However, no evidence has been found of Sc^{2+}. Also, the doubly charged ions are also typically in an order of magnitude lower intensities, therefore unfavorable for collection, compared to singly charged ones.

Scandium fluoride release from irradiated ^{nat}Ti foil TISS

From the implanted radionuclide activity measurements throughout collections as well as investigated thermal release, it was observed, that for the ^{nat}Ti foil target, $^{47}ScF_2^+$ release was fast, compared to ^{nat}TiC target material. This was also observed in Figure 5.17, that the separated ion beam current increased rapidly at 1100–1300 °C and the collected radionuclide activity on the collection foil increased. The later decrease of separated and total ion beams after reflected issues with fluorinating gas (NF_3) supply and clogged calibrated gas leak.

According to the thermal release measurements in Chapter 3, full release from the target material is expected within an hour at 1450 °C. Although issues with calibrated gas leak hindered the collection, a fraction of the reactive gas was still reaching the target container. If one assumes, that Sc effuse to ion source as ScF_3, then the collection rate would be slow, but collected activity should increase. Even by further collection, no significant increase in collected activity could be observed, therefore suggesting that in this case also full release was achieved. The low activity yield then points toward the ScF_3 formation kinetics with respect to atomic Sc release from material and ionization efficiency. Later laser ionization tests confirmed that no atomic Sc was being released from the target material. Any additionally collected radionuclides at the end of the collection were most likely released from adsorbed states of target container and transfer line cold spots.

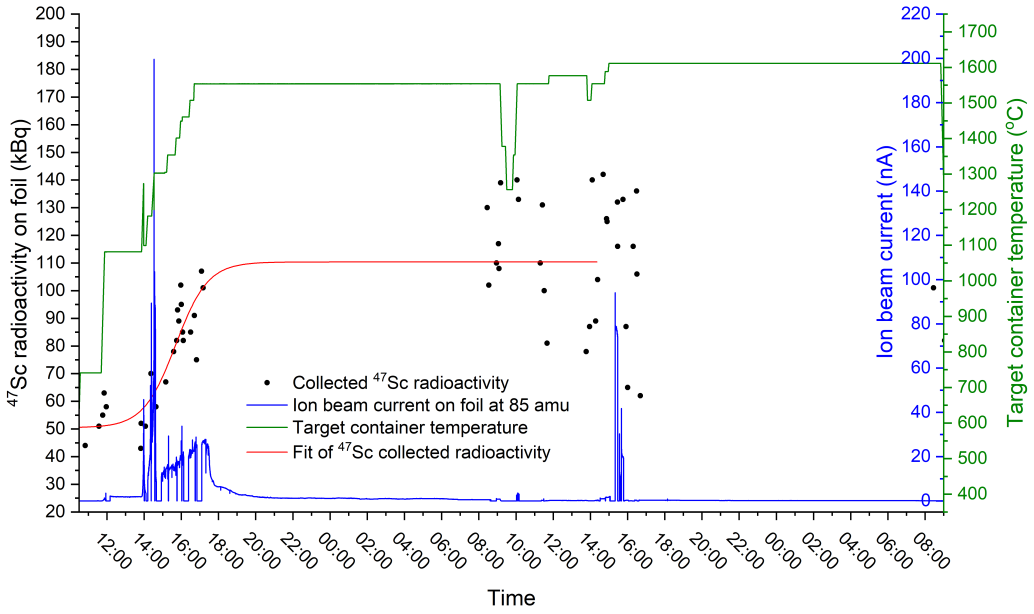

Figure 5.17: Ion beam current (85 amu), collected ^{47}Sc radioactivity and target container measurements during $^{44g/m}$Sc/^{47}Sc collection with ^{nat}Ti foil TISS (#741M) and NF_3 as the reactive gas.

5.2.4 Scandium fluoride ionization efficiency

Ionization efficiency typically is one of the main limiting factors for any RIB successful production and mass separation. The first approximation of ionization efficiency can be estimated, from a stable isotope sample, assuming the whole sample is released from the target container and effuse through the ion source without interactions with the TISS, which is most applicable for noble gases.

An indirect efficiency measurement was done and explained in Figure 5.1. From the obtained collection efficiency of 4.90 $\pm$0.07 %, an indicative value the global f-factor and cross section value for ScF_3 ionization could be estimated through equation 2.2, under the conditions of:

- whole $^{45}Sc_2O_3$ sample reacted with NF_3 forming ScF_3 and was completely released into the ion source;
- the formed $^{45}ScF_3$ accounts for the majority of partial pressure in the ion source;
- the estimated ionization efficiency is a combination of upon ionization dissociated ScF_3 and recombined ScF_2 direct ionization to form ScF_2^+.

To estimate the electron density in the ion source, the electron transport from the cathode to the ionization volume through the anode grid f_{elec} must be taken into account. This factor depends mainly on the ion source construction and was deducted from noble gas mixture ionization efficient measurements to be $\sim$54 %.

Taking into account the branching, and transmission efficiency and the global f-factor to be 0.996 for ScF_3, the estimated ionization and first dissociation cross section for ScF_3 to ScF_2^+ computes to 7×10^{-16} cm^2 with 130 V anode potential and 2 mm cath-

ode/anode distance. This would be the lowest estimate, as any lower cross section would result in the f-factor being higher than 1, therefore unrealistic. No uncertainty could be applied to this value as the exact number of particles entering the ion source is not exactly known and the formation of ScF_3 was assumed to follow simplified equation 5.19 because of the full NF_3 dissociation.

$$Sc_2O_{3(s)} + 2\,NF_{3(g)} \rightleftharpoons 2ScF_{3(g)} \;+\; N_{2(g)} \;+\; \frac{3}{2}\,O_{2(g)} \tag{5.19}$$

Although no ScF_3 ionization or dissociation cross sections are published, the first approximation of the ScF_3/ScF_2^+ ionization cross section in a FEBIAD type ion source is comparable to the published values of SiF_3, SF_3, CF_3, BCl_3, BF_3 and more complex molecules, being in the range of 3–13 $\times 10^{-16}$ cm^2 and 10.02 $\times 10^{-16}$cm^2 for ScC_2 [210, 219–225]. The ionization efficiency with the same ScF_2^+ formation cross section and global f-factor in an electron space charge limited regime (cathode at 2000 °C) and anode potential of 150 V, computes to 7–13 % with 2.0 and 1.5 mm cathode/anode distance respectively.

5.2.5 Transmission efficiency

The transmission efficiency ϵ_{transm} accounts for the total ion beam losses in the mass separator. It can be estimated from the difference in total beam and integrated separate beam currents (see equation 5.20).

$$\epsilon_{transm} = \frac{\int I_{Separated} damu}{I_{Total}} \tag{5.20}$$

where ϵ_{transm} is the transmission efficiency, $I_{\text{Separated}}$ is the separated ion beam current [A], I_{Total} is the total ion beam current [A], and *amu* is the atomic mass unit [a.u.].

The CERN-MEDICIS mass separator magnet is operated only up to 90–95 A current which corresponds to 230–240 amu region with TISS at 60 kV potential. It is known that a large contribution to the total beam during fluorination is given by TaF_4^+ ions at amu 257 and hence the transmission efficiency measurement in a fluorination regime is not precise. As a reference for the transmission efficiency, a noble gas mix mass scan was performed (see Figure 5.18) and the value was computed to ∼92 %.

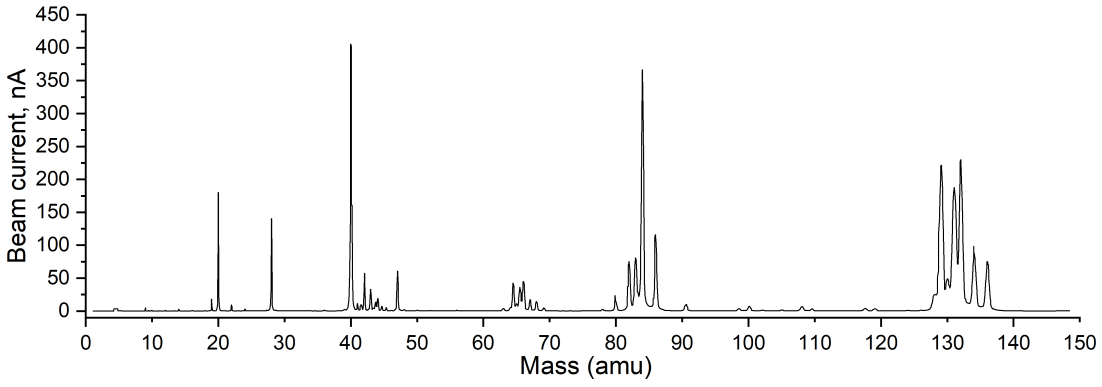

Figure 5.18: Mass spectra of noble gas mix for target #702M with ion source at 2000 °C.

The transmission efficiency can be maximized by optimizing the beam optics of the mass separator and any losses in transmission efficiency may arise from large contaminant species in the total ion beam [64]. Losses also occur from any vacuum impurities ant the beam collision with neutral particles in the ion beam path. The transmission from the first to the second Faraday cup at the Offline-1 mass separator is typically around 75 % [11]. During the stable beam tests an efficiency of 84 % was obtained.

5.2.6 Collection rate measurements

The collection rate is typically measured by one of the two available Kromek detectors placed behind and under the collection chamber of the CERN-MEDICIS mass separator as indicated in Figure 2.13. A very important note is that the measured collection rates are the ones exceeding radioactive decay. Therefore one expects to see an increase in activity if the rate of the corresponding radionuclide decay is exceeded. The main value of the collections is collected activity on the foil at the EOC. Because of the relatively long half-life of the Sc isotopes, compared to the collection time, the decay can be often neglected.

After the sample retrieval, the collected radionuclide activity is measured with a different HPGe detector and gives the exact amount collected directly on the foil. The measured ^{47}Sc radioactivity with HPGe detector was observed to differ by a factor of 2–4 less than indicated by the Kromek. The discrepancy in the obtained values could be attributed to the Kromek detector calibration, positioning, and attenuating materials, such as collection foil material and thickness, glass, and stainless steel used for collection chamber housing. As can be seen in Figure 5.19, the efficiency slope from 100–200 keV is steep and would benefit from additional calibration points. For example, if a different fit is applied for the experimental calibration source measurement points [142], the efficiency of 3.55×10^{-6} at ^{47}Sc energy is varied by 32 % to 4.67×10^{-6} and therefore the Kromek reflected activity is reduced by 32 %.

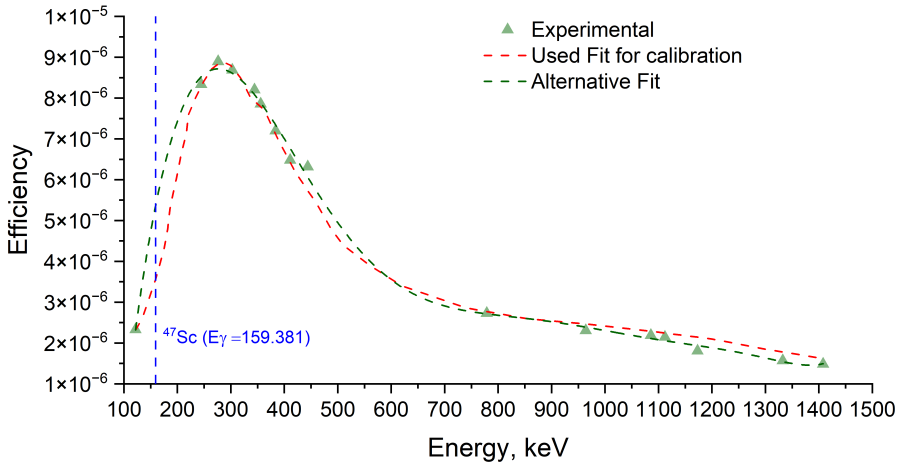

Figure 5.19: Efficiency calibration curve acquired from ^{60}Co, ^{133}Ba and ^{152}Eu calibration sources for the secondary GR-1 detector.

While collecting Sc halide ion beams with a VADIS from a ^{nat}Ti element containing target material, high-intensity isobaric ^{47}Ti contaminants are found on the same mass.

During ScF_2^+ collections, the separated ion beam can reach 100–120 nA. An intense ion beam (>10 nA) results in large beam emittance and part of the beam being implanted in the collimator of the implantation foil support. The collection foils are usually perforated (see Figure 2.13) and due to the large beam emittance and strong beam deflection, a part of the radionuclides could also be implanted in the glass separating collection chamber and the Kromek detector. In this case, the radionuclides are closer to the detector than calibrated, hence giving higher activity readings. Because such difference between Kromek GR-1 and HPGe was not observed for ^{46}Sc (E_γ=1121 keV) collection with the same TISS, the discrepancies point towards the calibration or activity calculation in particular for ^{47}Sc. In order to retain maximum of the separated radionuclides on collection foil, a larger collimator could be installed, designed for high-intensity ion beams.

Another reason for discrepancies is the self-sputtering and thermal evaporation of the already implanted ions. It results in the loss of activity on the foil and dispersion within the collection chamber. Consequently, it is still measured by the Kromek, but with no validity of correct results due to unknown distribution within the chamber and geometry modelization. The sputtering effect of each collection was estimated when the collection foil was removed from the collection chamber. The residual activity without the sample holder is then again measured by the Kromek detector.

For Zn-coated gold foils large portion (up to $\sim$ 27 %) of already implanted ions can escape and even set the upper limit of collected activity [63]. By varying the material in which radionuclides are implanted to Al/Al_2O_3, Cu, NaCl, KNO_3, Ti, V, the sputtering effects can be minimized, however, the subsequent radiochemical separation method must be adjusted. Another way to reduce the sputtering and local heating effect is to frequently change the collection foils and wobble the separated ion beam - intentional migration across the foil.

The uncertainty in the collection rate comes from the approximation of a constant rate per set temperature, Due to the differences between measured activity on the collection foil with HPGe and the one deducted from Kromek measurements during collection, the collection rates for ^{47}Sc are not absolute and are assessed for a relative comparison or normalized according to respective sample HPGe measurement.

5.3 Mass separation of a cyclotron irradiated external sample

Since ^{43}Sc cannot be produced without $^{44g/m}$Sc impurities by using a cyclotron, the feasibility of mass separation was tested for an $ScCl_3$ sample, from irradiated ^{44}CaO at Paul Scherrer Institute (PSI), Villigen, Switzerland. The irradiated sample was radiochemically separated from the target material, for recovery and obtained as $^{43}ScCl_3/^{44g/m}ScCl_3$ in 0.05 M HCl. At PSI on 19.07.2023 10:42 an aliquot of 3 µL was measured and showed 6.68 MBq total activity. A total volume of 125 µL of $ScCl_3$ in 0.05 M HCl was shipped for the experiment resulting in $\sim$280 MBq ($\pm$20 %) at 10:42. After transfer and drying in a Ta boat, the sample was measured at 16:19 on 19.07.2023. The measured radioactivity of the sample is shown in Table 5.12.

Based on the measured activities and assuming no release had happened before each point in time, total ion currents of radioactive species at a certain mass were estimated

Table 5.12: Radioactivity measured of the transferred and dried sample at 16:19 on 19.07.2023.

Radionuclide	Half-life	Radioactivity, Bq
^{43}Sc	3.89 h	$6.1 \pm 0.6 \times 10^7$
^{44g}Sc	3.93 h	$2.55 \pm 0.12 \times 10^7$
^{44m}Sc	2.44 d	$1.19 \pm 0.12 \times 10^6$

(see Figure 5.20). ^{44m}Sc decay into ^{44g}Sc has been taken in account. This information was used to to determine time when mass separation of ^{43}Sc was switched to $^{44g/m}$Sc.

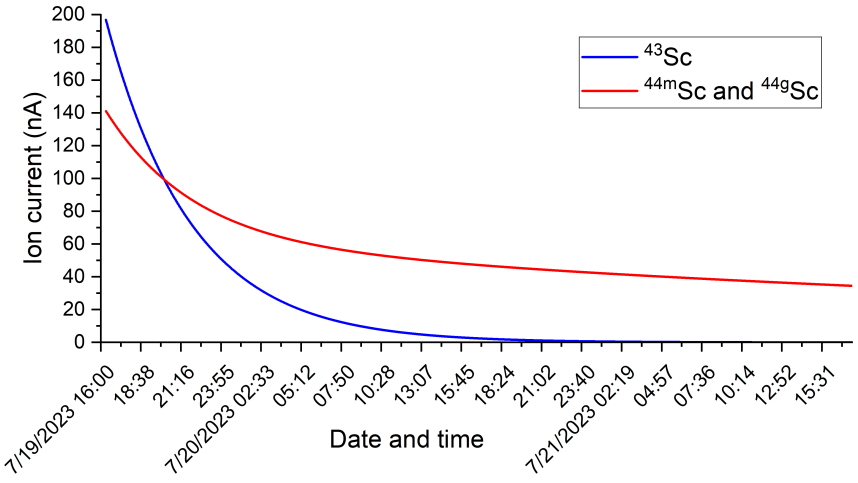

Figure 5.20: Theoretical ^{43}Sc and $^{44g/m}$Sc radionuclide ion currents, assuming no prior release.

$ScCl_3 \cdot 6H_2O$ upon heating above 60 °C starts to lose water and above 275 °C begins to decompose rapidly forming Sc_2O_3 [82]. Opposite as per other lanthanides and Yttrium chloride hydrates, $ScCl_3 \cdot 6H_2O$ upon decomposition do not form ScOCl. Sc_2O_3 fluorination offline mass separation experiments showed fluoride molecular beam formation above 1400 °C. This was the motivation to use CF_4 as fluorinating gas (1.15–2.31 nmol/s) and collect the Sc radionuclides on $^{43}ScF_2^+$ molecular sideband. In opposite to the expected, during and after the collection, no ^{43}Sc or $^{44g/m}$Sc were detected on the collection foil. Therefore, no elemental Sc or ScF_x^+ (x = 1–2) were collected at any point of the collection.

During the collection, multiple mass scans were done periodically to monitor total beam composition as well as chemical and molecular beam formation dynamics. Intense beams of chlorine (up to 20 nA) were observed and diminished to low values, suggesting almost complete evaporation of the Cl^+ and HCl^+ species at the temperature range of 780–1100 °C. As the sample was dissolved in 0.05M HCl, it cannot be concluded that $ScCl_3$ was dissociating.

The external sample was the main source of activity in the mass separator bunker, besides traces due to internal contamination of the mass separator from previous collections. Therefore the dose rate in the mass separator bunker was investigated during the mass separation and collection (see Figure 5.21). The detector is located on the

opposite side of the target container opening, where the sample was loaded. The first increase in bunker dose rate happened by moving the extraction electrode closer to the ion source, which relates to the displacement of radionuclides that had adsorbed on the extraction electrode from previous collections. Another increase in dose rate was observed due to the heating of the transfer line and the displacement of radionuclides within the target container due to indirect heat.

The third noticeable dose rate increase was observed at target container temperatures of 1500–1760 °C (blue square in Figure 5.21). During the same timeframe, the target pressure increased slightly as well indicating particle evaporation and release. The increase in the dose rate in the bunker suggests outgassing together with radioactive material, as the only source that could give such an increase with the transfer line and ion source at constant parameters could be the target container where the sample was located.

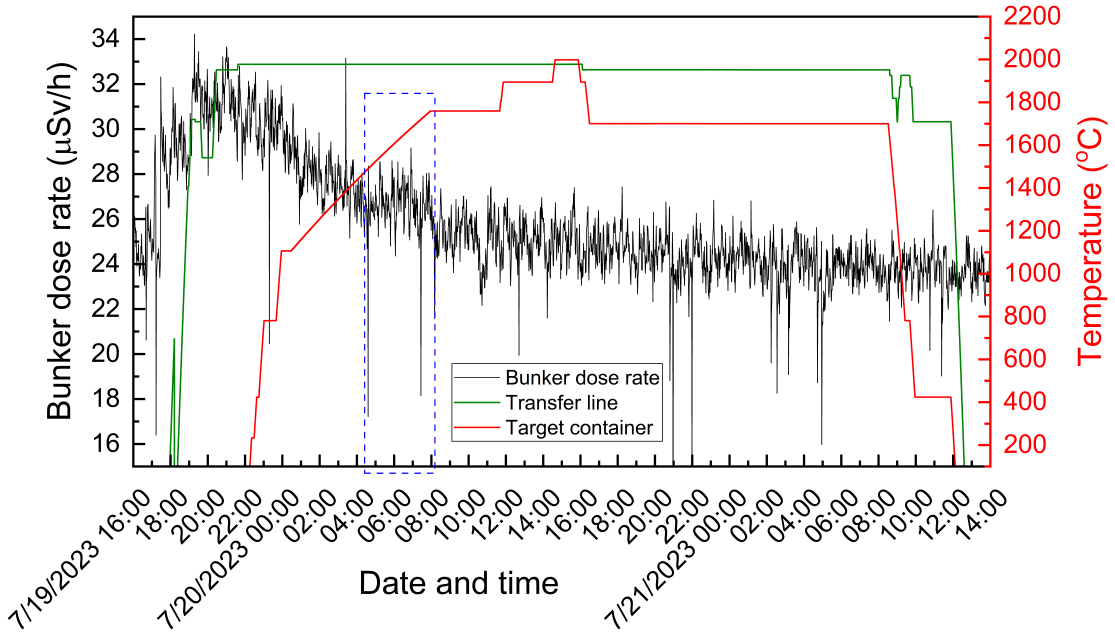

Figure 5.21: Transfer line and target container temperature against the mass separator bunker dose rate during collection.

The explanation of fluoride sideband absence observation could be $ScCl_3$ evaporation at the 1500–1760 °C range. The evaporation of $ScCl_3$ could not be reproduced in the stable beam tests, as no chloride sidebands were observed. The release of atomic Sc was also observed to happen above 1500 °C. Therefore, the above-mentioned increase in bunker dose rate at 1500 – 1760 °C could be attributed to elemental Sc(g) or molecular ScO(g) release from the decomposition of Sc_2O_3.

5.3.1 Dose rate measurements of the retrieved TISS

After the collection, the target was retrieved from CERN-MEDICIS mass separator frontend, opened and inspected. γ-ray dose rate measurements were taken at various places of the target (see Figure 5.22). The dose rate of the target container plug was measured

separately and contamination activity was measured with the γ-ray spectrometer. The dose rate measurements were done approximately at a 5 cm distance. One has to consider the TISS structure attenuation of the γ-rays and dose rate. Ta target container and transfer line makes the measurements underestimate the actual dose rate inside.

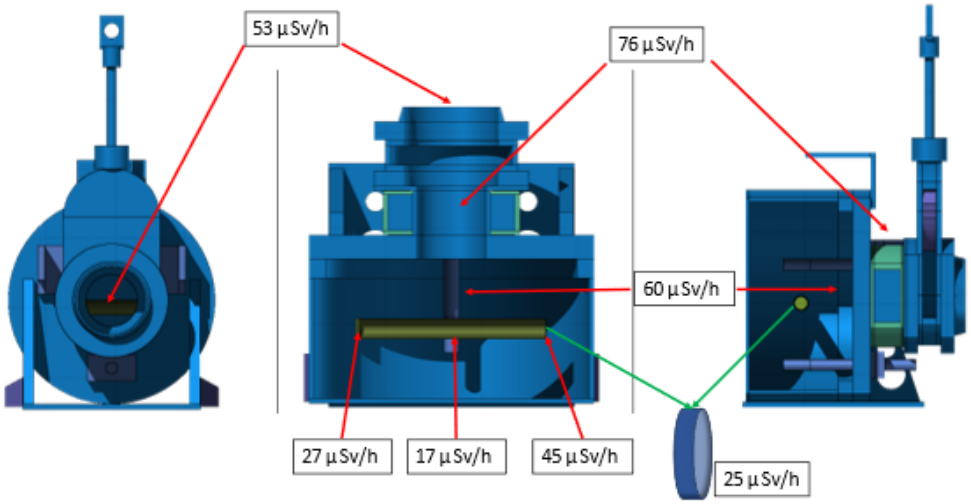

Figure 5.22: Dose rate measurements of opened TISS after collection.

The highest dose rate was measured where the ion source anode cavity is located (76 μSv/h), which can be explained as contamination from mass separator front-end. No dose rate and radionuclide activity by γ-ray spectrometry were measured in the retrieved Ta sample boat. Due to previously observed condensation of samples at the plug of the target container, it was expected that the plug to give the highest dose rate, however, this was not the case. The measured radioactivity of the plug was 4.3 $\pm$ 0.9 kBq after 2 days ($\sim$1 half-life of ^{44m}Sc. This suggests that all the sample was evaporated during the collection. According to the dose rate and radioactivity measurements of the TISS after separation, it can be concluded that the sample was released from the target container at temperatures of 1500–1760 °C either as atomic or another molecule sideband - ScO or $ScCl_x$ (x=1-3), with no fluorination happening to the sample throughout the collection.

5.4 Mono-atomic Sc resonant laser ionization

5.4.1 Stable isotope beam tests

Laser ionization tests were performed using a stable isotope $^{45}Sc_2O_3$ sample, which was dried on Ta foil and loaded into an empty TISS target container. Resonance laser ionization of Sc isotopes is only possible for mono-atomic Sc vapor. The obtained response to laser ionization shows that a chemical reduction and dissociation of the oxide molecule in the Ta target container had happened. Laser ionization was performed using a two-step resonant ionization scheme shown in Figure 5.23 developed at the AG LARISSA, Institute of Physics, Johannes Gutenberg University Mainz, Germany and CERN-MELISSA.

The first step laser excites the Sc from the 168.34 cm^{-1} state, for which the relative

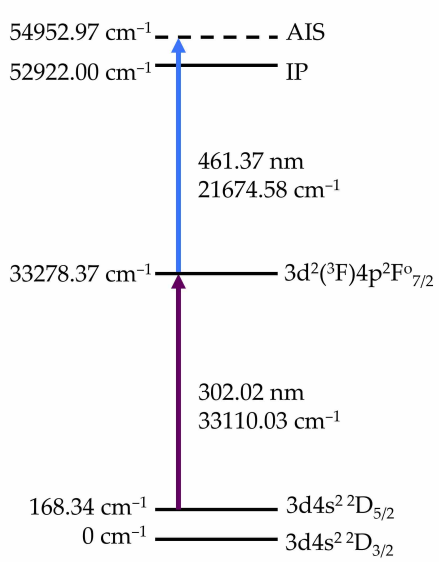

Figure 5.23: Two-step Sc laser resonant ionization scheme.

population is calculated to be 57.4% at 2000 °C, to the 33278.37 cm^{-1} energy level determined from [226]. The laser light for this step (302.02 nm) was generated using a titanium:sapphire (Ti:Sa) laser with an external frequency tripling unit [227]. The light for the second step (461.37 nm) was produced using an intra-cavity doubled Ti:Sa laser. A scan of the second ionization step in the range 21600.00–22400.00 cm^{-1} was first performed to determine the auto-ionization state AIS that gave the highest ion current. Several AIS were measured and compared, with the strongest observed at an energy of 54952.97 cm^{-1}. The second step laser was operated at this frequency for the efficiency test. The power of the lasers during the efficiency test was 25 mW and 225 mW for the 302.02 nm and 461.37 nm light respectively. Figure 5.24 shows the saturation curve of both excitation steps. The parameter indicated in the figure, P_{80} is the laser power of the step that is required to observe 80% of the maximum possible achievable laser ion current and is taken as the power at which the transition is considered saturated. In this case, step 1 is well-saturated, whereas step 2 has not reached saturation. With a higher power for step 2, the laser ion beam current could be improved by a factor of up to $\times 1.5$.

During the tests, mono-atomic laser ionized Sc ions were observed when the target container temperature was increased over 1530 ± 10 °C for two different TISS with a transfer line temperature of 2000 °C. One of the TISS was equipped with Re and the other with a W surface ion source. In order to obtain relevant beam current for the Sc collection, the target container temperature had to be increased over 2000 °C. This temperature well exceeds the metallic foil target material melting points that are considered as suitable for radioactive Sc production, making it almost impossible to collect atomic Sc with high efficiency and reasonable collection time. In addition, from a TISS with W transfer line/surface source, from a stable sample of 600 nAh (1 μg), 0.38 nAh were detected on the separated beam Faraday cup over the course of 2 days corresponding to a collection efficiency of around 0.06 %. This is the lower estimation of efficiency and the actual value should be measured in future research. Also, the

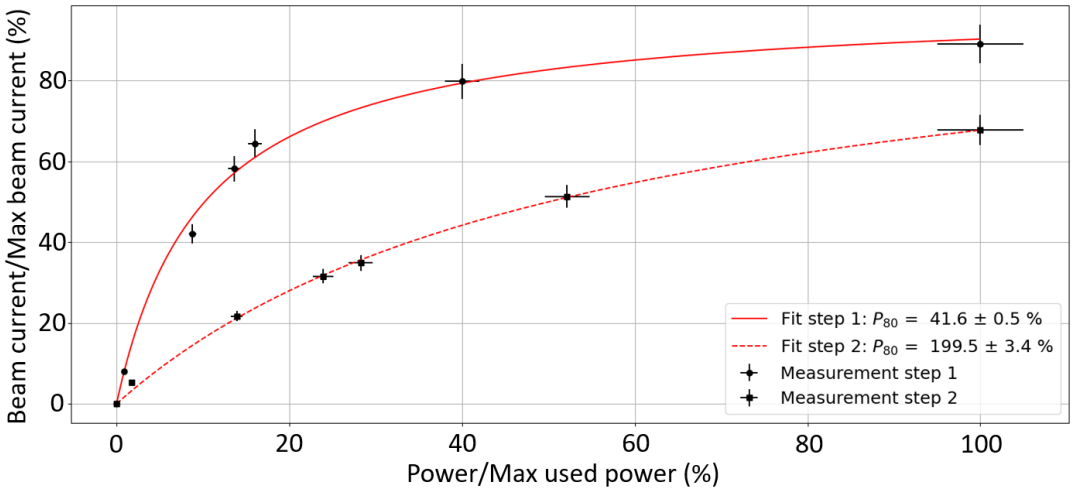

Figure 5.24: Laser power saturation for Sc ionization. Data was fitted with $\frac{I}{I_0} = \frac{P/P_{sat}}{1+P/P_{sat}}$. X-axis: Power as a fraction of the nominal operating power during the efficiency tests.

chemical dissociation impact may underestimate the efficiency and the actual value may be higher for radionuclides, released from metallic ^{nat}Ti and ^{nat}V foils.

5.4.2 Radioactive Sc ionization

The same ionization scheme was tested for the ionization of Sc with an irradiated ^{nat}V foil TISS #805M. The TISS used for this experiment was equipped with the back of the transfer line heated container and VADIS ion source. Even though the VADIS ion source is not the best fit for laser ionization, atomic $^{45}Sc^{+}$, $^{46}Sc^{+}$ and $^{47}Sc^{+}$ were observed with laser resonance when the target container temperature of 1570–1700 °C was achieved. After one day of operation, mono-atomic laser ionized species were no longer observed even by increasing the target container temperature, indicating full release of the Sc isotopes from the target material in an atomic form. Later tests, however, showed that molecular form Sc radionuclides could still be obtained, suggesting condensation in a target container cold spot of a fraction that was previously released. Laser ionization tests of Sc were also performed with a target material fluorinated before irradiation, however, no laser resonance and mono-atomic Sc presence was observed with the same operating conditions.

Branching of atomic laser ionized Sc

Performing 2 sets of same-speed mass scans with the lasers being directed in the ion source (laser ON) or blocked by a shutter (lasers OFF) can indicate the approximate ratio and confirm the Sc laser resonant ionization. As the target was not loaded with a stable ^{45}Sc sample, the observed ^{45}Sc comes from impurities in the target material or proton irradiation of the ^{nat}V material.

The ratio of observed isotopes does not correspond to the produced isotope ratio, because of the unsuitable ion source design for laser ionized isotope collection. Without applied voltage for the VADIS, the ion source acts as a trap and can delay ions, produced in the transfer line. For such a mode of operation, a surface (hot cavity) or the Versa-

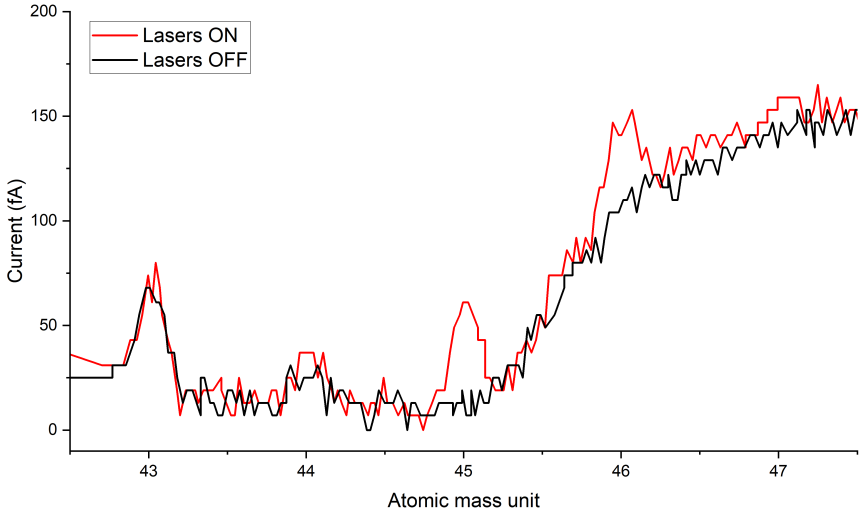

Figure 5.25: Mass scans with lasers ON and OFF on elemental Sc isotope atomic mass region

Table 5.13: The laser ionized Sc isotope currents, radioactivity and ratios for target #805M.

Isotope	Laser ionized isotope current, fA	Laser ionized isotope radioactivity, Bq/s	Laser ionized isotope ratio[a]	Produced radioactivity (decay corrected), Bq	Produced isotope ratio[a]
^{44g}Sc[b]	11.95	1.6×10^{-2}	1	5.1×10^{7}	0.03
^{44m}Sc[b]	0.05	2.5×10^{-1}	23	7.8×10^{8}	6
^{45}Sc	48	-	-	-	-
^{46}Sc	37	1.1×10^{-2}	1	1.2×10^{8}	1
^{47}Sc	18	2.7×10^{-1}	25	1.0×10^{9}	8

[a] Normalized to ^{46}Sc. [b] Isomer corrected ratio.

tile Arc Discharge Laser Ion Source (VADLIS) are more applicable [228]. The observed collection rates would be too low for a regular collection, nevertheless, laser ionization can act as a probe to verify Sc isotope release from the TISS. It should be noted that no laser-ionized isotopes could be observed after the fluorination of the TISS.

5.5 Radiochemical separation

Mass separation is an effective tool to increase the isotopic purity of the radionuclide of interest. High chemical selectivity of mass separation could be obtained with laser ionization, but ways to increase atomic Sc density in the ion source still have to be developed. The molecular beam approach has low chemical selectivity on the collection. For instance, if a beam of 110 nA (85 amu) is implanted onto a collection foil and the $^{47}ScF_2^+$ implantation rate is 16.9 kBq/min, the ratio of $^{47}TiF_2^+$ isobars ^{47}Ti/^{47}Sc is $\sim$ 5800/1 per second.

Conventional radiochemical separation is also needed to remove the radionuclides from

the implantation foil matrix, with no interference of metallic impurities on the radiolabelling. For Sc radionuclide collections, multiple materials, such as Zn, Al, Cu, NaCl, were used as stopping layers during the collection. Based on the collection foil used, different parameters for the separation had to be applied.

Typically metal-covered gold foils are used for radionuclide collections. As full removal of the radionuclides is difficult to achieve within a few minutes dissolution, or the implantation had happened in the gold layer, recycling of the gold layer becomes challenging. Another challenge is the relatively large amount of metallic isobars collected or dissolved from the collection foil, which can affect the resin efficiency. For these reasons, larger-scale electrochemical methods are promising, where a less expensive foil can be used, dissolved, and fully recovered on the electrodes. Sc radiochemical purification methods are summarized in Figure 5.26.

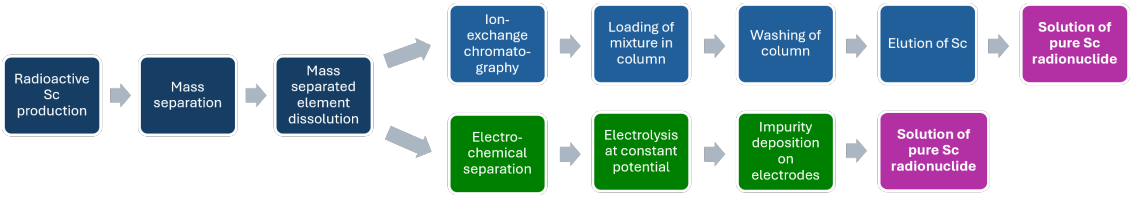

Figure 5.26: Full Sc radionuclide separation and purification process flowchart

5.5.1 Ion exchange column separation

The Diglycolamide (DGA) resins are the most widely used for Sc radiochemical separation from other contaminants. On the market, there are two types of resin - either N,N,N′,N′-tetra-n-octyldiglycolamide (DGA Resin, Normal) or N,N,N′,N′-tetrakis-2-ethylhexyldiglycolamide (DGA Resin, Branched). For the ion exchange chemical separations, the DGA branched resins were used. HNO_3 or HCl in various concentrations were used as eluent, depending on the collection foil used for the particular collection.

Stable Sc separation from implantation foil matrix

The chemical separation efficiency of Sc from the main stopping layer material (Zn or Al) was initially tested with a simple gravitational force column and standard solution mixture. Various columns for the resin were tested, with 3 mm columns yielding the best separation. Before separation, 70 mg of DGA resin (50–100 μm) for each separation was immersed and soaked in 2.5 M HNO_3 for a period of $\sim$24 hours.

The resin was loaded in the column on a glass wool and 4 mL 8 M HNO_3 was used to condition the resin. The standard sample (Zn/Sc) was dried and then dissolved with 6 mL 8 M HNO_3 and introduced into the column. 5 mL of 2 M HNO_3 were used to wash the column. Elution was performed with 2 mL of Deionized (DI) water. For the samples (Al/Sc), HCl was used instead of HNO_3. For these tests, an aqueous mixture of 2 ppm (mg/L) of Sc^{3+} and 135 ppm of Zn^{2+} ions in 8 M HNO_3 or Al^{3+} in 8 M HCl were used. The samples were analyzed with Inductively Coupled Plasma - Mass Spectrometry (ICP-MS) The obtained separation results are shown in Table 5.14 and 5.15

Table 5.14: Results of ^{45}Sc chemical separation from Zn[a].

Fraction	Sc concentration, mg/L	Sc fraction from initial sample, %	Zn concentration, mg/L	Zn fraction from initial sample, %
Feedthrough	<LOD	-	128	95
Wash	<LOD	-	3.92	2.90
Product	1.90	95	0.33	0.25

[a] Corrected by dilution factors

Table 5.15: Results of ^{45}Sc chemical separation from Al[a].

Fraction	Sc concentration, mg/L	Sc fraction from initial sample, %	Al concentration, mg/L	Al fraction from initial sample, %
Feedthrough	<LOD	-	117	87
Wash	4.12×10^{-4}	0.02	8.98	6.65
Product	1.81	91	0.43	0.32

[a] Corrected by dilution factors

To simulate the mass separation aspect, a stable $^{45}ScF_2^+$ was implanted in Zn and Al-coated gold foils and used as starting samples for the automated setup development. Although no Sc was successfully implanted in multiple cases, the separation still resulted < 0.63 % of the metallic layer material in the product fraction, measured by Inductively Coupled Plasma - Mass Spectrometry (ICP-MS). The obtained results indicate that full separation from the implantation foil metallic layer can be achieved with a >90 % Sc recovery with the DGA resin and 3 mm inner diameter column. A concentration of 8 M HNO_3 was considered appropriate for these tests since similar concentrations have been reported for the conditioning of the resin [114].

Semi-automated separation

The gravitational separation process time was limited by the flow rate of the eluent, which resulted in ∼5 hours for the whole separation process. Therefore an automated setup with a controlled flow rate was developed. A peristaltic pump was added to the column, to increase and control the flow rate of the eluent. A typical flow rate of the eluent was set in the range of 0.3–1.0 mL/min. Two additional peristaltic pumps were added to automate the dissolution in a closed environment and loading of the eluents for the column (see Figure 5.27). The setup was designed in a way that almost no interaction, besides the insertion of foil in the sample vial, is needed. This is important from the radiation protection aspect, as the collected activities on the foil would increase.

Tests with Diba Omnifit Microbore Benchmark 3 mm and Diba Omnifit EZ 5 mm inner diameter columns were conducted to verify the setup integrity. The 5 mm column features an adjustable frit disc plunger to decrease the dead volume (see Figure 5.28). The stainless steel frit discs of the columns were tested in 8 M HNO_3 (24-hour hold time) for possible Fe^{3+} contamination. After two holds, only 0.14 ppm Fe^{3+} was observed

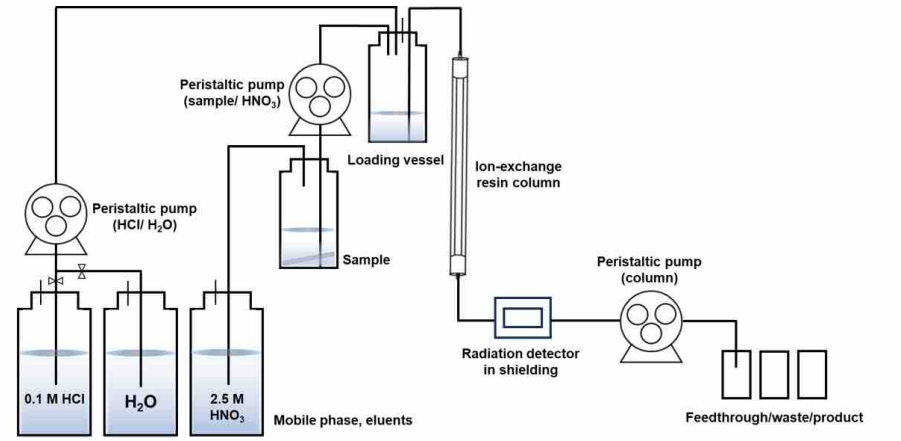

Figure 5.27: Automated radiochemical separation schematic

and no trace of corrosion or Fe^{3+} was present in the subsequent H_2O wash phase. It should be noted, that only 2.5 M HNO_3 was used for the separation process. 0.1 M HCl was used for the elution of Sc from the columns and this concentration is within the manufacturer's chemical compatibility evaluation [229].

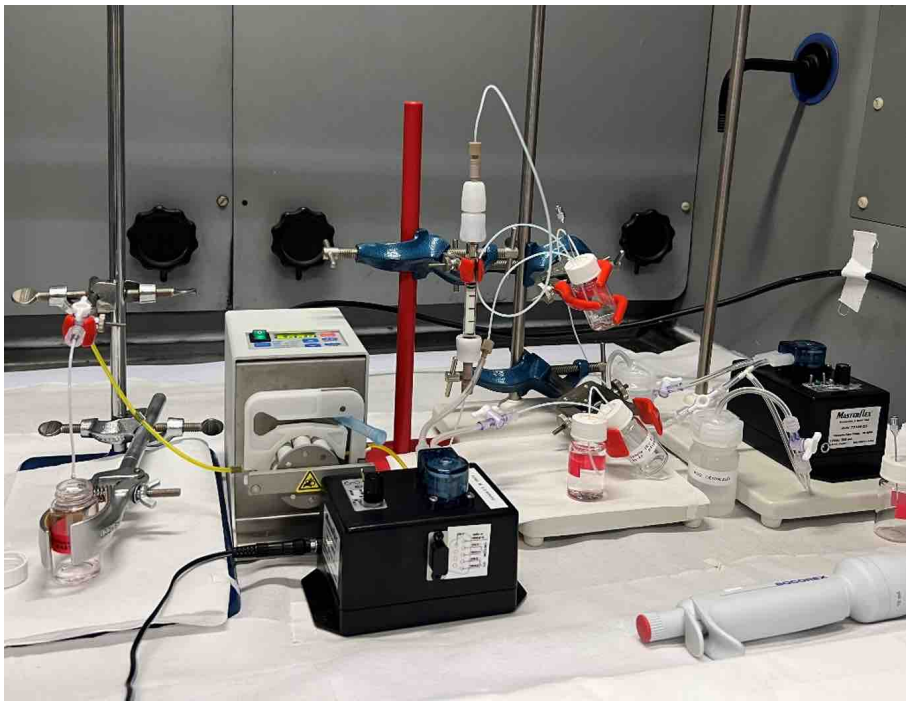

Figure 5.28: Automated radiochemical separation test setup

The automated setup was tested twice with mass-separated radioactive ^{47}Sc, collected at CERN-MEDICIS. Each separation was done with a different diameter column. The resin mass used was ∼0.10 g for the Diba Omnifit Benchmark Microbore 3 mm column achieving a resin bed height of 3 cm and 0.18 g for the Diba Omnifit EZ column with 5 mm inner diameter column resulting in a resin bed height of 3.2 cm. During mass separation, ^{47}Sc was implanted in a NaCl-covered Al foil and used as the test samples.

The obtained results are shown in Tables 5.16 and 5.17. The uncertainty for the obtained results originates from γ-ray spectrometry measurements.

Table 5.16: Results of ^{47}Sc automated chemical separation with Diba Omnifit Benchmark Microbore 3 mm column.

Sample	**Radioactivity[a], Bq**
NaCl foil before separation	8006 $\pm$ 880
NaCl foil after separation	323 $\pm$ 109
^{47}Sc eluate[b]	6516 $\pm$ 820

[a] Decay-corrected to the time of chemical separation
[b] Elution maximum speed was 0.34 mL/min

Table 5.17: Results of ^{47}Sc automated chemical separation with Diba Omnifit EZ 5 mm column.

Sample	**Radioactivity[a], Bq**
NaCl foil before separation	8128 $\pm$ 890
NaCl foil after separation	372 $\pm$ 77
^{47}Sc eluate[b]	6171 $\pm$ 684

[a] Decay-corrected to the time of chemical separation
[b] Elution maximum speed was 0.45 mL/min

In both separations, no ^{47}Sc was trapped within the column or capillaries of the system, indicating a high recovery yield (>99%). In both cases also a small fraction of 4–6 % remained on the initial foil, which could be accounted for implantation in the Al layer, which was not attacked by the HNO_3. The radiochemical yield for the Diba Omnifit Benchmark Microbore 3 mm column test resulted in 81 $\pm$ 9 % and 76 $\pm$ 12 for the % Diba Omnifit EZ 5 mm column test. The chemical purity of the obtained samples must still be evaluated employing ICP-MS and ICP-OES.

The elution profile with a portable γ-ray ThermoScientific FH 40G-L10 radiometer was measured to determine the onset and end of the ^{47}Sc elution from the automated chemical separation with Diba Omnifit EZ 5 mm column (see Figure 5.29). The elution profile measurement was started once the eluent was switched to 0.1 M HCl. The time for the complete elution process took 12 minutes. It was found that the total volume of 0.1 M HCl in which all ^{47}Sc had eluted was 5 mL. The saturation was achieved in 3 mL, therefore the initial eluent collected up to 400 seconds (see Figure 5.29) could be discarded in the upcoming separations, to obtain higher concentration precursor for radiolabelling.

With the automated setup, the total time of the radiochemical separation, including the setup, column conditioning, and disassembly, required $\sim$2.5 hours and minimal manual actions, such as loading the foil in the vial and switching the valves. The automated setup provides the possibility to dissolve the layer with collected radionuclides in a continuous flow of the solvent, maximizing the overall recovery yield and minimizing radiation and contamination risks. Ion-exchange chromatography offers the means of separating Sc from impurities at good efficiency (more than 90 %). However, it must be noted that not all metal ions can be separated with the same efficiency and still require further method optimization. A more advanced system, with reduced "dead volume"

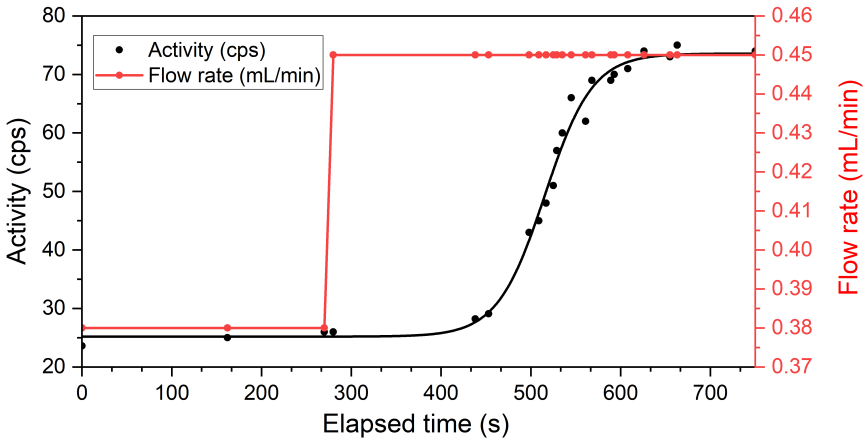

Figure 5.29: Automated radiochemical separation product fraction elution profile with Diba Omnifit EZ 5 mm column.

in the valves, bypass loop, flow meter, and fractional collection system is proposed for further development, see Figure 5.30.

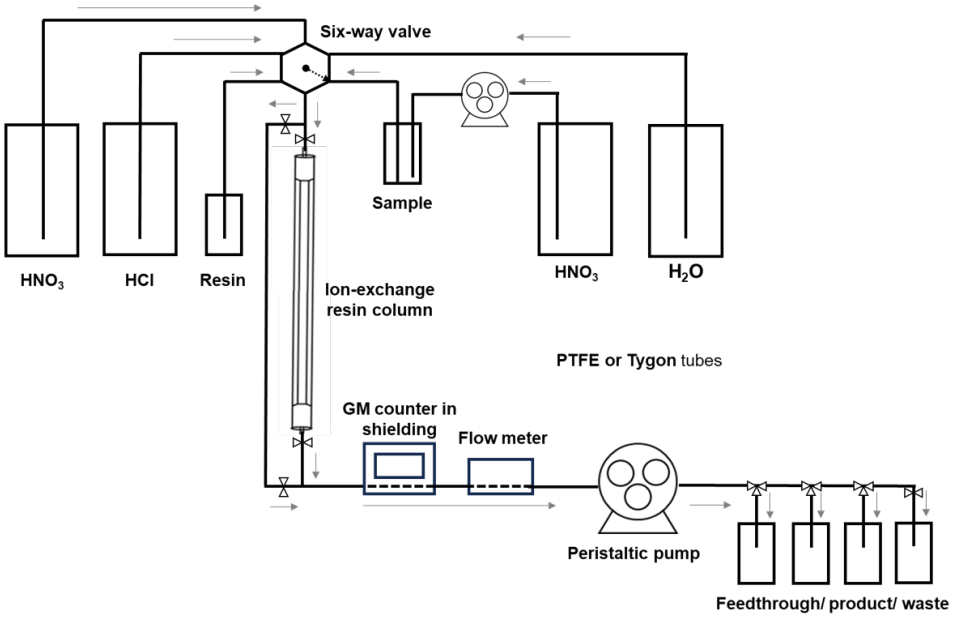

Figure 5.30: Schematic of proposed upgrade for automated radiochemical separation

5.5.2 Electrochemical separation

The electrochemical method was investigated to increase the ion exchange chromatography efficiency by removing fully or partially contaminant ions, such as V^{2+}, Ti^{3+} and Zn^{2+}. These ions are expected to be in higher concentration after collection foil dissolution due to the isobar collection during mass separation or found as the implantation layer. The initial assembly consisted of two graphite electrodes (see Figures 5.31 and 5.32a). Stable isotope tests with aqueous solutions using relevant chemical element

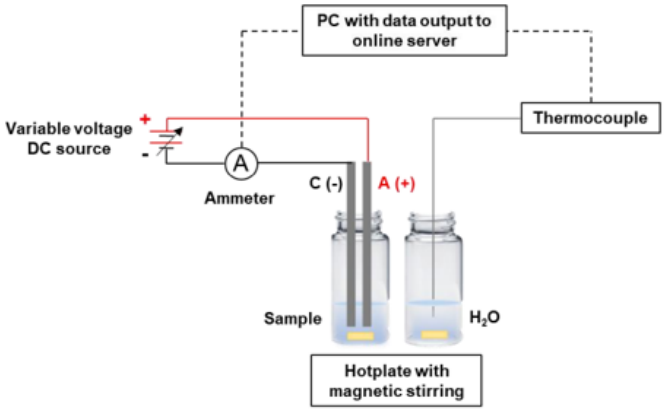

Figure 5.31: Schematic of electrochemical separation setup

standard solution mixtures showed partial removal of impurities such as Zn, V and Ti. Various key factors impact the separation process time and efficiency, such as the temperature of electrolysis bath, net-ionic force in the solution, electrode type and surface area and solution stirring rate.

A ^{47}Sc sample, collected on a NaCl-coated Al foil was used for a test separation. Since the rate of deposition on the cathode is directly proportional to the cathodic current, therefore, in cases of low electrolyte concentration (ionic strength < 1 M) the solution was heated up to 55 °C and to increase ion mobility and the current.

8.0 % from the initial sample activity of 8698 $\pm$ 965 Bq was retained on the anodes used in the electrolysis, due to the porosity of electrodes. This finding led to create a solid Pt coating layer on a pair of electrodes for further development (see Figure 5.32b). The results from the electrochemical separation confirmed that Sc cannot be deposited on an electrode in aqueous electrolysis, which becomes useful if a less expensive Cu foil is used to collect the radionuclides during mass separation. The Cu can be fully recovered, leaving the radionuclides in the solution.

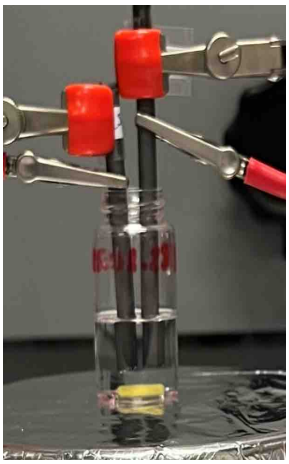

(a) Graphite electrodes

(b) Platinated electrodes

Figure 5.32: Graphite electrodes used for electrochemical separation

Electrochemical separation in aqueous solutions presents challenges regarding water electrolysis overtaking metal ion deposition at voltages >1.23 V. A non-aqueous method in anhydrous ethanol promises better separation possibilities. Initial tests showed that in a non-aqueous solution at a voltage of 1.40 V, Sc deposits better than in an aqueous solution at voltages of 1.80 V, 2.10 V and 2.20 V. Nevertheless, limitations due to solvent properties (volatility, hygroscopy) must be addressed. To sum up, the aqueous electrochemical method should still be used with ion exchange chromatography.

5.6 Conclusions and outlook

The highest Sc radionuclide collection rate (kBq/min) per flux of injected reactive gas at 1550 °C via molecular ion beam method was obtained for ^{nat}V foil target. However, the ^{nat}TiC target in terms of overall collection efficiency and collection rate, that were controlled by the slow diffusion of Sc radionuclides, compared to foil target materials. The collection rate of up to ∼0.5 MBq/min could be estimated from ^{nat}TiC target, with the current collection parameters and increased reactive gas flux.

Based on the results and release behavior from ^{nat}V metallic foils and ^{nat}TiC powder target materials, the parameters for Sc collection from ^{nat}Ti metallic foils should be again investigated, for example, increasing the specific surface area in the target container to facilitate Sc molecular beam formation.

Generator radionuclides can also be collected by mass separation but do not provide an advantage over the radiochemical methods. The newly identified sustained and controlled release of Sc radionuclides over 1–2 weeks from fluorinated high specific surface area ^{nat}TiC target materials shows the potential in ^{nat}VC, ^{nat}VB powder and nanoscale ^{nat}TiC investigation as target materials for Sc collections.

Stable and radioactive atomic Sc^+ was obtained for the first time with a two-step laser resonance ionization scheme and Ti:Sa crystal lasers. Collection efficiency tests with stable $^{45}Sc_2O_3$ show the limitations of this approach because of the low collection efficiency and required collection temperatures that are well above the melting points of ^{nat}Ti and ^{nat}V. As the collection rate may be limited due to $^{45}Sc_2O_3$ chemical dissociation, its impact on the obtained value should be investigated in future studies. The laser resonant ionization of Sc showed that the $^{45}Sc_2O_3$ undergoes non-ionizing dissociation within the TISS. It was also shown that, combined with VADIS ion source, laser ionization could serve as a monitor to verify Sc radionuclide release onset from metallic foil target materials before reactive gas injection and molecular ion beam formation.

The external $^{43}ScCl_3/^{44g/m}ScCl_3$ sample was released from the target container at temperatures of 1500–1760 °C as atomic Sc, ScO or $ScCl_x$ (x=1-3) molecules. No reaction with CF_4 had happened throughout the collection

Methods of Sc radiochemical separation from various collection foils were implemented and included in a semi-automated setup with >80 % radiochemical yield. The process can still be optimized to reduce the final elution volume. Further investigations have to be done with ICP-MS to investigate chemical purity.

6 Conclusions

1. The thermal release studies indicated that the limiting factor for Sc radionuclide release from metallic foil rolls is desorption from the material surface. Full Sc release from target material within one hour after reaching the set temperature was achieved at 1200 °C for non-embossed, 1450 °C for embossed ^{nat}Ti and 1600 °C for non-embossed ^{nat}V foil samples. In contrast to the expected, the same Sc radionuclide relative release fraction from embossed metallic ^{nat}Ti foils was achieved at temperatures ∼300 °C higher than from the corresponding non-embossed ones.

2. Once thermally released from the target material, the Sc migration within the TISS and effusion was not the limiting cause of low collection efficiency of < 1 %, being in contradiction to the theoretical estimations. Sc radionuclide release in atomic and molecule form from TISS were observed at target material temperatures above 1550 °C, therefore high melting point and cyclotron-suitable target materials, such as ^{nat}V metallic foils (T_m = 1910 °C) and ^{nat}TiC (T_m = 3160 °C), are more suitable for ISOL than ^{nat}Ti foil target.

3. Comparing the thick target activity yield (TTY) theoretical estimations of ^{47}Sc for 1-hour irradiation of the ^{nat}Ti and ^{nat}V target materials, Sc radionuclide production cycle with a pulsed 2 μA 1.4 GeV proton beam in a 200 mm thick ISOL target and subsequent Sc isotope mass separation step results in ∼40 MBq is equivalent to a typical 1 mm cyclotron Sc production cycle without mass separation step and 10 μA 30–70 MeV protons result in 50–70 MBq.

4. Evaporation of Sc radionuclides was achieved in the form of ScF_3. The ScF_x^+ (x=1–2) molecular ion beams were obtained from all target materials used in this thesis with the highest abundance for ScF_2^+ ions. The ^{nat}TiC target material in terms of collection efficiency (∼2 %), high material temperature (∼2050 °C) and achieved collection rate (17 kBq/min) was the most suitable ISOL target material for ScF_2^+ molecular ion beam mass separation and collection. With a maximized CF_4 reactant gas flux of 1.1 nmol/s, a ^{47}Sc collection rate of up to ∼0.5 MBq/min from irradiated ^{nat}TiC ISOL target could be envisaged.

5. Sc generator ^{44}Ti and ^{47}Sc radionuclide collection by mass separation was achieved, however does not provide advantages over radiochemical methods due to low radionuclide production yield of <10 MBq per batch in the 200 mm ISOL mass separator targets.

6. Atomic Sc^+ radionuclides from irradiated ^{nat}V with a two-step laser resonance

ionization scheme were obtained for the first time. A potential limitation of laser ionization when combined with metallic ^{nat}Ti and ^{nat}V target materials is the chemical dissociation and reduction rate of Sc radionuclides that are stabilized as Sc_2O_3 molecules. To obtain a collection efficiency of at least 0.06 %, target temperatures higher than 2000 °C were required, which are well above the target material melting points.

7. Methods of Sc radiochemical separation from various collection foils were implemented in a semi-automated setup with >80 % radiochemical yield, which helps to minimize manipulations with liquids and exposure to ionizing radiation for personnel. For large-scale V^{2+}, Ti^{3+} and Zn^{2+} isobar contaminant removal before ion exchange chromatography column separation, an electro-radiochemical separation method was established.

8. The production of high molar activity (TBq/μmol) and high radiochemical purity (>98 %) ^{43}Sc, $^{44g/m}$Sc and ^{47}Sc radionuclides from pre-clinical up to single clinical doses is achievable by mass separation from 200 mm thick and cyclotron-suitable ISOL target materials.

Bibliography

[1] F. Bray, M. Laversanne, H. Sung, J. Ferlay, R.L. Siegel, I. Soerjomataram, A. Jemal, *Global cancer statistics 2022: GLOBOCAN estimates of incidence and mortality worldwide for 36 cancers in 185 countries*, CA: a cancer journal for clinicians **74**, 229 (2024)

[2] C. Müller, K.A. Domnanich, C.A. Umbricht, N.P. van der Meulen, *Scandium and terbium radionuclides for radiotheranostics: current state of development towards clinical application*, The British journal of radiology **91**, 20180074 (2018)

[3] *Nucleonica*, `https://nucleonica.com/`, accessed: 2023-01-10

[4] J.V. Kratz, *Nuclear and radiochemistry: Fundamentals and applications* (John Wiley & Sons, 2022)

[5] G. Friedlander, J.W. Kennedy, E.S. Macias, J.M. Miller, *Nuclear and radiochemistry* (John Wiley & Sons, 1981)

[6] J.P. Fernandes Pinto Ramos, Ph.D. thesis, *Titanium carbide-carbon porous nanocomposite materials for radioactive ion beam production processing, sintering and isotope release properties*, EPFL, Lausanne (2017)

[7] A. Vértes, S. Nagy, Z. Klencsár, *Handbook of nuclear chemistry*, **2** (2003)

[8] R. Bonetti, M. Chadwick, P. Hodgson, B. Carlson, M. Hussein, *The Feshbach-Kerman-Koonin multistep compound reaction theory*, Physics Reports **202**, 171 (1991)

[9] S. Benck, *Mesures de sections efficaces doublement différentielles de particules chargées légères induites par neutrons rapides sur 16 O et 27 Al (En=25-65 MeV).* (1999), `https://api.semanticscholar.org/CorpusID:93265885`

[10] C. Duchemin, Ph.D. thesis, *Étude de voies alternatives pour la production de radionucléides innovants pour les applications médicales*, Université de Nantes (2015), `http://www.theses.fr/2015NANT2061`

[11] J. Ballof, Ph.D. thesis, *Radioactive Molecular Beams at CERN-ISOLDE*, Johannes Gutenberg-Universität Mainz (2021), presented 09 Dec 2021, `https://cds.cern.ch/record/2797475`

[12] L.M. Kerby, S.G. Mashnik, A.J. Sierk, *Preequilibrium Emission of Light Fragments in Spallation Reactions*, Nuclear Data Sheets **118**, 316 (2014)

[13] J.C. David, *Spallation reactions: A successful interplay between modeling and applications*, The European Physical Journal A **51**, 68 (2015)

[14] J. Klimo, *Properties and production possibilities of exotic nuclei* (2019)

[15] H. Dadgar, E. Jafari, H. Ahmadzadehfar, S.J. Rekabpour, M.R. Ravanbod, M. Kalantarhormozi, I. Nabipour, M. Assadi, *Feasibility and therapeutic potential of the 68Ga/177Lu-DOTATATE theranostic pair in patients with metastatic medullary thyroid carcinoma*, in *Annales d'Endocrinologie* (Elsevier, 2023), Vol. 84, pp. 45–51

[16] E. Lopci, A. Chiti, M.R. Castellani, G. Pepe, L. Antunovic, S. Fanti, E. Bombardieri, *Matched pairs dosimetry: 124 I/131 I metaiodobenzylguanidine and 124 I/131 I and 86 Y/90 Y antibodies*, European journal of nuclear medicine and molecular imaging **38**, 28 (2011)

[17] *Prismap - sc medical radionuclide nuclear properties*, `https://www.prismap.eu/radionuclides/portfolio/`, accessed: 2024-4-19

[18] T.V. Lima, S. Gnesin, K. Strobel, M.d.S. Pérez, J.E. Roos, C. Müller, N.P. van der Meulen, *Fifty shades of scandium: Comparative study of pet capabilities using sc-43 and sc-44 with respect to conventional clinical radionuclides*, Diagnostics **11**, 1826 (2021)

[19] *National nuclear data center*, `https://www.nndc.bnl.gov/nudat3/`, accessed: 2023-12-12

[20] E. Garcia-Torano, V. Peyres, M. Roteta, A. Sanchez-Cabezudo, E. Romero, A.M. Ortega, *Standardisation and precise determination of the half-life of 44Sc*, Applied Radiation and Isotopes **109**, 314 (2016)

[21] A. Singh, N.P. van der Meulen, C. Müller, I. Klette, H.R. Kulkarni, A. Türler, R. Schibli, R.P. Baum, *First-in-human PET/CT imaging of metastatic neuroendocrine neoplasms with cyclotron-produced 44Sc-DOTATOC: a proof-of-concept study*, Cancer biotherapy and radiopharmaceuticals **32**, 124 (2017)

[22] C. Müller, M. Bunka, S. Haller, U. Köster, V. Groehn, P. Bernhardt, N. van der Meulen, A. Türler, R. Schibli, *Promising prospects for 44Sc-/47Sc-based theragnostics: application of 47Sc for radionuclide tumor therapy in mice*, Journal of nuclear medicine **55**, 1658 (2014)

[23] L. Deilami-Nezhad, L. Moghaddam-Banaem, M. Sadeghi, M. Asgari, *Production and purification of Scandium-47: A potential radioisotope for cancer theranostics*, Applied Radiation and Isotopes **118**, 124 (2016)

[24] D. Giovagnoli, Theses, *Image reconstruction for three-gamma PET imaging*, Ecole nationale supérieure Mines-Télécom Atlantique (2020), `https://theses.hal.science/tel-03123557`

[25] C. Duchemin, A. Guertin, F. Haddad, N. Michel, V. Métivier, *Production of scandium-44m and scandium-44g with deuterons on calcium-44: cross section measurements and production yield calculations*, Physics in Medicine & Biology **60**, 6847 (2015)

[26] *Experimental nuclear reaction data (exfor). database version of 2023-11-13*, `https://www-nds.iaea.org/exfor/`, accessed: 2023-12-12

[27] K.A. Domnanich, C. Müller, M. Benešová, R. Dressler, S. Haller, U. Köster, B. Ponsard, R. Schibli, A. Türler, N.P. van Der Meulen, *47Sc as useful β—emitter for the radiotheragnostic paradigm: a comparative study of feasible production routes*, EJNMMI Radiopharmacy and Chemistry **2**, 1 (2017)

[28] R. Mikolajczak, S. Huclier-Markai, C. Alliot, F. Haddad, D. Szikra, V. Forgacs, P. Garnuszek, *Production of scandium radionuclides for theranostic applications: towards standardization of quality requirements*, EJNMMI Radiopharmacy and Chemistry **6**, 1 (2021)

[29] C.S. Loveless, L.L. Radford, S.J. Ferran, S.L. Queern, M.R. Shepherd, S.E. Lapi, *Photonuclear production, chemistry, and in vitro evaluation of the theranostic radionuclide 47 Sc*, EJNMMI research **9**, 1 (2019)

[30] K. Minegishi, K. Nagatsu, M. Fukada, H. Suzuki, T. Ohya, M.R. Zhang, *Production of scandium-43 and -47 from a powdery calcium oxide target via the nat/44Ca(α,x)-channel*, Applied Radiation and Isotopes **116**, 8 (2016)

[31] T.S. Carzaniga, M. Auger, S. Braccini, M. Bunka, A. Ereditato, K.P. Nesteruk, P. Scampoli, A. Türler, N. van der Meulen, *Measurement of 43Sc and 44Sc production cross-section with an 18 MeV medical PET cyclotron*, Applied radiation and isotopes **129**, 96 (2017)

[32] T.J. De Waal, M. Peisach, R. Pretorius, *Activation cross sections for proton-induced reactions on calcium isotopes up to 5· 6 MeV*, Journal of Inorganic and Nuclear Chemistry **33**, 2783 (1971)

[33] K.A. Domnanich, R. Eichler, C. Müller, S. Jordi, V. Yakusheva, S. Braccini, M. Behe, R. Schibli, A. Türler, N.P. Van der Meulen, *Production and separation of 43Sc for radiopharmaceutical purposes*, EJNMMI radiopharmacy and chemistry **2**, 1 (2017)

[34] C.S. Loveless, J.R. Blanco, G.L.D. III, R.T. Elbahrawi, T.S. Carzaniga, S. Braccini, S.E. Lapi, *Cyclotron Production and Separation of Scandium Radionuclides from Natural Titanium Metal and Titanium Dioxide Targets*, Journal of Nuclear Medicine **62**, 131 (2021), `https://jnm.snmjournals.org/content/62/1/131.full.pdf`

[35] R. Chakravarty, S. Chakraborty, R. Ram, A. Dash, *An electroamalgamation approach to separate 47Sc from neutron-activated 46Ca target for use in cancer theranostics*, Separation Science and Technology **52**, 2363 (2017)

[36] A. Jafari, M.R. Aboudzadeh, H. Azizakram, M. Sadeghi, B. Alirezapour, S. Rajabifar, K. Yousefi, *Investigations of proton and deuteron induced nuclear reactions on natural and enriched Titanium, Calcium and Vanadium targets, with special reference to the production of 47Sc*, Applied Radiation and Isotopes **152**, 145 (2019)

[37] G. Pupillo, L. Mou, A. Boschi, S. Calzaferri, L. Canton, S. Cisternino, L. De Dominicis, A. Duatti, A. Fontana, F. Haddad et al., *Production of 47Sc with natural vanadium targets: results of the PASTA project*, Journal of Radioanalytical and Nuclear Chemistry **322**, 1711 (2019)

[38] E. Mamis, C. Duchemin, V. Berlin, C. Bernerd, M. Bovigny, E. Chevallay, B. Crepieux, V. Gadelshin, R. Heinke, R. Hernandez et al., *Target Development*

towards First Production of High-Molar-Activity ^{44g}Sc and ^{47}Sc by Mass Separation at CERN-MEDICIS, Pharmaceuticals **17**, 390 (2024)

[39] R. Michel, R. Bodemann, H. Busemann, R. Daunke, M. Gloris, H.J. Lange, B. Klug, A. Krins, I. Leya, M. Lüpke et al., *Cross sections for the production of residual nuclides by low-and medium-energy protons from the target elements C, N, O, Mg, Al, Si, Ca, Ti, V, Mn, Fe, Co, Ni, Cu, Sr, Y, Zr, Nb, Ba and Au*, Nuclear Instruments and Methods in Physics Research Section B: Beam Interactions with Materials and Atoms **129**, 153 (1997)

[40] R. Michel, M. Gloris, H.J. Lange, I. Leya, M. Lüpke, U. Herpers, B. Dittrich-Hannen, R. Rösel, T. Schiekel, D. Filges et al., *Nuclide production by proton-induced reactions on elements ($6 \leq Z \leq 29$) in the energy range from 800 to 2600 MeV*, Nuclear Instruments and Methods in Physics Research Section B: Beam Interactions with Materials and Atoms **103**, 183 (1995)

[41] E. Porras, F. Sánchez, V. Reglero, B. Cordier, A. Dean, F. Lei, J. Pérez, B. Swinyard, *Production rate of proton-induced isotopes in different materials*, Nuclear Instruments and Methods in Physics Research Section B: Beam Interactions with Materials and Atoms **160**, 73 (2000)

[42] Y.V. Aleksandrov, A. Bogdanov, S. Vasil'ev, R. Ivanov, M. Mikhajlova, T. Popova, V. Prikhodtseva, *Cross section of radionuclides production in 1 GeV proton interaction with mean atomic weight nuclei*, Izvestiya Akademii Nauk SSSR, Seriya Fizicheskaya;(USSR) **54** (1990)

[43] W. Wojdowska, D. Pawlak, I. Cieszykowska, M. Żółtowska, T. Janiak, T. Barcikowski, A. Stolarz, J. Choiński, J. Parus, P. Garnuszek et al., *Improved procedures of Sc (OH) 3 precipitation and UTEVA extraction for 44Sc separation*, Nuclear Medicine Review **22**, 56 (2019)

[44] N.P. van der Meulen, M. Bunka, K.A. Domnanich, C. Müller, S. Haller, C. Vermeulen, A. Türler, R. Schibli, *Cyclotron production of 44Sc: from bench to bedside*, Nuclear medicine and biology **42**, 745 (2015)

[45] G. Severin, J. Engle, H. Valdovinos, T. Barnhart, R. Nickles, *Cyclotron produced 44gSc from natural calcium*, Applied Radiation and Isotopes **70**, 1526 (2012)

[46] R. Mikolajczak, D. Pawlak, W. Wojdowska, T. Janiak, T. Barcikowski, M. Zoltowska, I. Cieszykowska, J. Parus, V. ForgÃ, D. Szikra et al., *Cyclotron production of sc-44 from natural calcium* (2018)

[47] N.P. van der Meulen, R. Hasler, Z. Talip, P.V. Grundler, C. Favaretto, C.A. Umbricht, C. Müller, G. Dellepiane, T.S. Carzaniga, S. Braccini, *Developments toward the implementation of 44Sc production at a medical cyclotron*, Molecules **25**, 4706 (2020)

[48] C. Hoehr, E. Oehlke, F. Benard, C.J. Lee, X. Hou, B. Badesso, S. Ferguson, Q. Miao, H. Yang, K. Buckley et al., *44gSc production using a water target on a 13 MeV cyclotron*, Nuclear medicine and biology **41**, 401 (2014)

[49] I.F. Chaple, S.E. Lapi, *Production and use of the first-row transition metal PET radionuclides 43, 44Sc, 52Mn, and 45Ti*, Journal of Nuclear Medicine **59**, 1655 (2018)

[50] J. Ramos, A. Senos, T. Stora, C. Fernandes, P. Bowen, *Development of a processing route for carbon allotrope-based TiC porous nanocomposites*, Journal of the European Ceramic Society **37**, 3899 (2017)

[51] M. Ballan, S. Corradetti, M. Manzolaro, G. Meneghetti, A. Andrighetto, *Thermal and Structural Characterization of a Titanium Carbide/Carbon Composite for Nuclear Applications*, Materials **15**, 8358 (2022)

[52] I. Alekseev, *Diffusion-thermal methods for recovering radionuclides from solid reactor and cyclotron Targets: an outlook*, Radiochemistry **45**, 429 (2003)

[53] Y. Hara, M. Aoki, H. Hayashi, *Composition for dissolving titanium oxide and dissolution method using it* (2006), uS Patent App. 10/914,197

[54] J. De Goeij, M. Bonardi, *How do we define the concepts specific activity, radioactive concentration, carrier, carrier-free and no-carrier-added?*, Journal of radioanalytical and nuclear chemistry **263**, 13 (2005)

[55] G. Herrmann, N. Trautmann, *Rapid chemical methods for identification and study of short-lived nuclides*, Annual Review of Nuclear and Particle Science **32**, 117 (1982)

[56] G.J. Beyer, *From Radiochemistry of the Lanthanides to 225Ac and the Interference with Richard Baum*, in *Beyond Becquerel and Biology to Precision Radiomolecular Oncology: Festschrift in Honor of Richard P. Baum* (Springer International Publishing Cham, 2024), pp. 53–74

[57] V. Radchenko, C.A.L. Meyer, J.W. Engle, C.M. Naranjo, G.A. Unc, T. Mastren, M. Brugh, E.R. Birnbaum, K.D. John, F.M. Nortier et al., *Separation of 44Ti from proton irradiated scandium by using solid-phase extraction chromatography and design of 44Ti/44Sc generator system*, Journal of Chromatography A **1477**, 39 (2016)

[58] D. Filosofov, N. Loktionova, F. Rösch, *A 44Ti/44Sc radionuclide generator for potential application of 44Sc-based PET-radiopharmaceuticals*, rca-Radiochimica Acta **98**, 149 (2010)

[59] T. Tamai, R. Matsushita, J. Takada, Y. Kiso, *Gamma-ray energies of Se-85 and Se-86*, Inorganic and Nuclear Chemistry Letters **9**, 1145 (1973)

[60] I. Alekseev, A. Antropov, D. Maslennikov, *Thermal recovery of 47Sc from irradiated metallic titanium*, Radiochemistry **43**, 523 (2001)

[61] D. Wittwer, R. Dressler, R. Eichler, H.W. Gäggeler, D. Piguet, A. Serov, A. Türler, A. Vögele, *The thermal release of scandium from titanium metal – a simple way to produce pure 44Sc for PET application*, Radiochimica Acta **99**, 193 (2011)

[62] Y. Martinez Palenzuela, Ph.D. thesis, *Characterization and optimization of a versatile laser and electron-impact ion source for radioactive ion beam production at ISOLDE and MEDICIS.*, KU Leuven (2019), presented 26 Apr 2019, `https://cds.cern.ch/record/2672954`

[63] M. Deseyn, *Maximizing the radionuclide collection efficiency at CERN-MEDICIS: A case study on terbium collections and sputtering* (2023), presented 30 Jun 2023, `https://cds.cern.ch/record/2866125`

[64] M. Au, Ph.D. thesis, *Production of actinide atomic and molecular ion beams at CERN-ISOLDE*, Johannes Gutenberg-Universität Mainz (2023), presented 13 Sep 2023, https://cds.cern.ch/record/2878875

[65] C. Seiffert, Ph.D. thesis, *Production of radioactive molecular beams for CERN-ISOLDE*, CERN (2015)

[66] R. Catherall, W. Andreazza, M. Breitenfeldt, A. Dorsival, G. Focker, T. Gharsa, T. Giles, J. Grenard, F. Locci, P. Martins et al., *The ISOLDE facility*, Journal of Physics G: Nuclear and Particle Physics **44**, 094002 (2017)

[67] *A spring awakening: Cern's accelerators gear up for 2023*, https://home.cern/news/news/accelerators/, accessed: 2024-06-12

[68] E. Kugler, D. Fiander, B. Johnson, H. Haas, A. Przewloka, H. Ravn, D. Simon, K. Zimmer, *The new CERN-ISOLDE on-line mass-separator facility at the PS-Booster*, Nuclear Instruments and Methods in Physics Research Section B: Beam Interactions with Materials and Atoms **70**, 41 (1992)

[69] P. Van Duppen, *Isotope separation on line and post acceleration*, in *The Euroschool Lectures on Physics with Exotic Beams, Vol. II* (Springer, 2006), pp. 37–77

[70] J. Ballof, J. Ramos, A. Molander, K. Johnston, S. Rothe, T. Stora, C.E. Düllmann, *The upgraded ISOLDE yield database–A new tool to predict beam intensities*, Nuclear Instruments and Methods in Physics Research Section B: Beam Interactions with Materials and Atoms **463**, 211 (2020)

[71] C. Bernerd, J. Johnson, E. Aubert, M. Au, V. Barozier, A.P. Bernardes, P. Bertreix, F. Bruchertseifer, R. Catherall, E. Chevallay et al., *Production of innovative radionuclides for medical applications at the CERN-MEDICIS facility*, Nuclear Instruments and Methods in Physics Research Section B: Beam Interactions with Materials and Atoms **542**, 137 (2023)

[72] C. Duchemin, J.P. Ramos, T. Stora, E. Ahmed, E. Aubert, N. Audouin, E. Barbero, V. Barozier, A.P. Bernardes, P. Bertreix et al., *CERN-MEDICIS: A review since commissioning in 2017*, Frontiers in Medicine **8**, 693 (2021)

[73] R. dos Santos Augusto, Ph.D. thesis, *On the feasibility of using radioactive ion beams in hadrontherapy: dosimetric and imaging studies*, Munich U. (2018), presented 11 Jul 2018, https://cds.cern.ch/record/2637861

[74] T. Stora, C. Duchemin, W. Andreazza, E. Aubert, C. Bernerd, T. Cocolios, M. Deschamps, A. Dorsival, M. Duraffourg, V. Fedosseev et al., *CERN-MEDICIS: Operational indicators to support the production of new medical radionuclides by mass-separation*, in *Journal of Physics: Conference Series* (IOP Publishing, 2024), Vol. 2687, p. 082039

[75] U. Köster, P. Carbonez, A. Dorsival, J. Dvorak, R. Eichler, S. Fernandes, H. Frånberg, J. Neuhausen, Z. Novackova, R. Wilfinger et al., *(Im-) possible ISOL beams*, The European Physical Journal Special Topics **150**, 285 (2007)

[76] U. Koester, O. Arndt, R. Catherall, J. Correia, B. Crepieux, R. Eichler, P. Fernier, L. Fraile, S. Hennrich, K. Johnston et al., *ISOL beams of hafnium isotopes and isomers*, The European Physical Journal Special Topics **150**, 293 (2007)

[77] P. Hoff, O. Jonsson, E. Kugler, H. Ravn, *Release of nuclear reaction products from refractory compounds*, Nuclear Instruments and Methods in Physics Research **221**, 313 (1984)

[78] L. Carraz, I. Haldorsen, H. Ravn, M. Skarestad, L. Westgaard, *Fast release of nuclear reaction products from refractory matrices*, Nuclear Instruments and Methods **148**, 217 (1978)

[79] J. Ballof, M. Au, E. Barbero, K. Chrysalidis, C.E. Düllmann, V. Fedosseev, E. Granados, R. Heinke, B.A. Marsh, M. Owen et al., *A cold electron-impact ion source driven by a photo-cathode–New opportunities for the delivery of radioactive molecular beams?*, in *Journal of Physics: Conference Series* (IOP Publishing, 2022), Vol. 2244, p. 012072

[80] M. Au, M. Athanasakis-Kaklamanakis, L. Nies, R. Heinke, K. Chrysalidis, U. Köster, P. Kunz, B. Marsh, M. Mougeot, L. Schweikhard et al., *Production of neptunium and plutonium nuclides from uranium carbide using 1.4-GeV protons*, Physical Review C **107**, 064604 (2023)

[81] J. Ballof, C. Seiffert, B. Crepieux, C.E. Düllmann, M. Delonca, M. Gai, A. Gottberg, T. Kröll, R. Lica, M. Madurga Flores et al., *Radioactive boron beams produced by isotope online mass separation at CERN-ISOLDE*, The European Physical Journal A **55**, 1 (2019)

[82] R. Eder, H. Grawe, E. Hagebø, P. Hoff, E. Kugler, H. Ravn, K. Steffensen, *The production yields of radioactive ion-beams from fluorinated targets at the ISOLDE online mass separator*, Nuclear Instruments and Methods in Physics Research Section B: Beam Interactions with Materials and Atoms **62**, 535 (1992)

[83] J. Ballof, K. Chrysalidis, C.E. Düllmann, V. Fedosseev, E. Granados, D. Leimbach, B. Marsh, J. Ramos, A. Ringvall-Moberg, S. Rothe et al., *A concept for the extraction of the most refractory elements at CERN-ISOLDE as carbonyl complex ions*, The European Physical Journal A **58**, 94 (2022)

[84] P. Hoff, L. Jacobsson, B. Johansson, P. Aagaard, G. Rudstam, H.U. Zwicky, *Production of molecular ions in the integrated target/ion-source of an isotope-separation-on-line system*, Nuclear Instruments and Methods **172**, 413 (1980)

[85] T. Giles, *Isolde V*, Nuclear Instruments and Methods in Physics Research Section B: Beam Interactions with Materials and Atoms **463**, 254 (2020)

[86] *C.duchemin cern-medicis: a unique facility for the production of non-conventional radionuclides for medical research*, `https://indico.cern.ch/event/1316940/book-of-abstracts.pdf`, accessed: 2024-5-6

[87] R. Froeschl, M. Brugger, S. Roesler, *The CERN high energy accelerator mixed field (CHARM) facility in the CERN PS east experimental area*, in *Proceedings, 12th meeting of task-force on shielding aspects of accelerators, targets and irradiation facilities* (2015), pp. 14–25

[88] Y. Martinez Palenzuela, V. Barozier, E. Chevallay, T.E. Cocolios, C. Duchemin, P. Fernier, M. Huyse, L. Lambert, R. Lopez, S. Marzari et al., *The CERN-MEDICIS Isotope Separator Beamline*, Frontiers in Medicine **8** (2021)

[89] N.T. Vuong, Ph.D. thesis, *Systematic investigations of uranium carbide composites oxidation from micro- to nano-scale: Application to waste disposal*, EPFL (2021), presented 10 Dec 2021, `https://cds.cern.ch/record/2797525`

[90] T. Mendonca, R. Hodak, V. Ghetta, M. Allibert, D. Heuer, E. Noah, S. Cimmino, M. Delonca, A. Gottberg, M. Kronberger et al., *Production and release of ISOL beams from molten fluoride salt targets*, Nuclear Instruments and Methods in Physics Research Section B: Beam Interactions with Materials and Atoms **329**, 1 (2014)

[91] K. Chrysalidis, J. Ballof, C.E. Düllmann, V. Fedosseev, C. Granados, B. Marsh, Y. Martinez Palenzuela, J. Ramos, S. Rothe, T. Stora et al., *Developments towards the delivery of selenium ion beams at ISOLDE*, The European Physical Journal A **55**, 173 (2019)

[92] R. Kirchner, *On the thermoionization in hot cavities*, Nuclear Instruments and Methods in Physics Research Section A: Accelerators, Spectrometers, Detectors and Associated Equipment **292**, 203 (1990)

[93] U. Köster, *Resonance ionization laser ion sources*, Nuclear Physics A **701**, 441 (2002)

[94] C. Seiffert, Ph.D. thesis, *Production of radioactive molecular beams for CERN-ISOLDE*, Darmstadt, Tech. U. (2014), presented 04 Feb 2015, `https://cds.cern.ch/record/2064456`

[95] B. Marsh, *Resonance ionization laser ion sources for on-line isotope separators*, Review of Scientific Instruments **85** (2014)

[96] V. Gadelshin, V. Barozier, T. Cocolios, V. Fedosseev, R. Formento-Cavaier, F. Haddad, B. Marsh, S. Marzari, S. Rothe, T. Stora et al., *MELISSA: laser ion source setup at CERN-MEDICIS facility. Blueprint*, Nuclear Instruments and Methods in Physics Research Section B: Beam Interactions with Materials and Atoms **463**, 460 (2020)

[97] L. Penescu, R. Catherall, J. Lettry, T. Stora, *Development of high efficiency versatile arc discharge ion source at CERN ISOLDE*, Review of scientific instruments **81** (2010)

[98] D. Toneli, R. Pessoa, M. Roberto, G. Filho, H. Maciel, *Study of* CF_4 *capacitive plasma chemistry through mass spectrometry technique and global model*, Digest of Technical Papers-IEEE International Pulsed Power Conference pp. 1–4 (2013)

[99] K. Zmbov, J. Margrave, *Mass Spectrometric Studies of Scandium, Yttrium, Lanthanum, and Rare-Earth Fluorides*, in *Mass Spectrometry in Inorganic Chemistry* (ACS Publications, 1968), chap. 19, pp. 267–290

[100] W. Lotz, *Electron-impact ionization cross-sections and ionization rate coefficients for atoms and ions from hydrogen to calcium*, Zeitschrift für Physik **216**, 241 (1968)

[101] R. Kirchner, E. Roeckl, *Investigation of gaseous discharge ion sources for isotope separation on-line*, Nuclear Instruments and Methods **133**, 187 (1976)

[102] F.M. Millan, C. Babcock, T.D. Goodacre, A. Gottberg, *Anomalous Ionization Regime in a Forced Electron Beam Induced Arc Discharge Ion Source for Singly Charged Radioactive Ion Beam Production*, in *Journal of Physics: Conference Series* (IOP Publishing, 2022), Vol. 2244, p. 012074

[103] L.C. Penescu, Ph.D. thesis, *Techniques to produce and accelerate radioactive ion beams. Tehnici de producere si accelerare a fasciculelor radioactive*, Bucharest, Polytechnic Inst. (2009), presented 2009, https://cds.cern.ch/record/2259078

[104] S. Rothe, M. Au, J. Ballof, E. Barbero, M. Bissell, A. Boucherie, M. Bovigny, K. Chrysalidis, B. Crepieux, J. Cruikshank et al., *Targets and ion sources at CERN-ISOLDE — Facilities and developments*, Nuclear Instruments and Methods in Physics Research Section B: Beam Interactions with Materials and Atoms **542**, 38 (2023)

[105] M. Au, C. Bernerd, Y.N.V. Gracia, M. Athanasakis-Kaklamanakis, J. Ballof, M. Bissell, K. Chrysalidis, R. Heinke, L. Le, R. Mancheva et al., *Developments at CERN-ISOLDE's OFFLINE 2 mass separator facility for studies of molecular ion beams*, Nuclear Instruments and Methods in Physics Research Section B: Beam Interactions with Materials and Atoms **541**, 144 (2023)

[106] R. Forman, *The role of oxygen in the low work function surface complex of barium on oxygen on tungsten (substrate)*, Applied Surface Science **25**, 13 (1986)

[107] R. Mueller, H. Wagner, *Influence of oxygen on the surface ionization of barium on tungsten.*, Tech. rep., Marburg Univ.(West Germany). Physikalisches Institut (1971)

[108] J.C. Batty, R.E. Stickney, *Quasiequilibrium Treatment of Gas–Solid Reactions. I. Evaporation Rates of Volatile Species Formed in the Reaction of O2 with W, Mo, and C*, The Journal of Chemical Physics **51**, 4475 (1969)

[109] D. Hildenbrand, *Thermochemistry*, Nuclear Instruments and Methods in Physics Research **186**, 357 (1981)

[110] D.E. Rosner, H.D. Allendorf, *Kinetics of the attack of refractory solids by atomic and molecular fluorine*, The Journal of Physical Chemistry **75**, 308 (1971)

[111] P.C. Nordine, *High temperature kinetics of refractory metal gasification by atomic fluorine*, Journal of the Electrochemical Society **125**, 498 (1978)

[112] A. Roine, *Hsc chemistry*, http://www.heelis.com/index.html, accessed: 2021-03-23

[113] C.K. Vyas, J.H. Park, S.D. Yang, *Application of extraction chromatographic techniques for separation and puri fi cation of emerging radiometals 44/47Sc*, Journal of Radiopharmaceuticals and Molecular Probes Vol **2** (2016)

[114] A. Ruiz Quiros, *A chromatographic method to separate sc (iii) from zn (ii) ions: A step in the purification of sc-44 (an isotope of medical interest)*, Tech. rep., CERN (2018)

[115] *Method for determination of Pu isotopes in soil and sediment samples by inductively coupled plasma mass spectrometry after simple chemical separation using TK200 resin*, Analytica Chimica Acta **1090**, 151 (2019)

[116] C. Dirks-Fandrei, Ph.D. thesis, *Development of methods for the selective separation of scandium, zirconium and tin for radiopharmaceutical applications* (2014)

[117] R.J. Zabolockis, *Automation and investigation of scandium separation from ionic contaminants using ion-exchange chromatography and electrochemical methods* (2023), https://cds.cern.ch/record/2869797

[118] M. Tabrizchi, F. Rouholahnejad, *Comparing the effect of pressure and temperature on ion mobilities*, Journal of Physics D: Applied Physics **38**, 857 (2005)

[119] A. Raveendran, M. Chandran, R. Dhanusuraman, *A comprehensive review on the electrochemical parameters and recent material development of electrochemical water splitting electrocatalysts*, RSC advances **13**, 3843 (2023)

[120] P. Vanysek, *Electrochemical series*, CRC handbook of chemistry and physics **8**, 8 (2000)

[121] Y. Castrillejo, P. Hernández, J. Rodriguez, M. Vega, E. Barrado, *Electrochemistry of scandium in the eutectic LiCl–KCl*, Electrochimica Acta **71**, 166 (2012)

[122] X.Z. Hunaid Nulwala, John D. Watkins, *Electrochemical deposition of elements in aqueous media*, Canadian Patent (2016)

[123] P.W. Atkins, J. De Paula, J. Keeler, *Atkins' physical chemistry* (Oxford university press, 2023)

[124] F. Cerutti, A. Ferrari, A. Mairani, P.R. Sala, *New developments in FLUKA* (2012)

[125] C. Ahdida, D. Bozzato, D. Calzolari, F. Cerutti, N. Charitonidis, A. Cimmino, A. Coronetti, G. D'Alessandro, A. Donadon Servelle, L. Esposito et al., *New capabilities of the FLUKA multi-purpose code*, Frontiers in Physics **9**, 788253 (2022)

[126] G. Battistoni, T. Boehlen, F. Cerutti, P.W. Chin, L.S. Esposito, A. Fassò, A. Ferrari, A. Lechner, A. Empl, A. Mairani et al., *Overview of the FLUKA code*, Annals of Nuclear Energy **82**, 10 (2015)

[127] C. Duchemin, C. Theis, H. Vincke, *Activation experiment at the cern-eu high-energy reference field (cerf) facility to benchmark actiwiz and fluka predictions: A comparison after 30 days of cooling time*, Nuclear Instruments and Methods in Physics Research Section A: Accelerators, Spectrometers, Detectors and Associated Equipment **937**, 72 (2019)

[128] D. Choudhury, S. Lahiri, N. Naskar, M. Delonca, T. Stora, J.P. Ramos, E. Aubert, A. Dorsival, J. Vollaire, R. Augusto et al., *Quantification of radioisotopes produced in 1.4 GeV proton irradiated lead–bismuth eutectic targets*, The European Physical Journal A **56**, 204 (2020)

[129] J.C. David, V. Blideanu, A. Boudard, D. Doré, S. Leray, B. Rapp, D. Ridikas, N. Thiollière, *Benchmark calculations on residue production within the eurisol ds project. part 1: thin targets* (2006)

[130] V. Vlachoudis et al., *FLAIR: a powerful but user friendly graphical interface for FLUKA*, in *Proc. Int. Conf. on Mathematics, Computational Methods & Reactor Physics (M&C 2009), Saratoga Springs, New York* (2009), Vol. 176

[131] H. Vincke, C. Theis, *ActiWiz–optimizing your nuclide inventory at proton accelerators with a computer code*, Prog. Nucl. Sci. Tech. **4**, 228 (2014)

[132] C. Theis, H. Vincke, *The use of ActiWiz in operational radiation protection*, in *Proceedings of the Twelfth Meeting of Task-Force on Shielding Aspects of Accelerators, Targets and Irradiation Facilities of Accelerator Technology, SATIF12 FNAL* (2014), pp. 28–30

[133] A.J. Plompen, O. Cabellos, C. De Saint Jean, M. Fleming, A. Algora, M. Angelone, P. Archier, E. Bauge, O. Bersillon, A. Blokhin et al., *The joint evaluated fission and fusion nuclear data library, JEFF-3.3*, The European Physical Journal A **56**, 1 (2020)

[134] H. Bateman, *The solution of a system of differential equations occurring in the theory of radioactive transformations*, in *Proc. Cambridge Philos. Soc.* (1910), Vol. 15, pp. 423–427

[135] F. Ogallar Ruiz, Ph.D. thesis, *Evaluation and criticality assessment of radiological source terms to be used for fire risk studies at accelerator facilities.*, University of Granada (2021), presented 03 Feb 2022, https://cds.cern.ch/record/2802879

[136] F. Ogallar Ruiz, H. Vincke, I. Porras, C. Theis, *A desorption model for the code SOLIDUSS and its experimental benchmarking*, Radiation Physics and Chemistry **201**, 110424 (2022)

[137] *Mirion spectroscopy and scientific analysis systems*, https://www.mirion.com/products/technologies, accessed: 2023-11-30

[138] F. Bronson, B. Young, *Mathematical calibration of ge detectors, and the instruments that use them*, Tech. rep., Lockheed Idaho Technologies Co., Idaho Falls, ID (United States) (1997)

[139] A. Bosko, N. Menaa, T. Spillane, F. Bronson, R. Venkataraman, W.R. Russ, W. Mueller, V. Nizhnik, *Efficiency Optimization Employing Random and Smart Search Using Multiple Counts and Line Activity Consistency Benchmarks-11398* (2011)

[140] C. Duchemin, F. La Torre, M. Magistris, M. Silari, *Activation experiment at the H4IRRAD facility: A comparison between experimental data, FLUKA and ActiWiz predictions after 15 days of cooling time*, Nuclear Instruments and Methods in Physics Research Section A: Accelerators, Spectrometers, Detectors and Associated Equipment **986**, 164717 (2021)

[141] P. Christodoulou, *An in situ gamma-spectrometry system for the characterization of non-conventional radionuclides for medical research.* (2020), presented 14 Sep 2020, https://cds.cern.ch/record/2732064

[142] P. Kalnina, Master's thesis, *CERN-MEDICIS isotope mass separation process optimization: the case of Scandium for release study and on-line monitoring of the implanted activity.* (2024), presented 06 Jun 2024, https://cds.cern.ch/record/2899635

[143] *Gr family*, https://www.kromek.com/product/gr-family/, accessed: 2023-11-30

[144] R. Heinke, E. Chevallay, K. Chrysalidis, T.E. Cocolios, C. Duchemin, V.N. Fedosseev, S. Hurier, L. Lambert, B. Leenders, B.A. Marsh et al., *Efficient production*

of high specific activity thulium-167 at Paul Scherrer Institute and CERN-MEDICIS, Frontiers in medicine **8**, 712374 (2021)

[145] J.I. Goldstein, D.E. Newbury, J.R. Michael, N.W. Ritchie, J.H.J. Scott, D.C. Joy, *Scanning electron microscopy and X-ray microanalysis* (springer, 2017)

[146] J.B. Condon, *Surface area and porosity determinations by physisorption: measurement, classical theories and quantum theory* (Elsevier, 2019)

[147] L. Zhou, Y. Zhou, Y. Sun, *Enhanced storage of hydrogen at the temperature of liquid nitrogen*, International Journal of Hydrogen Energy **29**, 319 (2004)

[148] M. Saberi, P. Rouhi, *Extension of the Brunauer-Emmett-Teller (BET) model for sorption of gas mixtures on the solid substances*, Fluid Phase Equilibria **534**, 112968 (2021)

[149] E. Mamis, P. Kalnina, C. Duchemin, L. Lambert, N. Conan, M. Deschamps, A. Dorsival, R. Froeschl, F.O. Ruiz, C. Theis et al., *Scandium thermal release from activated natTi and natV target materials in mixed particle fields: Investigation of parameters relevant for isotope mass separation*, Nuclear Instruments and Methods in Physics Research Section B: Beam Interactions with Materials and Atoms **553**, 165400 (2024)

[150] G.J. Beyer, E. Hagebø, A. Novgorodov, H. Ravn, I. Collaboration et al., *The role of diffusion in ISOL targets for the production of radioactive ion beams*, Nuclear Instruments and Methods in Physics Research Section B: Beam Interactions with Materials and Atoms **204**, 225 (2003)

[151] S. Fernandes, Ph.D. thesis, *Submicro and Nano Structured Porous Materials for the Production of High-Intensity Exotic Radioactive Ion Beams*, Ecole Polytechnique, Lausanne (2010), presented on 03 Dec 2010, https://cds.cern.ch/record/1312950

[152] L.A. Currie, *Limits for qualitative detection and quantitative determination. Application to radiochemistry*, Analytical chemistry **40**, 586 (1968)

[153] D. Wittwer, R. Dressler, R. Eichler, H. Gäggeler, D. Piguet, A. Serov, A. Türler, A. Vögele, *The thermal release of scandium from titanium metal–a simple way to produce pure 44Sc for PET application*, Radiochimica acta **99**, 193 (2011)

[154] H. Mehrer, *Diffusion in Metals and Intermetallics: an Overview* (2022)

[155] H. Mehrer, *Diffusion in solids: fundamentals, methods, materials, diffusion-controlled processes*, Vol. 155 (Springer Science & Business Media, 2007)

[156] H. Mehrer, S.V. Divinski, *Diffusion in metallic elements and intermetallics*, in *Defect and Diffusion Forum* (Trans Tech Publ, 2009), Vol. 289, pp. 15–38

[157] K. GSCHNEIDNER, *CHAPTER 8 - Inorganic Compounds*, in *Scandium: Its Occurrence, Chemistry Physics, Metallurgy, Biology and Technology*, edited by C. HOROVITZ, K. GSCHNEIDNER, G. MELSON, D. YOUNGBLOOD, H. SCHOCK (Academic Press, 1975), pp. 152–251, ISBN 978-0-12-355850-3, https://www.sciencedirect.com/science/article/pii/B9780123558503500137

[158] E.O. Ezugwu, R. Batista Da Silva, W. Falco Sales, A. Rocha Machado, *Overview of the Machining of Titanium Alloys*, in *Encyclopedia of Sustainable Technologies*, edited by M.A. Abraham (Elsevier, Oxford, 2017), pp. 487–506, ISBN 978-0-12-804792-7, https://www.sciencedirect.com/science/article/pii/B9780124095489102167

[159] H. Roßbach, B. Eichler, *Adsorption von Metallen auf metallische Oberflächen und Möglichkeiten ihrer Nutzung in der Kernchemie*, ZfK Report Rossendorf (1984)

[160] M. Fujioka, Y. Arai, *Diffusion of radioisotopes from solids in the form of foils, fibers and particles*, Nuclear Instruments and Methods in Physics Research **186**, 409 (1981)

[161] G.J. Beyer, W.D. Fromm, A.F. Novgorodov, *Trace diffusion of different nuclear reaction products in polycrystalline tantalum*, Nuclear Instruments and Methods **146**, 419 (1977)

[162] J. Askill, G. Gibbs, *Tracer Diffusion in β-Titanium*, physica status solidi (b) **11**, 557 (1965)

[163] B. Eichler, S. Huebener, H. Rossbach, *Adsorption of volatile metals on metal surfaces and the possibilities of its application in nuclear chemistry*, Tech. rep., Zentralinstitut fuer Kernforschung (1986)

[164] A. Miedema, R. Boom, F. De Boer, *On the heat of formation of solid alloys*, Journal of the Less Common Metals **41**, 283 (1975)

[165] A. Miedema, *On the heat of formation of solid alloys. II*, Journal of the Less Common Metals **46**, 67 (1976)

[166] Y.N. Starodubtsev, V.S. Tsepelev, K.M. Wu, Y.A. Kochetkova, N.P. Tsepeleva, *Vacancy formation energy of metals*, Key Engineering Materials **861**, 46 (2020)

[167] A. Roy, P. Singh, G. Balasubramanian, D.D. Johnson, *Vacancy formation energies and migration barriers in multi-principal element alloys*, Acta Materialia **226**, 117611 (2022)

[168] C. Kittel, P. McEuen, *Introduction to solid state physics* (John Wiley & Sons, 2018)

[169] A. Ruiz Quiros, *A Chromatographic Method to Separate Sc(III) from Zn(II) Ions: A Step in the Purification of Sc-44 (an isotope of medical interest). Sc: scandium* (2018)

[170] T. Bjørnstad, E. Hagebø, P. Hoff, O. Jonsson, E. Kugler, H. Ravn, S. Sundell, B. Vosicki, I. collaboration et al., *Methods for production of intense beams of unstable nuclei: new developments at ISOLDE*, Physica Scripta **34**, 578 (1986)

[171] J. Ramos, *Thick solid targets for the production and online release of radioisotopes: The importance of the material characteristics–A review*, Nuclear Instruments and Methods in Physics Research Section B: Beam Interactions with Materials and Atoms **463**, 201 (2020)

[172] A. Kronenberg, E.H. Spejewski, H.K. Carter, B. Mervin, C. Jost, D.W. Stracener, S. Lapi, T. Bray, *Molecular sidebands of refractory elements for ISOL*, Nuclear Instruments and Methods in Physics Research Section B: Beam Interactions with Materials and Atoms **266**, 4252 (2008)

[173] *The isolde yield database, version 0.2*, https://cern.ch/isolde-yields (2021), [Online; accessed 08.01.2024]

[174] R. Brodzinski, L. Rancitelli, J. Cooper, N. Wogman, *High-energy proton spallation of titanium*, Physical Review C **4**, 1250 (1971)

[175] S. Corradetti, M. Manzolaro, S. Carturan, M. Ballan, L. Centofante, G. Lilli, A. Monetti, L. Morselli, D. Scarpa, A. Donzella et al., *The SPES target production and characterization*, Nuclear Instruments and Methods in Physics Research Section B: Beam Interactions with Materials and Atoms **488**, 12 (2021)

[176] W.S. Williams, *The thermal conductivity of metallic ceramics*, Jom **50**, 62 (1998)

[177] J. Ramos, T. Stora, A. Senos, P. Bowen, *Thermal stability of nanometric TiC-carbon composites: effects of carbon allotropes and Zr milling impurities*, Journal of the European Ceramic Society **38**, 4882 (2018)

[178] J.s. Maa, H. Ying, F. Zhang, *Effect of temperature on etch rate of iridium and platinum in CF 4/O 2*, Journal of Vacuum Science & Technology A: Vacuum, Surfaces, and Films **19**, 1312 (2001)

[179] *Goodfellow cambridge ltd.*, https://www.goodfellow.com/c/metal, accessed: 2024-03-07

[180] *Tu wien legacy pages of the institute of applied physics: Vapor pressure calculator*, https://www2.iap.tuwien.ac.at/www/surface/vapor_pressure, accessed: 2024-04-22

[181] B. Liu, R. Han, C. Yuan, H. Sun, Z. Chen, G. Tian, F. Shi, X. Zhang, P. Luo, H. Jia, *Excitation functions of proton induced reactions on titanium and copper*, Applied Radiation and Isotopes **173**, 109713 (2021)

[182] F. Ditrói, F. Tárkányi, S. Takács, A. Hermanne, *Activation cross-sections of proton induced reactions on vanadium in the 37–65 MeV energy range*, Nuclear Instruments and Methods in Physics Research Section B: Beam Interactions with Materials and Atoms **381**, 16 (2016)

[183] *Talys-based evaluated nuclear data library*, https://tendl.web.psi.ch/tendl_2023/proton_html/proton.html (2023), [Online; accessed 10.01.2024]

[184] J.F. Ziegler, M.D. Ziegler, J.P. Biersack, *SRIM–The stopping and range of ions in matter (2010)*, Nuclear Instruments and Methods in Physics Research Section B: Beam Interactions with Materials and Atoms **268**, 1818 (2010)

[185] R.M.d.S. Augusto, L. Buehler, Z. Lawson, S. Marzari, M. Stachura, T. Stora, C.M. collaboration, *CERN-MEDICIS (medical isotopes collected from ISOLDE): a new facility*, Applied Sciences **4**, 265 (2014)

[186] M. Chernysheva, S.C. Loveless, T. Brossard, K. Becker, S. Cingoranelli, E. Aluicio-Sarduy, J. Song, P. Ellison, J. Nolen, D.A. Rotsch et al., *Accelerator production of scandium radioisotopes: Sc-43, Sc-44, and Sc-47*, Current radiopharmaceuticals **14**, 359 (2021)

[187] M. Dombsky, P. Bricault, V. Hanemaayer, *Increasing beam currents at the TRIUMF-ISAC Facility; techniques and experiences*, Nuclear Physics A **746**, 32 (2004), proceedings of the Sixth International Conference on Radioactive Nuclear Beams (RNB6)

[188] M. Dombsky, P. Bricault, P. Schmor, M. Lane, *ISAC target operation with high proton currents*, Nuclear Instruments and Methods in Physics Research Section B: Beam Interactions with Materials and Atoms **204**, 191 (2003)

[189] J. Mitchell, G. Foti, L. Howe, J. Davies, S. Campisano, E. Rimini, *A channeling investigation of proton and deuteron damage in germanium*, Radiation Effects **26**, 193 (1975)

[190] R. Mlekodaj, E. Spejewski, B. Ritchie, *A new high temperature isol ion source*, Nuclear Instruments and Methods **171**, 451 (1980)

[191] F. Tárkányi, F. Ditroi, S. Takacs, A. Hermanne, M. Baba, A. Ignatyuk, *Investigation of activation cross-sections of deuteron induced reactions on vanadium up to 40 MeV*, Nuclear Instruments and Methods in Physics Research Section B: Beam Interactions with Materials and Atoms **269**, 1792 (2011)

[192] C. Duchemin, A. Guertin, F. Haddad, N. Michel, V. Métivier, *Cross section measurements of deuteron induced nuclear reactions on natural tungsten up to 34 MeV*, Applied radiation and Isotopes **97**, 52 (2015)

[193] *Charged-particle cross section database for medical radioisotope production*, `https://www-nds.iaea.org/medical/`, accessed: 2024-03-12

[194] A. Hermanne, A. Ignatyuk, R. Capote, B. Carlson, J. Engle, M. Kellett, T. Kibédi, G. Kim, F. Kondev, M. Hussain et al., *Reference Cross Sections for Charged-particle Monitor Reactions*, Nuclear Data Sheets **148**, 338 (2018), special Issue on Nuclear Reaction Data

[195] M. Choudhary, A. Gandhi, A. Sharma, N. Singh, P. Dubey, M. Upadhyay, S. Dasgupta, J. Datta, A. Kumar, *Measurement of alpha-induced reaction cross-sections on nat Mo with detailed covariance analysis*, The European Physical Journal A **58**, 95 (2022)

[196] R. Kirchner, *On the release and ionization efficiency of catcher-ion-source systems in isotope separation on-line*, Nuclear Instruments and Methods in Physics Research Section B: Beam Interactions with Materials and Atoms **70**, 186 (1992)

[197] J. Frenkel, *Theorie der Adsorption und verwandter Erscheinungen*, Zeitschrift für Physik **26**, 117 (1924)

[198] M. Santana-Leitner, Ph.D. thesis, *A Monte Carlo code to optimize the production of Radioactive Ion Beams by the ISOL technique*, UPC-ETSEIB Catalunya TU (2005), presented 29 Jul 2005, `https://cds.cern.ch/record/905537`

[199] A.S. Murphy, D. Schumann, T. Stora, *Exploitation of accelerator waste for radioactive ion beams: a nuclear astrophysics application*, Nuclear Physics News **25**, 23 (2015)

[200] U. Köster, Ph.D. thesis, *Yields and spectroscopy of radioactive isotopes at LOHENGRIN and ISOLDE. Ausbeuten und Spektroskopie radioaktiver Isotope bei LOHENGRIN und ISOLDE*, Munich, Tech. U. (1999), presented on 30 Dec 1999, `https://cds.cern.ch/record/494272`

[201] D. Brennan, M. Graham, *The adsorption of krypton and xenon on evaporated metal films*, Philosophical Transactions of the Royal Society of London. Series A, Mathematical and Physical Sciences **258**, 325 (1965)

[202] A.S. Murphy, D. Schumann, T. Stora, *Exploitation of accelerator waste for radioactive ion beams: a nuclear astrophysics application*, Nuclear Physics News **25**, 23 (2015)

[203] S. Fernandes, R. Bruetsch, R. Catherall, F. Groeschel, I. Guenther-Leopold, J. Lettry, E. Manfrin, S. Marzari, E. Noah, S. Sgobba et al., *Microstructure evolution of nanostructured and submicrometric porous refractory ceramics induced by a continuous high-energy proton beam*, Journal of nuclear materials **416**, 99 (2011)

[204] A. Gottberg, *Target materials for exotic ISOL beams*, Nuclear Instruments and Methods in Physics Research Section B: Beam Interactions with Materials and Atoms **376**, 8 (2016)

[205] R.E. Goans, Ph.D. thesis, *A Study of the Release Properties of Sn and SnS from an ISOL-type Target/Ion Source System* (2011)

[206] C. Horovitz, *Scandium: its occurrence, chemistry, physics, metallurgy, biology, and technology.[extensive bibliography for each chapter]* (1975)

[207] A. Shih, J. Yater, C. Hor, R. Abrams, *Oxidation of thin scandium films*, Applied surface science **211**, 136 (2003)

[208] M.G. Inghram, W.A. Chupka, J. Berkowitz, *Thermodynamics of the Ta–O System : The Dissociation Energies of TaO and TaO2*, The Journal of Chemical Physics **27**, 569 (1957)

[209] P. Kofstad, *The oxidation behavior of tantalum at 700–1000° C*, Journal of The Electrochemical Society **110**, 491 (1963)

[210] F.J. Kohl, C.A. Stearns, *Mass spectrometric knudsen cell studies of vaporization of lanthanum and scandium carbides and dissociation energy of lac2, lac3, lac4, scc2, and scc4*, Tech. rep. (1971)

[211] M. Nikitin, D. Kayumova, A. Alikhanyan, *Revision of Data on the Thermochemistry of Scandium Fluorides*, Russian Journal of Inorganic Chemistry **68**, 1776 (2023)

[212] R.I. Masel, *Principles of adsorption and reaction on solid surfaces*, Vol. 3 (John Wiley & Sons, 1996)

[213] D.M. Lemal, *Perspective on fluorocarbon chemistry*, The Journal of organic chemistry **69**, 1 (2004)

[214] J. Dean, *Properties of atoms, radicals, and bonds*, Lange's handbook of chemistry **15**, 4 (1999)

[215] R.M. Reese, V.H. Dibeler, *Ionization and dissociation of nitrogen trifluoride by electron impact*, The Journal of Chemical Physics **24**, 1175 (1956)

[216] S.J. Blanksby, G.B. Ellison, *Bond dissociation energies of organic molecules*, Accounts of chemical research **36**, 255 (2003)

[217] O. Greis, J.M. Haschke, *Rare earth fluorides*, Handbook on the physics and chemistry of rare earths **5**, 387 (1982)

[218] L. Yu, W. Ji, S. Zhang, Y. Song, H. Liu, Z. Wang, Q. Liu, X. Wang, *Design and preparation of continuous titanium carbide fibers via simple precursor route*, Ceramics International **46**, 25485 (2020)

[219] D. Rapp, P. Englander-Golden, D.D. Briglia, *Cross Sections for Dissociative Ionization of Molecules by Electron Impact*, The Journal of Chemical Physics **42**, 4081 (1965)

[220] L. Zhong, B. Wu, S. Zheng, Q. Gu, *A database of electron-impact ionization cross sections of molecules composed of H, C, N, O, and F*, Physics of Plasmas **28** (2021)

[221] H. Deutsch, K. Becker, S. Matt, T. Märk, *Theoretical determination of absolute electron-impact ionization cross sections of molecules*, International Journal of Mass Spectrometry **197**, 37 (2000)

[222] *Electron-impact ionization cross section database*, `http://plasma.mathboylinlin.com/db/cs/ion/`, accessed: 2024-05-17

[223] *Nist electron-impact cross sections for ionization and excitation database*, `https://physics.nist.gov/PhysRefData/Ionization/molTable.html`, accessed: 2024-05-17

[224] J.B. Mann, *Ionization cross sections of the elements calculated from mean-square radii of atomic orbitals*, The Journal of Chemical Physics **46**, 1646 (1967)

[225] K.H. Becker, *Electron impact induced dissociative excitation and ionization of halogen-containing molecules*, in *Electron Collisions with Molecules, Clusters, and Surfaces* (Springer, 1994), pp. 127–140

[226] R.J. Kramida A, Ralchenko Yu, N.A.T. (2023)., *Nist atomic spectra database (version 5.11).*, `https://physics.nist.gov` (2023), [Online; accessed 11.01.2024], National Institute of Standards and Technology, Gaithersburg, MD. DOI: `https://doi.org/10.18434/T4W30F`

[227] S. Rothe, B. Marsh, C. Mattolat, V. Fedosseev, K. Wendt, *A complementary laser system for ISOLDE RILIS*, **312**, 052020 (2011)

[228] Y.M. Palenzuela, B. Marsh, J. Ballof, R. Catherall, K. Chrysalidis, T. Cocolios, B. Crepieux, T.D. Goodacre, V. Fedosseev, M. Huyse et al., *Enhancing the extraction of laser-ionized beams from an arc discharge ion source volume*, Nuclear Instruments and Methods in Physics Research Section B: Beam Interactions with Materials and Atoms **431**, 59 (2018)

[229] *Fisher scientific, diba omnifit benchmark microbore chromatography columns 3 mm, (2023).*, `https://www.fishersci.com/shop/products/omnifit-benchmark-microbore-chromatography-columns-4`, accessed: 2023-09-07

[230] S. Mateti, K. Yang, X. Liu, S. Huang, J. Wang, L.H. Li, P. Hodgson, M. Zhou, J. He, Y. Chen, *Bulk hexagonal boron nitride with a quasi-isotropic thermal conductivity*, Advanced Functional Materials **28**, 1707556 (2018)

[231] J. Ramos, A. Senos, T. Stora, C. Fernandes, P. Bowen, *Development of a processing route for carbon allotrope-based TiC porous nanocomposites*, Journal of the European Ceramic Society **37**, 3899 (2017)

[232] H.O. Pierson, *Handbook of refractory carbides & nitrides: properties, characteristics, processing and applications* (William Andrew, 1996)

[233] J. Zhu, C. Deng, Y. Liu, N. Lin, S. Liu, *Effects of annealing temperature on recrystallization texture and microstructure uniformity of high purity tantalum*, Metals **9**, 75 (2019)

[234] R.D. Scheele, A.M. Casella, *Assessment of the use of nitrogen trifluoride for purifying coolant and heat transfer salts in the fluoride salt-cooled high-temperature reactor*, Tech. rep., Pacific Northwest National Lab.(PNNL), Richland, WA (United States) (2010)

[235] R. Babu, C. Gupta, *Beryllium Extraction—A Review*, Mineral Procesing and Extractive Metallurgy Review **4**, 39 (1988)

[236] K.A. Walsh, E.E. Vidal, B. Mishra, *Beryllium compounds*, ChemInform **42**, no (2011)

Appendix 1

A

Contents

A.1 ^{nat}V(d,x) reaction product γ-ray and x-ray energies.

Cr-51		**Cr-49**		**V-49**		**V-48**		**Sc-48**		**Sc-47**		**Sc-46**		**Ca-47**		**Ca-45**	
Decay:	ec/β+	Decay:	ec/β+	Decay:	ec	Decay:	ec/β+	Decay:	β-	Decay:	β-	Decay:	β-	Decay:	β-	Decay:	β-
Gamma lines																	
Eg (keV)	Ig (%)	Eg (keV)	Ig (%)	Eg (keV)	Ig (%)	Eg (keV)	Ig (%)	Eg (keV)	Ig (%)	Eg (keV)	Ig (%)	Eg (keV)	Ig (%)	Eg (keV)	Ig (%)	Eg (keV)	Ig (%)
320.082	**10**	62.289	**16.39**			802.87	0.15	175.361	**7.485**	159.377	**68.3**	889.277	**99.984**	41.06	0.0059	12.4	3.00E-06
		90.639	**53.2**			928.29	0.77	**983.517**	**100.1**			1120.545	**99.987**	489.23	**6.2**		
		152.928	**30.32**			938	0.0008	1037.599	**97.6**			2010	1.30E-05	530.6	0.091		
		595.35	<0.00027			944.104	**7.76**	1212.88	2.38					731.6	0.0121		
		657.6	<0.00027			**983.517**	**99.98**	**1312.096**	**100.1**					767.1	0.191		
		1021.63	<0.0011			1063.19	0.005							807.86	**6.2**		
		1026.8	0.00011			**1312.096**	**97.5**							1297.09	**71**		
		1361.61	0.045			1437.487	0.12							1878.2	0.027		
		1423.6	0.01			2240.375	2.41										
		1508.37	0.008			2375.211	0.01										
		1514.4	0.026			2420.9	0.01										
		1570.83	0.02														
		2090.7	0.0004														
		2142.9	0.00092														
		2181.6	<0.000027														
		2218.6	0.00019														
		2234.4	0.00022														
Main X-rays																	
Eg (keV)	Ig (%)	Eg (keV)	Ig (%)	Eg (keV)	Ig (%)	Eg (keV)	Ig (%)	Eg (keV)	Ig (%)	Eg (keV)	Ig (%)	Eg (keV)	Ig (%)	Eg (keV)	Ig (%)	Eg (keV)	Ig (%)
4.945	6.9	4.945	0.86	4.505	5.80	4.505	3.04	4.505	0.00397	0.452	0.00026	4.505	0.00159	4.086	0.00051	4.086	3.14E-05
4.952	13.6	4.952	1.71	4.511	11.50	4.511	6	4.511	0.0079	4.505	0.0262	4.511	0.00315	4.091	0.00101	4.091	6.30E-05
		5.427	0.099	4.93	2.30	4.932	0.342	4.932	0.000446	4.511	0.052	4.932	0.000351			4.461	3.44E-06
		5.427	0.193			4.932	0.67	4.932	0.00088	4.932	0.00294					4.461	6.70E-06
										4.932	0.0058						
Decay product																	
V-51		**V-49**		**Ti-49**		**Ti-48**		**Ti-48**		**Ti-47**		**Ti-46**		**Sc-47**		**Sc-45**	
		Ti-49												**Ti-47**			

Figure A.1: ^{nat}V(d,x) reaction product inventory and the respective radionuclide γ-ray and x-ray lines [19].

Appendix 2

B

Contents

Multiple Target and Ion Source System modes of failure with the VADIS ion source used for Sc molecular beam studies were observed. The most frequent modes of failure were investigated in a more detailed manner and together with the observed results and conclusions are discussed. These investigations allowed to take measures to limit such failures or counter them during radionuclide mass separation and collections.

B.1 Investigation of leak rate decrease for the TISS calibrated gas leaks

The calibrated gas leak is an integral part of a TISS and molecular ion beam formation for refractory element extraction. Therefore the calibrated gas leak degradation was investigated more thoroughly. In a separate experiment, the thermal radiation heat from the hot target container was observed to melt Polyether ether ketone (PEEK) structures attached to the actively cooled Al base plate. This suggests, that the temperature at the base plate reaches over 340 °C during operations. The melting temperature of stainless steel is in the range of 1375–1400 °C. In addition, hexagonal BN has a high thermal conductivity of 390 $Wm^{-1}K^{-1}$ [230]. The sintering of conventional powders is expected at about 50-80 % of the material melting point (T_m) [231]. Because of these properties and fact that consistent gas leak rate changes were not observed with other gases (CF_4, He, Ne, Ar, Kr and Xe) at high target container temperatures, the direct sintering could be excluded.

The temperature is, however, sufficient to induce chemical reactions with the NF_3 gas and components of the stainless steel, such as iron (Fe), chromium (Cr), nickel (Ni) and molybdenum (Mo), leading to larger particulate formation and reduced gas leak rate. For instance, ^{nat}TiN formation has been observed after stable isotope beam tests with NF_3 (see Figure B.1a) and Mo gas supply tubing melting at the point where it was attached to the hot target container (see Figure B.1) [232].

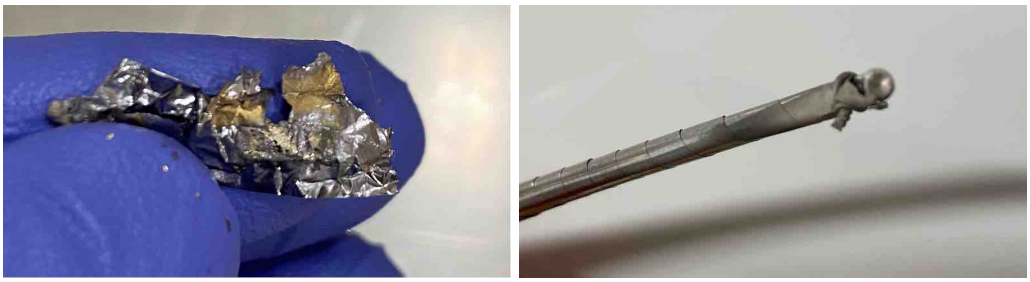

(a) Traces of ^{nat}TiN on a Ta foil from ^{nat}Ti foil.

(b) Molten Mo gas supply tubing at the connection with the target container.

Figure B.1: Reaction effects on Ti and Mo from NF_3 gas at high target container temperatures.

The created volatile gaseous particles from a hot target container or gas supply line tubes can also migrate back to the calibrated gas leak, where they condense on the surface of stainless steel, in the calibrated gas leak pores or the BN insulator. It was observed that the inside of a BN insulator was coated after such calibrated gas leak failure (see Figure B.2a), confirming the particle deposition. The deposited particles also created a conductive layer allowing the target container heating current to flow and cause the gas leak to heat up and promote the reactivity.

The calibrated gas leak removal from the TISS and placement in the Offline-1 front-end gas supply line allowed them to retain their leak rate values unchanged, even by operating the target container at temperatures over 1600 °C (see Figure B.2b).

Placement of gas leaks separate from a TISS in the gas supply system is not feasible for radionuclide mass separation and collections due to TISS integrity deprivation, time-

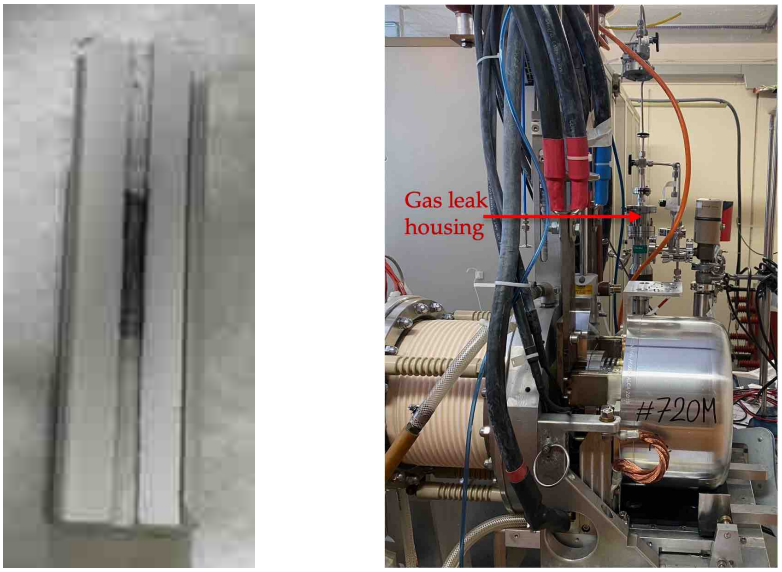

(a) BN insulator cut open after a gas leak failure

(b) Calibrated gas leak external housing position on Offline-1 front-end

Figure B.2: VD-5 TISS BN insulator and Offline-1 frontend.

consuming calibrated gas leak exchange and radiation safety hazards. In such a case, the target material would be exposed to air and oxidation during irradiation. As the target material heats up during irradiation (roughly 80–120 °C), there is a risk of releasing volatile radionuclides out of the TISS. Another issue is stable oxide molecule formation, which can then affect the radionuclide release and collection efficiency.

B.2 VADIS ion source modes of failure

VADIS cathode-anode contact

The VADIS ion source at 150 V potential can reach the accelerated electron current space-charge limit at ∼2025 °C when the distance of cathode and anode is at standard 1.5 mm [103]. At this configuration, the ion source can fail by forming direct contact between the cathode and anode due to the thermal expansion of Ta metal exposed to high temperatures and reactive gases.

A failed VADIS from TISS #723M, before dismantling was examined by Computed Tomography (CT) and X-ray tomography and the obtained images in Figure B.3 revealed that due to the transfer line thermal dilatation (expansion), the cathode surface was pushed towards to the anode grid until full contact was obtained. The contact creates a short circuit and no electron acceleration is anymore possible. The transfer line stayed in the lateral bend position (see Figure B.3a).

Disassembly of the failed ion source revealed that a metallic crystal had fused with the anode grid. The particle was torn from the re-crystallized Ta cathode (see Figure B.4) [233].

This kind of ion source failure is best fixed by opening the TISS and replacing the ion source. Typically the Ta cathode fuses with the transfer line and target container (not the

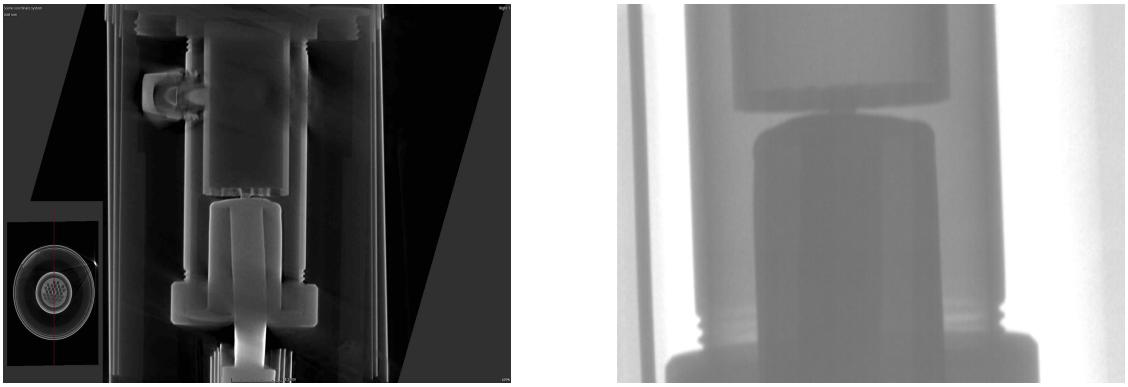

(a) CT image of failed ion source (b) X-ray image of VADIS failed ion source

Figure B.3: CT and X-ray investigation of short circuit for VADIS before dismantling.

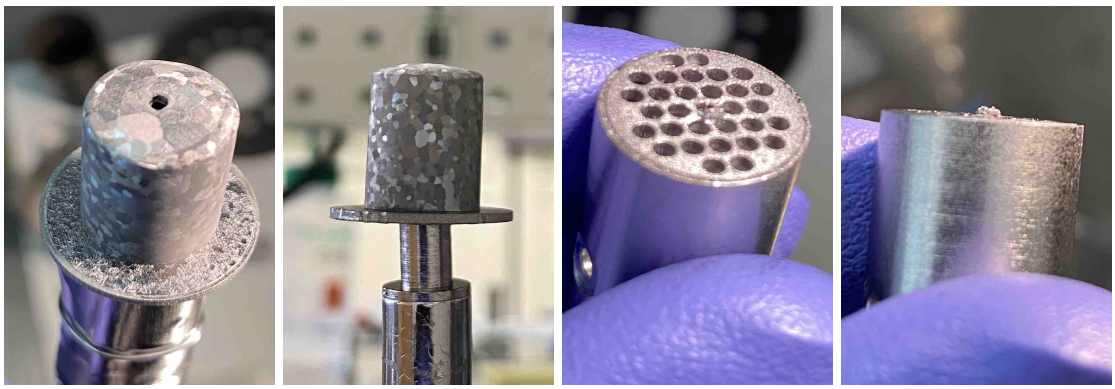

(a) Ta cathode - top (b) Ta cathode - side (c) Anode body - top (d) Anode body - side

Figure B.4: Re-crystallized cathode and anode body from a failed VADIS disassembly.

case for TISS with Re ion source), and both have to be replaced and calibrated again. For VD-5 TISS, that could be opened (non-radioactive, low dose rate, low contamination, and external sample TISS), the target container can also be pulled backward by 0.5-1.0 mm. This mode of recovery decreases the ion source efficiency because the gap between the anode and cathode is increased, however, the TISS could still be used in certain experiments. The efficiency for noble gasses decreased by a factor of $\times 3$ when the container was pulled back by 1 mm. During radionuclide collections, the contact between the cathode and anode could be reversed by reducing the transfer line temperature and may be the only possible recovery to continue a collection. Afterward, the temperatures could be slowly increased to a point before another short circuit is observed. The lower cathode temperatures decrease the efficiency of the ion source (see Chapter 2, section 2.2.3).

Insulator coating

The most frequent case of VADIS ion source failure was caused by the damage to the BeO insulator that holds the anode body in its place. Due to metallic particle and molecule condensation on the insulators or BeO reaction with the applied reactive gases, the insulator surface can become conductive and cause increasing drain current (elec-

tron current drawn from the cathode over a given geometry) and eventually - a short circuit. This prevents the operation of the ion source at the desired electric potential. In contrast, to cathode-anode contact, the ion source most of the time would still be operational, but with a limited acceleration potential.

Too rapid volatile molecule formation may cause the number of particles reaching the ion source in higher quantities than can get ionized and extracted. The excess neutrals migrate within the VADIS body and can cause a buildup and condensation on colder ion source structures, such as the BeO insulators shown in Figure B.5. The onset of these excess particles can be monitored by measuring the total beam and controlled by limiting it below 15 μA for an efficient ion source operation. As a reference for ion source efficiency comparison, the noble gas ionization efficiencies are used - He (0.1%), Ne (1.7%), Ar (7.3%), Kr (16.9%) and Xe (32.0%) [103].

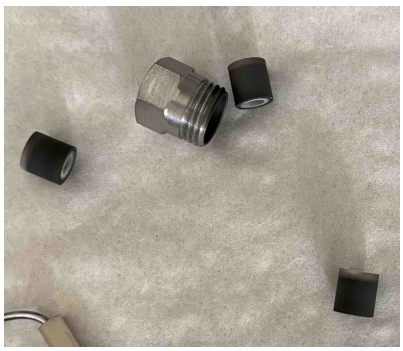

(a) Black permanent coating on the insulators after CF_4 use

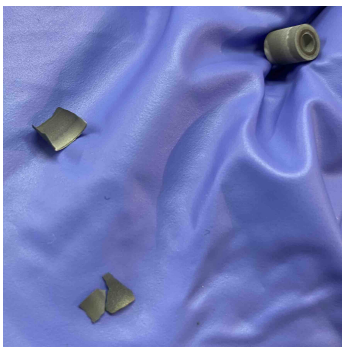

(b) Gray brittle insulator coating after NF_3 use

Figure B.5: BeO insulators from a failed VADIS ion source after stable isotope ion beam tests with reactive gases. Non-coated BeO insulators are white.

BeO is reactive towards halogens such as Cl^- and F^-, causing an increase of contaminants in the total beam as well as degradation of the insulators [234, 235]. Also, the carbon from CF_4 can cause the BeO to convert to Be_2C [236]. Nevertheless, the highest impact in an empty TISS comes from Ta and TaO, creating volatile tantalum fluorides and oxy-fluorides. A sample was analyzed with SEM–EDX indicating mainly deposits from Ta and C in the coating. When target materials, such as Ti or V are present, the formation of volatile TI and V halides and oxy-halides also must be taken into consideration.

The insulator replacement involves complete disassembly of the VADIS, therefore not feasible for irradiated TISS. During the collection, the coating can also be reversed by bake-out procedure. It involves the heating from the cathode/transfer line and target container as well as short circuit power deposition on the coating itself. The most impactful is the power that is causing a local overheating and release of the coating.

The recovery for a hot transfer line is done, by setting a safe drain current limit on the anode power supply (260–500 mA) and requesting the anode potential to a typical value of 100–200 V. The potential is limited by the drain current and over time increases, as the deposits are removed and released as shown in Figure B.6. The recovery can take anywhere from a few minutes up to a few days. In cases, where metallic particles were suspected to be deposited on the insulators, the target container temperature was

lowered and reactive gas was applied, shifting the chemical reactivity towards the ion source region and volatilizing and the coating for a faster recovery. In the majority of cases, the TISS were manipulated in these conditions to reduce the coating until satisfactory drain current and potential stability conditions were reached to continue with the mass separation.

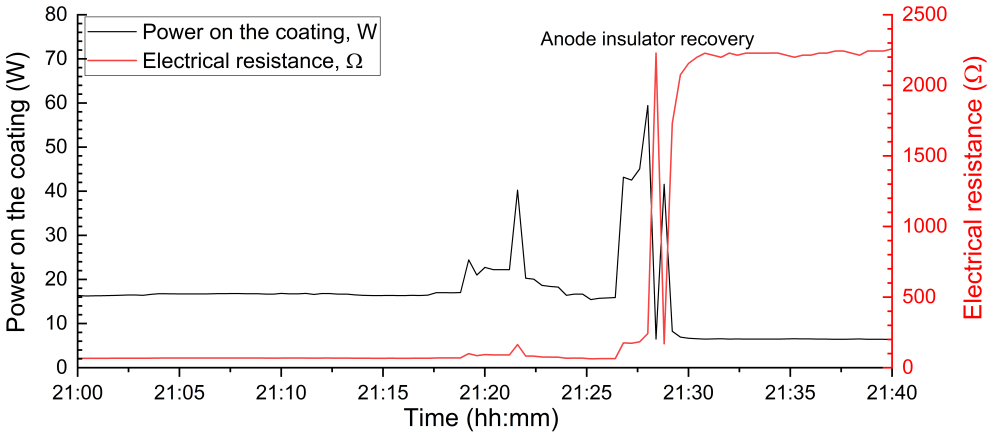

Figure B.6: VADIS anode electrical resistivity and power on the coating during the recovery of insulators.

Scientific arcticles

C

Contents